Physics, Compact Modeling and TCAD of SiGe HBT for Wide Temperature Range Operation

by

Lan Luo

A dissertation submitted to the Graduate Faculty of
Auburn University
in partial fulfillment of the
requirements for the Degree of
Doctor of Philosophy

Auburn, Alabama
December 12, 2011

Keywords: SiGe HBT, Cryogenic Temperature, Compact Modeling, TCAD, Carrier freezeout

Approved by

Guofu Niu, Chair, Alumni Professor of Electrical and Computer Engineering
Bogdan Wilamowski, Professor of Electrical and Computer Engineering
Fa Foster Dai, Professor of Electrical and Computer Engineering
Vishwani Agrawal, James J. Danaher Professor of Electrical and Computer Engineering

Abstract

One of the remarkable characteristics of SiGe HBT is the ability to operate over a wide temperature range, from as low as sub 1K, to as high as over 400 K. The SiGe HBT investigated and measured in this work is a first-generation, 0.5 μm SiGe HBT with f_T/f_{max} of 50 GHz/65 GHz and BV_{CEO}/BV_{CBO} of 3.3 V/10.5 V at 300 K. The base doping is below but close to the Mott-transition (about $3 \times 10^{18}\ cm^{-3}$ for boron in silicon). In this dissertation, some important SiGe HBTs physics at cryogenic temperature are analyzed. New compact models equations for SiGe HBT are developed, which can function from 43 to 393K. Device TCAD simulations are used to help understand the device physics at cryogenic temperatures.

First, the temperature dependence of semiconductors critical metrics are reviewed, including bandgap energy E_g, effective conduction band density-of-states N_C and valence band density-of-states N_V, intrinsic carrier concentration at low doping n_i, bandgap narrowing ΔE_g, carrier mobility μ, carrier saturation velocity v_{sat} and carrier freezeout. The *dc* and *ac* low temperature performance of SiGe HBT are analyzed, including collector current density, current gain, Early effect, avalanche multiplication factor, transit time, cut-off frequency and maximum oscillation frequency. This illustrates why SiGe HBT demonstrates excellent analog and RF performance at cryogenic temperatures.

The current dependence of multiplication factor M-1 at low temperatures are investigated based on a substrate current based avalanche multiplication technique. The M-1 at high current is considerably lower than it at low current. Then, the temperature dependence of forced-I_E pinch-in maximum operation voltage limit, which is of interest for many space exploration application is investigated. In particular, we discuss how the critical base current I_B^* varies with temperature, and introduce the concept of critical multiplication factor (M-1)*, critical collector-base bias V_{CB}^* where M-1 reaches (M-1)*. A decrease of the voltage limit is observed with cooling, and attributed to the

increase of intrinsic base resistance due to freezeout as well as increase of avalanche multiplication factor M-1. A practically high emitter current I_E is shown to alleviate the decrease of V_{CB}^* with cooling, primarily due to the decrease of M-1 with increasing I_E.

The existing commercial compact models are shown to fail below 110 K. In this work, new temperature scaling equations are developed. As much physics basis are implemented as possible to fit temperature dependence of SiGe HBTs *dc* and *ac* characteristics, such as ideality factor, saturation current, series resistances and thermal resistance. In particular, carrier freezeout is now modeled accounting for latest research on Mott transition, leading to successful modeling of temperature dependences for all series resistances in SiGe HBT. These new temperature equations give reasonably accurate fitting of the *dc* characteristics from 393 to 43 K, *ac* characteristics from 393 to 93 K.

Furthermore, the impact of the non-ideal temperature dependence of I_C-V_{BE} in SiGe HBTs on the output of a BGR is examined. These non-idealities actually help make the BGR output voltage vary less at cryogenic temperatures than traditional Shockley theory would predict. Successful cryogenic temperature modeling of both ΔV_{BE} and V_{BE} components of the BGR output is demonstrated for the first time.

Acknowledgments

I would like to express my gratitude to my supervisor, Dr. Guofu Niu. Without his guidance, this dissertation would not have been finished smoothly. I thank him for his patience and encouragement that carried me on through difficult times, and for his insights and suggestions that helped to shape my research skills. I appreciate his vast knowledge and skill in many areas, and his valuable feedback that greatly contributed to my research and this dissertation. I would like to thank the other members of my committee, Dr. Bogdan Wilamowski, Dr. Fa Foster Dai and Dr. Vishwani Agrawal for the valuable assistance they provided.

I would like to extend my gratitude to former and current members in our SiGe HBT research group. I would like to thank Ziyan Xu for our memorable collaborations in SiGe compact modeling, Yan Cui, Kejun Xia and Tong Zhang for their fruitful discussions in semiconductor device physics and TCAD. And I would like to thank Xiaoyun Wei for her patient guide in device DC/RF/Noise characterization. I am also very grateful to the strong support from Professor John D. Cressler's SiGe group at Georgia Tech, especially the cryogenic temperature device and circuit measurements.

This work was supported by NASA, under grant NNL05AA37C and NNL06AA29C. I am grateful for the support of NASA, JPL and the IBM SiGe development group, as well as the many contributions of the SiGe ETDP team.

Finally, I am greatly indebted to my parents, Yuling Luo and Zhijiang Zhang, for the support they provided me through my entire life. I would like to thank my sister, Qian Luo, who is always there when I need help. In particular, I would like to thank my husband, Wei Jiang, who has been my best friend since college. I would sincerely thank my little son, Richard Z. Jiang, whose arrival is a precious gift from God.

Table of Contents

List of Figures

List of Tables

Chapter 1

Introduction

1.1 Motivation

SiGe heterojunction bipolar transistor (HBT) technology is currently being used to develop electronics for space applications due to the excellent analog and RF performance of SiGe HBTs over an extremely wide range of temperatures, along with its built-in radiation hardness [5] [6]. SiGe HBT technology has recently been used to develop electronic sub-systems for NASA's envisioned lunar missions. For instance, SiGe electronic components can operate reliably in the extreme ambient environment found on the lunar surface, where the extremely cold environmental temperature drops to -180° C (93 K) during the lunar night and -230° C (43 K) in the shadowed polar craters. To enable the design of circuits that can operate over such a wide temperature range, we need to investigate the physics of SiGe HBTs at low temperatures, and importantly also develop robust compact models that can work over a wide temperature range with good fidelity, particularly at lower temperatures.

The SiGe HBT investigated and measured in this work is a first-generation, 0.5 μm SiGe HBT with f_T/f_{max} of 50 GHz/65 GHz and BV_{CEO}/BV_{CBO} of 3.3 V/10.5 V at 300 K, with base doping below but close to the Mott-transition (about $3 \times 10^{18}\ cm^{-3}$ for boron in silicon). The emitter area is $0.5 \times 2.5\ \mu\text{m}^2$. The schematic cross section of this SiGe HBT is shown in Fig. 1.1. The vertical doping and Ge profile from secondary ion mass spectrometry (SIMS) is shown in Fig. 1.2.

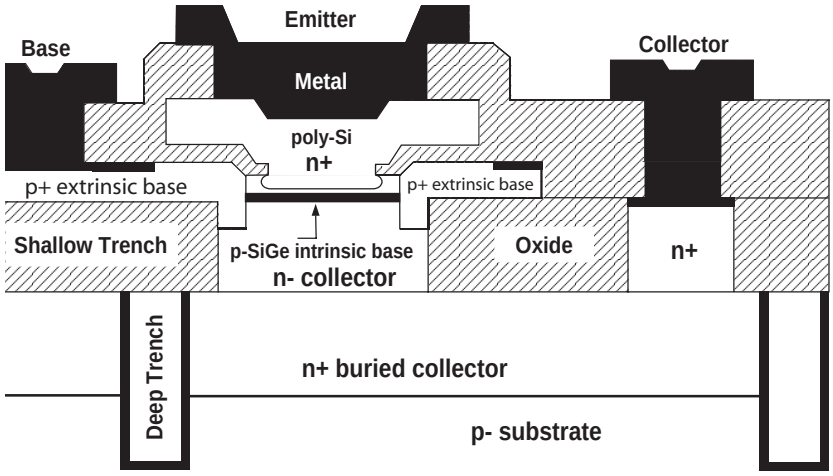

Figure 1.1: Cross section of a first-generation SiGe HBT used in this work.

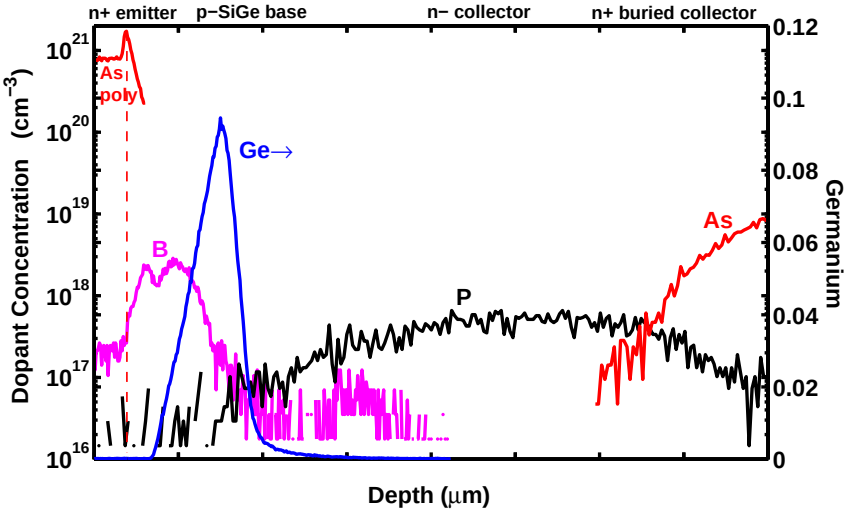

Figure 1.2: Vertical doping and Ge profile of a first-generation SiGe HBT used in this work.

1.2 SiGe HBT physics over temperature

Bandgap engineering has a positive impact on the low temperature characteristics of transistor. As will be shown in chapter 2, the SiGe HBT is ideally suited for cryogenic operation as the bandgap engineering induced improvements in current gain β, cutoff frequency f_T, and Early voltage V_A all become more pronounced with cooling [7].

In this work, the impact of temperature on bandgap energy E_g, electron and holes density of states N_C/N_V, intrinsic carrier concentration n_i, bandgap narrowing BGN, carrier mobility μ, carrier saturation velocity v_{sat} and carrier freezeout effect will be reviewed first. Following, the dc and ac low temperature performance of SiGe HBT will be analyzed theoretically and experimentally.

1.3 SiGe HBT compact modeling over temperature

Today‘s IC design heavily relies on circuit simulation and circuit simulation needs compact device models. The industry standard bipolar transistor modeling is based on SPICE Gummel-Poon (SGP) model [8]. Several advanced models, such as VBIC (vertical bipolar inter-company) [9], HICUM (high current model) [10] and MEXTRAM (most exquisite transistor model) [3] have been proposed.

The Mextram model was introduced by Philips Electronics in 1985 [11]. Appearing to be the fifth existing bipolar transistor model (after the previous four described in Ref. [12]). The first Mextram release was introduced as Level 501 in 1985. Mextram has appeared later in several update releases: Level 502 in 1987 [13], Level 503 in 1994, and Level 504 in 2000 [3]. The latest version of Mextram is 504.9.1 which was released in January, 2011.

In this work, the main purpose is to develop a temperature scalable SiGe HBT model that can work over the desired cryogenic temperature range. We choose Most EXquisite TRAnsistor Model (Mextram) [3] as our basis because of its excellent description of vertical bipolar transistors around room temperature. We are particularly interested in its unique collector epilayer modeling [14], which is very important for Kirk effect and quasi-saturation. Germanium induced effects in the

base are also taken into consideration. The new models developed in this work, however, can be readily ported to other compact models, e.g. VBIC.

1.4 Dissertation contributions

Chapter 1 gives the motivation of this work, including an overview of topics related to low temperature physics and compact modeling.

Chapter 2 reviews the impact of temperature on semiconductor bandgap energy E_g, electron and holes density of states N_C/N_V, intrinsic carrier concentration n_i, bandgap narrowing BGN, carrier mobility μ, carrier saturation velocity v_{sat} and carrier freezeout effect firstly. Following, the dc and ac low temperature performance of SiGe HBT are analyzed.

Chapter 3 extends the substrate current based avalanche multiplication technique [15] down to 43 K and gives the current dependence of avalanche multiplication factor M-1 at low temperatures. In chapter 4, the forced-I_E pinch-in maximum output voltage limit in SiGe HBTs operating at cryogenic temperatures is investigated. A decrease of the voltage limit is observed with cooling, and attributed to the increase of intrinsic base resistance due to freezeout as well as increase of avalanche multiplication factor M-1. A practically high I_E is shown to alleviate the decrease of V_{CB}^* with cooling, primarily due to the decrease of M-1 with increasing emitter current I_E [16].

In chapter 5, some new temperature scaling models are presented [1][2] [17]. In particular, the temperature characteristics of mobility and ionization rate are investigated. The classic ionization model, together with a single power law mobility model, enables resistance vs. temperature modeling of the substrate and the collector region, where doping levels are below Mott-transition. Based on the Altermatt ionization model, a new incomplete ionization model that accounts for the temperature dependence of the bound state fraction factor is developed. This new model enables accurate temperature dependent modeling of the intrinsic base sheet resistance, which has a doping level close to the Mott-transition. For the buried collector and the silicided extrinsic base, where doping levels are well above the Mott-transition, two approaches are proposed and both give good results. In chapter 6, a new parameter extraction strategy is implemented. With the extracted model

parameters, we obtain reasonably accurate fitting of the *dc* characteristics from 393 to 43 K. Good *ac* fitting from 393 to 93 K have been achieved.

Chapter 7 examines the impact of the non-ideal temperature dependence of I_C-V_{BE} in SiGe HBTs on the output of a BGR. These non-idealities are shown to actually help make the BGR output voltage vary less at cryogenic temperatures than traditional Shockley theory would predict. Successful cryogenic temperature modeling of both ΔV_{BE} and V_{BE} components of the BGR output is demonstrated for the first time [18].

Chapter 8 concludes the work in this dissertation.

Chapter 2

Device Physics of SiGe HBT at Cryogenic Temperatures

In this chapter, the temperature characteristics of semiconductors critical metrics are reviewed first, including bandgap energy E_g, effective conduction band density-of-states N_C and valence band density-of-states N_V, intrinsic carrier concentration at low doping n_i, bandgap narrowing ΔE_g, carrier mobility μ, carrier saturation velocity and carrier freezeout. Further, the *dc* and *ac* low temperature performance of SiGe HBT are analyzed. Bandgap engineering generally produces positive influence on the low temperature operations of bipolar transistors [7]. As will be shown, SiGe HBTs work very well in the cryogenic temperature.

2.1 Semiconductor physics at cryogenic temperatures

2.1.1 Bandgap energy

The bandgap E_g is the difference between the conduction band edge energy E_C and the valence band edge energy E_V. The most popular nonlinear bandgap temperature relation of silicon is [19]:

$$E_{g,Si}(T) = E_{g0,Si} - \frac{\alpha T^2}{T+\beta}, \tag{2.1}$$

where $E_{g0,Si}$ is the bandgap of silicon at 0 K, and α and β are material parameters with $\alpha = 4.45 \times 10{-}4$ V/K, $\beta = 686$ K.

From optical experiments of MacFarlane [20], above a certain temperature ($T > T_0$), the bandgap can be approximated by a linear function of temperature $E_g = E_{g,0} - \alpha T$. Such approximation is widely used in bipolar transistor's compact modeling. However, nonlinear behavior of E_g-T can be observed below T_0=250 K, as shown in Fig. 2.1.(a), and will impact the compact modeling at low temperature.

The resultant energy band structure obtained in a strained SiGe alloys with respect to its original Si constituent is clearly key to its usefulness in transistor engineering. For the purpose of designing a SiGe HBT, we desire a SiGe alloy which [7]:

• Has a smaller bandgap than that of Si;

• Has a band offset that is predominantly in the valence band;

• Either improves or at least does not substantially degrade the carrier transport parameters (motilities or lifetime) with respect to Si.

As will be seen below, strained SiGe fulfills all of these requisite conditions.

Because Ge has a significantly smaller bandgap than Si, the bandgap of SiGe will be smaller than that of Si. The Ge-induced band offsets can be written as $\Delta E_g \approx \Delta E_V = 0.74 x_{mol}$, where x_{mol} is the Ge mole fraction. Hence,

$$E_{g,SiGe}(T) = E_{g,Si}(T) - 0.74 x_{mol}. \tag{2.2}$$

Fig. 2.1.(b) illustrates the Ge and temperature dependence of bandgap $E_{g,SiGe}$.

2.1.2 Density-of-states

It is generally agreed upon that the effective conduction and valence band density-of-states product ($N_C N_V$) is reduced strongly due to strain-induced distortion of both the valence and conduction band extreme, a consequence of which is the reduction in the electron and hole effective masses [21].

The N_C and N_V ratio between SiGe and Si are given by [22] [23]:

$$\begin{aligned} \frac{N_{C,SiGe}}{N_{C,Si}} &\approx \frac{4 + 2e^{-\frac{\Delta E_{cb}}{kT}}}{6}, \\ \frac{N_{V,SiGe}}{N_{V,Si}} &\approx \frac{1 + e^{-(\frac{\Delta E_{hl}}{kT})} + e^{-(\frac{\Delta E_{so,SiGe}}{kT})}}{2 + e^{-(\frac{\Delta E_{so,Si}}{kT})}}, \end{aligned} \tag{2.3}$$

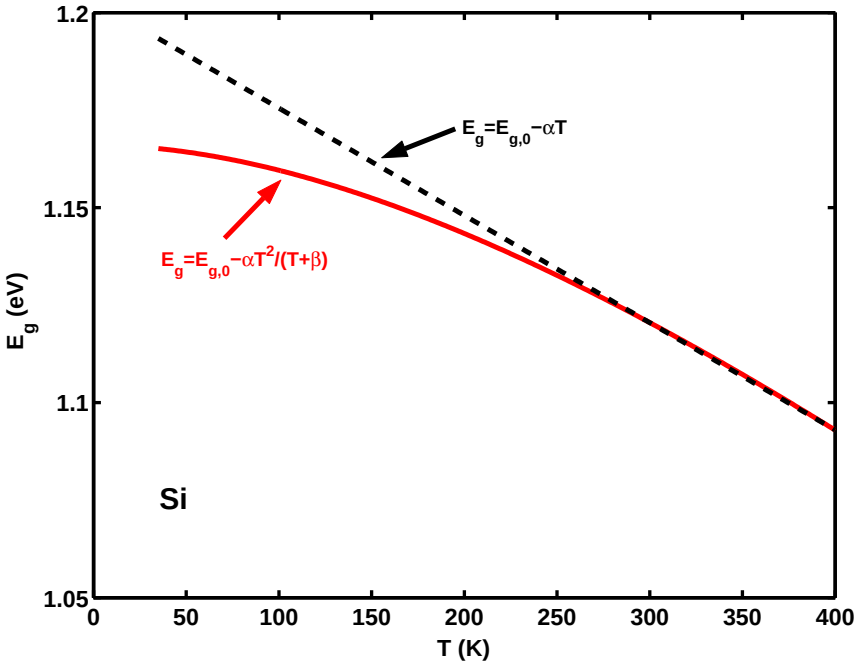

(a)

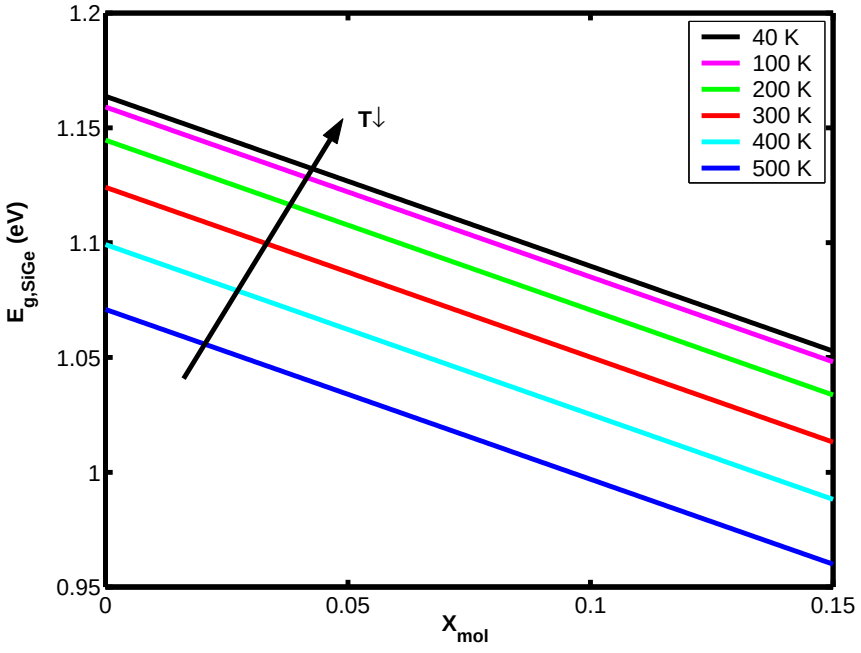

(b)

Figure 2.1: (a) Bandgap of silicon $E_{g,Si}$ versus T. (b) Ge and temperature dependence of SiGe bandgap $E_{g,SiGe}$.

where ΔE_{hl} is the splitting between the heavy and light hole valence bands in SiGe, and $\Delta E_{so,SiGe}$ and $\Delta E_{so,Si}$ are the distances between the split-off band and valence band edge in SiGe and Si respectively, and ΔE_{cb} is the conduction band splitting due to the biaxial strain. The resulting $(N_C N_V)_{SiGe}/(N_C N_V)_{Si}$ is weakly dependent on temperature.

Fig. 2.2.(a) - (c) explain the Ge and temperature dependence of $N_{C,SiGe}/N_{C,Si}$, $N_{V,SiGe}/N_{V,Si}$ and $(N_C N_V)_{SiGe}/(N_C N_V)_{SiGe}$ respectively. N_C and N_V decreases with increasing Ge mole fraction first, and then "saturates" when the band split exceeds a couple of kT. Such substantial reduction in $N_C N_V$ with increasing Ge mole fraction can be considered undesirable since it translate directly to a reduction in collector current in the SiGe HBT, and hence reduce the current gain. Fortunately, however, the same reduction in effective masses that produces the decrease in $N_C N_V$ also increases the carrier motilities, which partially offset the impact on the collector current.

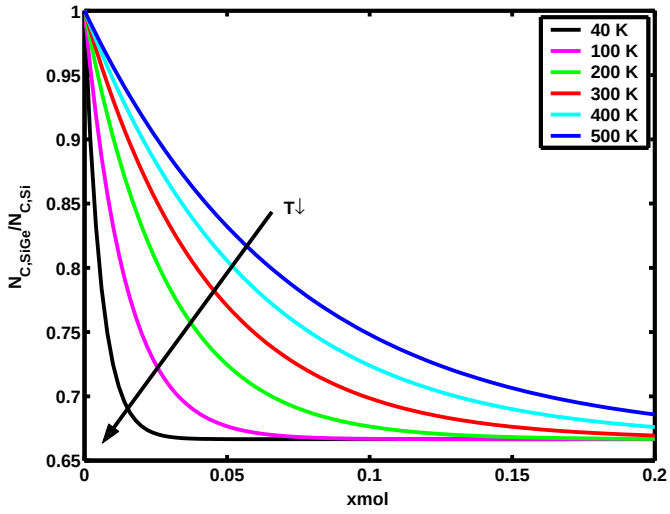

(a)

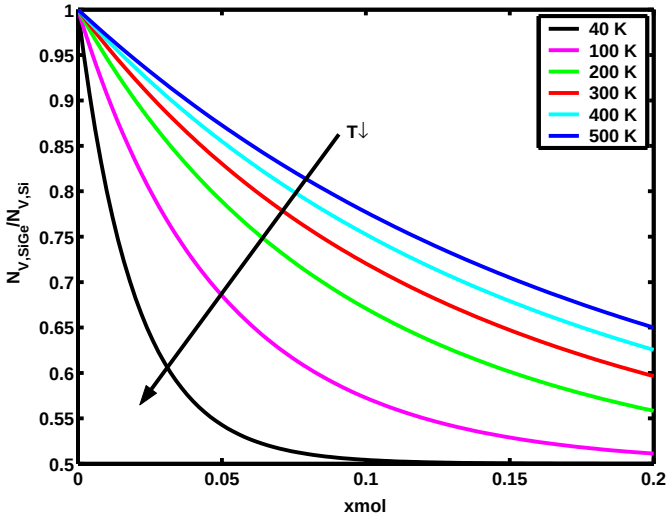

(b)

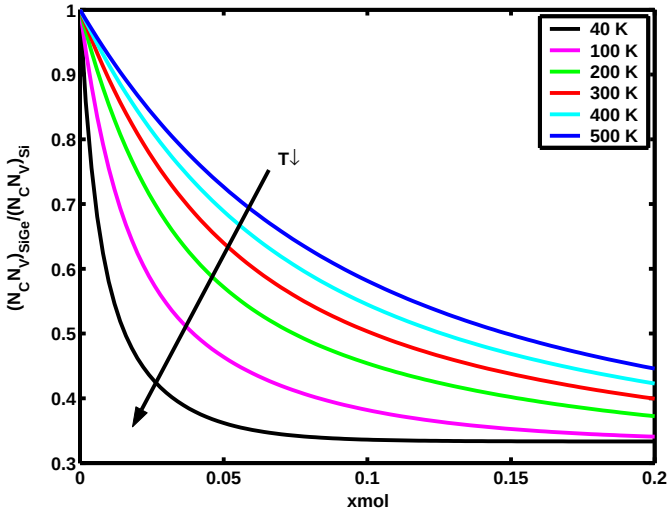

(c)

Figure 2.2: (a) Ge and temperature dependence of $N_{C,SiGe}/N_{C,Si}$. (b) Ge and temperature dependence of $N_{V,SiGe}/N_{V,Si}$. (c) Ge and temperature dependence of $(N_C N_V)SiGe/(N_C N_V)SiGe$.

2.1.3 Intrinsic carrier concentration at low doping

The band gap and band edge density-of-states are summarized in the intrinsic density $n_i(T)$ (for undoped semiconductors):

$$n_{i0}(T) = \sqrt{N_C(T)N_V(T)}\exp\left(-\frac{E_g(T)}{2kT}\right). \tag{2.4}$$

Fig. 2.3 show the temperature dependence of intrinsic carrier concentration at low doping n_{i0} using (2.1), (2.2), (2.3) and (2.4). n_{i0} increases dramatically with increasing Ge content, especially at low temperatures. At 30K, n_{i0} boosts by 12 orders of magnitude and 6 orders of magnitude for $x_{mol} = 20\%$ and $x_{mol} = 10\%$, respectively.

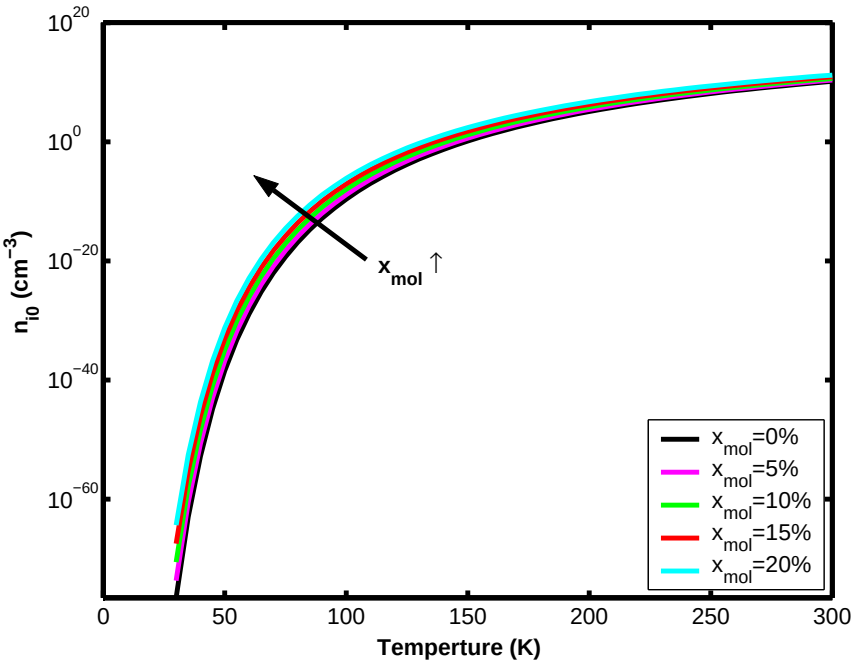

Figure 2.3: Temperature dependence of intrinsic carrier concentration at low doping n_{i0}.

2.1.4 Bandgap narrowing

It is well known that the bandgap narrows at heavy doping, which increases the *pn* products at equilibrium. This is often referred to as heavy doping induced bandgap narrowing ΔE_g.

The most widely used bandgap narrowing (BGN) model is the Slotboom bandgap narrowing model [24] which is experimentally determined from the I_C-V_{BE} of NPN bipolar transistors. Slotboom bandgap narrowing model is derived based on some assumptions. Firstly, it assumes that the minority carriers in the base obey the Boltzmann distribution law, which however is not valid for heavily doped semiconductor or low temperature environment. Secondly, a linear temperature dependence of bandgap energy $E_g = E_{g,0} - \alpha T$ is approximated in the equation of intrinsic carrier concentration n_i. Thirdly, the total number of holes Q_B in base region is assumed as constant across temperature which is not valid at low temperatures due to carrier freezeout effect.

Boltzmann statistics is no long accurate for heavily doping and Fermi-Dirac statistics is needed instead. The idea of Slotboom BGN model is to artificially decrease the apparent electrical bandgap narrowing $\Delta E_{g,app}$ by $\Delta E_{g,FD}$ (correction to reduce the error introduced by Boltzmann statistics) so that one can continue to apply Boltzmann statistics to describe the equilibrium *pn* product at heavy doping. The apparent bandgap narrowing $\Delta E_{g,app}$ can be given as [24].

$$\Delta E_{g,app} = E_{ref}\left[\ln\left(\frac{N_{tot}}{N_{ref}}\right) + \sqrt{\left(\ln\left(\frac{N_{tot}}{N_{ref}}\right)\right)^2 + 0.5}\right]. \tag{2.5}$$

Hence the true bandgap narrowing $\Delta E_{g,true}$ can be written as:

$$\Delta E_{g,true} = \Delta E_{g,app} - \Delta E_{g,FD}. \tag{2.6}$$

and

$$\begin{aligned}
&\Delta E_{g,FD} \\
&= \begin{cases} kT\left[\ln\left(\frac{n}{N_C}\right) - F_{1/2}^{-1}\left(\frac{n}{N_C}\right)\right] & n\text{-type doping,} \\ \\ kT\left[\ln\left(\frac{p}{N_V}\right) - F_{1/2}^{-1}\left(\frac{p}{N_V}\right)\right] & p\text{-type doping.} \end{cases}
\end{aligned} \tag{2.7}$$

Fig. 2.4 shows the doping dependence of bandgap narrowing $\Delta E_{g,app}$, $\Delta E_{g,true}$ and $\Delta E_{g,FD}$ respectively. One should use Boltzmann statistics in device simulation if the apparent BGN $\Delta E_{g,app}$ parameters are used. For device simulation using Fermi-Dirac statistics, the true BGN $\Delta E_{g,true}$ parameters should be used.

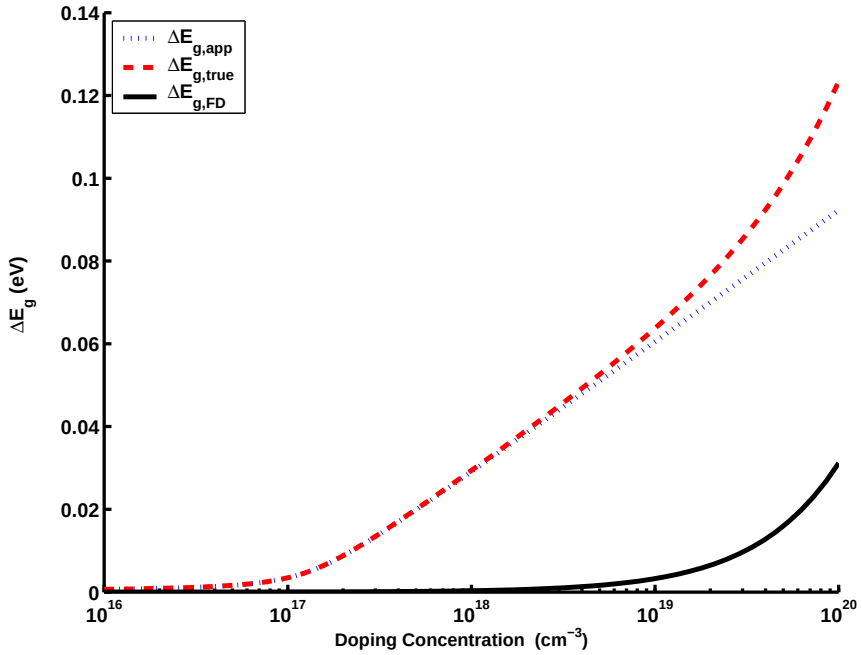

Figure 2.4: Doping dependence of bandgap narrowing ΔE_g.

2.1.5 Carrier freezeout and Mott-transition

Complete ionization of dopants in Si and SiGe is typically assumed at room temperature. However, when the Fermi level E_F is situated close to the dopant level, the dopant states are noticeably occupied, leading to incomplete ionization even at room temperature. The free carrier density is then noticeably smaller than the dopant density. This semiconductor physics is so called "carrier freezeout" and shows strong dependence on doping concentration and temperature.

The numerical solution of quasi-Fermi energy E_F and ionization rage IR are illustrated here. The analytical solution will be presented in 5.11.3 in detail.

$$p + N_D^+ = n + N_A^-, \tag{2.8}$$

$$n = N_C \exp\left(-\frac{E_C - E_F}{kT}\right), \tag{2.9}$$

$$p = N_V \exp\left(-\frac{E_F - E_V}{kT}\right), \tag{2.10}$$

$$N_D^+ = \frac{N_D}{1 + g_D \exp\left(\frac{E_F - E_D}{kT}\right)}, \tag{2.11}$$

$$N_A^- = \frac{N_A}{1 + g_A \exp\left(\frac{E_A - E_F}{kT}\right)}, \tag{2.12}$$

where E_A is acceptor impurity energy, g_A is acceptor degeneracy factor, E_D is donor impurity energy, g_D is donor degeneracy factor, n is electron density, p is hole density, N_D is active donor concentration, N_A is active acceptor concentration, N_D^+ is ionized donor concentration, N_A^- is ionized acceptor concentration.

Substituting (2.10) and (2.11) into left-hand-side of (2.8) and substituting (2.9) and (2.12) into right-hand-side of (2.8) respectively, we can plot out the $p + N_D^+$ and $n + N_A^-$ as function of $(E_F - E_I)$ for different doping concentrations and different temperatures. By applying (2.8), Fermi energy level E_F can be solved numerically. Fig. 2.5 illustrates this graphical solution strategy for three n-type doping levels at 300 K. Fig. 2.6 shows the variation of Fermi level $E_f - E_i$ versus doping concentration over 40-500 K.

Because the E_F locates near intrinsic Fermi level E_I at low concentration and high temperature, complete ionization assumption is valid for low doping and high temperature. However, when concentration increases together with cooling, E_F moves towards and even above dopant energy level E_D. Hence, incomplete ionization (carrier freezeout) occurs. Fig. 2.7.(a)-(b) show the solved doping and temperature dependence of ionization rate *IR* for n-type doping. The *IR* drops towards "0" at low temperature and high concentration. For example, at 300 K, for doping above 1×10^{18} cm^{-3}, *IR* drops quickly, thus limits doping's effectiveness in increasing carrier concentration.

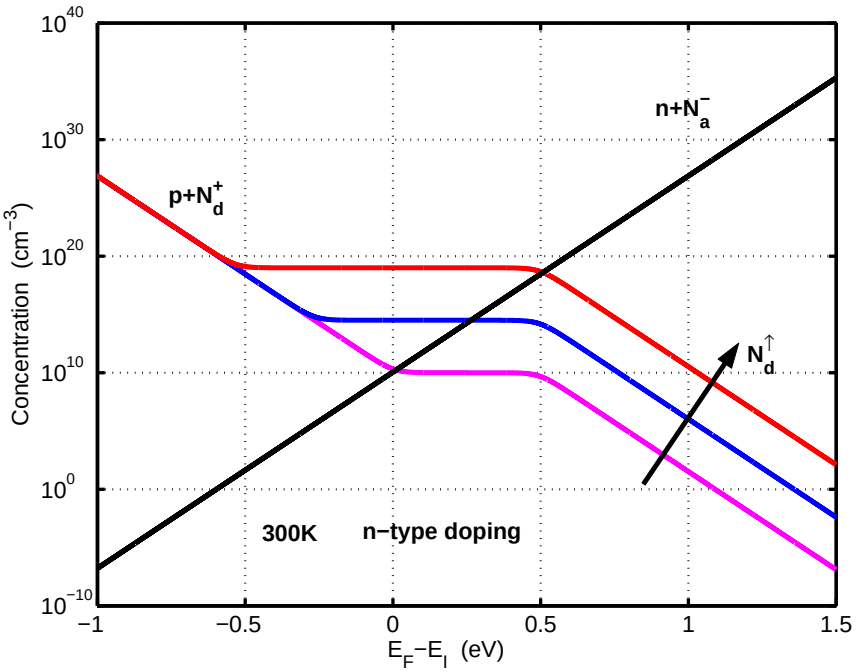

Figure 2.5: Concentration versus $E_F - E_I$.

However, experimentally, we use doping much higher than 1×10^{18} cm^{-3} in devices, such as source/drain of CMOS transistors and emitter of BJT transistor. They continue to provide reduced resistance. Hence this classic freezeout model fails at such high doping. In practice, the ionization rate at 300 K is 100% at low doping, drops at higher doping near 1×10^{18} cm^{-3}, but then increases back to 100% when doping is around 1×10^{19} cm^{-3} or so.

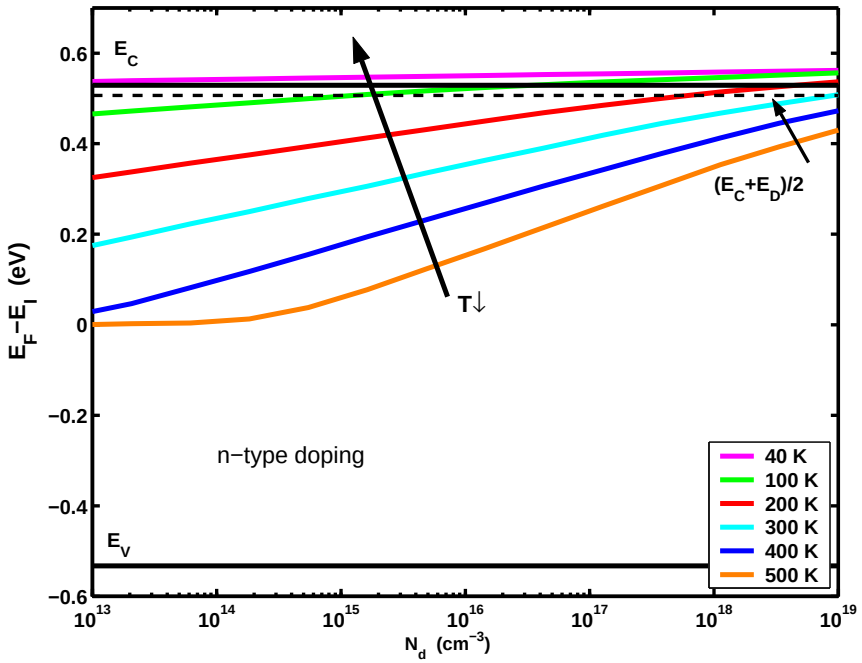

Figure 2.6: Variation of Fermi level $E_f - E_i$ versus doping concentration over 40-500 K.

Numerous theories of how impurity concentration and temperature affect ionization rate have been developed in the past several decades [25][26][27][28] [29][30][31][32]. At higher doping, density-of-state of dopant states broaden into dopant band and dopant band touches E_C/E_V at Mott-transition (3×10^{18} cm^{-3}). The ionization energy E_{dop} drops towards "0" hence causes dopants completely ionized, despite cooling [33]. To accurately model the incomplete ionization for heavily doping device, Mott-transition should be considered with freezeout model.

In the most recent Altemmatt's incomplete ionization model [26][27], not all of the dopant states are localized (or bound) states. At high concentration, once dopant band touches E_C/E_V, they become free and do not contribute to the local states. The fraction of bound states is named as "b". In Altemmatt's incomplete ionization model [26][27], both the bound state fraction "b" and dopant energy E_{dop} decreases with increasing doping. Fig. 2.8.(a)-(b) show the doping dependence of b and E_{dop} respectively. (2.11) and (2.12) then can be written as [17]:

$$N_D^+ = (1-b)N_D + \frac{bN_D}{1 + g_D \exp\left(\frac{E_F - E_D}{kT}\right)}, \tag{2.13}$$

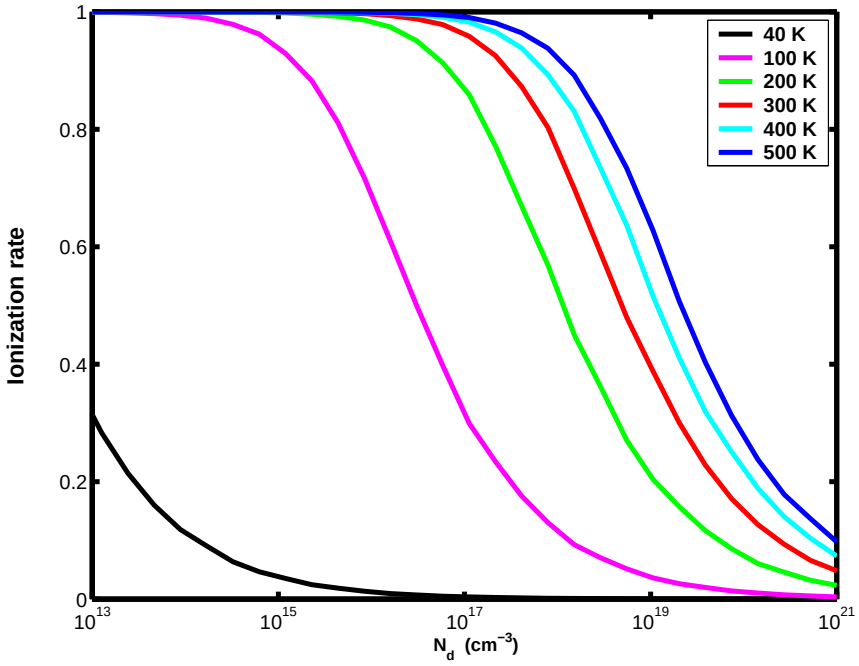

(a)

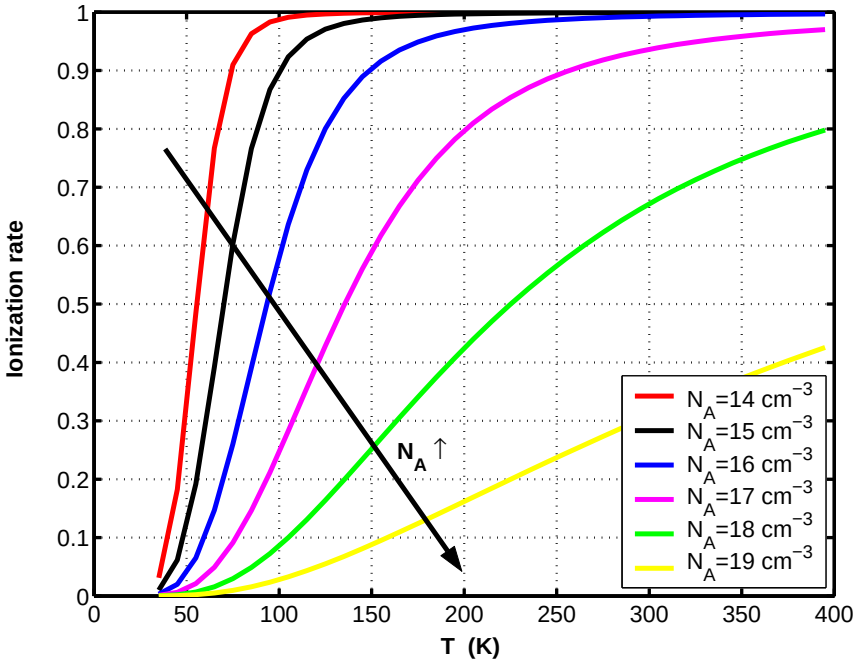

(b)

Figure 2.7: (a) Doping dependence of *IR* at different temperatures. (b) Temperature dependence of *IR* at different doping levels.

$$N_A^- = (1-b)N_A + \frac{bN_A}{1+g_A \exp\left(\frac{E_A - E_F}{kT}\right)}, \tag{2.14}$$

Fig. 2.9 show the calculated doping dependence of *IR* at different temperatures using Altemmatt's model. At 300 K, ionization rate is not complete around 1×10^{18} cm^{-3}. Ionization rate decreases with increasing doping concentration, but comes back at heavy doping levels towards complete ionization (100%). At heavy doping, ionization remains complete even if temperature goes down- this is where the "b" factor comes into play, because at higher doping the "b" factor drops to "0" and represents all states are free states, or ionized.

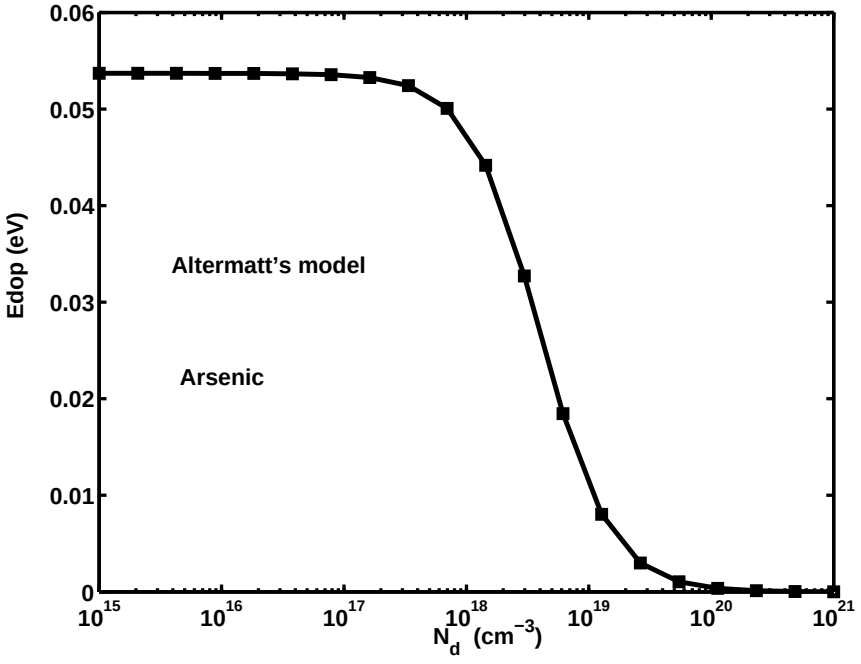

(a)

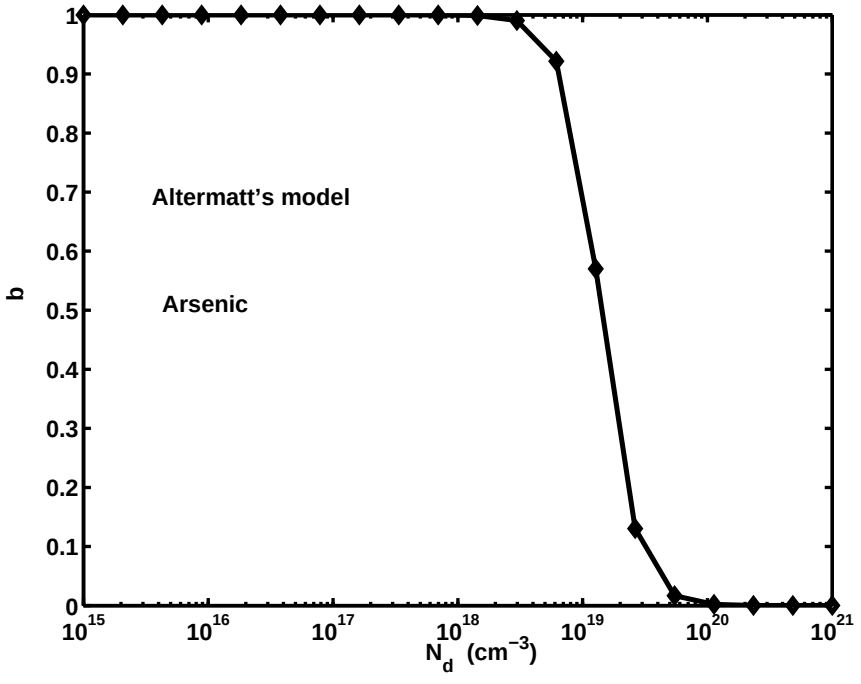

(b)

Figure 2.8: (a) E_{dop}-N_d. (b) b-N_d.

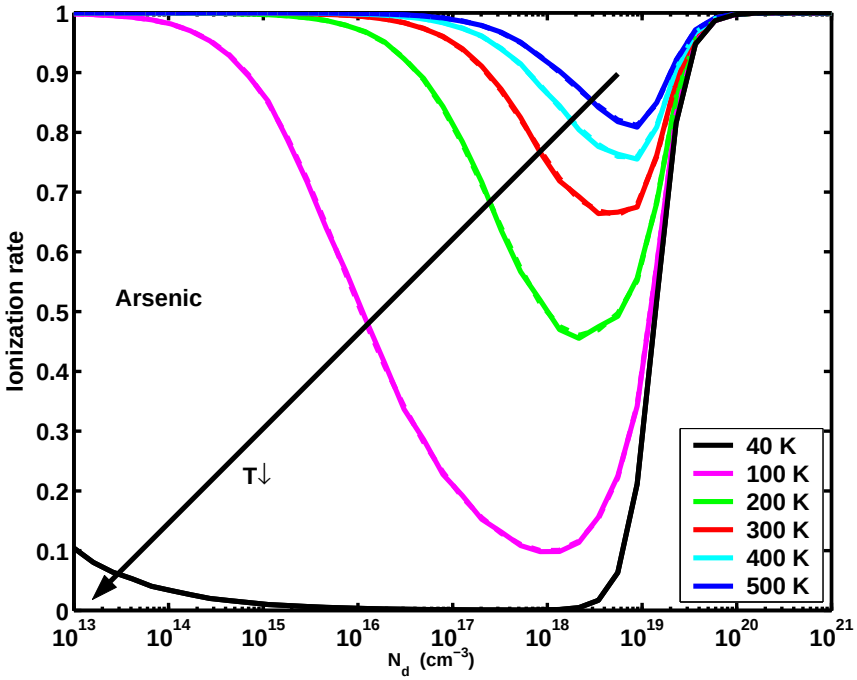

Figure 2.9: Doping dependence of *IR* at different temperatures using Altemmatt's model.

2.1.6 Low field carrier mobility

At low electric field, the relation between carrier velocity v_{sat} and electric field $\vec{E}$ is given by $v = \mu\vec{E}$, where μ is the low field carrier mobility. At high electric field, the carrier velocity v_{sat} becomes saturate. The most popularly used mobility model is Philips unified mobility model [34] [35], which unifies the description of majority and minority carrier bulk motilities. Besides lattice, donor and acceptor scattering, electron-hole scattering is also incorporated. Screening of impurities by charge carriers and the temperature dependence of both majority and minority carrier mobility are included. Ultra-high concentration effects are also taken into account.

Based on Matthiesen's rule to sum all the contributions to mobility,

$$\frac{1}{\mu_{e,h}} = \frac{1}{\mu_L} + \frac{1}{\mu_{DAeh}}, \tag{2.15}$$

where μ_L represents the lattice scattering contribution, and the μ_{DAeh} accounts for all other bulk scattering mechanisms due to free carriers and ionized donors and acceptors. The first term μ_L can be written by the well-known power dependence on temperature [36][37]:

$$\mu_L = \mu_{max}(\frac{300}{T})^{\theta}, \tag{2.16}$$

where θ is determined in comparison with experimental data. The second term μ_{DAeh} is a complicated function of electron density n, hole density p, donor concentration N_D, acceptor concentration N_A and the temperature T. The complete equations can be found in [34] [35].

In this section's discussion, all of the calculations are using the equation and parameters of Philips unified mobility model [34] [35].

Carrier freezeout effect

Based on the previous discussion of carrier freezeout effect, incomplete ionization occurs the mostly when doping concentration is near Mott-transition ($\approx 10^{18}$ cm^{-3}) at low temperatures. Hence in the following discussion, for better understanding the hole (majority carrier) and electron (minority carrier) mobilities in the base region of a NPN SiGe HBT, the hole and electron mobilities are calculated for p-type Boron from 50 K to 300 K, with doping concentration is from 10^{14} cm^{-3} to 10^{20} cm^{-3}. In the Philips unified mobility model [34] [35], carrier freezeout effect is taken in consideration from carrier scattering (electron-hole scattering) by introducing the strong temperature dependence of hole density and electron density.

Fig. 2.10.(a)-(b) are the calculated hole mobilities with complete ionization assumption and incomplete ionization assumption respectively. Altemmatt's incomplete ionization model [26][27] are used in these calculations. The first observation is, whatever the carrier freezeout is taken in account or not, at low concentration and higher temperature, lattice scattering factor μ_L dominates. At high concentration and low temperature, bulk scattering factor μ_{DAeh} mechanisms overwhelm lattice scattering factor μ_L. Secondly, by comparing Fig. 2.10.(a) and Fig. 2.10.(b), it is found that the most difference is near Mott transition ($\approx 10^{18}$ cm^{-3}), which is plotted in Fig. 2.10.(c). Since the semiconductor sheet resistance is not only a function of majority density, but also a function of majority mobility, it implies that not only the carrier freezeout effect should be considered into majority density modeling but also into the majority mobility modeling, especially near Mott-transition. The further discussion will be found in compact modeling chapter 5.11.3.

Fig. 2.11.(a)-(b) are the calculated electron mobilities with complete ionization assumption and incomplete ionization assumption respectively. Similarly, whatever the carrier freezeout is taken in account or not, at low concentration and higher temperature, lattice scattering factor μ_L dominates. At high concentration and low temperature, bulk scattering factor μ_{DAeh} mechanisms overwhelm lattice scattering factor μ_L. Secondly, by comparing Fig. 2.11.(a) and Fig. 2.11.(b), it is found that the most difference is near Mott transition ($\approx 10^{18}$ cm^{-3}), which is plotted in Fig. 2.11.(c).

As the base transit time, which limits the frequency response of the SiGe HBT in most cases, is determined by the minority electron mobility in the base region, the carrier freezeout effect should be considered into the transit time calculation.

Ultra-high concentrations effect

The effects of ultra-high concentrations on the mobility can be accounted for by assuming that above certain impurity concentration ($\approx 10^{20}$ cm^{-3}), the carriers are no longer scattered by impurities possessing one electronic charge and a concentration N, but by impurities with Z electronic charges and a "cluster" concentration N^*. Therefore, the ultra-high concentration effects can be modeled by replacing N by $Z(N) \times N$, where $Z(N)$ is the "clustering" function [34] [35].

$$Z = 1 + \frac{1}{c + (\frac{N_{ref}}{N})^2}. \tag{2.17}$$

Fig. 2.12.(a) is the calculated clustering function vs. impurity concentration. The effects of ultra-high concentrations on the mobility become noticeable when doping concentration is larger than 10^{20} cm^{-3}. Fig. 2.12.(b)-(c) are the calculated concentration dependence of electron majority and minority mobility μ_e at 300 K and 100 K respectively. The dotted lines represent the results with $Z_{A,D} = 1$. The Z factor introduces the second "knee-like" shape transition for mobilities at ultra-high concentration.

In the past, the minority carrier mobility has been assumed equal to the majority carrier mobility for simplicity in device modeling. However, results reported on carrier transport characteristics in Si show higher minority carrier mobility than the majority carrier mobility. This discrepancy is believed to originate from the difference in ionized impurity scattering [38]. In Fig. 2.12, the ratio of the two mobilities is 1.5 near Mott-transition (1×10^{18}cm^{-3}) at room temperature. And this ratio increases to 3 near Mott-transition (1×10^{18}cm^{-3}) at 100 K.

However, because bulk scattering mechanism dominates at high concentration and low temperature, difference between majority mobility and minority mobility is observed when doping is above

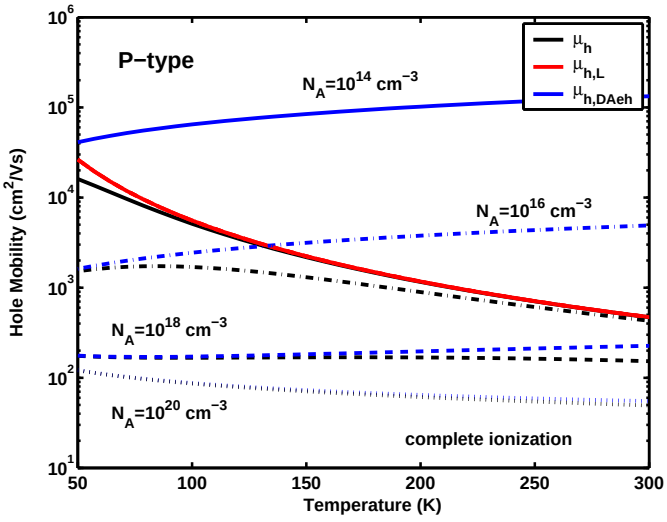

(a)

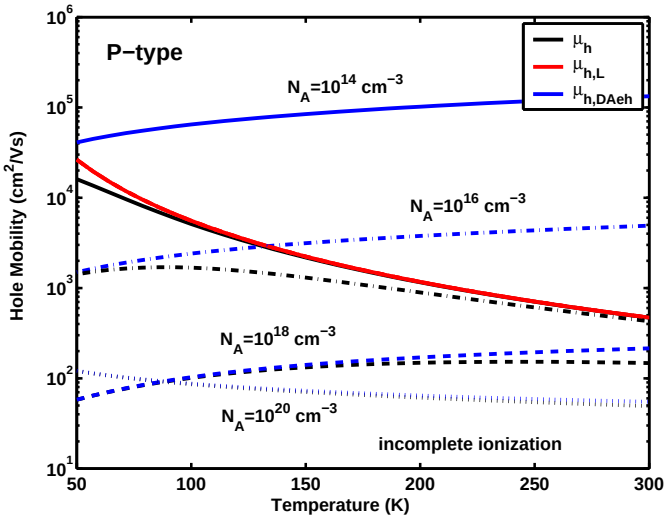

(b)

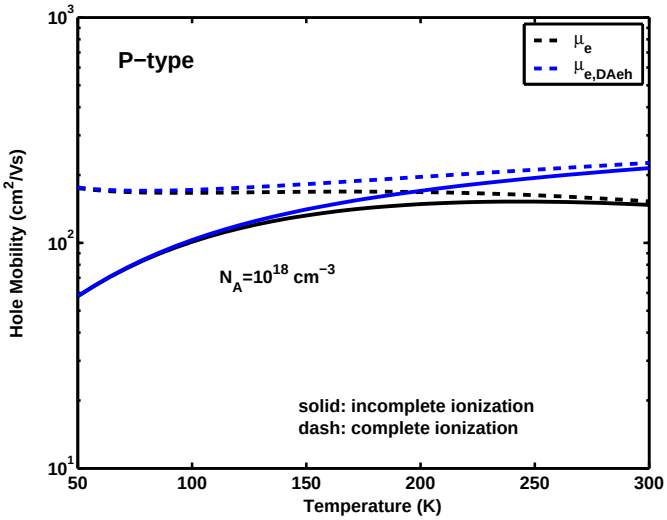

(c)

Figure 2.10: (a) Temperature and concentration dependence of hole mobility μ_h, w/o carrier freeze-out effect. (b) Temperature and concentration dependence of hole mobility μ_h, w/ carrier freezeout effect. (c) Temperature dependence of hole mobility μ_h near Mott-transition.

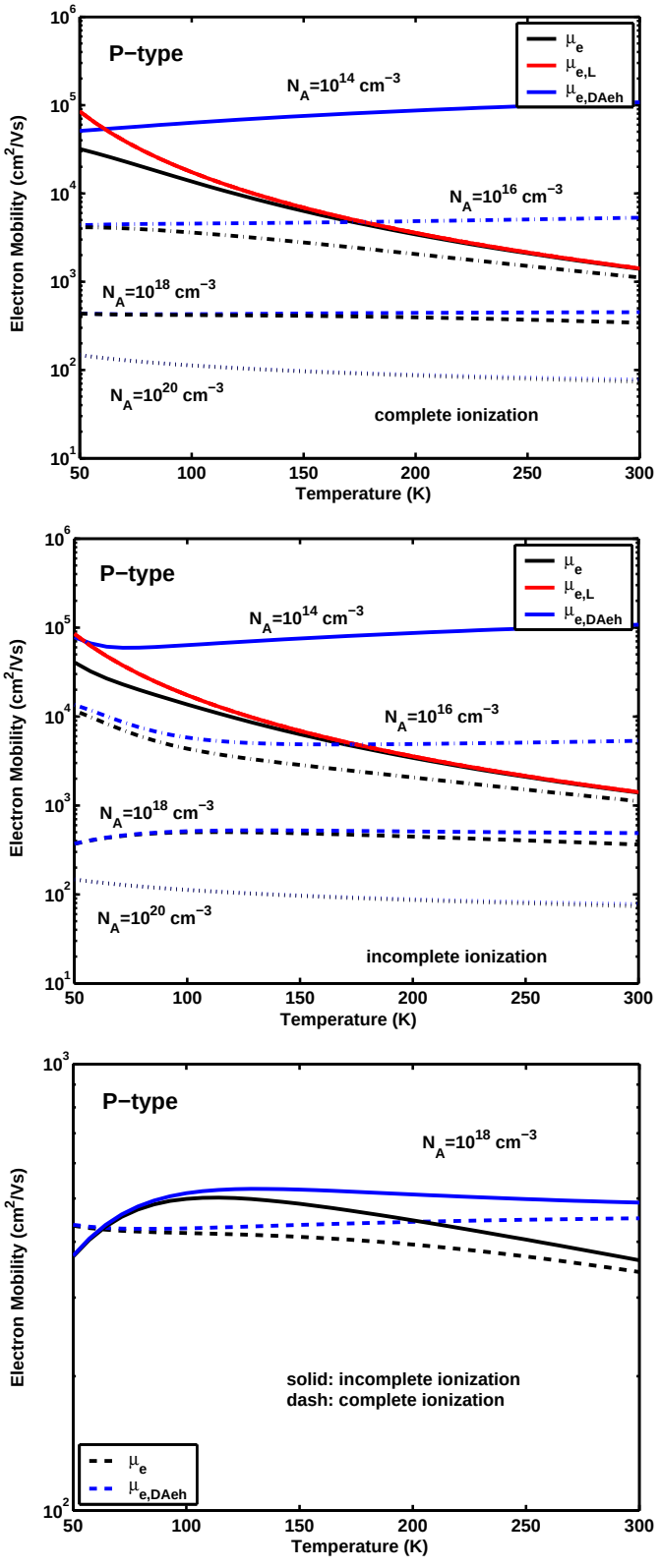

Figure 2.11: (a)Temperature and concentration dependence of electron mobility μ_e, w/o carrier freezeout effect. (b) Temperature and concentration dependence of electron mobility μ_e, w/ carrier freezeout effect. (c) Temperature dependence of electron mobility μ_e near Mott-transition.

$1 \times 10^{18}\text{cm}^{-3}$ at 100 K, as shown in Fig. 2.12.(c). The concentration dependence of hole majority and minority mobilities μ_h is similar to that of electron mobility μ_e and is not shown here.

Ge effect

Many investigations have been taken on the germanium dependence of mobility [39][40][41]. Both the holes and electrons mobility enhancement have been demonstrated in strained Si devices, including dual stress liner (DSL), embedded SiGe source/drain and stress memory technique (SMT) of CMOS technology. Uniaxial strain reduces carrier effective mass, increasing low field mobility and velocity. NFET is enhanced by in-plane tension or vertical compression and PFET is enhanced by compression along the channel or tension perpendicular to channel [39][40][41].

In [42][43], the theoretical analysis reported on the minority electron mobility in p-type strained Si Ge alloys for low Ge compositions ($x \leq 0.3$) and mainly focused on room temperature mobility. In [43], the low-field minority and majority mobilities in strained SiGe perpendicular, μ_{zz}, and parallel to the Si/SiGe interface, μ_{xx}, as well as the mobility μ in unstrained SiGe, are displayed as a function of Ge content for different doping concentrations. As a general trend, the mobility is reduced with increasing Ge content at low doping concentrations by alloy scattering. At higher doping, μ_{zz} in strained SiGe increases, μ_{xx} in strained SiGe and μ in unstrained SiGe reduce more or less equally strong.

In [44], temperature dependence of minority electron mobilities in p-type SiGe has been measured for the first time for Ge composition between $0.2 \leq x \geq 0.4$. The measurements were made on NPN SiGe HBT with a heavily doped base (7×10^{19} cm^{-3}), from 5 K to 300 K. The measured minority electron mobilities show a sharp increase with decreasing temperature, and exhibit saturation for temperature below 50 K.

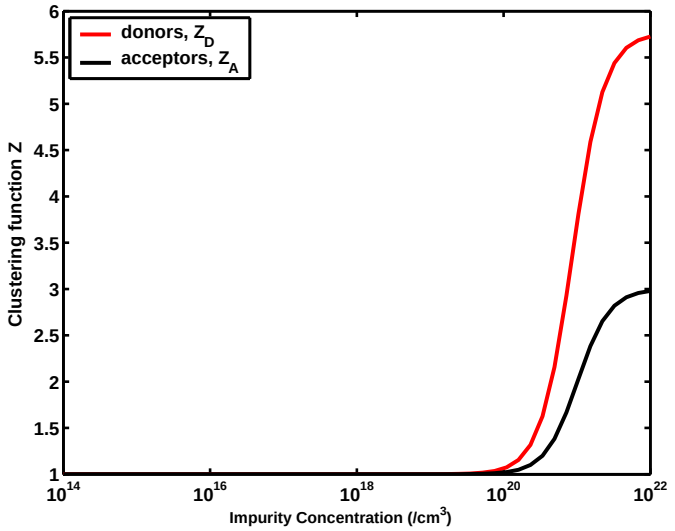

(a)

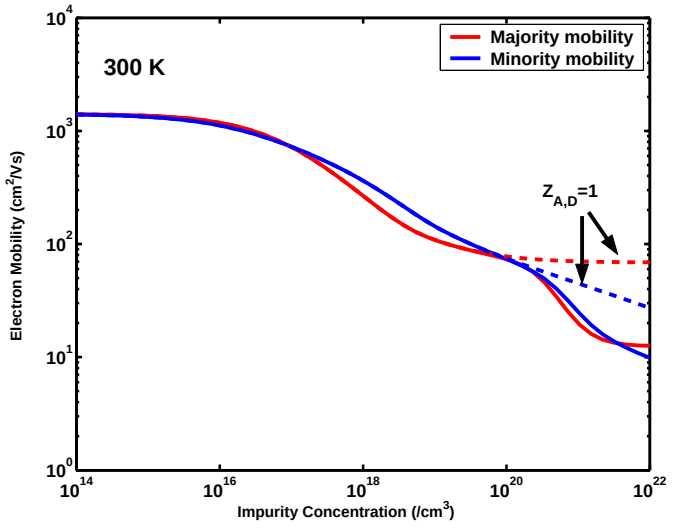

(b)

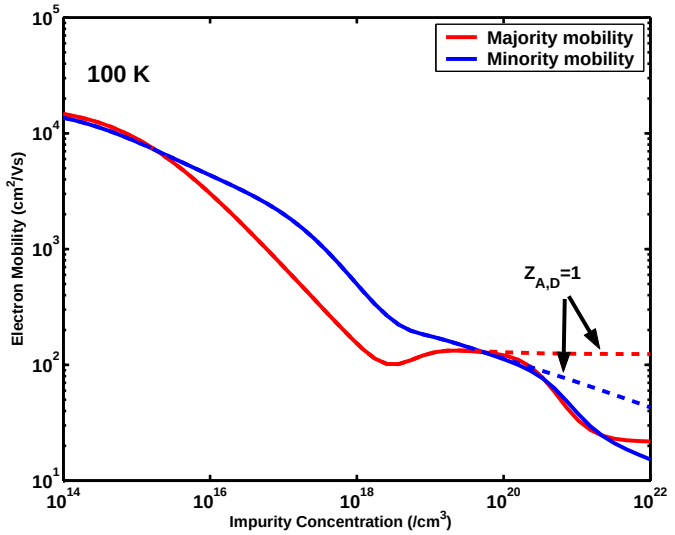

(c)

Figure 2.12: (a) Calculated clustering function vs. impurity concentration. (b) Calculated concentration dependence of electron mobilities μ_e at 300 K. (c) Calculated concentration dependence of electron mobilities μ_e at 100 K.

2.1.7 Carrier saturation velocity

The bulk carrier saturation velocity v_{sat} used in high-field mobility is modeled as a function of temperature with the following two-parameter model [45][46]:

$$v_{sat}(T) = \frac{v_{sat,300}}{(1-A_v)+A_v(\frac{T}{300})}, \tag{2.18}$$

where $v_{sat,300}$ represents the saturation velocity at room temperature and A_v is temperature coefficient. The model assumes that the v_{sat} is independent of the doping concentration, which is in good agreement with published data [46]. A_v reflects the temperature dependence of various materials. For a material of $A_{1-x}B_x$, the saturation velocity can be interpolated according to the material composition.

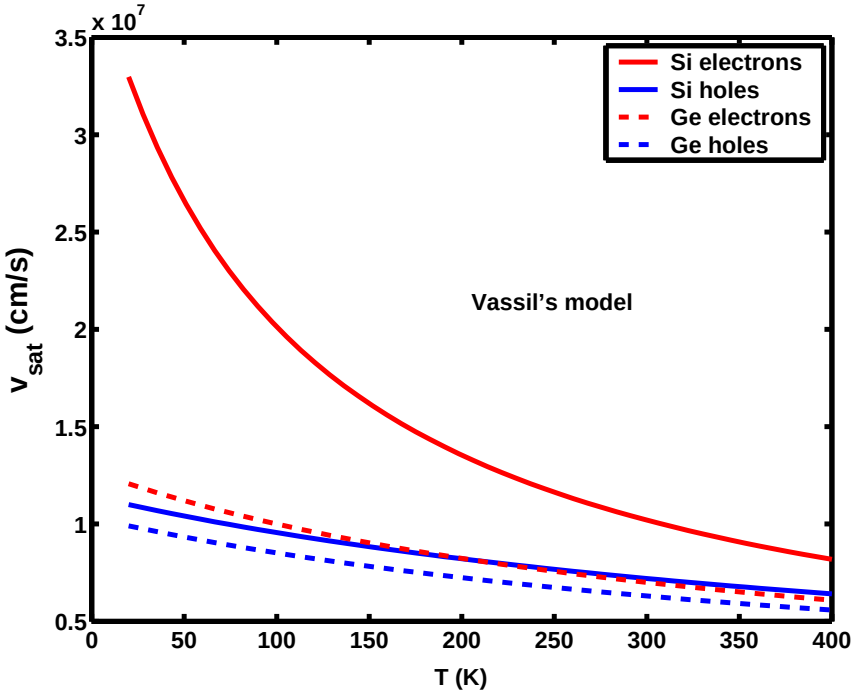

Figure 2.13: Saturation velocity as a function of temperature for Si and Ge.

2.1.8 Sheet resistance and resistivity

Semiconductor's sheet resistance or resistivity is closely related to majority carrier mobility, majority carrier concentration and hence incomplete ionization rate.

$$R_{sh} = \left(q \int_0^W N_{dop}^{-}(x)\mu(x)dx \right)^{-1}, \tag{2.19}$$

where W is neutral region width, N_{dop}^{-} is ionized majority carrier density, μ is majority carrier mobility. Temperature dependence of W is from the variation of p-n junction depletion layer thickness, which is much smaller than that of N_{dop}^{-} and μ and is thus neglected.

For example, intrinsic base neutral region width W_B is a function of the thickness of emitter-base and collector-base junction depletion layers on the base side. Here, we calculate depletion layer thickness W_{dep} versus T from 30-300 K using Altermatt and classic incomplete ionization models in Fig. 2.14. The chosen doping levels are similar to those of the SiGe HBT in this work. In the calculations, we have included T-dependence of N_V, N_C and bandgap E_g. As shown in Fig. 2.14, both of these two *IR* models give very weak T-dependence of W_{dep}, which is much smaller than those of N_{dop}^{-} and μ. Hence T-dependence of W is negligible compared to those of N_{dop}^{-} and μ.

Here, sheet resistance and substrate resistivity were measured on-wafer from 300 K to 30 K in a first-generation 0.5 μm SiGe HBT technology featuring 50 GHz peak f_T at 300 K, with base doping below but close to the Mott-transition (about 3×10^{18} cm^3 for boron in silicon). The detail description of test structure and measurement technique will be discussed in 5.11.3. Fig. 2.15 shows the measured substrate resistivity, the collector sheet resistance, the intrinsic base sheet resistance, the buried collector sheet resistance, and the silicided extrinsic base sheet resistance, from 30 to 300 K.

For the n^+ buried collector, the resistance increases slightly with temperature at high temperatures due to a decreases in the majority carrier mobility. At low temperatures, the resistance remains approximately constant, indicating that freezeout of carriers is not occurring to any significant extent. This is expected since the doping is well above the Mott-transition and ionization is complete

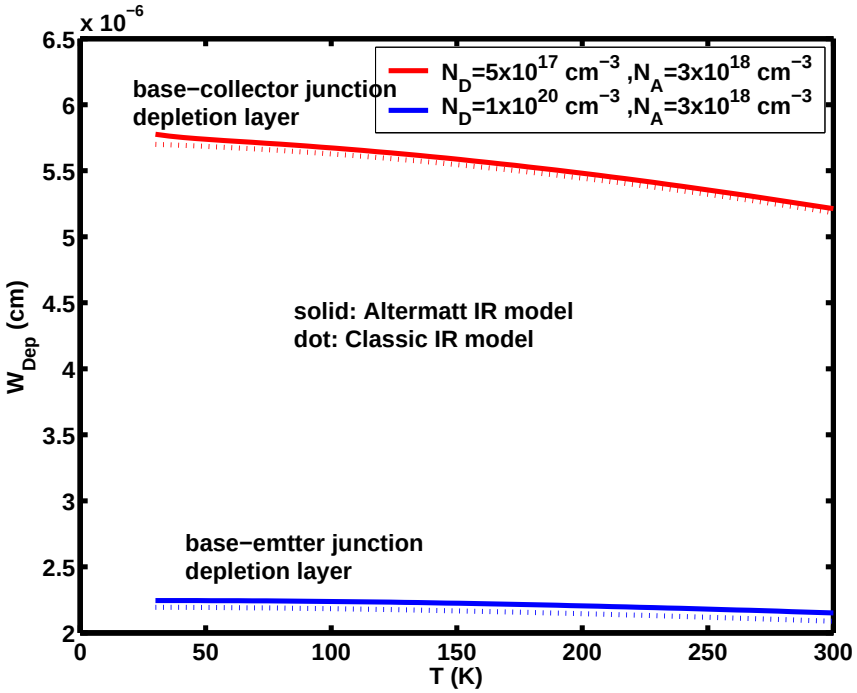

Figure 2.14: calculate depletion layer thickness W_{dep} versus T from 30-300 K using Altermatt and classic incomplete ionization models.

at all temperatures. For the p^+ silicided extrinsic base, it has similar temperature function as the n^+ buried collector but with smaller sheet resistance values. In contrast, for the p^- substrate, n^- collector and the p-type intrinsic base, the resistance increases strongly at low temperatures, indicating that freezeout of dopant is occurring. This is again expected because the p^- substrate and n^- collector doping is well below the Mott-transition [33], while the doping of the p-type intrinsic base is close to Mott-transition.

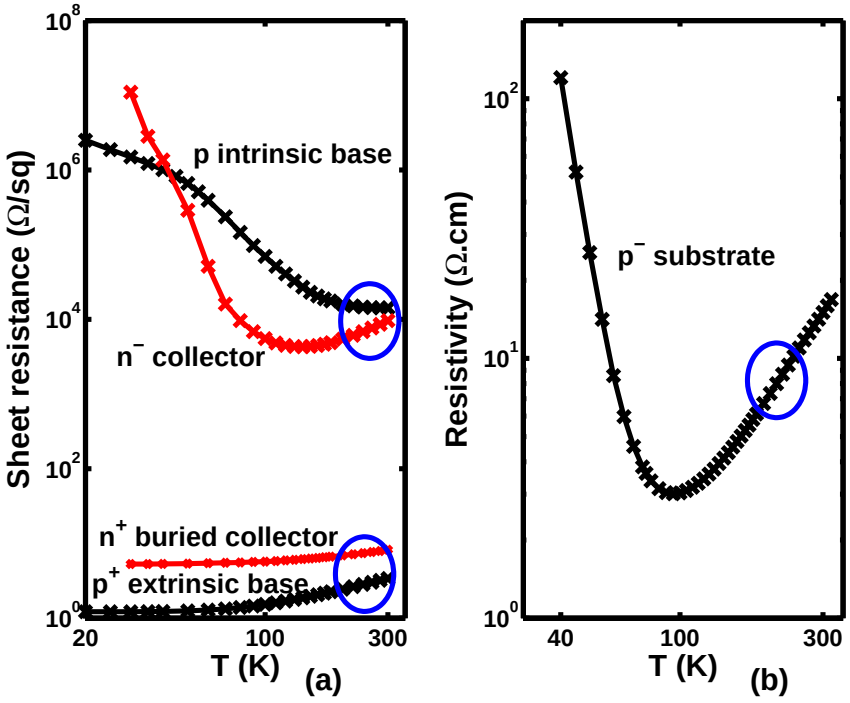

Figure 2.15: (a)Measured sheet resistance for collector, intrinsic base, extrinsic base and buried layer from 30-300 K. (b) Measured substrate resistivity from 30-300 K.

2.2 SiGe HBT characteristics at cryogenic temperature

2.2.1 Limitations of Si BJT

Simultaneous increase of current gain β, cut-off frequency f_T , and decrease of base resistance, however, are conflicting goals when translated into device design. To increase f_T , base width W_B needs to be reduced, which increases base resistance unfortunately. The total base dopants $N_B W_B$ must be kept at least to keep base resistance, requiring the increase of base doping N_B. The emitter structure, which determines the base current, is normally fixed with device scaling for manufacturing bipolar technologies.

The emphasis is often to achieve a low but reproducible base current while minimizing the emitter resistance. As a result, there is no β and base resistance improvement at all from such a W_B scaling even if realizable. The best result is an increase of f_T and a smaller increase of f_{max}. While a simultaneous increase of f_T , increase of β, and reduction of base resistance is desired for better transistor performance. Furthermore, a thin W_B with high base doping N_B is very difficult to achieve in traditional implanted BJT technologies.

2.2.2 SiGe HBT fundamental

The essential operational differences between the SiGe HBT and the Si BJT are best illustrated by considering a schematic energy band diagram. For simplicity, we consider an ideal, graded-base SiGe HBT with constant doping in the emitter, base and collector regions. The Ge content is linearly graded from 0% near the metallurgical emitter-base (EB) junction to some maximum value of Ge content near the metallurgical collector-base (CB) junction, and then rapidly ramped back down to 0%. The resultant overlaid energy band diagrams for both the SiGe HBT and the Si BJT, biased identically in forward-active mode, are shown in Fig. 2.16. A Ge-induced reduction in base bandgap occurs at the EB edge of the quasi-neutral base ($\Delta E_{g,Ge}(x=0)$), and at the CB edge of the quasi-neutral base ($\Delta E_{g,Ge}(x=W_b)$). This grading of the Ge across the neutral base induces a

built-in quasi-drift field ($(\Delta E_{g,Ge}(x=W_b)-\Delta E_{g,Ge}(x=0))/W_b$) in the neutral base that will impact minority carrier transport [47][7].

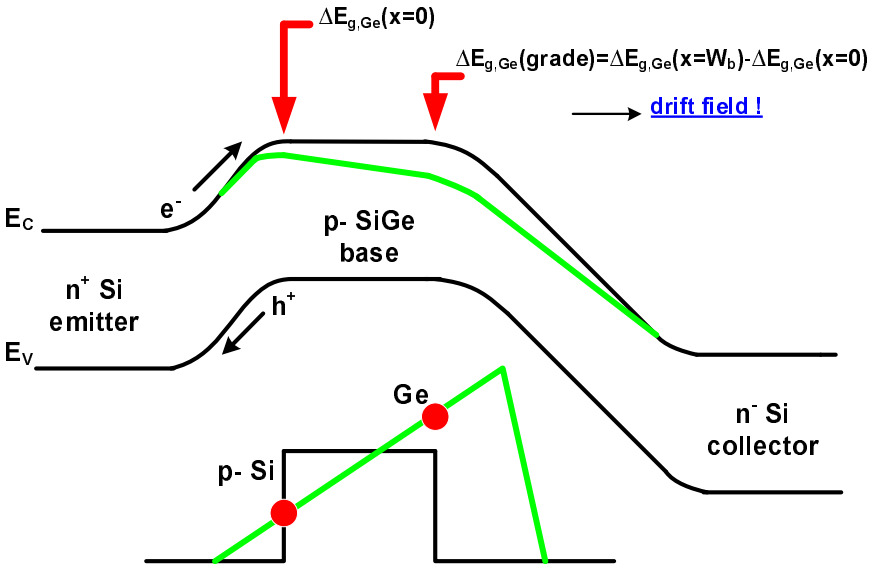

Figure 2.16: Energy band diagram for a Si BJT and graded-base SiGe HBT.

2.2.3 Collection current density and current gain

The theoretical consequences of the Ge-induced bandgap changes to collection current density J_C can be derived in closed-form for a constant base doping profile by considering the generalized Moll-Ross collector current density relation, which holds for low-injection in the presence of both non-uniform base doping and non-uniform base bandgap at fixed V_{BE} and temperature (T) [47].

$$J_C = \frac{q(e^{qV_{BE}/kT}-1)}{\int_0^{W_b} \frac{p_b(x)dx}{D_{nb}(x)n_{ib}^2(x)}}, \tag{2.20}$$

where $x=0$ and $w=W_b$ are the neutral base boundary values on the emitter-base and collector-base sides of the base respectively. n_{ib}, D_{nb} and p_b are intrinsic carrier concentration, electron diffusion constant and hole density in the base respectively. Through the Ge-induced bandgap offset, n_{ib} and D_{nb} are position-dependent.

The intrinsic carrier concentration in the SiGe HBT base can be written as eqn(2.4). In [7], detailed derivations of the collector current in SiGe HBT are discussed and can be finally written as:

$$J_C = \frac{qD_{nb}}{N_{ab}^- W_b}\left(e^{qV_{BE}/kT}-1\right)n_{io}^2 e^{\Delta E_{gb}^{app}/kT}\left\{\frac{\overline{\gamma\eta}\Delta E_{g,Ge}(grade)/kTe^{\Delta E_{g,Ge}(0)/kT}}{1-e^{-\Delta E_{g,Ge}(grade)/kT}}\right\},$$
$$\Delta E_{g,Ge}(grade) = \Delta E_{g,Ge}(W_b) - \Delta E_{g,Ge}(0), \overline{\eta} = \frac{D_{nb,SiGe}}{D_{nb,Si}}, \overline{\gamma} = \frac{(N_C N_V)_{SiGe}}{(N_C N_V)_{Si}}. \quad (2.21)$$

where $\overline{D_{nb}}$ and $\overline{\gamma}$ is position-averaged quantities across the base region.

For a comparably structure SiGe HBT and Si BJT, the base current density J_B should be comparable between the two devices, while J_C at fixed V_{BE} should be enhanced for the SiGe HBT.

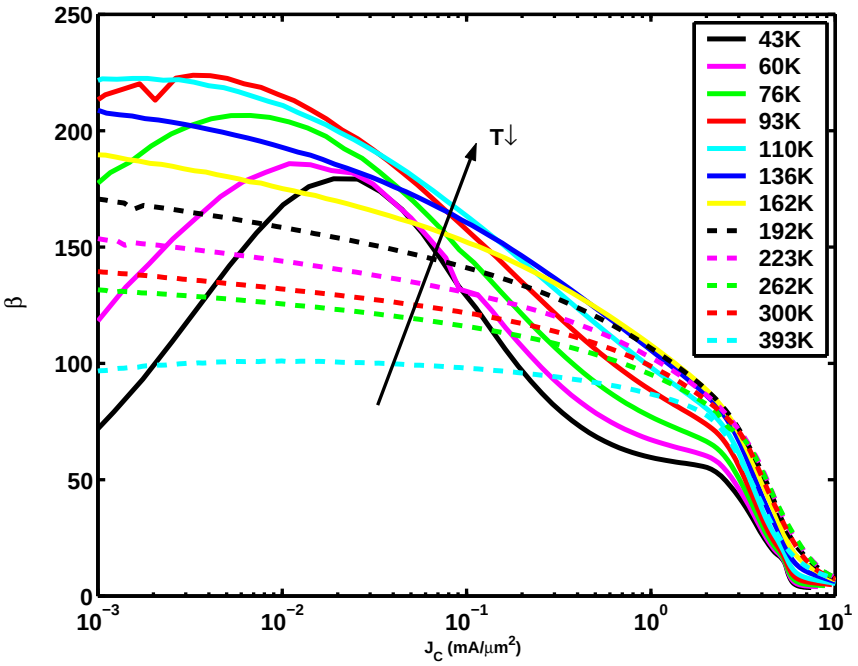

Figure 2.17: Measured current gain β-V_{BE} for a graded-base SiGe HBT.

Fig. 2.17 shows the measured current gain β-V_{BE} for a graded-base SiGe HBT. Given the nature of an exponential dependence, it is obvious that strong enhancement in J_C for fixed V_{BE} can be obtained

for small amounts of introduced Ge, and that the ability to engineer the device characteristics to obtain a desired current gain is easily accomplished.

2.2.4 Early effects

The dynamic output conductance, $\frac{\partial J_C}{\partial V_{CE}}$ at fixed V_{BE}, of a transistor is a critical design parameter for many analog circuits. As we increase collector-base voltage V_{CB}, we deplete the neutral base from the backside , thus moving the neutral base boundary ($x = W_b$) inward. Since W_b determines the minority carrier density on the CB side of the neutral base, the slope of the minority electron profile, and hence the collector current I_C rises [48]. This mechanism is known as "Early effect'.

For a linearly graded Ge profile, the ratio of V_A between a comparably constructed SiGe HBT and Si BJT to be [49][7] can be written as:

$$\left.\frac{V_{A,SiGe}}{V_{A,Si}}\right|_{V_{BE}} = e^{\Delta E_{g,Ge}(grade)/kT}\left[\frac{1-e^{-\Delta E_{g,Ge}(grade)/kT}}{\Delta E_{g,Ge}(grade)/kT}\right]. \tag{2.22}$$

The fundamental difference between V_A in a SiGe HBT and Si BJT arises from the variation of n_{ib}^2 as a function of position. The base profile is effectively "weighted" by the increasing Ge content on the collector side of the neutral base, making it harder to deplete the neutral base for a given V_{CB} and it effectively increasing the Early voltage of the transistor.

2.2.5 Avalanche multiplication and breakdown voltage

Under reverse bias, the electric field in the space-charge region of the CB junction is large. Electrons injected from the emitter drift to the collector through the CB space-charge region. For a sufficiently high electric field, electrons can gain enough energy from the electric field to create an electron-hole pair during the carrier generation process known as "impact ionization". Electrons and holes generated by impact ionization can subsequently acquire energy from this strong electric field, and create additional electron-hole pairs by further impact ionization. This process of multiplicative impact ionization is known as "avalanche multiplication". The ratio of

the electron current leaving CB space-charge region to that entering the CB space-charge region is known as the avalanche multiplication factor M. In practice, (M-1) instead of M is often used because (M-1) better describes the yield of the resulting collector current increase.

Avalanche multiplication is an important effect that must be accurately measured and modeled. The avalanche multiplication (M-1) determines the breakdown voltage as well as the base current reversal voltage, which in turn determines the maximum useful V_{CB} for stable circuit operation [50].

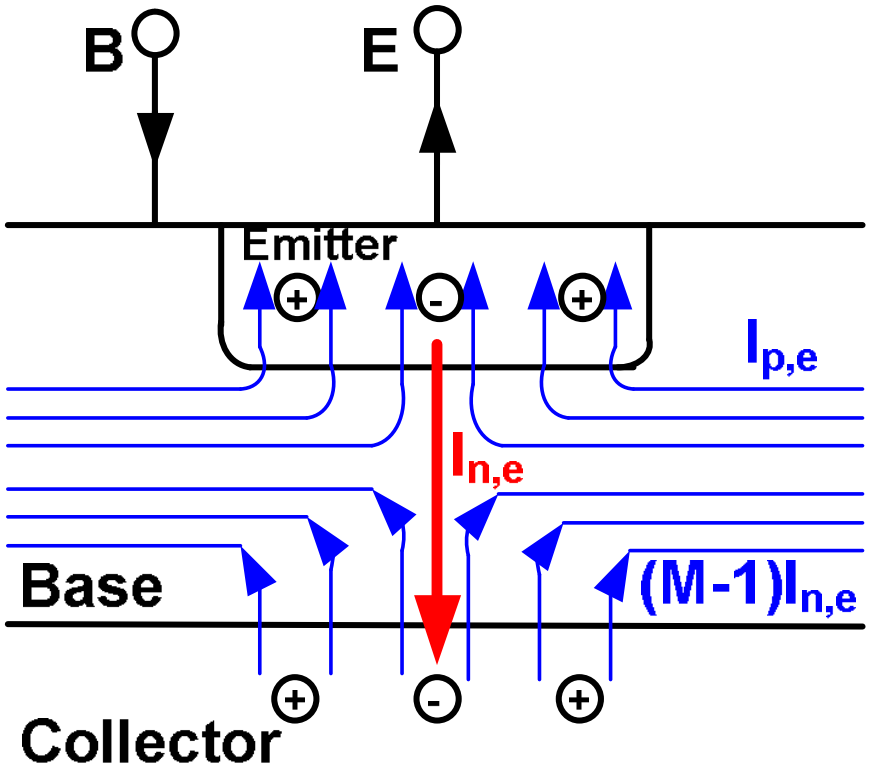

Figure 2.18: The avalanche multiplication process in a BJT.

Forced-I_E (M-1) measurement is widely used instead of forced-V_{BE} (M-1) measurement to avoid self-heating effect at high J_C or high V_{CB}, because the total amount of current injected into the CB space-charge region is always limited by emitter current I_E [51].

Fig. 2.19 shows the (M-1) versus collector-base voltage V_{CB} for a typical graded-base SiGe HBT. Fig. 2.20 shows the (M-1) as a function of $1000/T$ at various V_{CB}'s. In contrast to the previous observations of a strongly exponential increase with cooling in Si BJT [52], the increase with cooling is much weaker in the SiGe BJT under study, particularly below 162 K. The difference in temperature sensitivity is not due to any Ge effect, but instead is attributed to the higher collector doping level in the device measured in this study than in the devices used in [52].

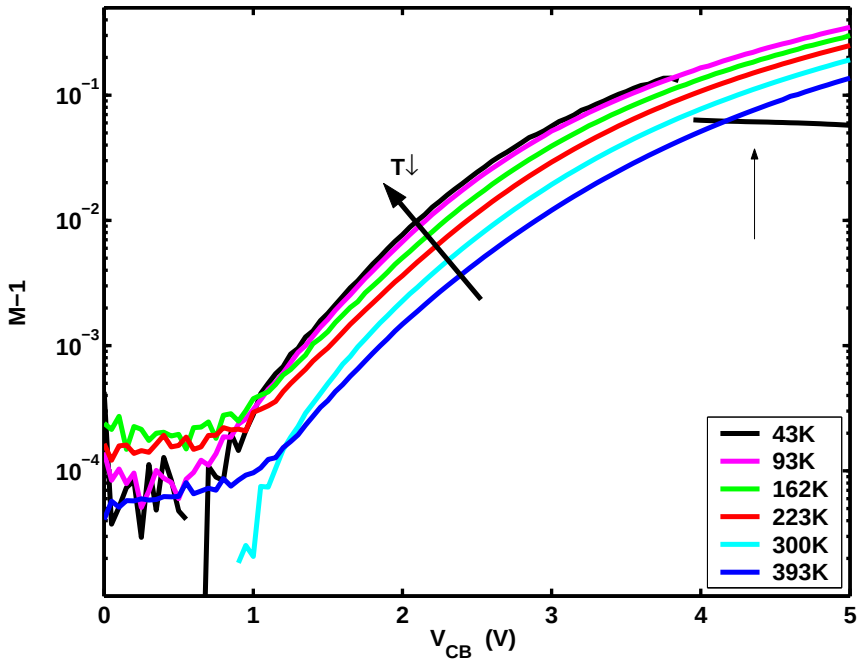

Figure 2.19: Measured M-1-T for a graded-base SiGe HBT over 43-393 K.

The maximum operation voltage limit of a bipolar transistor is generally dictated by avalanche multiplication. Two often used voltage limits are open-base BV_{CEO} and short-base BV_{CBO}, which represent the worst and best cases for forced-I_B and forced-V_{BE} configurations, respectively. Another frequently employed bias configuration is forced-I_E, which has virtually the same collector-to-emitter breakdown voltage as BV_{CBO}, due to the fixed I_E. However, at practically high currents, a lateral current instability due to avalanche multiplication induced pinch-in effect [50] may occur before the BV_{CBO} limit is reached. This can occur for forced-V_{BE} as well. Pinch-in occurs when avalanche induced hole current dominates over the normal hole current injected into the emitter.

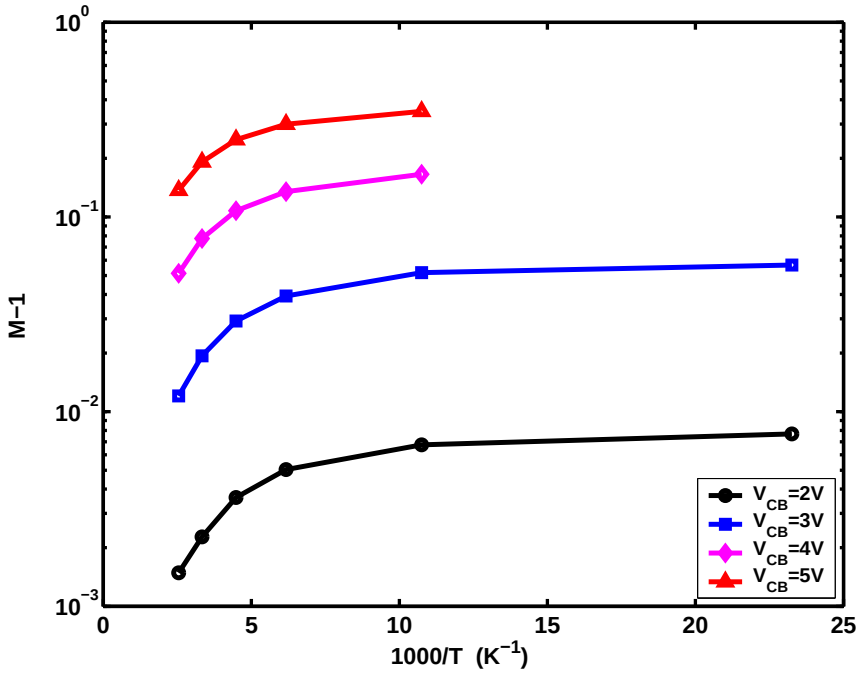

Figure 2.20: Measured multiplication factor M-1 versus $1000/T$ at various V_{CB}'s for a graded-base SiGe HBT.

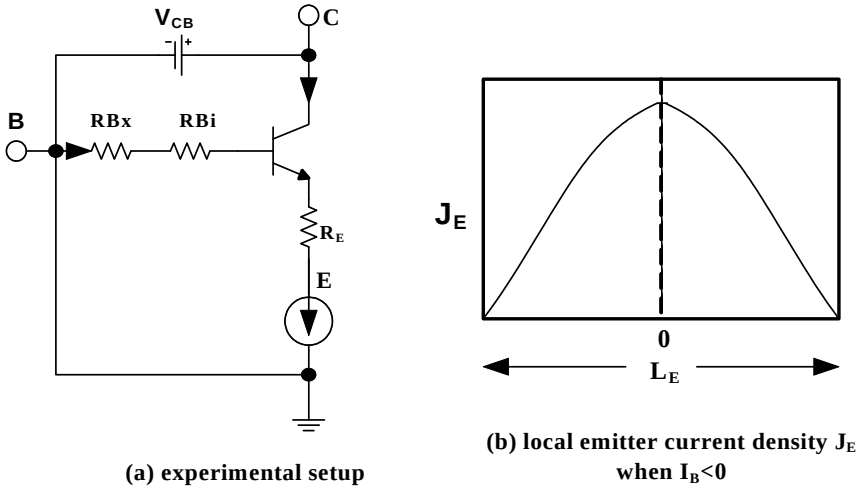

Figure 2.21: (a) Experimental setup. (b) Local emitter current density J_E when $I_B < 0$.

The net base current flows out of the base, creating a lateral V_{BE} and emitter current density J_E variation that is highest at the emitter center and lowest at the edge, which is shown in Fig. 2.21. At a critical base current I_B^*, an abrupt pinch-in of the emitter current to a very small area of the emitter center occurs, and sets an upper limit of stable operation.

In chapter 4, forced-I_E pinch-in maximum output voltage limit in SiGe HBTs operating at cryogenic temperatures will be investigated, which is of interest for many space exploration applications [5].

2.2.6 AC characteristics

At low injection, the unity-gain cutoff frequency f_T in a bipolar transistor can be written as:

$$f_T = \frac{1}{2\pi\tau_{ec}} = \frac{1}{2\pi}\left[\frac{V_T}{I_C}(C_{te}+C_{tc}) + \tau_b + \tau_e + \frac{W_{CB}}{2v_{sat}} + r_c C_{tc}\right]^{-1}, \tag{2.23}$$

where g_m is the intrinsic transconductance, C_{te} and C_{tc} are the emitter-base and base-collector depletion capacitances, τ_b is the base transit time, τ_e is the emitter transit time, W_{CB} is the collector-base space-charge region width, v_{sat} is the saturation velocity, and r_c is the dynamic collector resistance, τ_{ec} is the total emitter to collector transit time.

In most cases, the base transit time τ_b overwhelms other components and determines the peak f_T. The ratio of base transit time between SiGe HBT $\tau_{B,SiGe}$ and Si HBT $\tau_{B,Si}$ can be written as [7]:

$$\frac{\tau_{b,SiGe}}{\tau_{b,Si}} = \frac{2}{\overline{\eta}}\frac{kT}{\Delta E_{g,Ge}(grade)}\left\{1 - \frac{kT}{\Delta E_{g,Ge}(grade)}\left[1 - e^{-\Delta E_{g,Ge}(grade)/kT}\right]\right\},$$
$$\tau_{b,Si} = \frac{W_b^2}{2D_{nb}}. \tag{2.24}$$

Fig. 2.22 are the calculated $\tau_{b,SiGe}$, $\tau_{b,Si}$ and τ_{SiGe}/τ_{Si}-T ratio as functions of temperature for a graded-base SiGe HBT. The base width is assumed as 50 nm with 1×10^{18} cm^{-3} uniform doping. The total Ge-induced bandgap grading in base is assumed as 100 meV. Ge effect on low field mobility is not included for simplicity. The Philips unified mobility model [34] [35] and Altemmatt's incomplete ionization model [26][27] are used in the calculation. The thermal energy kT residing in the denominator of eqn(2.24) decreases τ_{SiGe}/τ_{Si} at low temperatures, which are demonstrated in Fig. 2.22.(b). Therefore, whatever the carrier freezeout is taken in account or not, $\tau_{b,SiGe}$ is smaller than $\tau_{b,Si}$, especially at cryogenic temperatures. This demonstrates the advantage of SiGe application at cryogenic temperatures.

Fig. 2.23.(a)-(b) show the measured f_T-J_C and f_{max}-J_C for a graded-base SiGe HBT respectively. As a result of the decreasing $\tau_{b,SiGe}$ with cooling, the peak f_T enhances at low temperature. Another

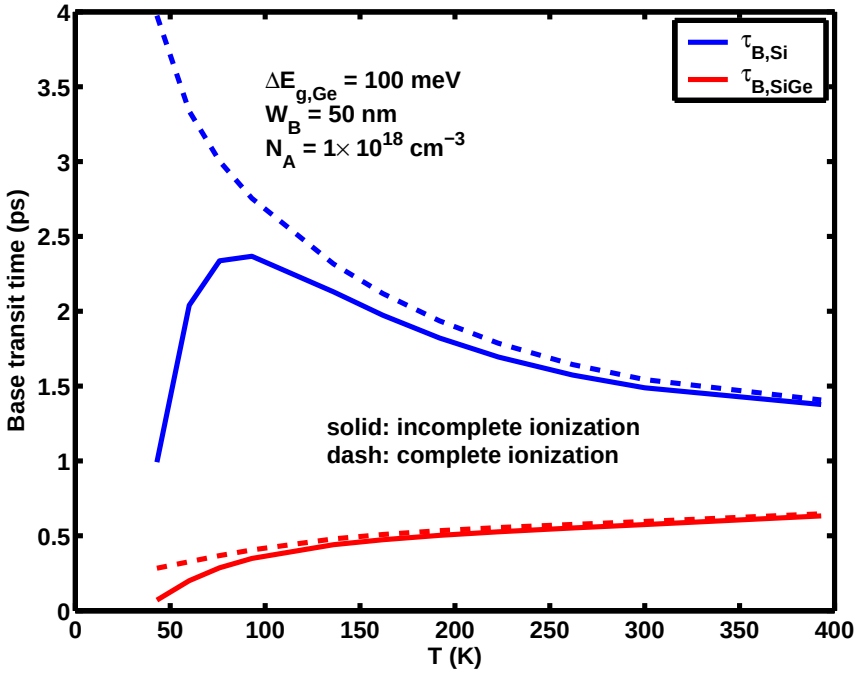

(a)

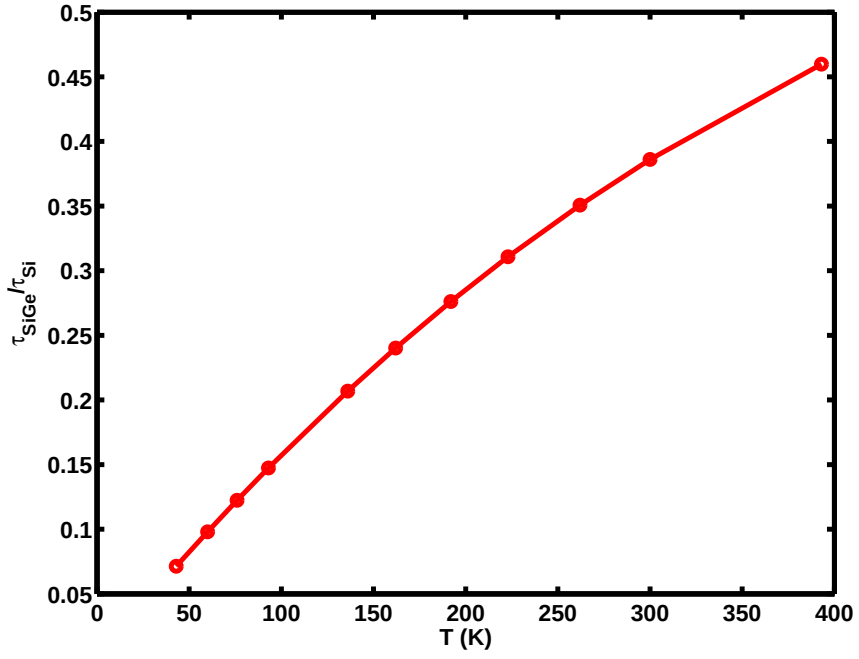

(b)

Figure 2.22: (a) Calculated $\tau_{b,SiGe}$-T and $\tau_{b,Si}$-T for a graded-base SiGe HBT. (b) Calculated ratio τ_{SiGe}/τ_{Si}-T for a graded-base SiGe HBT.

observation from Fig. 2.23.(a) is the improved f_T roll-off at low temperatures. Lower the temperature, larger collector current density where base push out effect occurs. The critical collector current density J_{cr} for the onset of base push-out is proportional to high field saturation velocity, $J_{cr} \propto v_{sat}$. From the previous discussion in 2.1.7, high field saturation velocity v_{sat} increases with cooling, hence f_T roll-off is improved due to the higher J_{cr} at low temperature.

The maximum oscillation frequency f_{max} is related to f_T by:

$$f_{max} = \sqrt{\frac{f_T}{8\pi C_{bc} r_b}}, \tag{2.25}$$

where C_{bc} is the Miller capacitance between base and collector ($\approx C_{tc}$), r_b is dynamic base resistance. Capacitance C_{bc} has much weaker temperature dependence than that of cut-off frequency f_T and dynamic base resistance r_b. Carrier freezeout effect induced base resistance increasing at low temperature lead to f_{max} degradation at 93 K, as shown in Fig. 2.23.(b).

2.3 Summary

In this chapter, the temperature characteristics of semiconductors critical metrics are studied, including bandgap energy E_g, effective conduction band density-of-states N_C and valence band density-of-states N_V, intrinsic carrier concentration at low doping n_i, bandgap narrowing ΔE_g, carrier mobility μ, carrier saturation velocity and carrier freezeout. The *dc* and *ac* low temperature performance of SiGe HBT are analyzed, including collector current density, current gain, Early effect, avalanche multiplication factor, transit time, cut-off frequency and maximum oscillation frequency. SiGe HBT demonstrates excellent analog and RF performance at cryogenic temperatures.

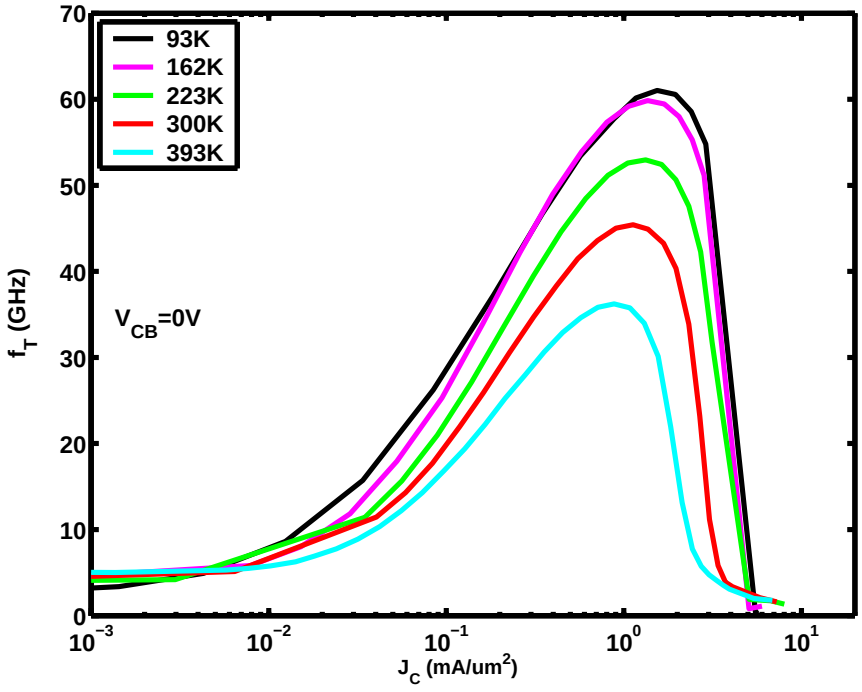

(a)

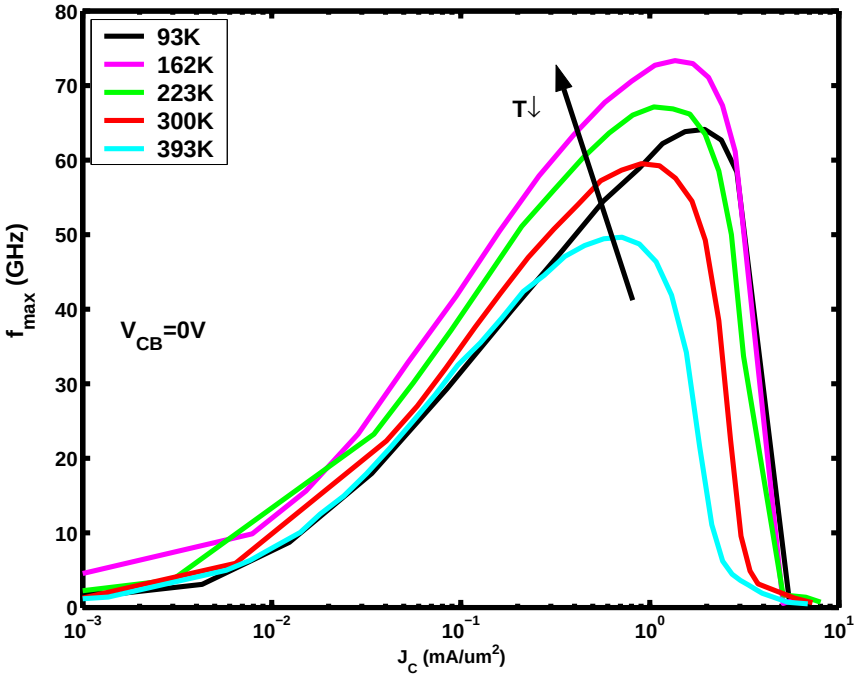

(b)

Figure 2.23: (a) Measured f_T-J_C for a graded-base SiGe HBT. (b) Measured f_{max}-J_C for a graded-base SiGe HBT.

Chapter 3

Substrate Current Based M-1 Measurement at Cryogenic Temperatures

3.1 Measurement theory

In [15], a new substrate current-based technique for measuring the avalanche multiplication factor (M-1) in high-speed SiGe HBTs is proposed, which enables (M-1) measurement at high operating current densities required for high-speed operation, where conventional techniques fail because of self-heating. The proposed technique is based on photo carrier generation by hot carrier induced light which produces electron-hole pairs in the collector-substrate junction, as shown in Fig. 3.1. Collection of these electron-hole pairs leads to a substrate current (I_{SUB}), which can be used as a monitor for the occurrence of avalanche multiplication [53].

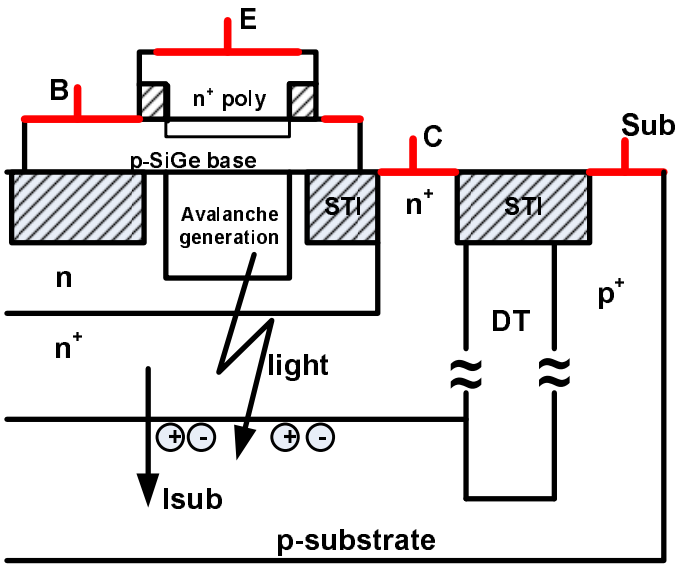

Figure 3.1: Illustration of photo carrier generation in the SiGe HBTs used.

Fig. 3.2 shows a schematic of the measurement setup. The base is grounded. The collector voltage V_C is set to desired V_{CB}. The substrate voltage is chosen such that the collector-substrate

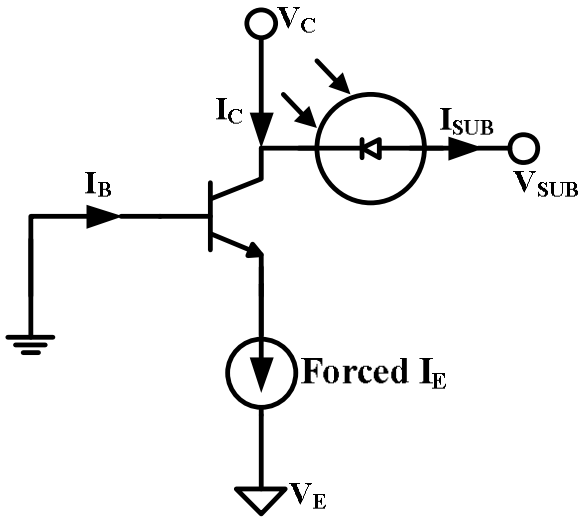

Figure 3.2: Experimental setup of the substrate current based M-1 measurement technique.

bias $V_{CS} \geq 0$. An emitter current I_E is forced, and the value of I_E is swept. V_{BE}, I_B, I_C and I_{SUB} are recorded during the I_E sweep. In the absence of self-heating, the avalanche current can be obtained as the difference in I_B between high V_{CB} and $V_{CB} = 0V$, denoted as I'_{AVE}:

$$I'_{AVE} = I_B(V_{BE}, V_{CB} = 0) - I_B(V_{BE}, V_{CB}), \tag{3.1}$$

where $I_B(V_{BE}, V_{CB} = 0)$ is the I_B at the V_{BE} values recorded during the I_E sweep for a 0 V V_{CB}, and can be determined using a separate measurement. $I_B(V_{BE}, V_{CB} = 0)$ represents the hole current injected into the emitter. At high I_E, self-heating becomes severe, and the junction temperature increases with V_{CB} significantly. Therefore $I_B(V_{BE}, V_{CB} = 0)$ gives the hole current injected into the emitter lower than at the desired V_{CB}. The hole current injected into the emitter at the desired V_{CB} are thus *underestimated* by $I_B(V_{BE}, V_{CB} = 0)$. Consequently, the avalanche current is underestimated by I'_{AVE}. Negative I'_{AVE} can be obtained, which is clearly unphysical for avalanche current.

Fig. 3.3 shows the measured I'_{AVE}, I_{SUB} and I_{SUB}/I'_{AVE} ratio versus I_E at 300 K, V_{CB}=4 V. I'_{AVE} first increases with I_E, as expected, but becomes negative at an of 3 mA, because of self-heating. However, for medium I_E (region B), I_{SUB} increases proportionally with I'_{AVE}, and a constant I_{SUB}/I'_{AVE}

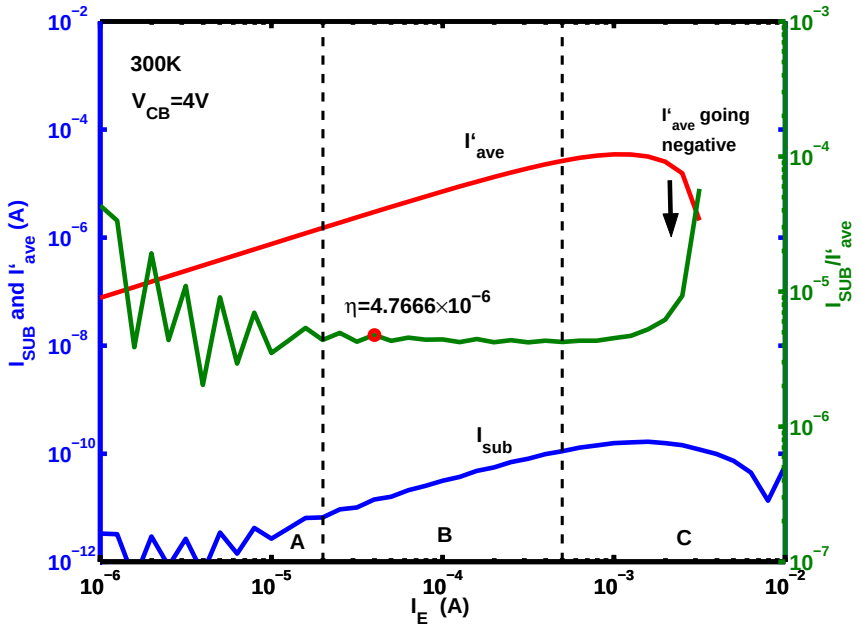

Figure 3.3: Measured $I_{AVE}^{'}$, I_{SUB} and $I_{SUB}/I_{AVE}^{'}$ ratio versus I_E at V_{CB}=4 V, 300 K.

ratio can be identified. Intuitively, this ratio can be viewed as the efficiency of substrate current generation due to avalanche, which we denote as η. Measurements show that η is independent of V_{CB} and V_{CS} [53]. In region C, due to self-heating, η loses its accuracy. There, the "true" avalanche current I_{AVE} in the high I_E region can be extracted by I_{SUB}/η. The overall avalanche current is given by:

$$I_{AVE} = \begin{cases} I_{AVE}^{'} & \text{region A and B,} \\ \frac{I_{sub}}{\eta} & \text{region C.} \end{cases} \tag{3.2}$$

Fig. 3.4 shows the extracted avalanche current I_{AVE} by (3.2) as a function of I_E at 300 K, V_{CB}=4 V. The rapid increase of I_{AVE} at very high I_E is caused by the rapid increase of I_{SUB} at very high I_E, due to the hole injection resulting from the forward biasing of the internal CB junction. This does not present a problem as it occurs at I_E well above the peak f_T.

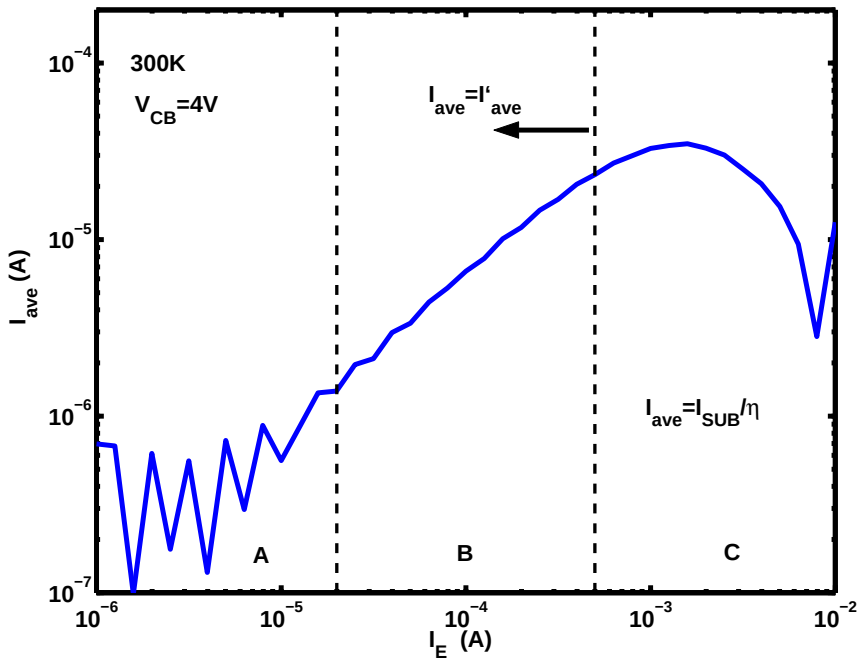

Figure 3.4: Extracted avalanche current I_{AVE} versus I_E at V_{CB}=4 V, 300 K.

3.2 Experimental results over temperatures and impact of current

This substrate current based avalanche multiplication technique has been investigated at 300K before [15]. Here we extend this technique down to 43 K. Fig. 3.5 and Fig. 3.6 show the measured I'_{AVE}, I_{SUB} and I_{SUB}/I'_{AVE} ratio versus I_E and extracted avalanche current I_{AVE} versus I_E at 43 K for example.

By definition, avalanche multiplication factor M-1 is obtained by:

$$M-1=\frac{I_{AVE}}{I_C-I_{AVE}}. \tag{3.3}$$

Fig. 3.7 show the measured M-1 and f_T versus J_E from 300 K to 43 K. Note that the decrease of M-1 starts much lower than the J_E of peak f_T. Physically this is reasonable because f_T rolls off when J_E is high enough to cause base push out, while M-1 decreases as long as the J_E is sufficient to cause a decrease of the CB junction peak field.

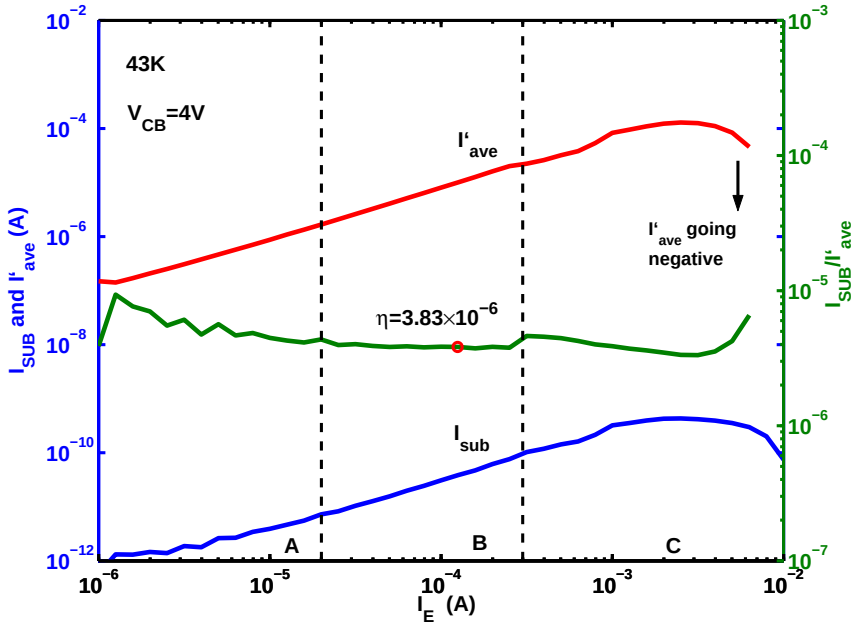

Figure 3.5: Measured I'_{AVE}, I_{SUB} and I_{SUB}/I'_{AVE} ratio versus I_E at V_{CB}=4 V, 43 K.

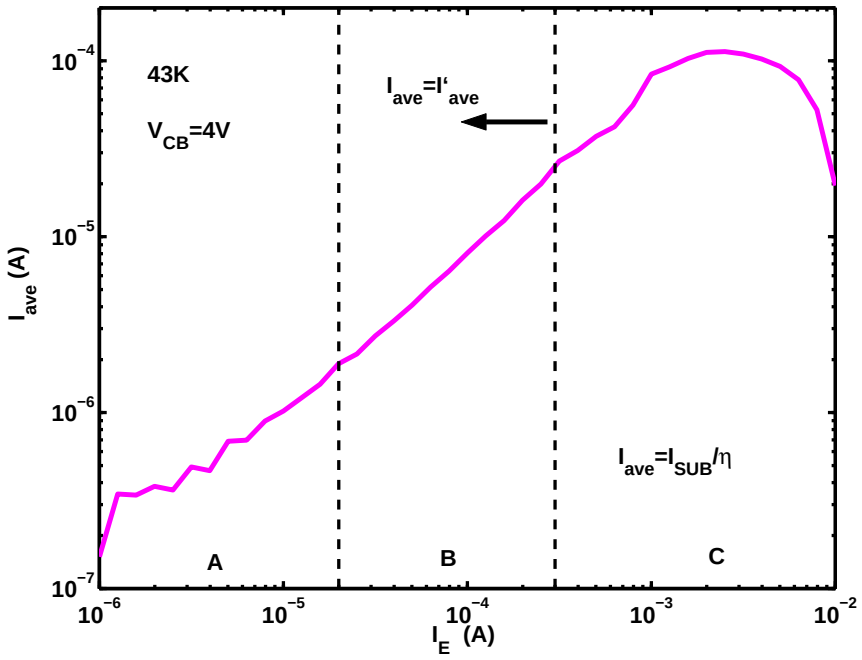

Figure 3.6: Extracted avalanche current I_{AVE} versus I_E at V_{CB}=4 V, 43 K.

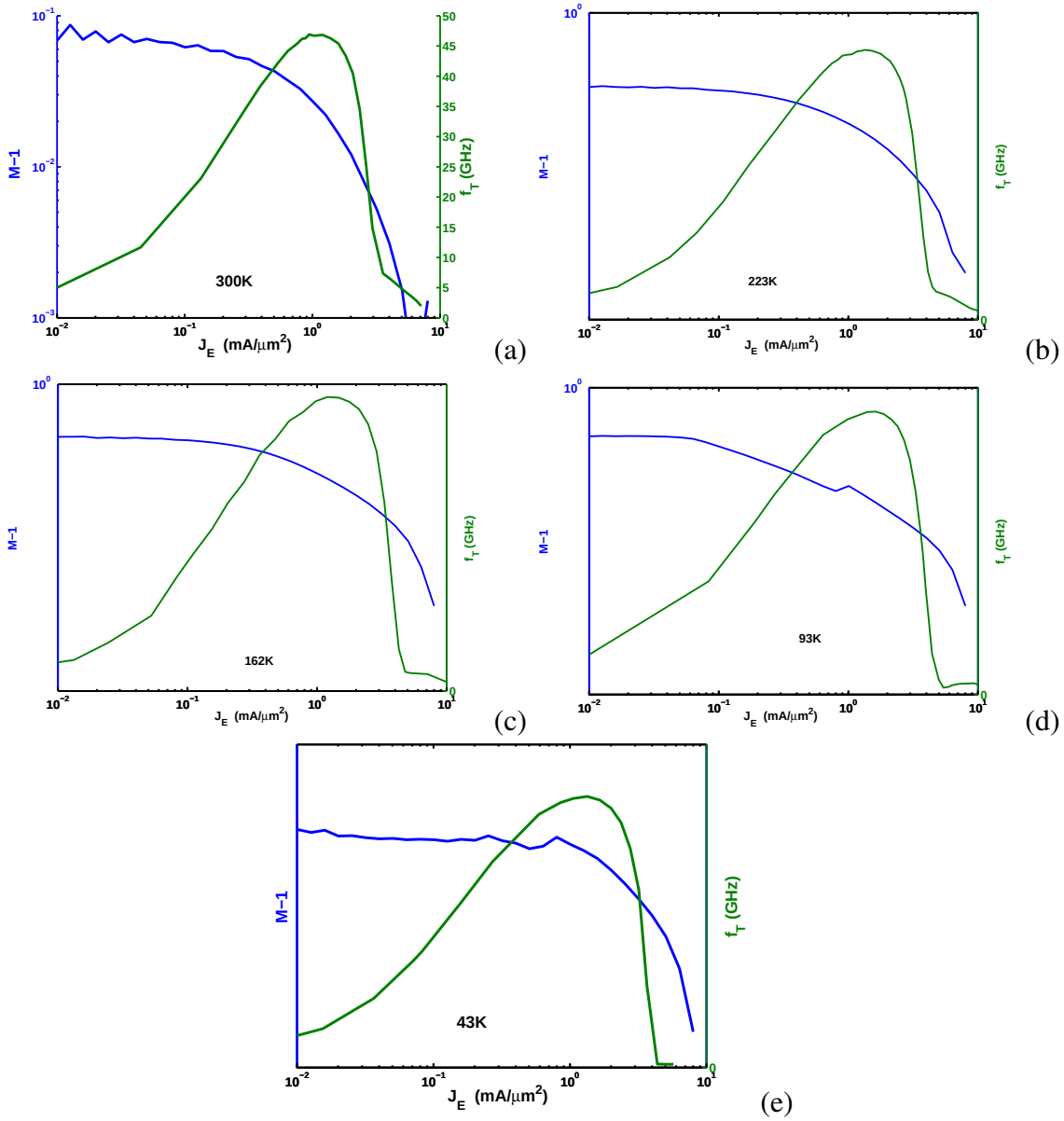

Figure 3.7: Measured M-1 and f_T vs. J_E at: (a) 300 K; (b) 223 K; (c) 162 K; (d) 93 K; (e) 43 K.

For transistors used in radio frequency (RF) power amplifiers, the maximum voltage handling capability depends on the details of M-1 versus V_{CB} characteristics. These applications require high I_E biasing for high speed, and high power density. It is therefore important to understand the M-1 versus V_{CB} characteristics at high biasing I_E. The breakdown voltage at high I_C is also an important concern for operating with mismatched load. Fig. 3.8 shows the measured M-1 versus V_{CB} for I_E=12.5 μA, 125 μA and 1.5 mA at 300 K. I_E=1 mA is where peak f_T located. The M-1 at 1 mA m is much smaller than the M-1 at 12.5 μA and 125 μA. Fig. 3.9 is the measured f_T and M-1 versus I_E over 162-300 K. It demonstrates that such current dependence of M-1 leads to a much higher breakdown voltage at high I_C, where f_T is maximized, than BV_{CEO} and BV_{CBO} which are typically measured at low I_C.

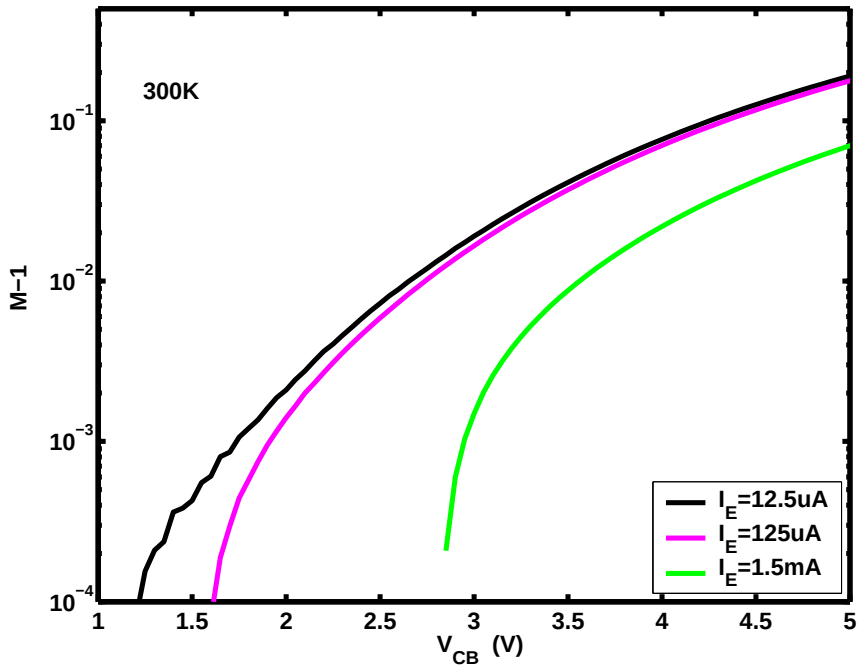

Figure 3.8: Measured M-1 versus V_{CB} for I_E=12.5 μA, 125 μA and 1.5 mA at 300 K.

3.3 Summary

In this chapter, the substrate current base avalanche multiplication technique has been extended from 300 K to 43 K. The current dependence of avalanche multiplication factor M-1 has been

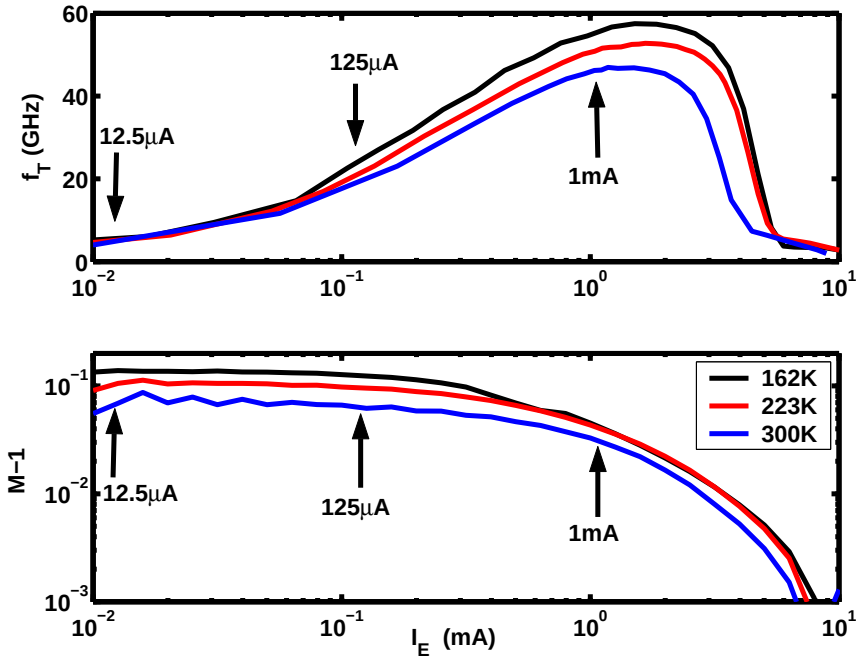

Figure 3.9: Measured f_T and M-1 vs. I_E over 162-300 K.

investigated. The M-1 at 1 mA m is much smaller than the M-1 at 12.5 μA and 125 μA. Such current dependence of M-1 leads to a much higher breakdown voltage at high collector current, where f_T is maximized, than BV_{CEO} and BV_{CBO} which are typically measured at low I_C.

Chapter 4

Forced-I_E Pinch-in Maximum Output Voltage Limit at Cryogenic Temperatures

In chapter 3, we discussed the current dependence of avalanche multiplication factor M-1 at cryogenic temperatures. In this chapter, we will investigate forced-I_E pinch-in maximum output voltage limit in SiGe HBTs operating at cryogenic temperatures, which is of interest for many space exploration applications [5]. In section 4.1, we first review the physics of emitter current pinch-in and analyze its temperature dependence. In particular we discuss how the critical base current I_B^* varies with temperature, and introduce the concept of critical multiplication factor (M-1)*. In section 4.2, we present measurement results of I_B^*, (M-1)*, and V_{CB}^* over temperature, from 43 to 300 K. V_{CB}^* is the collector-base bias where M-1 reaches (M-1)*. Implications to device design and circuit application for cryogenic operation are discussed in section 4.3.

4.1 Physics of emitter current pinch-in and temperature dependence analysis

For long emitter stripe ($l_E \gg w_E$), where l_E is emitter length and w_E is emitter width, the differential equation for local current distribution can be analytically solved. The instabilities start mainly at emitter length direction and can be modeled by a linear transistor chain. The critical base current of instability I_B^* for driving condition $I_E = const.$ can be modeled as [50]:

$$I_B^* = -\frac{V_T + r_e I_E}{R_{Bx} + r_{bi}} \left[1 + (\frac{w_E}{l_E})^2\right], \tag{4.1}$$

where $V_T = kT/q$ is thermal voltage, r_{bi} is the small-signal value of the internal intrinsic base resistance R_{Bi}, r_e is the small-signal value of emitter resistance R_E, R_{Bx} is extrinsic base resistance.

From (4.1), it is clear that T-dependence of V_T, r_e, R_{Bx} and r_{bi} all affect I_B^*. Due to the highly doped emitter and extrinsic base, and the weak T-dependence of mobility at such doping, the T-dependence of r_e and R_{Bx} are weak. We also neglect the difference between small-signal r_{bi}/r_e and large-signal R_{Bi}/R_E respectively. T-dependence of I_B^* comes from the V_T and r_{bi} terms. Intrinsic base sheet resistance R_{sBi} can be written as:

$$R_{sBi} = \left(q \int_0^{W_B} p_p(x)\mu_p(x)dx \right)^{-1}, \tag{4.2}$$

where W_B is base width, p_p is base hole density, μ_p is hole mobility.

W_B is almost constant over 43-300 K. μ_p is a function of temperature, and its temperature dependence is also related to doping concentration [35]. As a SiGe HBT of around 2×10^{18} cm^{-3} peak base doping is used here, μ_p is a weak function of temperature over 70-300 K. p_p decreases with cooling as a result of freezeout because the base peak concentration is below the Mott transition ($\approx 3 \times 10^{18}$ cm^{-3}). R_{sBi} will thus increase with cooling. Fig. 4.1 shows R_{sBi} versus temperature simulated using Sentaurus device [54]. Note that as a simple incomplete ionization model is implemented in Sentaurus, without considering Mott transition effect, the simulated T-dependence of r_{sBi} is weaker than the measurement. Nevertheless, a sizable increase of R_{Bi} with cooling down to 43 K is expected. Therefore, with cooling, $|I_B^*|$ will decreases as V_T decreases and R_{Bi} increases. This suggests that instabilities can occur more easily at low temperatures.

Forced-I_E avalanche multiplication factor M-1 can be written as [7]:

$$M - 1 = \frac{I_{B0} - I_B}{I_E - I_{B0}}. \tag{4.3}$$

$$I_{B0} = I_B(V_{BE})|_{V_{CB}=0} \approx \frac{I_E}{\beta_0 + 1},$$
$$\beta_0 = \beta(V_{BE})|_{V_{CB}=0}, \tag{4.4}$$

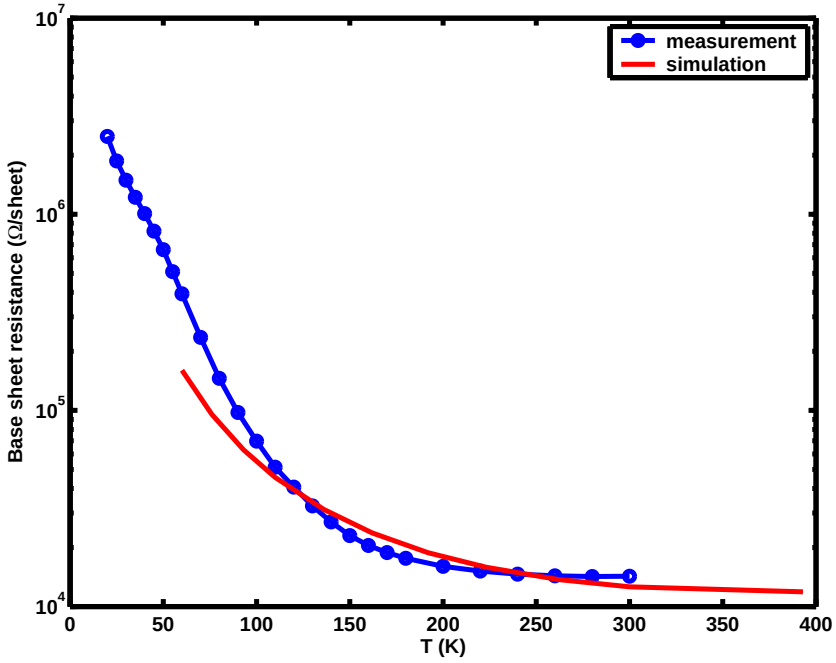

Figure 4.1: Measured and simulated intrinsic base sheet resistance R_{sBi}-T.

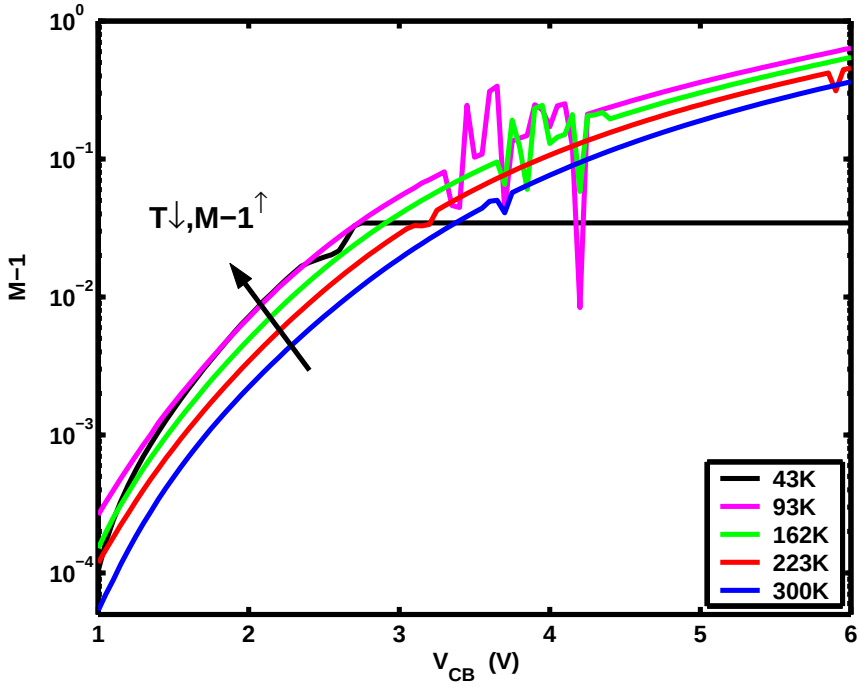

Figure 4.2: Measured M-1 vs. V_{CB} at forced-V_{BE} over 43-300 K.

where I_{B0} is found from the $I_B - V_{BE}$ curve obtained at $V_{CB} = 0$V. Here we introduce critical multiplication factor (M-1)* which correspond to I_B^*. V_{CB}^* is the collector-base bias where M-1 reaches (M-1)*.

$$(M-1)^* = \frac{I_{B0} - I_B^*}{I_E - I_{B0}}. \tag{4.5}$$

Substituting (4.4) into (4.5),

$$(M-1)^* = \frac{\frac{I_E}{\beta_0+1} - I_B^*}{I_E - \frac{I_E}{\beta_0+1}} \approx \frac{1}{\beta_0} - \frac{1}{\beta^*},$$
$$\beta^* = \frac{I_E}{I_B^*}. \tag{4.6}$$

β^* is negative when $I_B < 0$. The T-dependence of (M-1)* originates from T-dependence of $\frac{1}{\beta_0}$ and $\frac{1}{\beta^*}$. The β_0 of SiGe HBTs is large (around 100) and hence for all practical situations $\frac{1}{\beta^*}$ dominates. For a given I_E, the absolute value of I_B^* decreases with cooling, causing a decrease of (M-1)* with cooling.

As I_E increases, from (4.1), $|I_B^*|$ increases accordingly. Because V_T dominates the whole $(V_T + r_e I_E)$ term, $-\frac{1}{\beta^*}$ will decrease even though I_E increases. This leads to a decreasing (M-1)* with increasing I_E.

4.2 Experimental results

4.2.1 T-dependence of M-1 from forced-V_{BE} measurements

Forced-V_{BE} M-1 measurements are taken to analyze the temperature dependence of M-1. Small V_{BE} were chosen to avoid self-heating and instabilities which still occurred at 43 K. Fig. 4.2 is the measured M-1 vs. V_{CB} over 43-300 K. At 43 K, instability occurs above $V_{CB} = 3$V due to the relatively high V_{BE} used to produce the same current for all temperatures. The oscillations seen near $V_{CB} = 4$V at 93 K and 162 K are believed to be measurement errors. At a given V_{CB}, M-1 increases with cooling and this is consistent with earlier measurements [52].

4.2.2 T-dependence of I_B^*,V_{CB}^* and (M-1)* from forced-I_E measurements

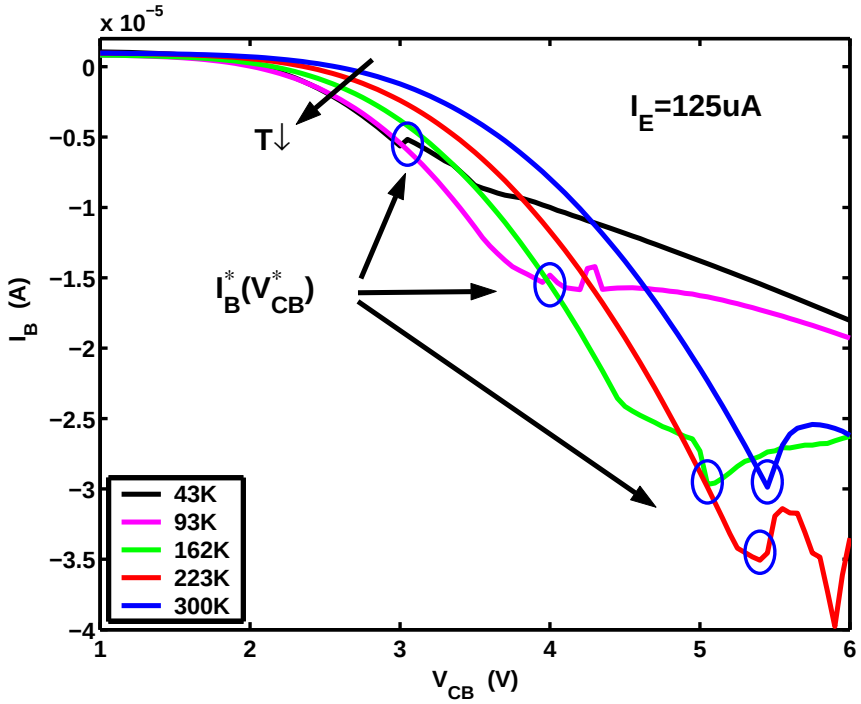

Figure 4.3: Measured I_B vs. V_{CB} at $I_E = 125\mu$ A over 43-300 K.

Forced-I_E M-1 measurements are taken at $I_E = 12.5\mu$A, 125μA and 1 mA which is near peak f_T. Fig. 4.3 shows the $I_B - V_{CB}$ at $I_E = 125\mu$A. I_B decreases first due to avalanche. Once pinch-in occurs, I_B becomes instable. I_B^* is where this abrupt transition occurs. Over 43-300 K, $|I_B^*|$ in general decreases with cooling, as shown in Fig. 4.9. It agrees with what we expect from (4.1). Fig. 4.4 shows the corresponding collector current I_C-V_{CB}. Sudden transitions occur at the same V_{CB}^* as shown in Fig. 4.3.

Fig. 4.6 shows the M-1-V_{CB} obtained using forced-I_E technique for $I_E = 125\mu$A. Observe that (M-1)* decreases at low temperatures. The extracted $1/\beta_0$ and $-1/\beta^*$ at three I_E are plotted in Fig. 4.8. It is clear that compared to $-1/\beta^*$, $1/\beta_0$ can be neglected safely in calculating (M-1)* from (4.6). With cooling, $-1/\beta^*$ decreases. This can explain why (M-1)* becomes smaller at low temperatures. When instabilities occur above V_{CB}^*, the forced-I_E M-1 curves become "saturated"

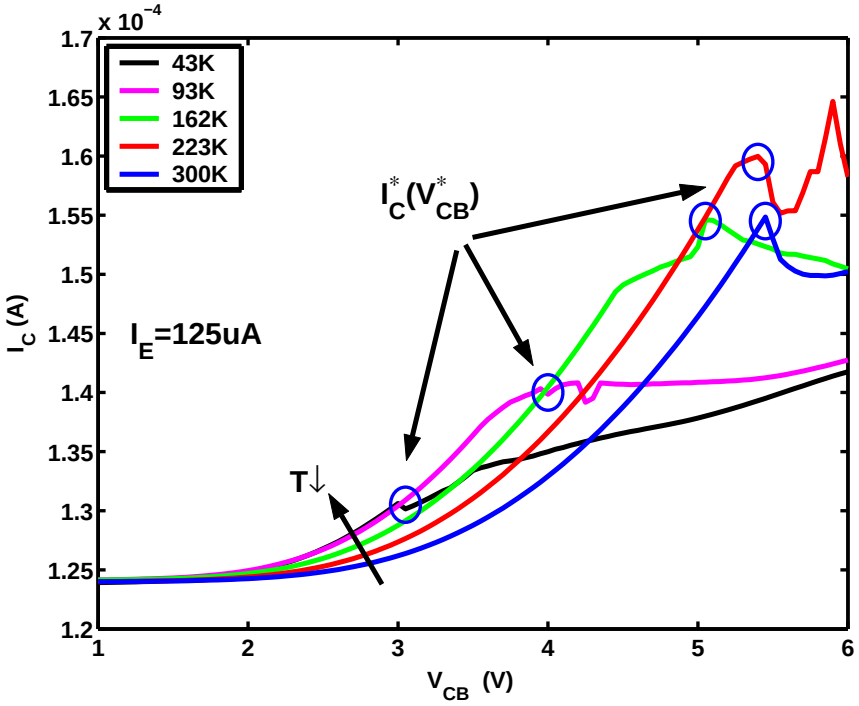

Figure 4.4: Measured I_C vs. V_{CB} at $I_E = 125\mu$ A over 43-300 K.

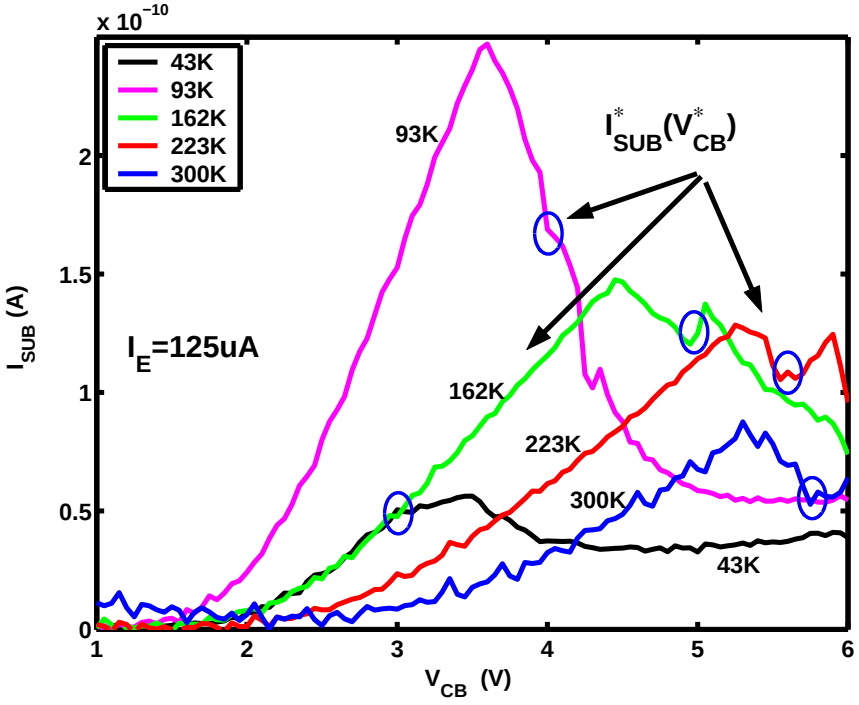

Figure 4.5: Measured I_{SUB} vs. V_{CB} at $I_E = 125\mu$ A over 43-300 K.

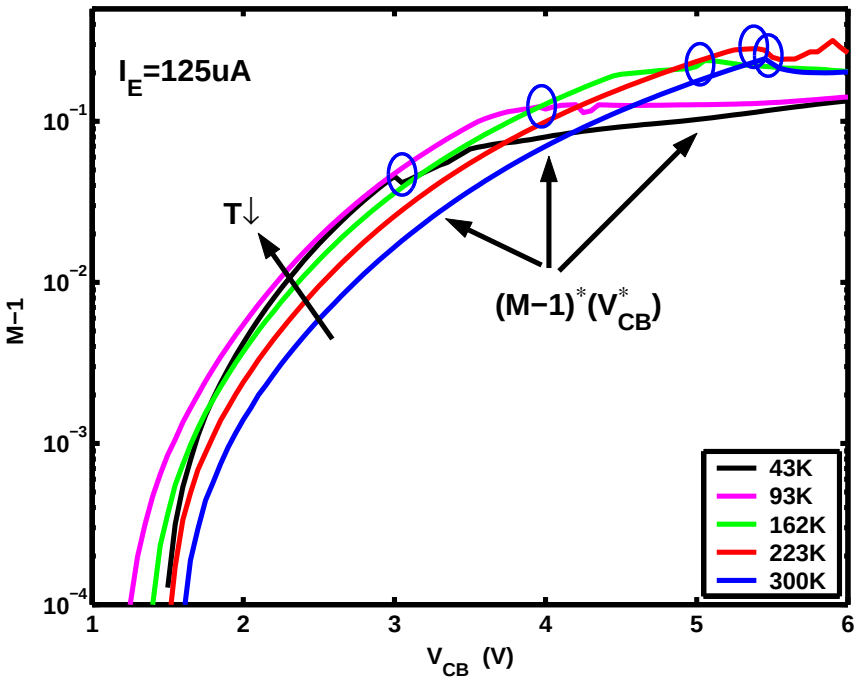

Figure 4.6: Measured M-1 vs. V_{CB} at $I_E = 125\mu A$ over 43-300 K.

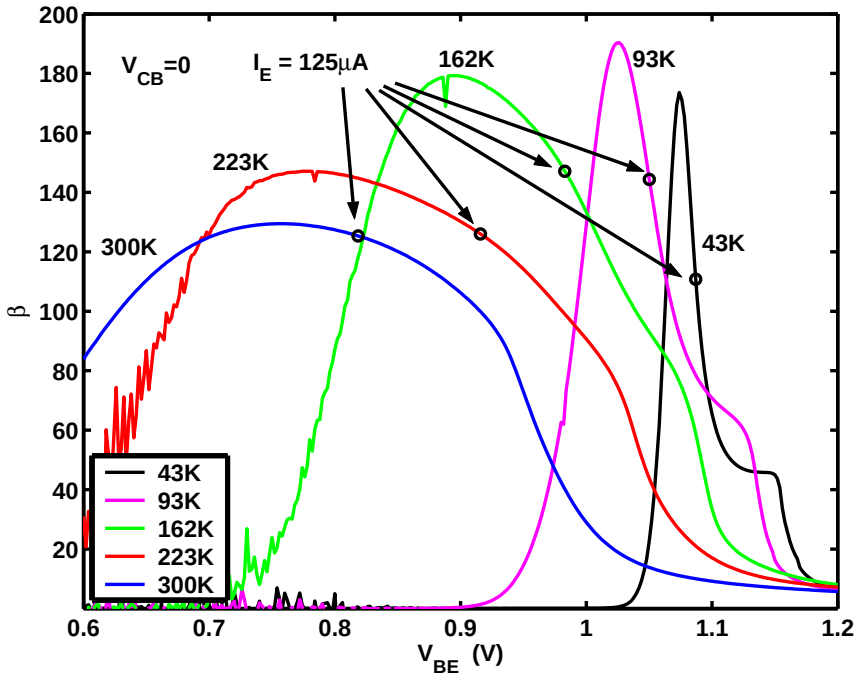

Figure 4.7: Measured β_0 vs. V_{BE} at $V_{CB} = 0$ V over 43-300 K.

at (M-1)* or even drops down. The M-1 obtained after V_{CB}^* is no longer the true M-1 because of pinch-in effect.

At $I_E = 125\mu$A, instabilities occur over 43-300 K in the V_{CB} range used. At $I_E = 12.5\mu$A, instabilities occur only at 43 K and 93 K. At $I_E = 1m$A, instabilities occur at 93 K and 162 K, and 43 K measurement was not successful. From Fig. 4.8, we can observe that $-1/\beta^*$ decreases as I_E increases, which is consistent with what we expect from the analysis made in Section II.

Fig. 4.9 shows the extracted I_B^* and V_{CB}^* vs. T. As expected, $|I_B^*|$ decreases with cooling. From Fig. 4.2, the true M-1 monotonically increasing with V_{CB} before instabilities occur. Now we know that (M-1)* decreases with cooling, even if M-1 versus V_{CB} is independent of temperature, the V_{CB}^* will decrease with cooling. The increase of M-1 with cooling for a given V_{CB} makes the decrease of V_{CB}^* with cooling even worse.

According to the analysis in Section II, $|I_B^*|$ increases as I_E increases. However, the V_{CB}^* decrease from $I_E = 12.5\mu$A to $I_E = 125\mu$A, and then increase from $I_E = 125\mu$A to $I_E = 1m$A. This can only be understood by considering the current dependence of M-1 vs. V_{CB} characteristics. Fig. 4.10 illustrates (M-1)* and V_{CB}^* at different I_E at 93 K, for which M-1 vs. V_{CB} varies. A higher I_E leads to a lower M-1. At low currents, such as $I_E = 12.5\mu$A and $I_E = 125\mu$A, the M-1 curves are very close to each other. Hence in general $(\text{M-1})^*_{12.5\mu A}$>$(\text{M-1})^*_{125\mu A}$ leads to $V^*_{CB,12.5\mu A} > V^*_{CB,125\mu A}$. At a high current $I_E = 1mA$, M-1 curve drops well below the low current curves. This makes possible $V^*_{CB,1mA} > V^*_{CB,12.5\mu A}$ even though $(\text{M-1})^*_{1mA}$<$(\text{M-1})^*_{12.5\mu A}$. Note that $I_E = 1m$A is close to peak f_T, and of interest to practical circuits. The fact that the maximum operation voltage range does not degrade as much with cooling at such high current density is certainly good news for circuit applications.

4.3 Circuit design implications

Both the T-dependence of M-1-V_{CB} and the T-dependence of (M-1)* determine the T-dependence of V_{CB}^*. (M-1)* in turn is related to I_B^*, and hence $V_T = kT/q$ and r_{bi}. The use of a high base doping [55] is expected to decrease r_{bi}. This is expected to increase the V_{CB}^*. We still expect V_{CB}^* at low

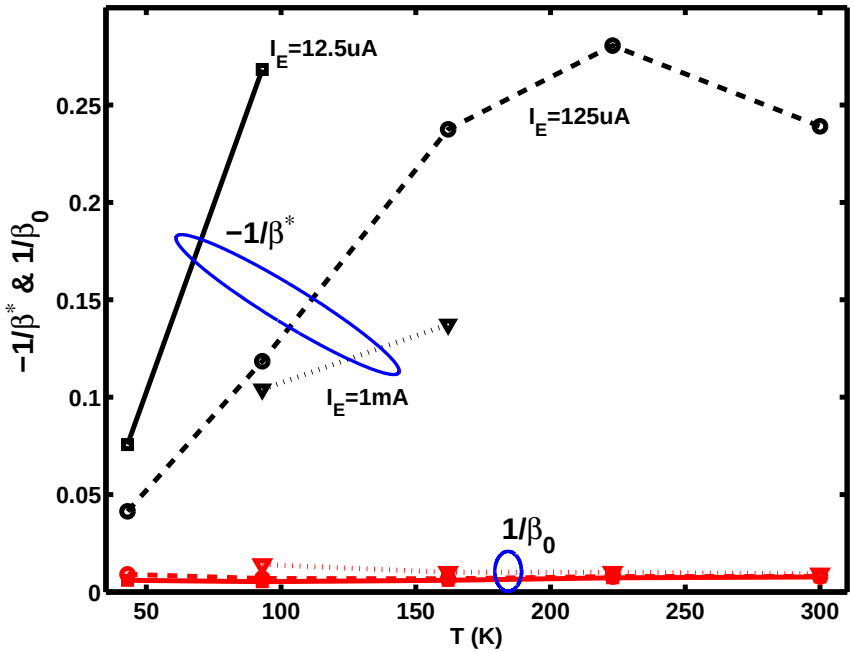

Figure 4.8: Measured $-\frac{1}{\beta^*}$, $\frac{1}{\beta_0}$ vs. T at $I_E = 12.5\mu$A, $I_E = 125\mu$A and $I_E = 1m$A.

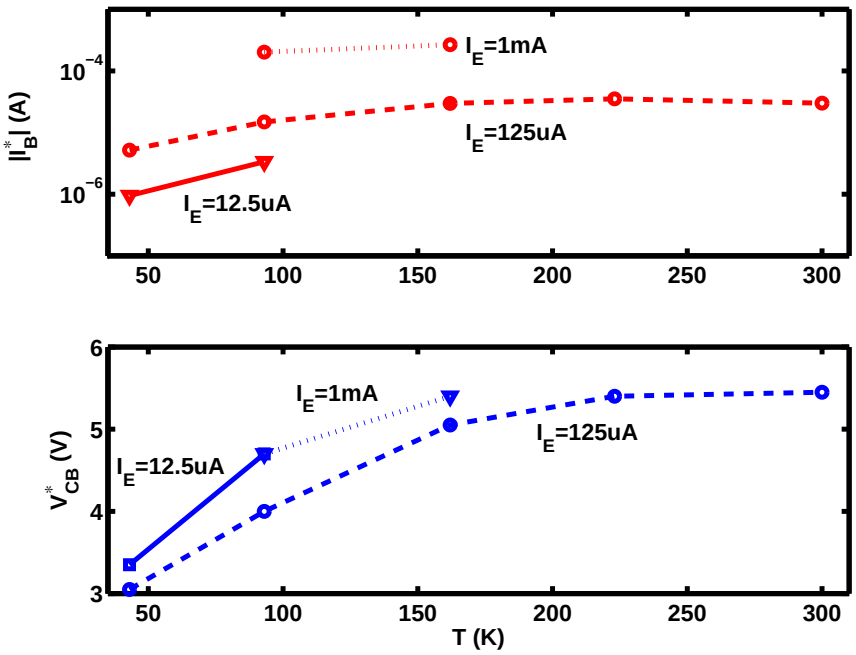

Figure 4.9: Measured $|I_B^*|$, V_{CB}^* vs. T at $I_E = 12.5\mu$A, $I_E = 125\mu$A and $I_E = 1m$A.

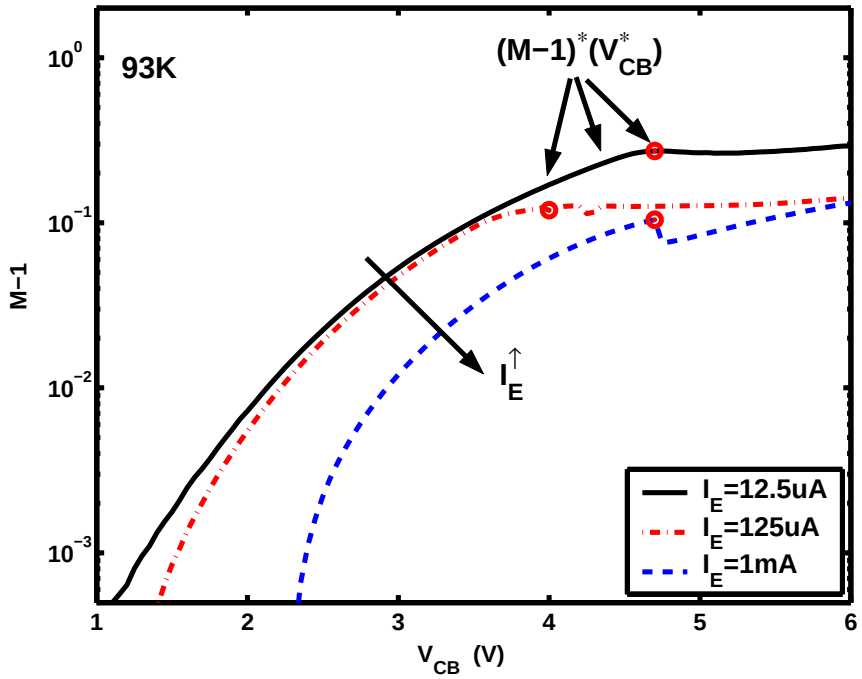

Figure 4.10: Measured M-1 vs. V_{CB} at $I_E = 12.5\mu$A, $I_E = 125\mu$A and $I_E = 1m$A at 93 K.

temperatures to be lower than 300 K, given the increase of M-1 with cooling and the decrease of V_T with cooling. Circuit designs for applications over a wide temperature range for space explorations should take this reduced V^*_{CB} into account to assure reliability of operations. Using a higher current density helps to alleviate the decrease of V^*_{CB} with cooling, and may be considered in circuit design.

4.4 Summary

In this chapter, the forced-I_E pinch-in maximum output voltage limit in SiGe HBTs operating at cryogenic temperatures has been investigated . A decrease of the voltage limit is observed with cooling, and attributed to the increase of intrinsic base resistance due to freezeout as well as increase of avalanche multiplication factor M-1. A practically high I_E is shown to alleviate the decrease of V^*_{CB} with cooling, primarily due to the decrease of M-1 with increasing I_E.

Chapter 5

Compact Modeling of SiGe HBT at Cryogenic Temperatures

5.1 Introduction of compact modeling

A compact transistor model tries to describe the I-V characteristics of a transistor in a mathematical way, such that the model equations can be implemented in a circuit simulator. The first bipolar model is the Ebers-Moll model [56] developed in 1954, which is the predecessor of today's computer simulation models and contains only two back-to-back diode currents. The two diodes represent the base-emitter and base-collector diodes. Depending on the base-emitter and base collector junction biases four operation regions are modeled, including forward active region, reverse active region, saturation region and cut-off region. The Gummel-Poon model invented in 1970's is based on the integral charge-control relation [8] and has served as a standard for more than three decades. On the basis of a general integral relation, high injection effect and Early effect are incorporated in Gummel-Poon model. When a device with light doped collector is operated at high injection level, dc current gain and cut-off frequency f_T roll off due to quasi-saturation effect [14]. Quasi-saturation effect is very necessary to be modeled accurately as high frequency circuits are biased at high collector densities in order to obtain maximum operating speed. However, in both Ebers-Moll model and Gummel-Poon compact model, the quasi-saturation effect is not addressed.

The VBIC model (Vertical Bipolar Inter-Company model) [9] was developed in 1995 as an industry standard replacement for the SPICE Gummel-Poon (SGP) model, to improve deficiencies of the SGP model that have become apparent over time because of the advances in BJT process technology. The Mextram (Most EXquisite TRAnsistor Model) model release was firstly introduced as Level 501 in 1985 [3] to improve on the standard Gummel-Poon model. HICUM (HIgh CUrrent Model) model was first described in [57][58] in 1987 to address modeling issue for high-speed and high current density operations [10]. VBIC, Mextram and HICUM all include avalanche

breakdown, self-heating, quasi-saturation effect, non-quasi-static effect and temperature effect. HICUM incorporates the epilayer charges in the total charge storage, and Mextram and VBIC do model the epilayer explicitly. HICUM model is useful in high current density and high speed circuits. The Mextram and VBIC bipolar transistor models are comparable for low and medium collector current densities and frequencies. The main deficiency of the VBIC model is the description of the velocity saturated behavior of the current though the collector epilayer in combination with base push-out. Therefore the VBIC model is not able to describe accurately the degradation of gain, output conductance and cut-off frequency at high current densities [59].

Our basis is the MEXTRAM 504.6 [3]. Mextram model is a widely used vertical bipolar transistor model. The first Mextram release was introduced as Level 501 in 1985 [60]. Later Level 502, 503 and 504 were respectively released in 1987 [13], 1994 and 2000 [3]. And development was never stopped following the requirement of updated technology. The latest version of Mextram is 504.9.1 which was released in January, 2011.

Fig. 5.1 shows the equivalent circuit of the Mextram model as it is specified in [3]. The branches representing model currents and charges are schematically associated with different physical regions of a bipolar transistor separated by the base-emitter (BE), base-collector (BC), and substrate-collector (SC) junctions. All current and charge branches in Mextram are given as explicit functions of external and internal nodal potentials [60]. The main transfer current I_N in Mextram, as in the Gummel-Poon model [6], is evaluated in the quasi-neutral base (QNB). Moreover, the effects of a graded Ge profile in QNB [61] are physically addressed in the transfer current description. A distinguishing feature of the Mextram model is the description of the epilayer transfer current I_{epi}. It is employed for intensive physical modeling of the quasi-saturation phenomena including the base widening, Kirk effect [14] and hot-carrier behavior in the epilayer.

The diode-like injection currents I_{B1},I_{B1}^{S} ,I_{B2}, I_{B3}, Iex, and XI_{ex} in the Mextram equivalent circuit describe various diffusion and recombination currents in the quasi-neutral and depletion transistor regions. The recombination in the modulated QNB, which is particularly important for SiGe HBT applications, is also included. The effect of a distributed hole injection across BE

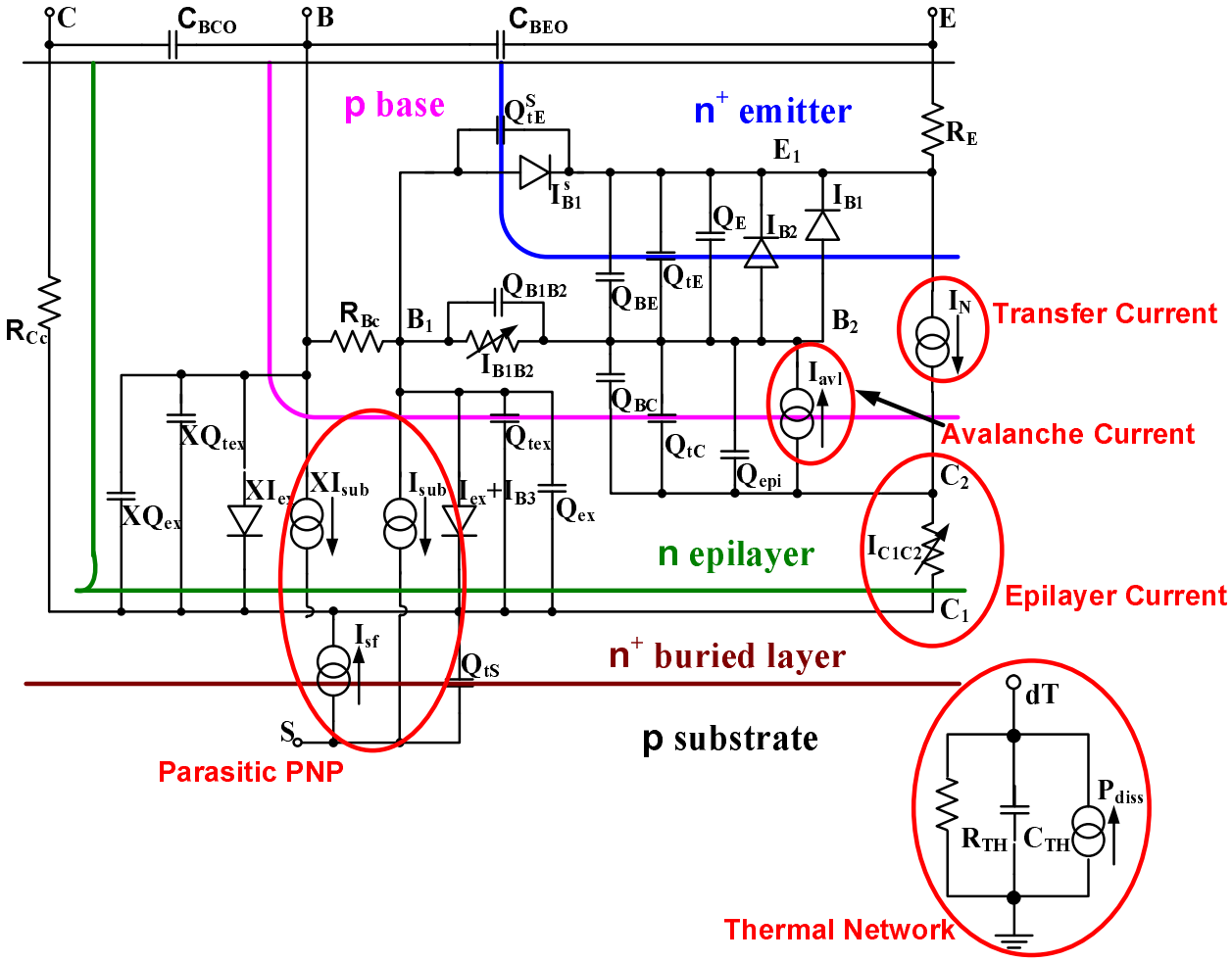

Figure 5.1: The Mextram equivalent circuit for the vertical NPN transistor.

junction is described by an additional current branch I_{B1B2}. Mextram provides also a sophisticated model for the weak avalanche current in the branch I_{avl}. The contribution of the parasitic PNP transistor transfer current to the substrate current, represented by the current sources I_{sub} and XI_{sub}, is implemented using a simplified Gummel-Poon integral charge control relationship.

Below effects are contained in Mextram:

1. Bias-dependent Early effect
2. Low-level non-ideal base currents
3. High-injection effects
4. Ohmic resistance of the epilayer
5. Velocity saturation effects on the resistance of the epilayer
6. Hard and quasi-saturation (including Kirk effect)
7. Weak avalanche (optionally including snap-back behavior)
8. Charge storage effects
9. Split base-collector and base-emitter depletion capacitance
10. Substrate effects and parasitic PNP
11. Explicit modeling of inactive regions
12. Current crowding and conductivity modulation of the base resistance
13. First order approximation of distributed high frequency effects in the intrinsic base (high frequency current crowding and excess phase-shift)
14. Recombination in the base (meant for SiGe transistors)
15. Early effect in the case of a graded bandgap (meant for SiGe transistor)

16. Temperature scaling

17. Self-heating

18. Thermal noise, shot noise and 1/f-noise

Some parts of the model are optional and can be switched on or off by setting flags. These are the extended modeling of reverse behavior, the distributed high-frequency effects, and the increase of the avalanche current when the current density in the epilayer exceeds the doping level.

5.2 Description of proposed wide temperature range compact model

In this work, various modifications and extensions are made to enable modeling of *dc* characteristics from 43-393 K, and *ac* characteristics from 93-393 K. New modeling equations were implemented using Verilog-A. Customized programs were written using the PEL (Parameter Extraction Language) of ICCAP [62] for parameter extraction. Main improvements include:

- Adding forward bias trap-assisted tunneling current $I_{B,tun}$[2].
- Adding substrate resistor R_{SUB} and capacitor C_{SUB}.
- developing new temperature-scaling equations of:

– Saturation current and ideality factor for main current and base currents [1]

– Base tunneling current $I_{B,tun}$ [2]

– Series resistance [17]

– Thermal resistance R_{TH}

– Epilayer current parameter I_{HC} and SCR_{CV}

Fig. 5.2 shows the equivalent circuit of the compact model. A new main current model I_N is developed to produce accurate collector current low and medium injection. Such new I_N includes

new models of forward and reverse saturation current $I_{S,F}$ and $I_{S,R}$, forward and reverse ideality factor N_F and N_R. The T-dependence of N_F is included in the T-dependence model of $I_{S,F}$, which is necessary to fit measured I_C-V_{BE} data at low temperatures[1]. Below 93 K, the trap-assisted tunneling (TAT) [63] current can be clearly observed in forward bias I_B-V_{BE}. $I_{B,tun}$ is added between B_2 and E_1 to account for this forward bias TAT current. Substrate resistance R_{SUB} and capacitance C_{SUB} are included as part of the model. New temperature scaling models of terminal resistance [17], thermal resistance R_{TH}, quasi-saturation parameters I_{HC} and SCR_{CV} are developed to model high injection region.

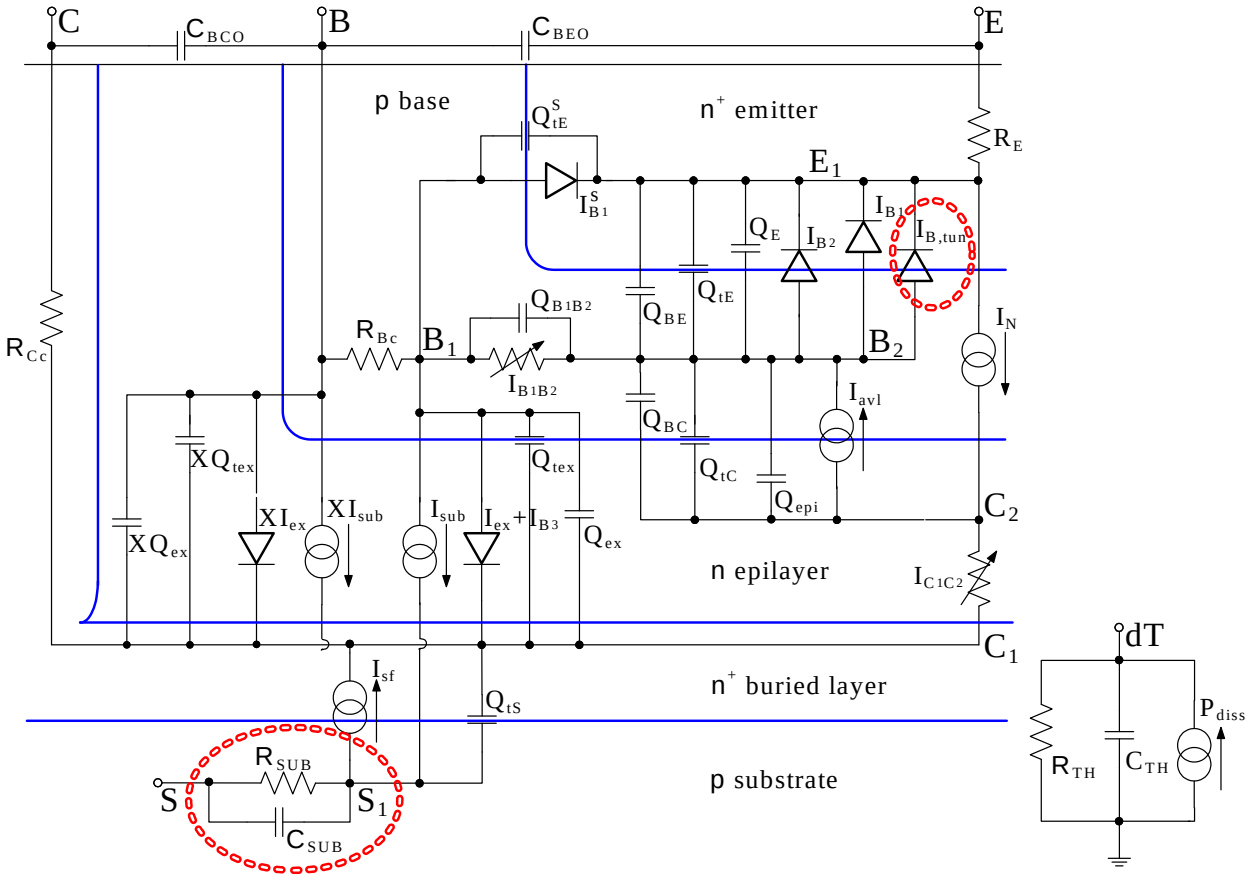

Figure 5.2: Equivalent circuit used in this work, with 1) added forward base tunneling current $I_{B,tun}$; 2) added R_{SUB} and C_{SUB}.

5.3 Main current

Fig. 5.3(a) shows the one-dimensional representation of a vertical n-p-n transistor. The transistor consists of an n^+ emitter, p-type base and an n-type collector. The n-type collector consists of a n^- epilayer and $n+$ buried layer. The starting substrate of a vertical n-p-n transistor is usually a p^- silicon. Fig. 5.3(b) shows the bias condition for an n-p-n transistor in normal operation. The emitter-base diode is forward biased by V_{BE}, and the base-collector diode is reverse biased by V_{BC}. Electrons flow from emitter into the base and the holes flow from the base into the emitter. The main current I_N caused by those electrons not recombined in the base arriving at the collector gives rise to collector current I_C. The current I_{BE} induced by the holes injected into the emitter gives rise to the base current I_B. Similarly, if the base-collector diode is forward biased, the current I_{BC} induced by the holes injected into the collector also contributes to the base current I_B.

Recalling that, the main current density J_N running through a bipolar transistor has been derived by Gummel's integral charge control relation (ICCR) [8]:

$$J_N = \frac{q(e^{qV_{BE}/kT} - e^{qV_{BC}/kT})}{\int_0^{W_b} \frac{p_b(x)dx}{D_{nb}(x)n_{ib}^2(x)}}, \tag{5.1}$$

where $x = 0$ and $w = W_b$ are the neutral base boundary values on the emitter-base and collector-base sides of the base respectively. n_{ib}, D_{nb} and p_b are intrinsic carrier concentration, electron diffusion constant and hole density in the base respectively. If we assume constant D_{nb} and constant n_{ib} (indicating constant E_g, N_C and N_V), the I_N becomes:

$$\begin{aligned} I_N &= \frac{q^2 D_{nb} A_{em}^2 n_{ib}^2}{Q_B}\left[\exp\left(\frac{V_{BE}}{V_T}\right) - \exp\left(\frac{V_{BC}}{V_T}\right)\right], \\ Q_B &= q\int_0^{W_b} p_b(x)dx, \end{aligned} \tag{5.2}$$

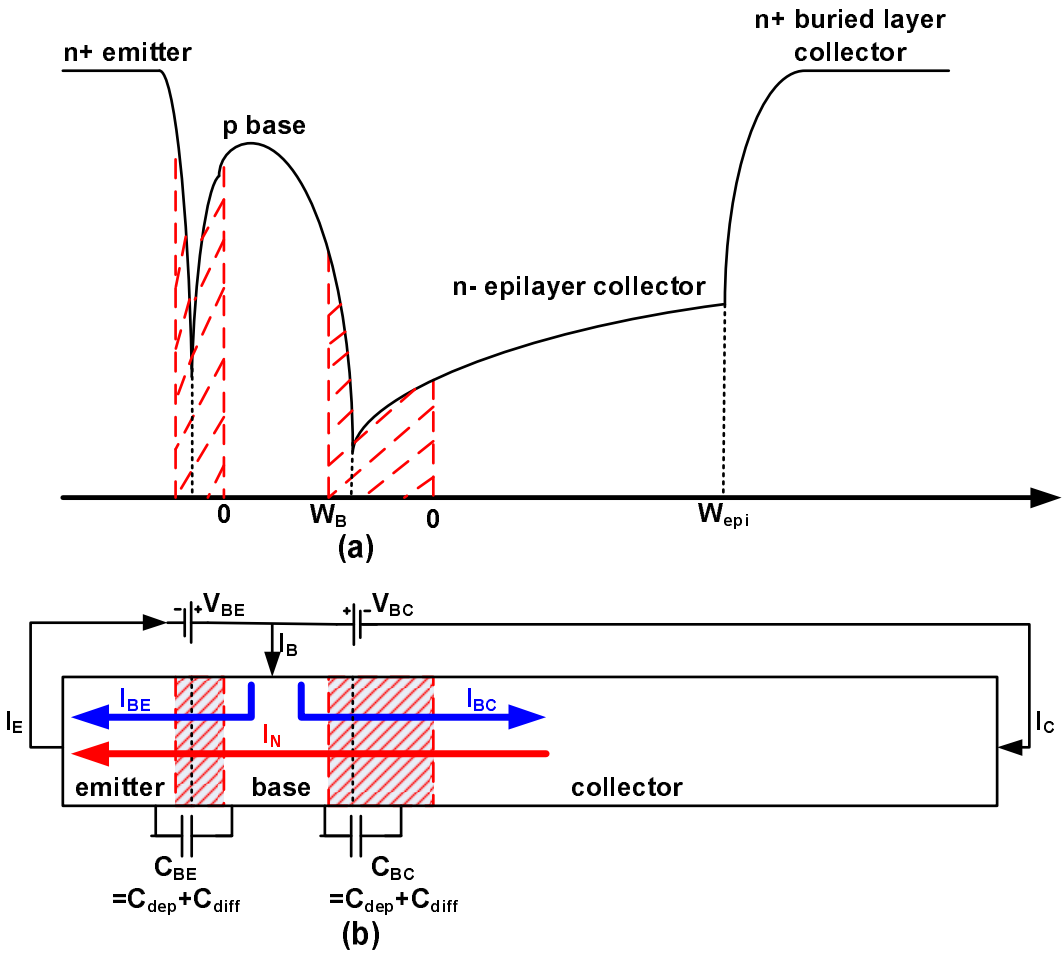

Figure 5.3: (a) Doping profile for a NPN transistor. (b) Schematic illustrating the applied voltages in normal operation.

where A_{em} is effective emitter area, Q_B is the total base charge. If we assume complete ionization and neutral region approximation, $p_b(x)$ can be approximated as:

$$p_b(x) \approx N_A(x) + n_{BE}(x) + n_{BC}(x), \tag{5.3}$$

where $N_A(x)$ is acceptor doping concentration, $n_{BE}(x)$ and $n_{BC}(x)$ are the injected electron densities due to applied V_{BE} and V_{BC} respectively.

$Q_B = q\int_0^{W_b} p_b(x)dx$ changes with applied V_{BE} and V_{BC} in several ways:

1. As we increase V_{BE}, the EB junction depletion thickness becomes smaller, this moves the neutral base boundary ($x = 0$) towards the EB metallurgical junction location. This V_{BE} dependent base boundary "0" causes extra depletion charges Q_{tE}, as shown in Fig. 5.4 (b). This is so called reverse Early effect.

2. Similarly, as we increase V_{BC}, the BC junction depletion thickness becomes smaller, this moves the neutral base boundary ($x = W_B$) towards the BC metallurgical junction location. This V_{BC} dependent base boundary "W_B" causes extra depletion charges Q_{tC}, as shown in Fig. 5.4 (b). This is so called forward Early effect.

3. $n_{BE}(0)$ is proportional to $\exp(\frac{V_{BE}}{V_T})$. Hence diffusion charge $n_{BE}(x)$ is V_{BE} dependent.

4. $n_{BC}(W_B)$ is proportional to $\exp(\frac{V_{BC}}{V_T})$. Hence diffusion charge $n_{BC}(x)$ is V_{BC} dependent.

$$\begin{aligned}
Q_B(V_{BE}, V_{BC}) &= Q_{N_A}(V_{BE}, V_{BC}) + Q_{BE}(V_{BE}) + Q_{BC}(V_{BC}), \\
Q_{N_A}(V_{BE}, V_{BC}) &= q\int_0^{W_b} N_A(x)dx = Q_{B0} + Q_{JE} + Q_{JC}, \\
Q_{BE}(V_{BE}) &= q\int_0^{W_b} n_{BE}(x)dx, \\
Q_{BC}(V_{BC}) &= q\int_0^{W_b} n_{BC}(x)dx,
\end{aligned} \tag{5.4}$$

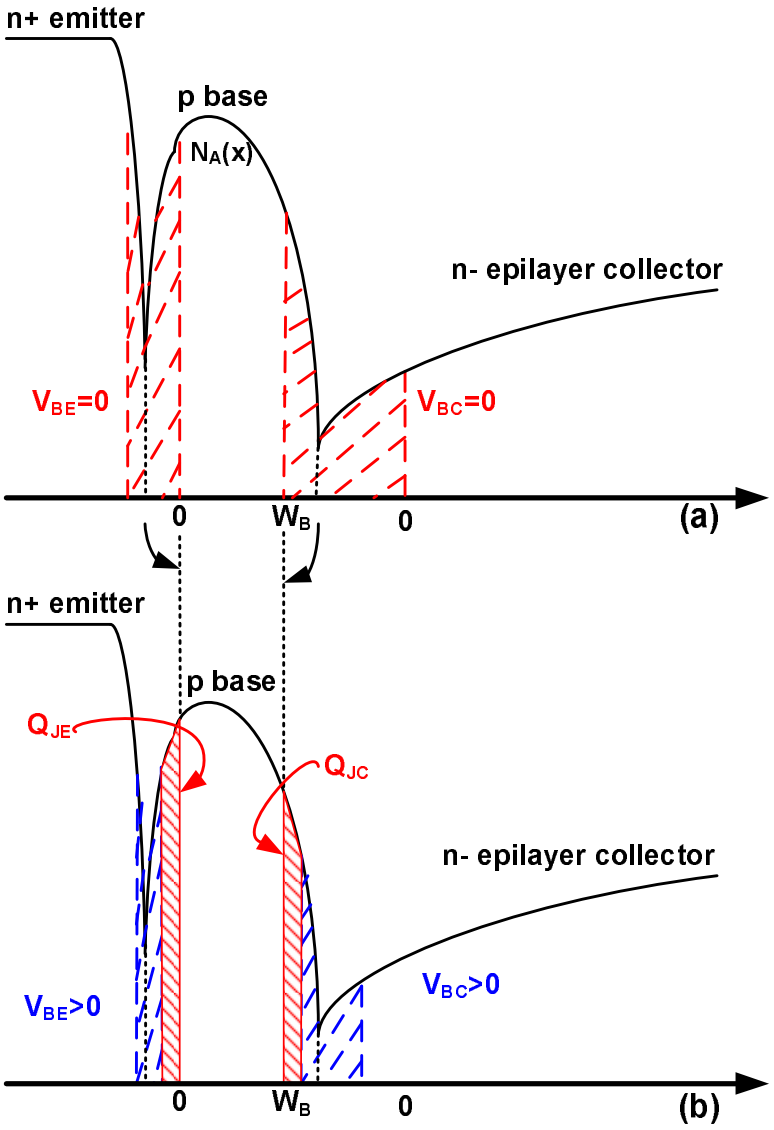

Figure 5.4: A schematic cross-section of the base region for a NPN transistor, showing the Early effect: EB and BC junction depletion thickness's variation with V_{BE} and V_{BC}.

where$Q_{B0} = Q_B|_{V_{BE}=0,V_{BC}=0} = Q_{N_A}|_{V_{BE}=0,V_{BC}=0}$ is the zero bias total base charge. Q_{BE} is the diffusion charges due to V_{BE}, Q_{BC} is the diffusion charges due to V_{BC}. The normalized base charge is then given by:

$$\begin{aligned} q_B &= \frac{Q_B}{Q_{B0}} = \frac{Q_{B0} + Q_{JE} + Q_{JC} + Q_{BE} + Q_{BC}}{Q_{B0}}, \\ &= 1 + \frac{Q_{JE}}{Q_{B0}} + \frac{Q_{JC}}{Q_{B0}} + \frac{Q_{BE}}{Q_{B0}} + \frac{Q_{BC}}{Q_{B0}}. \end{aligned} \tag{5.5}$$

The main current (5.2) then can be reorganized as:

$$\begin{aligned} I_N &= \frac{I_S\left[\exp\left(\frac{V_{BE}}{V_T}\right) - \exp\left(\frac{V_{BC}}{V_T}\right)\right]}{q_B}, \\ I_S &= \frac{q^2 D_{nb} A_{em}^2 n_{ib}^2}{Q_{p0}}. \end{aligned} \tag{5.6}$$

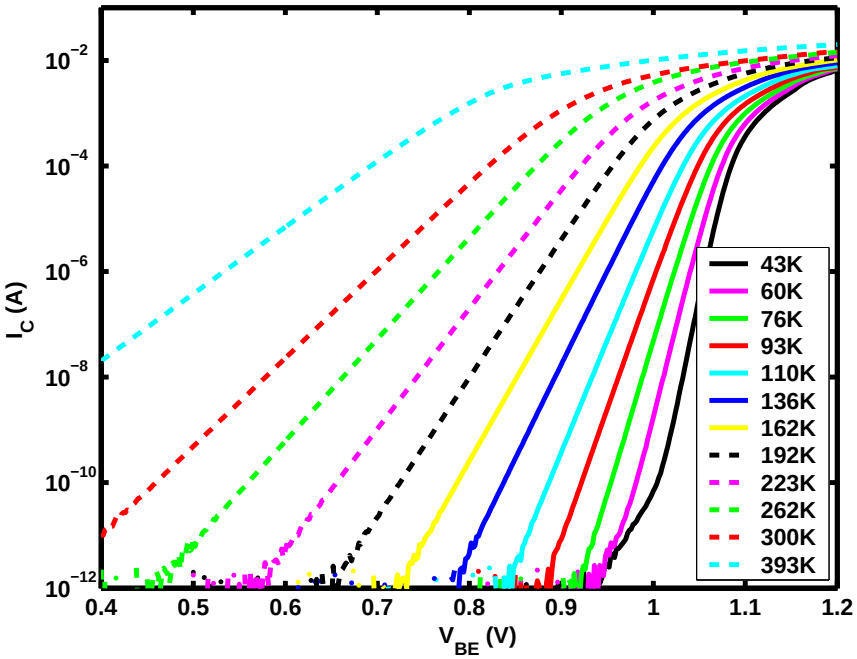

Figure 5.5: Measured I_C-V_{BE} for a graded-base SiGe HBT.

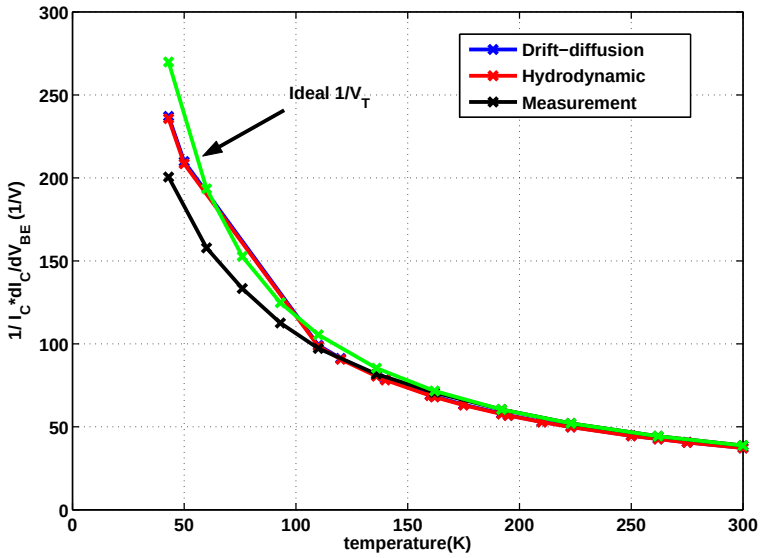

Figure 5.6: The slope of I_C-V_{BE} from device simulation [1].

Fig. 5.5 shows the measured I_C-V_{BE} for a graded-base SiGe HBT. A logarithmic scale is used for I_C and it facilitates the examination of the slope of I_C at fixed V_{BE} at low temperatures. For first-order approximation, the slope of I_C-V_{BE} is proportional to $\frac{1}{V_T}$ in semilog scale. Therefore, lower the temperature, sharper the slope. However, the slope of measured I_C-V_{BE} significantly deviates from the ideal $\frac{1}{V_T}$ approximation at low temperatures. To identify the physical reasons, we performed both drift-diffusion and hydrodynamic device simulation of this graded-base SiGe HBT using Sentaurus Device [54]. The simulated I_C-V_{BE} slope, however, shows a much less deviation from ideal value than what we observed in measurement, as shown in Fig. 5.6. As all of the higher order physics effects are naturally included in device simulation, such as Philips unified mobility model, Ge-dependent bandgap, Ge-dependent density-of-states, incomplete ionization, Early effect and Ge ramping effect, we conclude that such a deviation is due to unknown physics to the best of our knowledge.

In Mextram, it was believed that q_B is sufficient in modeling the slope of I_C-V_{BE}, and using ideality factors like in SGP and VBIC could complicate the parameter extraction. However, at low temperatures, we found that the deviation of I_C-V_{BE} slope from ideal $1/V_T$ is much larger than what

can be modeled with q_B. Even though the underlying physics is not understood yet, one can model this with a N_F factor that increases with cooling, such that the slope $1/(N_F V_T)$ does not increase as much as the ideal $1/V_T$. The T-dependence of N_F is included in the T-dependence model of $I_{S,F}$, which is necessary to fit measured I_C-V_{BE} data [1].

Fig. 5.7 (b) and (c) show the N_F and I_S extracted versus temperature. Observe that N_F is close to 1 above 200 K, but increases rapidly below 200 K, to 1.35 at 43 K. Fig. 5.8 shows simulated I_C-V_{BE} using default Mextram models from 43 K to 393 K. Above 110 K, default Mextram models can produce reasonably good I_C-V_{BE} at moderate injection as shown in Fig. 5.8 (a). From 43-93 K, however, default Mextram models fails, as shown in Fig. 5.8 (b). Clearly, N_F is necessary to model the I_C slope correctly below 110 K.

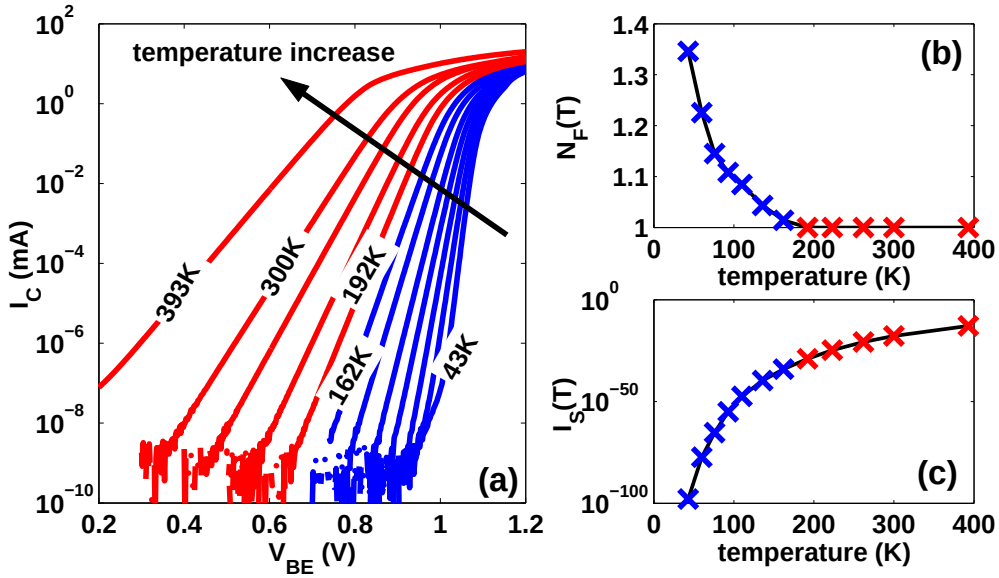

Figure 5.7: (a) Measured I_C-V_{BE} from 43 to 393 K. (b) Extracted N_F at each temperature. (c) Extracted I_S at each temperature [1].

In our previous work [1], the main current I_N is modeled as:

$$I_N = \frac{I_{S,F} e^{\frac{V_{B_2E_1}}{N_F V_T}} - I_{S,R} e^{\frac{V^{\star}_{B_2C_2}}{N_R V_T}}}{q_B}, \tag{5.7}$$

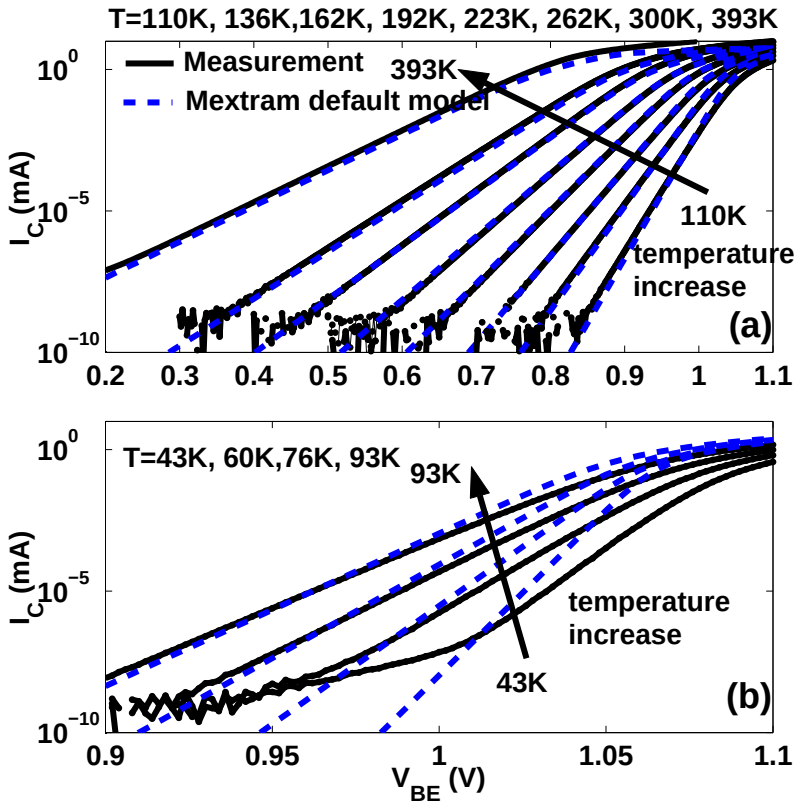

Figure 5.8: (a) Simulated versus measured I_C-V_{BE} at high temperatures. (b) Simulated versus measured I_C-V_{BE} at low temperatures [1].

where all the symbols have their usual meanings in Mextram except for forward and reverse saturation current $I_{S,F}$ and $I_{S,R}$, forward and reverse ideality factor N_F and N_R. Ideality factor N is extracted from medium injection region.

In section 2.1.8, we have clarified that the depletion thickness has weak temperature dependence. In Mextram parameter $A_{Q_{B0}}$ is mainly introduced to model carrier freezeout effect. As we will discuss in chapter 5.11.3, the incomplete ionization rate $IR(T)$ is a complicated function of temperature. However, in Mextram, the carrier freezeout effect is only taken into account through relation $\frac{Q_{B0,T}}{Q_{B0}} = t_N^{A_{Q_{B0}}}$.

5.4 Depletion charges and capacitances

The early effect is the effect that the main current gets modulated due to a variation in effective base width on both base-emitter side and base-collector side. At low injection, the diffusion charges Q_{BE} and Q_{BC} can be neglected and the normalized base charge q_B is usually denoted as q_1:

$$q_1 \approx 1 + \frac{Q_{tE}}{Q_{B0}} + \frac{Q_{tC}}{Q_{B0}}. \tag{5.8}$$

In compact modeling, we cannot determine depletion charges directly. The depletion charges Q_t are directly related to the well-known junction capacitance C_j. The basic model for depletion capacitance is [64][65] [12],

$$C_j = \frac{C_{j0}}{(1 - V/V_d)^p}, \tag{5.9}$$

where C_{j0} is zero bias depletion capacitance, V is applied voltage, V_d is the diffusion voltage and p is the grading coefficient. p has a theoretical value of $1/2$ for an abrupt junction and $1/3$ for a graded junction. By taking the integration of $Q_t = \int_0^V C_j dV$, the depletion charge corresponding to

the ideal depletion capacitance C_j is:

$$\begin{aligned} Q_t &= C_{j0} \cdot V_t, \\ V_t &= \frac{V_d}{1-p}\left[1-(1-V/V_d)^{1-p}\right], \end{aligned} \tag{5.10}$$

where V_t is a function of applied voltage V, V_d and p.

To avoid the singularity at $V = V_d$, an effective junction bias V_j is employed in (5.10) instead of V [12] [3]:

$$\begin{aligned} V_f &= V_d\left(1-\alpha_j^{-1/p_E}\right), \\ V_j &= V - 0.1V_d \ln\left\{1+\exp\left[{}^{(V-V_f)}/_{0.1V_d}\right]\right\}, \\ V_t &= \frac{V_d}{1-p}\left[1-\left(1-{}^{V_j}/_{V_d}\right)^{1-p}\right] + \alpha_j\left(V-V_j\right), \\ Q_t &= C_{j0} \cdot V_t. \end{aligned} \tag{5.11}$$

The quantity α_j is a constant and is different for each of the depletion capacitances. Fig. 5.9 is the calculated C_j versus applied voltage V for an abrupt junction ($p = 1/2$) and a graded junction ($p = 1/3$). The effective junction bias V_j help force the capacitance to asymptotically approach the constant value $\alpha_j C_{j0}$ for $V > V_j$.

The depletion charges of base-emitter junction is split into two parts, an intrinsic component and the side-wall component [3].

$$\begin{aligned} Q_{tE} &= (1-XC_{jE})C_{jE}V_{tE}, \\ Q_{tE}^S &= XC_{jE}C_{jE}V_{tE}, \end{aligned} \tag{5.12}$$

where C_{jE} represents the zero bias base-emitter junction depletion capacitance, V_{tE} is related to the effective junction bias V_{jE} of base-emitter depletion junction, XC_{jE} is defined as the fraction of the emitter-base depletion capacitance that belongs to the sidewall.

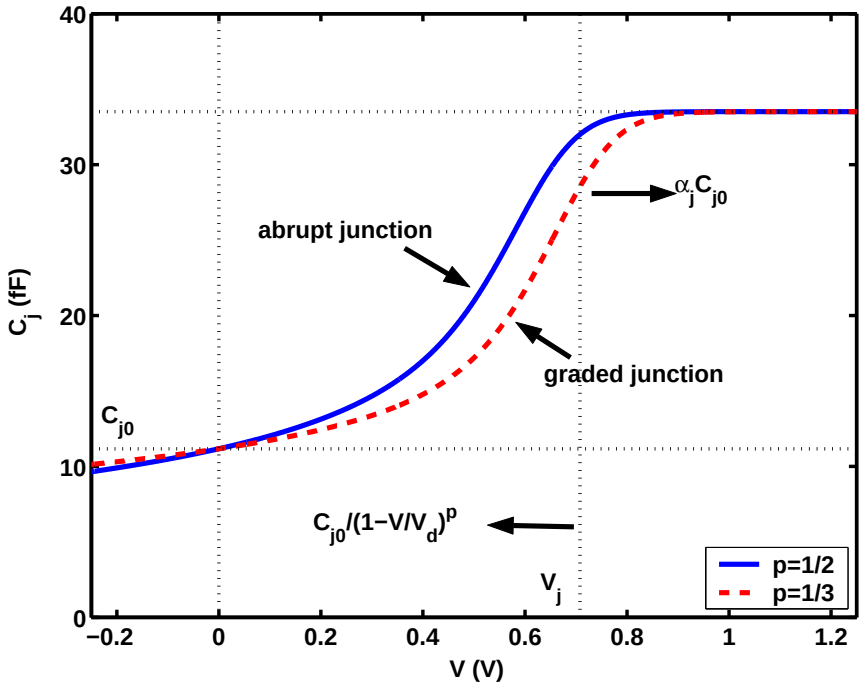

Figure 5.9: Calculated C_j versus applied voltage V for an abrupt junction ($p = 1/2$) and a graded junction ($p = 1/3$).

Similarly, for the intrinsic base-collector depletion capacitance [3]:

$$Q_{tC} = XC_{jC}C_{jC}V_{tC}, \tag{5.13}$$

where C_{jC} represents the zero bias base-collector junction depletion capacitance, V_{tC} is related to the effective junction bias V_{jC} of base-collector depletion junction. XC_{jC} is the fraction of the collector-base depletion capacitance under the emitter. For the extrinsic part of base-collector depletion capacitance, it is partitioned between nodes C_1 and B_1 and nodes C_1 and B respectively.

Fig. 5.10 shows the modeled Q_{te} and $\partial Q_{te}/\partial I$ from 93-393 K. Fig. 5.11 shows the modeled Q_{tc} and $\partial Q_{tc}/\partial I$ from 93-393 K. The Q_{te} shows strong temperature dependence however Q_{tc} shows very week temperature dependence. Meanwhile, the Q_{te} shows weak current dependence however Q_{tc} shows very strong current dependence.

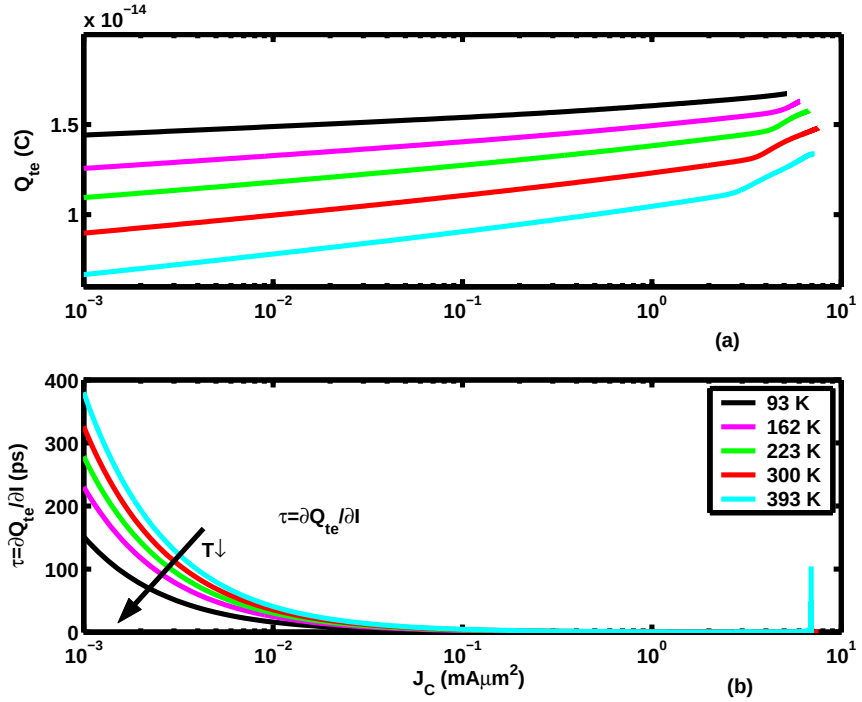

Figure 5.10: (a) Modeled Q_{te} from 93-393 K. (b) Modeled $\partial Q_{te}/\partial I$ from 93-393 K.

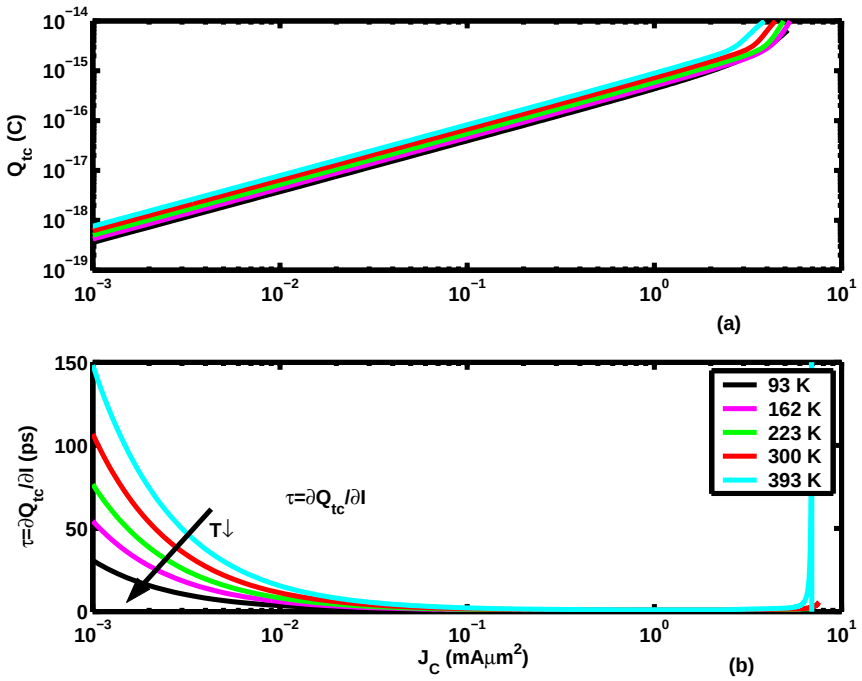

Figure 5.11: (a) Modeled Q_{tc} from 93-393 K. (b) Modeled $\partial Q_{tc}/\partial I$ from 93-393 K.

5.5 Early effects and Ge ramp effect

By introducing the model parameters of reverse Early voltage V_{er} and forward Early voltage V_{ef},

$$V_{er} = \frac{Q_{B0}}{(1-XC_{jE})C_{jE}}, V_{ef} = \frac{Q_{B0}}{XC_{jC}C_{jC}}. \tag{5.14}$$

(5.8) can be written as:

$$q_1 = 1 + \frac{(1-XC_{jE})C_{jE}V_{tE}}{Q_{B0}} + \frac{XC_{jC}C_{jC}V_{tC}}{Q_{B0}} = 1 + \frac{V_{tE}}{V_{er}} + \frac{V_{tC}}{V_{ef}}. \tag{5.15}$$

Model parameters V_{er} and V_{ef} can be extracted from reverse-Early measurement and forward-Early measurement respectively. Model parameters XC_{jE} and XC_{jC} can be estimated from C-V curves. Although q_1 is physically related to XC_{jE} and XC_{jC} through Early voltage parameters V_{er} and V_{ef} , there is no explicit couple between q_1 and XC_{jE} and XC_{jC} directly.

With a close look of the derivation of Gummel's charge control relation [8], the main current is determined by the base Gummel number:

$$G_B = \int_{x_E}^{x_C} \frac{p_b(x)}{D_n(x)} \frac{n_{i0}^2}{n_i^2(x)} dx, \tag{5.16}$$

where n_{i0} is intrinsic carrier concentration of un-doped Si. x_C and x_C are the boundary of base-emitter junction and base-collector junction, which are V_{BE} and V_{BC} bias dependent due to reverse and forward early effect. For a linearly graded base SiGe HBT, the intrinsic carrier concentration including Ge gradient profile can be written as:

$$n_i^2 = n_{i0}^2 \exp(\frac{x}{W_B} \frac{\Delta E_g}{kT}), \tag{5.17}$$

where W_B is base width, $\Delta E_g = \Delta E_g(W_B) - \Delta E_g(0)$ is the difference in bandgap between the neutral edges of the base at zero bias. The major part of this bandgap narrowing is due to Ge, but also be a result of bandgap narrowing due to heavy base doping.

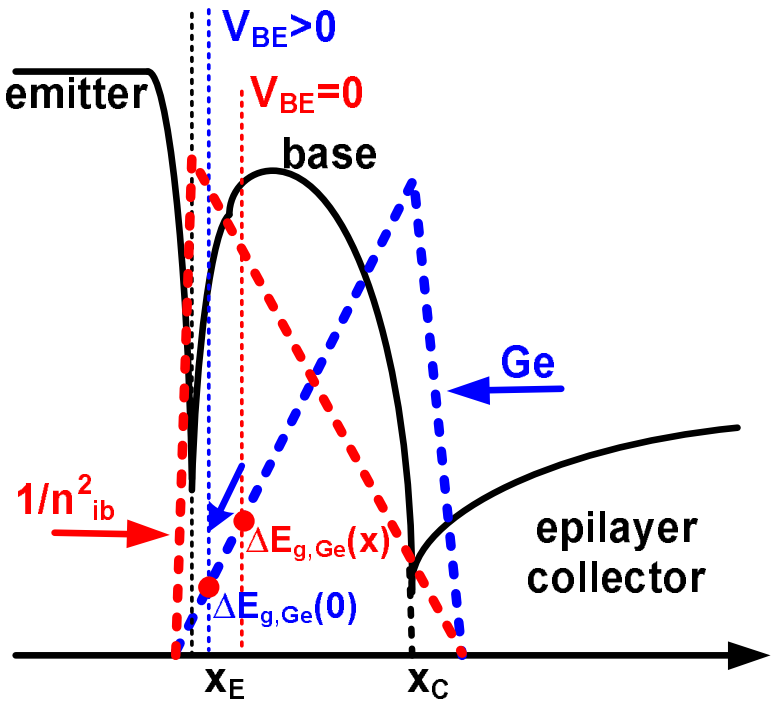

Figure 5.12: Schematic Ge and $1/n_{ib}^2$ profile of SiGe transistor with a gradient Ge content.

Because n_i is a much stronger function of position across base region, majority carrier concentration p_b and electron diffusion constant D_n can be estimated as average values across base. Assume complete ionization, $p_b(x) = N_A(x)$, hence the Gummel number becomes:

$$\begin{aligned} G_B &= \overline{N_A n_{i0}^2/D_n} \int_{x_E}^{x_C} \frac{1}{n_i^2(x)} dx \\ &= \overline{N_A n_{i0}^2/D_n} \int_{x_E}^{x_C} \exp(-\frac{x}{W_B}\frac{\Delta E_g}{kT}) dx \\ &= \overline{N_A n_{i0}^2/D_n} \frac{kTW_B}{\Delta E_g} \left[\exp(-\frac{x_E}{W_B}\frac{\Delta E_g}{kT}) - \exp(-\frac{x_C}{W_B}\frac{\Delta E_g}{kT}) \right] \end{aligned} \tag{5.18}$$

Due to reverse and forward early effect, the positions of x_C and x_C change with V_{BE} and V_{BC}. At zero bias, $x_E = 0$, $x_C = W_B$, the zero bias Gummel number can be written as:

$$G_{B0} = \overline{N_A n_{i0}^2/D_n} \frac{kTW_B}{\Delta E_g} \left[1 - \exp(-\frac{\Delta E_g}{kT}) \right] \tag{5.19}$$

By constant base doping profile assumption,

$$Q_{B0} = qA_{em}N_A W_B,$$
$$Q_B = qA_{em}N_A(x_C - x_E). \tag{5.20}$$

Therefore the depletion charges Q_{tE} and Q_{tC} are given by:

$$Q_{tE} = qA_{em}N_A(0 - x_E),$$
$$Q_{tC} = qA_{em}N_A(x_C - W_B), \tag{5.21}$$

From the definitions of early voltage, we get:

$$\frac{V_{tE}}{V_{er}} = \frac{(0 - x_E)}{W_B}, \frac{V_{tC}}{V_{ef}} = \frac{(x_C - W_B)}{W_B}. \tag{5.22}$$

Combining eqn(5.18), eqn(5.19) and eqn(5.22), we get the ratio of the Gummel number and Gummel number at zero bias [66]:

$$\frac{G_B}{G_{B0}} = \frac{\exp([\frac{V_{tE}}{V_{er}} + 1]\frac{\Delta E_g}{kT}) - \exp(\frac{-V_{tC}}{V_{ef}}\frac{\Delta E_g}{kT})}{\exp(\frac{\Delta E_g}{kT}) - 1}. \tag{5.23}$$

If carrier freezeout effect is taken into account, $p_b(x) \neq N_A(x)$. With assuming constant $p_b(x)$ profile across base or take an average $p_b(x)$ over the base region, we can reach the same $\frac{G_B}{G_{B0}}$ equation because eqn(5.23) as the ionization rate appearing in the denominator and numerator cancels by each other.

From the depletion charges modeling standpoint, we still use the base charge. However, from the current modeling standpoint, we should use Gummel number [3].

$$q_1^Q = \frac{Q_B}{Q_{B0}} = 1 + \frac{V_{tE}}{V_{er}} + \frac{V_{tC}}{V_{ef}},$$
$$q_1^I = \frac{G_B}{G_{B0}} = \frac{\exp([\frac{V_{tE}}{V_{er}} + 1]\frac{\Delta E_g}{kT}) - \exp(\frac{-V_{tC}}{V_{ef}}\frac{\Delta E_g}{kT})}{\exp(\frac{\Delta E_g}{kT}) - 1}. \tag{5.24}$$

5.6 Diffusion charges and transit times

For uniformly doped base, at high injection, Q_{BE} and Q_{BC} in eqn(5.5) begin playing a role. Both $n_{BE}(x)$ and $n_{BC}(x)$ can be modeled as a linear function of position in a short base ($n_{BE}(W_b) = 0$, $n_{BC}(0) = 0$), as shown in Fig. 5.13.

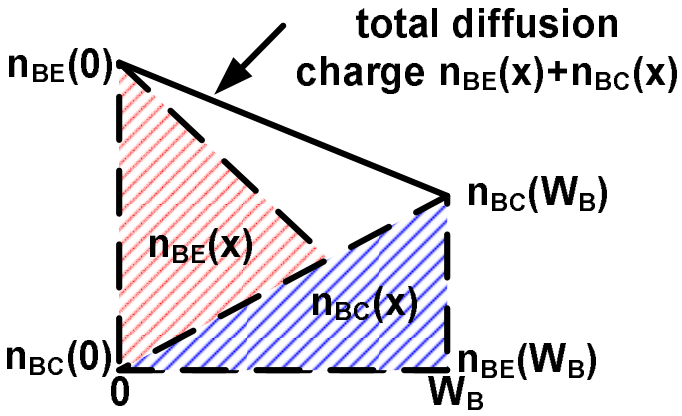

Figure 5.13: Injected electron densities profile in the base region for a NPN transistor.

The V_{BE} induced diffusion charge Q_{BE} and V_{BC} induced diffusion charge Q_{BC} can be expressed as:

$$Q_{BE}(V_{BE}) = q\int_0^{W_B} n_{BE}(x)dx = \frac{1}{2}qW_B n_{BE}(0) = \frac{1}{2}Q_{B0}n_0,$$
$$Q_{BC}(V_{BC}) = q\int_0^{W_B} n_{BC}(x)dx = \frac{1}{2}qW_B n_{BC}(0) = \frac{1}{2}Q_{B0}n_B, \tag{5.25}$$

where $n_0 = n_{BE}(0)/N_A$ and $n_B = n_{BC}(W_B)/N_A$ are the normalized electron densities at the edges of the neutral base region in terms of the zero bias base charge.

The base transit time τ_B is assumed constant at low injection of forward operation. Taking no account of Early effect first, and using the charge control relations $Q_{BE} = \tau_B I, Q_{B0} = \tau_B I_K$ (I_K is knee current), (5.7) becomes:

$$I = \frac{I_S \exp\left(\frac{V_{B_2E_1}}{N_F V_T}\right)}{1 + \frac{\tau_B I}{Q_{B0}}} = \frac{I_S \exp\left(\frac{V_{B_2E_1}}{N_F V_T}\right)}{1 + \frac{I}{I_K}}. \tag{5.26}$$

Current I can be solved as:

$$I = \frac{2I_S \exp\left(\frac{V_{B_2E_1}}{N_F V_T}\right)}{1 + \sqrt{1 + \frac{4I_S}{I_K} \exp\left(\frac{V_{B_2E_1}}{N_F V_T}\right)}}, \tag{5.27}$$

From eqn(5.25),

$$n_0 = \frac{2Q_{BE}}{Q_{B0}} = \frac{2I}{I_K}, \tag{5.28}$$

Hence

$$f_1 = \frac{4I_S}{I_K} \exp\left(\frac{V_{B2E1}}{N_F V_T}\right), n_0 = \frac{f_1}{1 + \sqrt{1 + f_1}}. \tag{5.29}$$

Similarly, for reverse operation,

$$f_2 = \frac{4I_{SR}}{I_{KR}} \exp\left(\frac{V^*_{B_2C_2}}{N_R V_T}\right), n_B = \frac{f_2}{1 + \sqrt{1 + f_2}}, \tag{5.30}$$

where we introduce knee current I_{KR} for reverse operation.

Therefore the normalized base charge (neglecting the early effect) q_2 is given by:

$$q_2 = \left(1 + \frac{1}{2}n_0 + \frac{1}{2}n_B\right)$$

The impact of Early effect on the diffusion charges is modeled by placing q_1 into eqn(5.25).

$$Q_{BE} = \frac{1}{2} q_1 Q_{B0} n_0,$$
$$Q_{BC} = \frac{1}{2} q_1 Q_{B0} n_B, \tag{5.31}$$

The Normalized base charge q_B then can be written as $q_B = q_1 q_2$.

Near peak f_T, diffusion charges dominate. Fig. 5.14 shows the modeled Q_{be} and $\partial Q_{be}/\partial I$ from 93-393 K. Fig. 5.15 shows the modeled Q_{bc} and $\partial Q_{bc}/\partial I$ from 93-393 K. With cooling, the diffusion charges decreases and hence the transit time decreases. This explains the higher peak f_T with cooling.

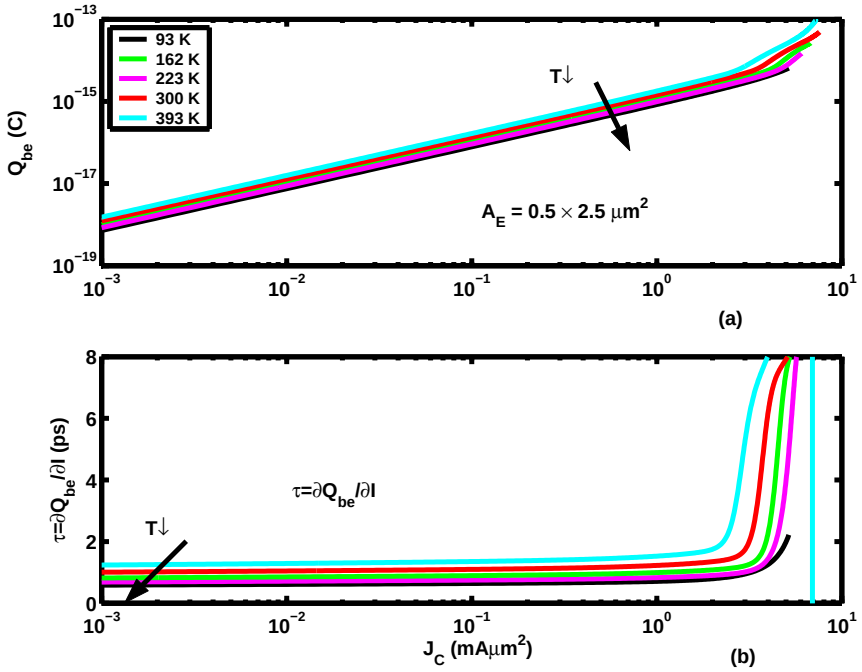

Figure 5.14: (a) Modeled Q_{be} from 93-393 K. (b) Modeled $\partial Q_{be}/\partial I$ from 93-393 K.

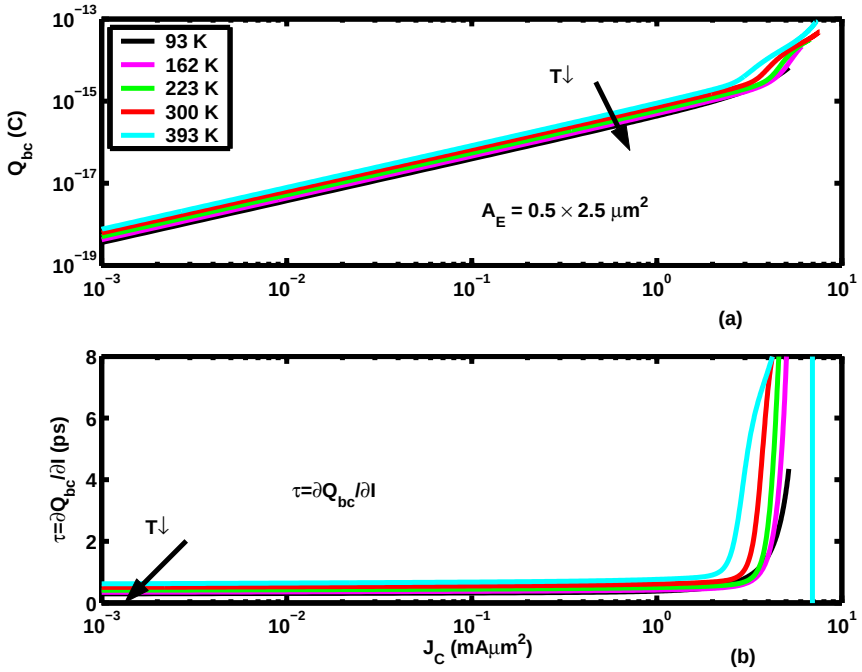

Figure 5.15: (a) Modeled Q_{bc} from 93-393 K. (b) Modeled $\partial Q_{bc}/\partial I$ from 93-393 K.

5.7 Non-quasi-static charges

Due to the distributed nature of the transistor, the quasi-static approximation is no longer valid for high-speed application. AC current crowding is a consequence of the distributed RC components in the lateral direction along the intrinsic base. At high frequencies this results in non-uniform vertical ac currents, thus affecting the small-signal base and collector currents [67][68][69].

AC current crowding is modeled as a capacitance C_{Bv} between nodes B_1 and B_2, equal to the capacitance of the base-emitter junction divided by 5, parallel to the variable base resistance R_{Bv}.

$$\begin{aligned} C_{B_v} &= \frac{1}{5}\frac{\partial Q_{B_2E_1}}{\partial V_{B_2E_1}} = \frac{1}{5}\frac{\partial (Q_{tE}+Q_{BE}+Q_E)}{\partial V_{B_2E_1}} \\ &= \frac{1}{5}\left(\frac{\partial Q_{tE}}{\partial v_{B_2E_1}} + \frac{1}{2}Q_{B0}q_1^Q\frac{\partial n_0}{\partial v_{B_2E_1}} + \frac{\partial Q_E}{\partial v_{B_2E_1}}\right), \end{aligned} \tag{5.32}$$

where

$$\frac{\partial n_0}{\partial V_{B_2E_1}} = 2\frac{I_S}{I_K}\exp(\frac{V_{B_2E_1}}{N_F V_T})\frac{1}{N_F V_T}\frac{1}{\sqrt{1+f_1}} \tag{5.33}$$

The non-quasi-static charge $Q_{B_1B_2}$ is:

$$Q_{B_1B_2} = C_{B_v}V_{B_1B_2}. \tag{5.34}$$

5.8 Base current

For the "ideal" BE and BC diode currents I_{B1}, I_{B1}^S, I_{ex} and XI_{ex}, we no longer use forward current gain β_F and reverse current gain β_R to describe them, as at low temperature, current gain β becomes more current dependent, making β_F and β_R difficult to extract. Instead, each diode current is modeled the same way as main current I_N, with its own saturation current I_S and N factor. At the same temperature, the N factor for I_B is found to be larger than for I_C [1].

Fig. 5.16 show the measured base currents from typical forward and reverse Gummel measurements. Clearly, a non-ideal base current component in the forward mode I_B is observed below 100 K, however, is not observed in reverse mode. Note that this non-ideal base current cannot be modeled as the space-charge recombination current, typically with an ideality factor of "2" and a slope of $q/2kT$, as the slope of TAT is nearly temperature independent. In [2], we contribute this non-ideal base current as the trap-assisted tunneling (TAT) current caused by the heavy doping nature of the base-emitter junction. The non-ideal forward base current I_{B2} (space-charge recombination current) is no longer sufficient to model such behavior with a constant ideality factor M_{LF}=2. This TAT current is modeled by $I_{B,tun}$ between B_2 and E_1 in Fig. 5.2.

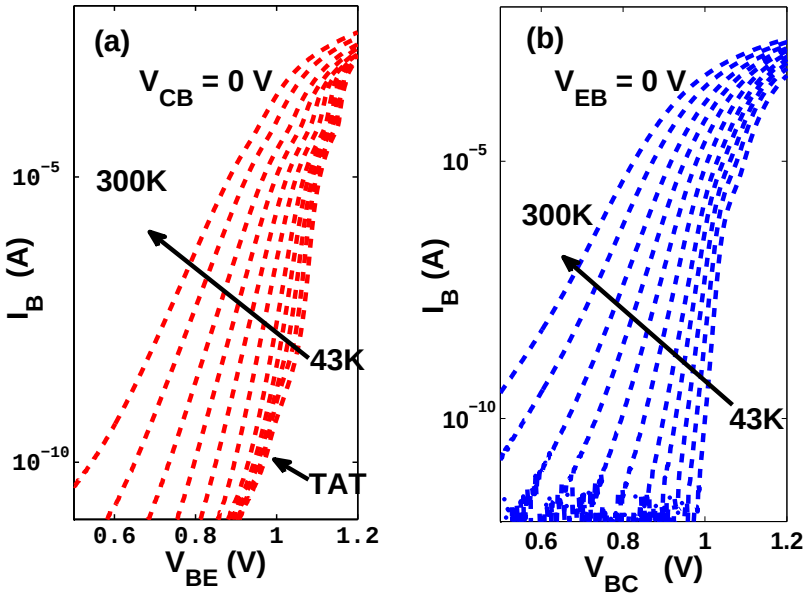

Figure 5.16: (a) I_B-V_{BE} from forward Gummel measurement; (b) I_B-V_{BC} from reverse Gummel measurement [1].

5.8.1 Ideal forward base current

The ideal forward base current is separated into a bulk part and a side-wall part, which has a fraction factor XI_{B_1}. Both depend on separate voltages.

$$I_{B_1} = (1 - XI_{B_1})I_{BEI}\left[\exp(\frac{V_{B_2E_1}}{N_{BEI}V_T}) - 1\right],$$
$$I^S_{B_1} = XI_{B_1}I_{BEI}\left[\exp(\frac{V_{B_1E_1}}{N_{BEI}V_T}) - 1\right], \tag{5.35}$$

where I_{BEI} is the saturation current, N_{BEI} is the ideality factor.

5.8.2 Non-ideal forward base current

The non-ideal forward base current is given by:

$$I^S_{B_2} = I_{Bf}\left[\exp(\frac{v_{B_2E_1}}{m_{Lf}V_T}) - 1\right], \tag{5.36}$$

where m_{Lf} is a non-ideality factor with a value close to "2".

5.8.3 Trap-assisted tunneling current

In [2], a physics based trap-assisted tunneling (TAT) current expression was then parameterized as follows:

$$I_{B,tun} = I_{BT}(T)\exp\left(\frac{V_{B_2E_1}}{V_{TUN}}\right)$$

$$I_{BT}(T) = I_{BT}\sqrt{t_N}\exp\left(K_{TN}\left(E_{g,TN} - E_{g,T}\right)\right)$$

I_{BT} is the nominal temperature saturation current, or intercept of $I_{B,tun}$-V_{BE}, and V_{TUN} represents the temperature independent slope of $I_{B,tun}$-V_{BE}. V_{TUN}, I_{BT}, K_{TN} are three model parameters specific to TAT. $E_{g,TN}$ and $E_{g,T}$ are the band gap at T_{nom} and T.

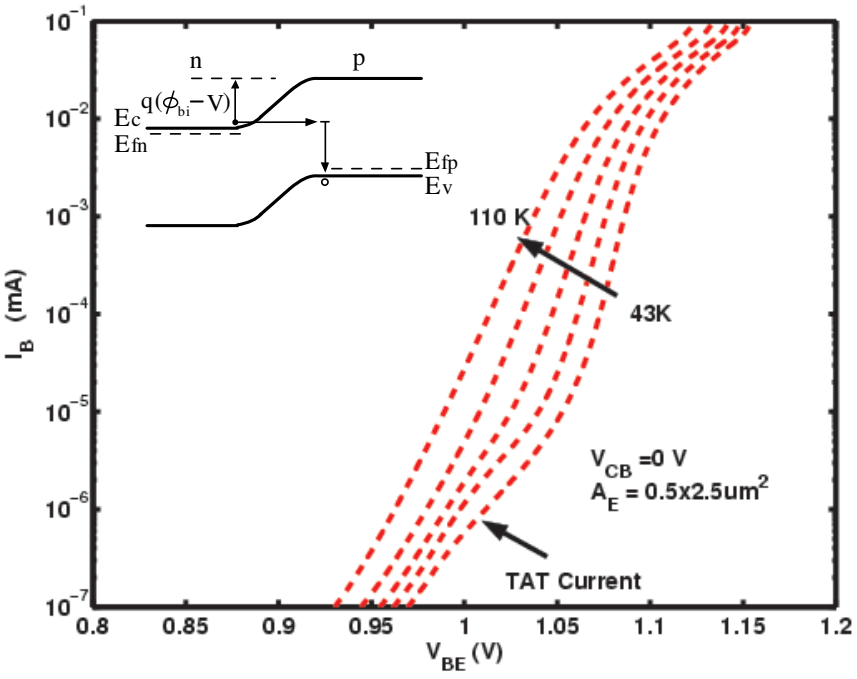

Figure 5.17: Measured I_B-V_{BE} with illustration of TAT in forward-biased E-B junction [2].

5.8.4 Non-ideal reverse base current

The non-ideal reverse base current is given by [3]:

$$I_{B_3} = I_{Br}\frac{\exp(\frac{v_{B_1C_1}}{V_T}) - 1}{\exp(\frac{v_{B_1C_1}}{2V_T}) + \exp(\frac{v_{Lr}}{2V_T})} \tag{5.37}$$

This expression is basically an approximation to the Shockley-Read-Hall recombination.

5.8.5 Extrinsic base current

Extrinsic base current I_{ex} is expressed in terms of the electron density, in this case n_{Bex}, at the end of the extrinsic base:

$$I_{ex} = I_{BCI}\left[\frac{2\exp\left(\frac{V_{B_1C_1}}{N_{CI}V_T}\right)}{1+\sqrt{1+\frac{4I_{S,R}}{I_{K,EX}}\exp\left(V_{B_1C_1}/N_{CI}V_T\right)}} - 1\right], \tag{5.38}$$

where we introduce knee current $I_{K,EX}$ for extrinsic base current.

5.9 Collector epilayer model

5.9.1 Epilayer current

The epilayer collector of a bipolar transistor is the most difficult part to model. At low current densities, the current I_{epi} flowing across epilayer is determined mainly by the main current I_N. At high current densities, the epilayer is flooded by holes and electrons. Since then, the main current I_N and the epilayer current I_{epi} depend on each other and their equations become coupled.

When a device with a lightly doped collector is operated at high injection levels, the minority carriers are injected into epilayer region, widening the electrical base of the device, which then degrades the current gain, increases transit time and decreases cut-off frequency. There are two competing effects that make this width either increases or decreases. First, the internal base-collector junction potential decreases with current when the ohmic potential drop over the epilayer increases. Hence the base-collector depletion width decreases with current. At certain current level, the base-collection depletion layer thickness vanishes and the whole electric filed is applied on the ohmic field region, as shown in Fig. 5.18 (a). At higher current, the internal base-collector metallurgical junction becomes forward biased while the external base-collector terminal remains reverse biased. The holes get injected into the epilayer and this effect is commonly known as quasi-saturation effect.

Secondly, the slope of the electric filed decreases due to the decreasing of the net charges with increasing current. Consequently, the depletion width continues to increase with increasing current until it reaches the highly doped buried collector. At some current level, the net charge and hence the electric field drop to zero and then change the sign, the electric field shifts to the n^-/n^+ junction, as shown in Fig. 5.18 (b). From this point, the high injection effects start to play a role. This is again quasi-saturation regime. When quasi-saturation is caused by the potential drop as a result of

the reversal of the slope of the electric field, this effect is better known as the Kirk effect.

$$\frac{dE}{dx} = \frac{qN_{epi}}{\varepsilon}(1 - \frac{I_{epi}}{I_{hc}}),$$
$$I_{hc} = qN_{epi}A_{em}v_{sat} \tag{5.39}$$

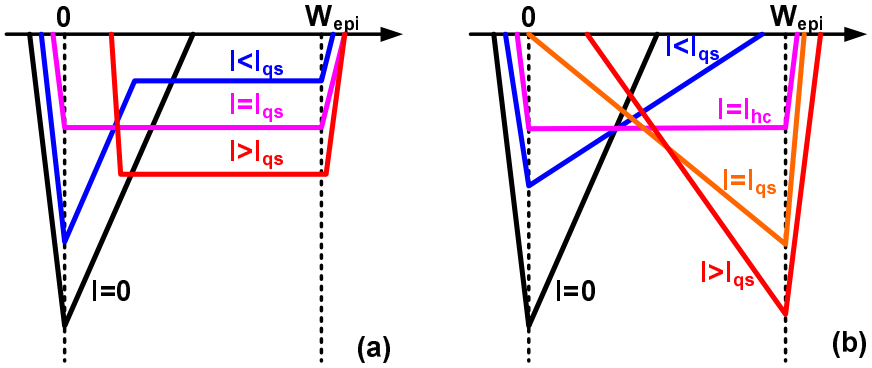

Figure 5.18: Electric field in the epilayer as a function of current. (a). Base-collector depletion thickness decreases with current. (b). Base-collector depletion thickness increases with current.

The quasi-saturation can be either due to voltage drop dominated by an ohmic resistance (Fig. 5.18 (a)), or due to a space-charge limited resistance (Fig. 5.18 (b)). As be shown in Fig. 5.19 (a), the potential of the buried layer, at the interface with the epilayer, is given by the node V_{C_1}. The potential of the internal base is given by V_{B_2}. The potential of intrinsic collector node is given by V_{C_2}. V_{C_2} is very important for the description of collector epilayer model, both for low current where it determines the depletion capacitance and for high currents where it determines the quasi-saturation effect. In Mextram 504 implementation, it extends the Kull model [14] by including velocity saturation. The intrinsic collector node potential has a double function, one is for low current and the other is for high injection. When the quasi-saturation occurs, holes from the base will be injected in the epilayer. Charge neutrality is maintained in this injection region layer, so also the electron density increase consequently, as shown in Fig. 5.19 (b). The effective width is

from the base-emitter junction to the n^-/n^+ junction and hence it degrades transistor's performance considerably.

Our analysis starts with the Kull model [14], but including the ideality factor into the *I*-*V* relation. The Kull model gives a good description of the currents and charges in the epilayer as long as the whole epilayer is quasi-neutral ($n = p + 1$). We can express the hole densities at both ends of the epilayer p_0 and p_w in terms of the node voltages:

$$p_0(p_0+1) = \exp\left[\left(v_{B_2C_2} - V_{d_C}\right)/N_R V_T\right] \tag{5.40a}$$

$$p_W(p_W+1) = \exp\left[\left(v_{B_2C_1} - V_{d_C}\right)/N_R V_T\right] \tag{5.40b}$$

Following Kull model [14], we introduce

$$K_0 = \sqrt{1+4\exp\left[\left(v_{B_2C_2} - V_{d_C}\right)/N_R V_T\right]}, \tag{5.41a}$$

$$K_w = \sqrt{1+4\exp\left[\left(v_{B_2C_1} - V_{d_C}\right)/N_R V_T\right]}. \tag{5.41b}$$

Following the derivation of Kull model [14], we get modified Kull result (without velocity saturation):

$$I_{C_1C_2} = I_{epi} = \frac{E_C + v_{C_1C_2}}{R_{Cv}}, \tag{5.42a}$$

$$E_C = N_R V_T \left(K_0 - K_W - \ln\frac{K_0+1}{K_W+1}\right), \tag{5.42b}$$

where $v_{C_1C_2} = v_{B_2C_2} - v_{B_2C_2}$, the epilayer resistance $R_{Cv} = \frac{W_{epi}}{q\mu_{n0}N_{epi}A_{em}}$.

For low injection, K_0 and K_w are very close to "1" and E_C is close to "0". The epilayer current I_{epi} shows ohmic behavior by $\frac{v_{C_1C_2}}{R_{Cv}}$. For high injection, in the case of quasi-saturation, the internal base-collector junction bias is in forward although the external base-collector bias is reverse. The epilayer consists of two parts. The first part is the injection part where the hole density is comparable to the electron density, which is between $x = 0$ and x_i. The second part is the ohmic region where the hole density is negligible, which is between $x = x_i$ and W_{epi}. The voltage of the ohmic region is

almost equal to the total voltage drop since the voltage drop across the injection region is negligible.

$$v_{C_1C_2} = v_{B_2C_2} - v_{B_2C_1} \approx v_{dC} - v_{B_2C_1} = I_{epi} R_{Cv} \left(1 - x_i / W_{epi}\right). \tag{5.43}$$

v_{dC} is used instead of $v_{B_2C_2}$ because both are almost the same as long as the injection occurs (x_i>0). Therefore, the injection region thickness x_i can be given as:

$$\frac{x_i}{W_{epi}} = 1 - \frac{V_{d_C} - v_{B_2C_1}}{I_{epi} R_{Cv}}. \tag{5.44}$$

By defining the onset current of quasi-saturation I_{qs} (when x_i=0), we have:

$$\frac{x_i}{W_{epi}} = 1 - \frac{I_{qs}}{\tilde{I}_{epi}}, \tag{5.45}$$

where

$$\begin{aligned} I_{qs} &= \frac{V_{d_C} - v_{B_2C_1}}{R_{Cv}}, \\ \tilde{I}_{epi} &= I_{qs} \frac{1 + \alpha_{xi} \ln\left\{1 + \exp\left[\left(I_{epi}/I_{qs} - 1\right)/\alpha_{xi}\right]\right\}}{1 + \alpha_{xi} \ln\left\{1 + \exp\left[-1/\alpha_{xi}\right]\right\}}, \end{aligned} \tag{5.46}$$

where α_{xi} is smooth parameter. To assure a non-negative x_i, $\tilde{I}_{epi}$ is always larger than I_{qs}, unless $I_{epi} = 0$ when $\tilde{I}_{epi} = I_{qs}$.

By combining eqn.(5.42b) and eqn.(5.43), we get:

$$\frac{x_i}{W_{epi}} I_{epi} R_{Cv} = E_C = V_T \left[2p_0^* - 2p_W - \ln\left(\frac{1 + p_0^*}{1 + p_W}\right)\right] \tag{5.47}$$

Following the derivation in [3], we can solve the internal base-collector bias $V^*_{B_2C_2}$ via the hole density p_0^*. In order to calculate p_0^* directly, eqn.(5.47) is approximated as.

$$\frac{x_i}{W_{epi}} I_{epi} R_{Cv} = 2N_R V_T \left(p_0^* - p_W\right) \frac{p_0^* + p_W + 1}{p_0^* + p_W + 2} \tag{5.48}$$

$$V^*_{B_2C_2} = V_{d_C} + N_R V_T \ln\left[p^*_0 (p^*_0 + 1)\right] \tag{5.49}$$

Hence p^*_0 can be solved from the second-order equation from p_W, I_{epi} and $\frac{x_i}{W_{epi}}$.

$$g = \frac{I_{epi} R_{CV}}{2 N_R V_T} \frac{x_i}{W_{epi}}, \tag{5.50a}$$

$$p^*_0 = \frac{g-1}{2} + \sqrt{(\frac{g-1}{2})^2 + 2g + p_W(p_W + g + 1)}, \tag{5.50b}$$

The internal base-collector bias $V^*_{B_2C_2}$ can be expressed by:

$$V^*_{B_2C_2} = V_{d_C} + V_T \ln\left[p^*_0 (p^*_0 + 1)\right] \tag{5.51}$$

In the original Kull model [14], velocity saturation is included under the assumption of the quasi-neutral, which no longer holds when $I_{epi} \geq I_{HC}$. In [3], eqn. (5.43) becomes:

$$V_{d_C} - v_{B_2C_1} = I_{hc} R_{Cv} \left(1 - \frac{x_i}{W_{epi}}\right) + (I_{epi} - I_{hc})\, SCR_{Cv} \left(1 - \frac{x_i}{W_{epi}}\right)^2, \tag{5.52}$$

where $I_{HC} = q N_{epi} A_{em} v_{sat}$ is the hot-carrier current, $SCR_{Cv} = \frac{W^2_{epi}}{2\varepsilon v_{sat} A_{em}}$ is the space-charge resistance of the epilayer.

Further, eqn. (5.46) becomes:

$$\begin{aligned} I_{qs} &= \frac{V_{d_C} - v_{B_2C_1}}{SCR_{Cv}} \frac{V_{d_C} - v_{B_2C_1} + I_{hc} SCR_{Cv}}{V_{d_C} - v_{B_2C_1} + I_{hc} R_{Cv}}, \\ \tilde{I}_{epi} &= \frac{V_{d_C} - v_{B_2C_1}}{SCR_{Cv}\left(1 - \frac{x_i}{W_{epi}}\right)^2} \frac{V_{d_C} - v_{B_2C_1} + I_{hc} SCR_{Cv}\left(1 - \frac{x_i}{W_{epi}}\right)}{V_{d_C} - v_{B_2C_1} + I_{hc} R_{Cv}}. \end{aligned} \tag{5.53}$$

• $V_{B_2C_2}$ is used to calculate the current $I_{C_1C_2}$ through the epilayer, using the Kull model .

• $V^\star_{B_2C_2}$ is the most physical one and it takes quasi-saturation effect into account. $V^\star_{B_2C_2}$ will be used in I_N, Q_{BC} and Q_{epi} modeling. First the current $I_{C_1C_2}$ is calculated using the external base-collector bias $V_{B_2C_1}$ and $V_{B_2C_2}$ based on Kull model [14]. Then the injection layer thickness x_i is

calculated using $I_{C_1C_2}$ and $V_{B_2C_1}$. Finally the hole density at collector side $p_0^\star$ and $V_{B_2C_2}^\star$ can be solved by using $I_{C_1C_2}$, x_i and $V_{B_2C_1}$.

• V_{junc} is the bias which is used to calculate the intrinsic base-collector depletion capacitance. V_{junc} is calculated using $I_{C_1C_2}$ and $V_{B_2C_1}$.

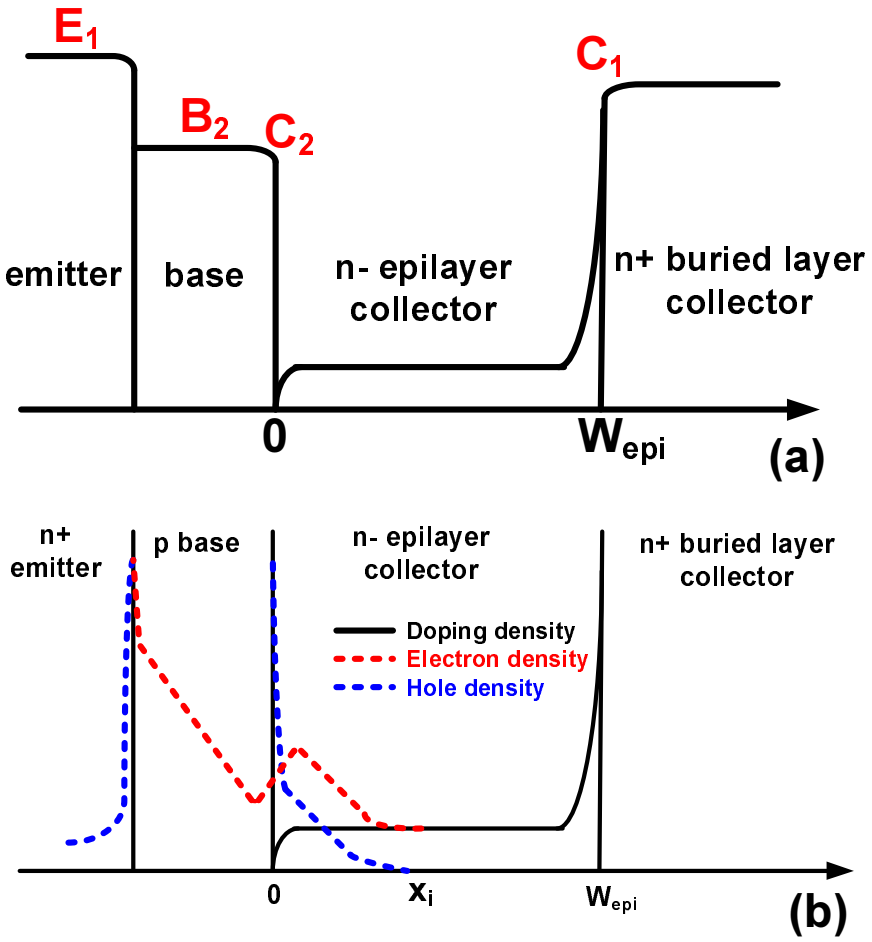

Figure 5.19: (a). Schematic of a bipolar transistor. (b). Doping, electron and hole densities in the base-collector region. [3]

5.9.2 Epilayer diffusion charge

The epilayer diffusion charge Q_{epi} is the charge of the holes in epilayer.

$$Q_{epi} = \frac{1}{2} Q_{epi0} \frac{x_i}{W_{epi}} (p_0^\star + p_W + 2), \tag{5.54}$$

where $p_0^\star$ and p_W is the normalized hole density at the both sides of epilayer. And $p_0^\star$ and p_W are related to $V^\star_{B_2C_2}$ and $V_{B_2C_1}$ respectively. Physically, $Q_{epi0} = qN_{epi}A_{em}W_{epi}$ is the background charge of epilayer. In Mextram504, however, it introduce an extra transit time τ_{epi} with typically value of $\frac{W_{epi}^2}{4D_n}$,

$$Q_{epi0} = \frac{4\tau_{epi}V_T}{R_{CV}}. \tag{5.55}$$

Fig. 5.20 is the modeled x_i/W_{epi} from 93-393 K. With cooling, the normalized thickness of the injection region x_i/W_{epi} starts to rise slowly, which indicates the larger onset current of quasi-saturation at low temperatures. Hence at high current, both epilayer diffusion charge Q_{epi} and $\partial Q_{epi}/\partial I$ are weakly dependent on current with cooling, as shown in Fig. 5.21.

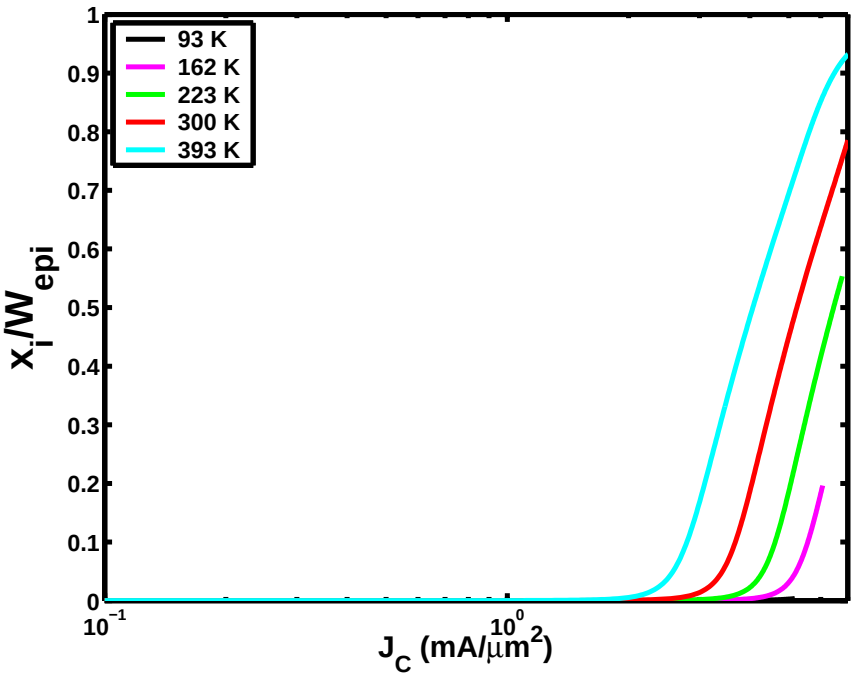

Figure 5.20: Modeled x_i/W_{epi} from 93-393 K.

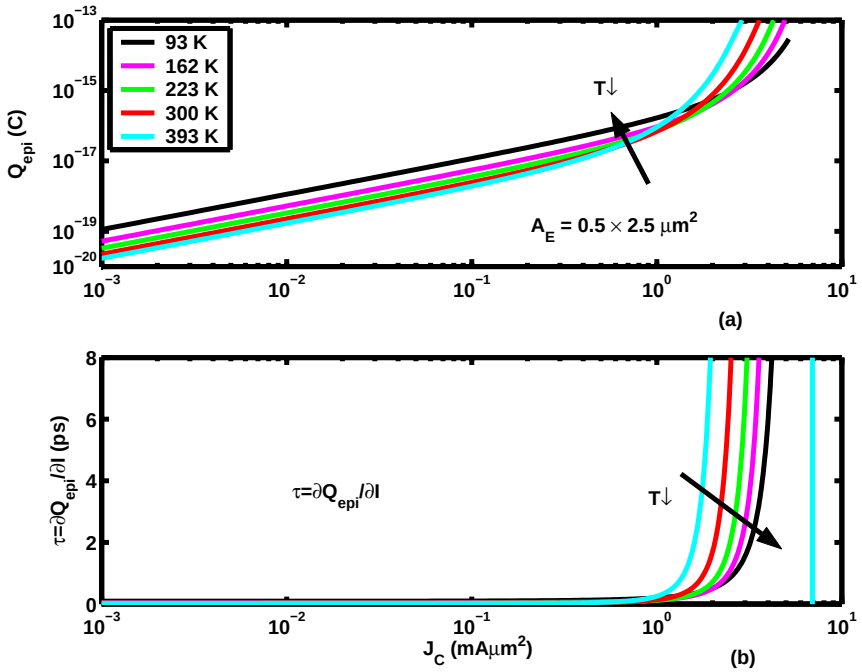

Figure 5.21: (a) Modeled Q_{epi} from 93-393 K. (b) Modeled $\partial Q_{epi}/\partial I$ from 93-393 K.

5.9.3 Intrinsic base-collector depletion charge

The intrinsic base-collector depletion charge Q_{tC} is current dependent. First of all, the depletion layer thickness x_d changes due to the charges of the electrons moving at the saturated velocity in the epilayer. Secondly, the voltage drop across the epilayer, $I_{epi}R_{CV}$, need to be taken into account when calculating junction voltage, V_{junc}, of the depletion charges, where the voltage drop is also current dependent. Therefore, $V_{junc} = V_{B_2C_1} + I_{epi}R_{CV}$ for low current. To calculate the intrinsic depletion thickness, from

$$\frac{dE}{dx} = \frac{qN_{epi}}{\varepsilon}(1 - \frac{I_{epi}}{I_{hc}}), \tag{5.56}$$

we get the solution of the electric field:

$$E(x) = E_0 + \frac{qN_{epi}}{\varepsilon}(1 - \frac{I_{epi}}{I_{hc}})x. \tag{5.57}$$

The depletion region is between 0 and x_d. The electric field is constant when $x > x_d$. By assuming the ohmic region between x_d to W_{epi} at low current, voltage drop over the epilayer is $I_{epi}R_{CV}$, then x_d can be solved by:

$$\frac{qN_{epi}}{2\varepsilon}(1-\frac{I_{epi}}{I_{hc}})x_d^2 = V_{dc} - V_{B_2C_1} - I_{epi}R_{CV}. \tag{5.58}$$

The modeling of intrinsic base-collector depletion charge Q_{tC} is given by:

$$\begin{aligned} V_{CV} &= \frac{V_{dcT}}{1-p_C}[1-f_I(1-V_{jC}/V_{dcT})^{1-p_C}] + f_I b_{jC}(V_{junc}-V_{jC}), \\ V_{tC} &= (1-X_{pT})V_{CV} + X_{pT}V_{B_2C_1}, \\ Q_{tC} &= XC_{jC}C_{jCT}V_{tC}, \end{aligned} \tag{5.59}$$

where f_I is introduced to model the current dependence of the capacitance,

$$f_I = \frac{I_{hc}I_{epi}}{I_{hc}+I_{epi}}. \tag{5.60}$$

In the description of V_{jC}, a current dependent $V_{ch} = V_{dcT}(0.1+\frac{2I_{epi}}{I_{epi}+I_{qs}})$ is introduced to avoid sudden changes in the capacitance and hence transit time when the transistor runs into hard saturation.

$$\begin{aligned} V_{FC} &= V_{dcT}(1-b_{jc}^{-1/p_C}), \\ V_{jC} &= V_{junc} - V_{ch}ln\{1+\exp[(V_{junc}-V_{FC})/V_{ch}]\}. \end{aligned} \tag{5.61}$$

The electric field in the epilayer is directly related to the base-collector depletion capacitance.

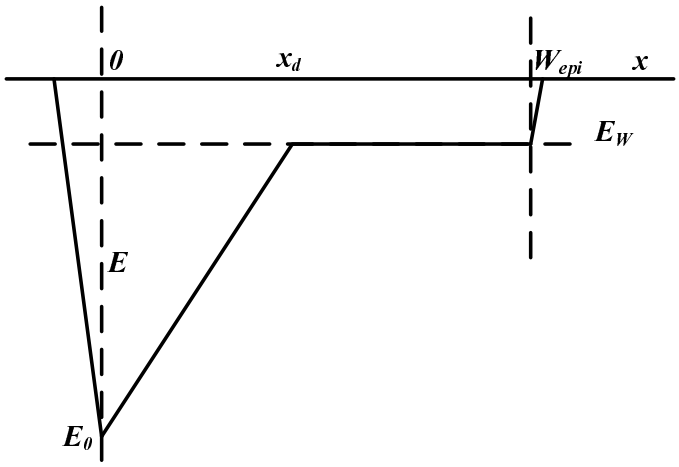

Figure 5.22: Electric field in the epilayer.

5.10 Self-heating

Since the junction temperature is determined by the thermal resistance for a given power dissipation, accurate modeling of the thermal resistance R_{TH} is critical for the modeling of junction temperature, and therefore the temperature characteristics of device.

In *dc* case, a linear relation $\Delta T = R_{TH} P_{diss}$ is used between the dissipated power P_{diss} and temperature change ΔT. In non-stationary case, driven by a temperature gradient, the dissipated power generates an energy flow from the transistor to some heat sink far away. Larger the temperature gradient, larger the energy flow is. This increased temperature ΔT is related to the increased energy density through a heat capacitance C_{TH} [70].

$$P_{diss} = \frac{\Delta T}{R_{TH}} + C_{TH} \frac{d\Delta T}{dT}. \tag{5.62}$$

5.11 Temperature modeling

As we discussed previously in chapter 2, SiGe HBTs operate very well in the cryogenic environment [7][5]. In this chapter we will discuss the temperature modeling of SiGe HBT. The

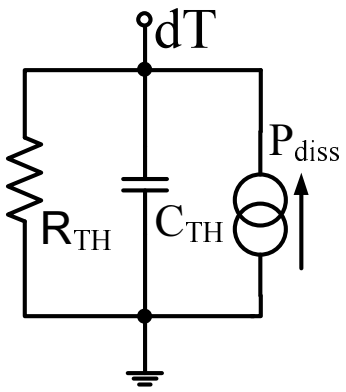

Figure 5.23: Self-heating network.

main purpose is to develop a temperature scalable SiGe HBT model that can work over the desired cryogenic temperature range over 93-300 K. In this chapter, some new temperature scaling models are developed to help obtain good *dc* and *ac* modeling. The same temperature scaling model as Mextram will not be duplicated here.

The actual device temperature is expressed as:

$$T = TEMP + DTA + 273.15 + V_{dT}, \tag{5.63}$$

where $TEMP$ is the ambient temperature in degree centigrade, DTA specifies a constant temperature shift to ambient temperature. V_{dT} is the increase in temperature ΔT due to self-heating. The difference in thermal voltage is given by:

$$\begin{aligned} \frac{1}{V_{\Delta T}} &= \frac{1}{V_T} - \frac{1}{V_{T_{nom}}} = \frac{q}{k}\left(\frac{1}{T} - \frac{1}{T_{nom}}\right). \\ t_N &= \frac{T}{T_{nom}} \end{aligned} \tag{5.64}$$

5.11.1 Saturation current and ideality factor

New temperature scaling models of saturation current and ideality factor were proposed in our previous work [1]. For the ideality factor of main current's forward and reverse parts, N_F and N_R,

the temperature dependence is modeled by [1]:

$$N_F(T) = N_F\left[1 - \frac{T - T_{nom}}{T_{nom}}\left(A_{NF}\frac{T_{nom}}{T}\right)^{X_{NF}}\right],$$
$$N_R(T) = N_R\left[1 - \frac{T - T_{nom}}{T_{nom}}\left(A_{NR}\frac{T_{nom}}{T}\right)^{X_{NR}}\right], \tag{5.65}$$

where T_{nom} is the nominal temperature, N_F and N_R are the forward and reverse ideality factor at nominal temperature respectively. A_{NF}, X_{NF}, A_{NR} and X_{NR} are fitting parameters.

Similarly, for the ideality factor of ideal base current's forward and reverse parts, N_{EI} and N_{CI}, the temperature dependence is modeled by [1]:

$$N_{EI}(T) = N_{EI}\left[1 - \frac{T - T_{nom}}{T_{nom}}\left(A_{NE}\frac{T_{nom}}{T}\right)^{X_{NE}}\right],$$
$$N_{CI}(T) = N_{CI}\left[1 - \frac{T - T_{nom}}{T_{nom}}\left(A_{NC}\frac{T_{nom}}{T}\right)^{X_{NC}}\right], \tag{5.66}$$

where N_{EI} and N_{CI} are the forward and reverse ideality factor at nominal temperature respectively. A_{NE}, X_{NE}, A_{NC} and X_{NC} are fitting parameters.

The most complete $I_S(T)$ expression derived using ideal Shockley transistor theory was given by Tsividis [71]. Using the popular nonlinear bandgap-temperature relation $E_{g,t} = E_{g,0} - \alpha T^2/(T+\beta)$ [72], the result can be rewritten in a form that resembles the $I_S(T)$ equations found in compact models [1]:

$$I_S(T) = I_{S,nom}\left(\frac{T}{T_{nom}}\right)^{X_{IS}} \exp\left(\frac{-E_{a,t}\left(1 - \frac{T}{T_{nom}}\right)}{V_T}\right), \tag{5.67}$$

$$E_{a,t} = E_{a,nom} - \frac{\alpha\beta {T_{nom}}^2}{(T_{nom}+\beta)^2} + \frac{\alpha\beta T T_{nom}}{(T+\beta)(T_{nom}+\beta)}, \tag{5.68}$$

where $E_{a,t}$ appears in the place of bandgap activation energy V_{GB} in Mextram (other compact models use different symbols), but is now temperature dependent due to the nonlinear temperature dependence of $E_{g,t}$. $E_{a,nom}$ is the extrapolated 0 K E_g at nominal temperature, usually 300 K, and $I_{S,nom}$ is I_S at nominal temperature. X_{IS} includes the temperature coefficient of mobility and density of states, α=4.45 $\times$ 10^{-4} V/K, β=686 K, and $E_{a,nom}$, $I_{S,nom}$, and X_{IS} are model parameters.

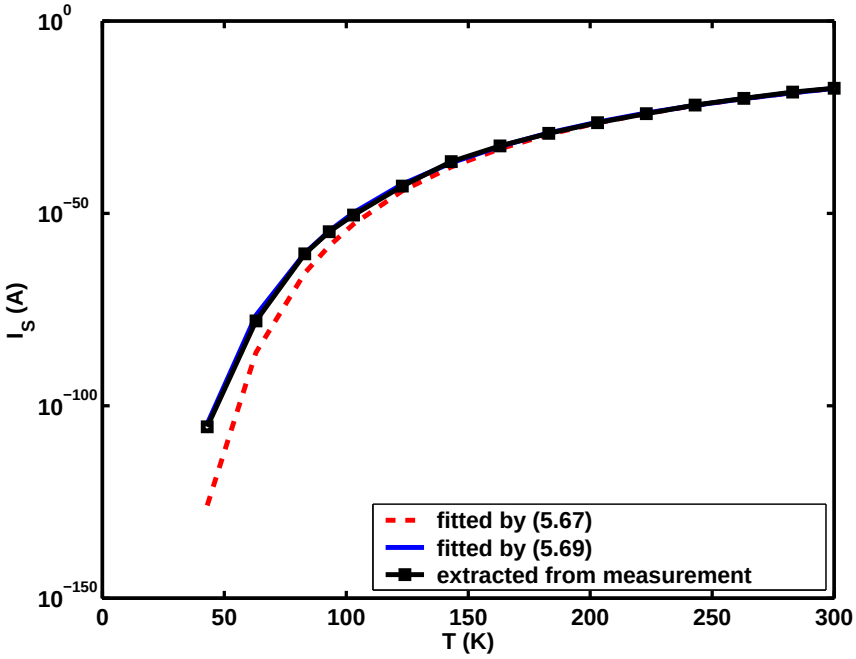

Figure 5.24: I_S extracted from measured I_C-V_{BE} vs. I_S fitted by (5.67) and (5.69) for single 0.5$\times$2.5 μm^2 SiGe HBT from 43-300 K.

We observe that the measured $I_S(T)$ is much higher than prediction of (5.67), by orders of magnitudes at lower temperatures, as shown in Fig. 5.24. Even though the underlying physics is not yet understood, the measured $I_S(T)$ -T can be well modeled by [1]:

$$I_S(T) = I_{S,nom}\left(\frac{T}{T_{nom}}\right)^{\frac{X_{IS}}{N_F(T)}} \exp\left(\frac{-E_{a,t}\left(1-\frac{T}{T_{nom}}\right)}{N_F(T)V_T}\right). \tag{5.69}$$

The effectiveness of (5.69) in modeling $I_S(T)$ can be seen in Fig. 5.24.

For main current I_N's forward and reverse component, $I_{S,F}$ and $I_{S,R}$, they share the same $E_{a,t}$, $I_{S,nom}$ and X_{IS}. However, $N_F(T)$ and $N_R(T)$ are used in eqn(5.69) for $I_{S,F}$ and $I_{S,R}$ expression respectively.

The temperature scaling of forward base saturation current I_{BEI} and reverse base saturation current I_{BCI} are very similar. $I_{BEI,nom}$, X_{IBEI}, $E_{a,BEI,nom}$, $I_{BCI,nom}$, X_{IBCI}, $E_{a,BCI,nom}$ are model parameters.

$$I_{BEI}(T) = I_{BEI,nom}\left(\frac{T}{T_{nom}}\right)^{\frac{X_{IBEI}}{N_{EI}(T)}} \exp\left(\frac{-E_{a,BEI,t}\left(1-\frac{T}{T_{nom}}\right)}{N_{EI}(T)V_T}\right).$$
$$E_{a,BEI,t} = E_{a,BEI,nom} - \frac{\alpha\beta {T_{nom}}^2}{(T_{nom}+\beta)^2} + \frac{\alpha\beta T T_{nom}}{(T+\beta)(T_{nom}+\beta)}, \tag{5.70}$$

$$I_{BCI}(T) = I_{BCI,nom}\left(\frac{T}{T_{nom}}\right)^{\frac{X_{IBCI}}{N_{CI}(T)}} \exp\left(\frac{-E_{a,BCI,t}\left(1-\frac{T}{T_{nom}}\right)}{N_{CI}(T)V_T}\right).$$
$$E_{a,BCI,t} = E_{a,BCI,nom} - \frac{\alpha\beta {T_{nom}}^2}{(T_{nom}+\beta)^2} + \frac{\alpha\beta T T_{nom}}{(T+\beta)(T_{nom}+\beta)}. \tag{5.71}$$

5.11.2 Base tunneling current

In our previous work [2], The physics based TAT current expression is then parameterized as follows:

$$I_{B,tun} = I_{BT}(T)\exp\left(\frac{V_{B_2E_1}}{V_{TUN}}\right)$$
$$I_{BT}(T) = I_{BT}\sqrt{t_N}\exp\left(K_{TN}\left(E_{g,TN}-E_{g,T}\right)\right)$$

I_{BT} is the nominal temperature saturation current, or intercept of $I_{B,tun}$-V_{BE}, and V_{TUN} represents the temperature independent slope of $I_{B,tun}$-V_{BE}. V_{TUN}, I_{BT}, K_{TN} are three model parameters specific to TAT. $E_{g,TN}$ and $E_{g,T}$ are the band gap at T_{nom} and T.

5.11.3 Series resistances

The resistances of a bipolar transistor strongly influence device large-signal and small-signal performance. Transistor I-V curves at practical operational biases are affected by the voltage drops across terminal resistances and hence modeling of resistances as a function of temperature is an important part of compact model development. The intrinsic and extrinsic base resistance fundamentally degrade noise figure, as they produce thermal noise at the transistor input. They also consume input power and degrade power gain and hence maximum oscillation frequency f_{max}. The intrinsic base sheet resistance is also related to the Gummel number (or effective Gummel number for HBTs) and hence the collector current. Furthermore, a decrease of the voltage limit can be observed with cooling, due to the increase of intrinsic base resistance as a result of freezeout, as well as the increase in the avalanche multiplication factor (M-1) [16].

This subsection investigates the physics and modeling of the temperature dependence of the resistances in various regions of SiGe HBTs, including the p^- substrate, the n^- collector, the p-type intrinsic base, the n^+ buried collector and the p^+ silicided extrinsic base. Sheet resistance and substrate resistivity were measured on-wafer from 300 to 30 K . The sheet resistance data of the p^+ non-silicided extrinsic base are not available in this work. Although the results presented are for first-generation SiGe HBTs, we expect the same resistance models to work for second- and third-generation SiGe HBTs given the similarities in resistor structures.

For the p^- substrate and n^- collector, the doping is well below the Mott-transition [33], while for the p-type intrinsic base, the doping is close to Mott-transition. The ionization rates are estimated from measured resistance vs. temperature data using the Philips unified mobility model (PHUMOB) [35], and the single power law mobility approximation. For doping well below the Mott-transition, the classic ionization model [25], together with single power law mobility approximation, enables accurate modeling of resistance vs. temperature down to 30 K. For doping close to the Mott-transition, however, the classic ionization model significantly underestimates the ionization rate, while the recent Altermatt model [26][27] significantly overestimates the ionization rate below 100 K. Analysis of experimental data shows that bound state fraction factor "*b*" increases towards "1"

with cooling below certain threshold temperature, while "*b*" is fixed at "1" in Altermatt *et al.*'s model. An empirical equation for temperature-dependent "*b*" is proposed and it enables resistances modeling from 300-30 K for doping close to the Mott-transition.

For the n^+ buried collector, the doping is well above the Mott-transition, and ionization is complete at all temperatures. In this case, the temperature dependence of the resistance is solely determined by the temperature dependence of the majority carrier mobility. However, a single power law mobility approximation can no longer be used, and a double power law mobility approximation utilizing the Mathiessen's rule of combination of the lattice and impurity scattering components is proposed. An alternative approach is to continue using a single power law approximation for mobility and then model part of the mobility temperature dependence as an effective decrease of the ionization rate with temperature, which, while purely empirical, also works well. This approach has the advantage of allowing the use of the same model equation for all resistances. The calculations also show that the PHUMOB is not very accurate for doping well above the Mott-transition at the cryogenic temperatures. This inaccuracy of PHUMOB, however, does not affect its use in estimating the ionization rate for doping below and close to the Mott-transition, as the ionization rate variation with temperature is larger than the inaccuracy of the mobility model. For the p^+ extrinsic silicided base, it is not doping related. However, from modeling standpoint, we need to model the silicide resistance too. The same equation for the n^+ buried collector works for silicided p+ extrinsic base very well [17].

Resistance measurements

The SiGe HBT under investigation employs a heavily-doped polysilicon emitter, an ultra-high-vacuum/chemical vapor deposition (UHV/CVD) grown SiGe base layer, a lightly-doped n-type collector epilayer, a heavily-doped buried collector on a p^- substrate and a heavily-doped silicided extrinsic base. The peak base doping is below but close to Mott-transition.

All resistance measurements used an Agilent 4156 Semiconductor Parameter Analyzer to perform Kelvin measurements on a variety of specially designed test structures. Temperature dependent

measurements of packaged test structures were carried out using a closed-cycle liquid-helium cryogenic test system capable of DC to 100 MHz operation from 10 K to 400 K. The measurements of p-type resistances reported here include the resistivity of the lightly-doped substrate, the sheet resistance of intrinsic base region, and the sheet resistance of the p^+ silicided extrinsic base. Measurements of n-type resistances include the lightly-doped epilayer in which the SiGe HBT collector is defined, and the heavily-doped n^+ buried collector. The substrate resistivity was measured using the standard four-point-probe technique. A custom test structure was designed with four collinear 1.6 μm substrate contacts which were equally spaced by 150 μm. The base sheet resistance was measured using a conventional ring-dot structure, which consists of an emitter ring bounded by two inner and two outer base contacts. For comparison of measurement and calculation using PHUMOB mobility model and Altermatt incomplete ionization model, the base sheet resistance shown below is from a Si test structure, as both models are developed with experimental data on Si. Under identical process conditions, Si and SiGe structures show similar base sheet resistance [73]. The slight difference is mainly due to suppression of boron out diffusion by Ge. The Ge in base slightly improves hole mobility, but the improvement is small for the relatively low average Ge mole fraction found in the SiGe HBTs used. For compact modeling, the model equations presented below are applicable to both Si and SiGe bases, only the parameters are slightly different. The remaining sheet resistances were measured using rectangular Kelvin structures of varying geometry.

Experimental results and analysis

Consider the sheet resistance of a semiconductor layer (R_{sh}). $R_{sh} = \left(q\mu N_{dop}^{-} W\right)^{-1}$, where N_{dop}^{-} is the ionized carrier concentration, μ is majority carrier mobility, and W is neutral region width. For example, W is the neutral base width for intrinsic base resistance. Temperature dependence of W is from the variation of PN junction depletion layer thickness, which is much smaller than that of N_{dop}^{-} and μ, and is thus neglected. In current compact models intended for applications near room temperature, only the mobility variation with temperature is considered through a single power law relation of $\mu = \mu_{T0}(T/T_0)^{-AR}$, where T_0 is the nominal temperature, μ_{T0} is the nominal

mobility, and AR is a doping dependent parameter. This leads to resistance temperature scaling model $R(T) = R_{T0}(T/T_0)^{AR}$, with R_{T0} being the nominal temperature resistance.

We first examine the measured temperature dependence of the various resistances and the applicability of current resistance temperature scaling model, and then analyze the variation of ionization rate with temperature for doping below and close to Mott-transition using PHUMOB. For the extrinsic base and buried collector, both doped above the Mott-transition, ionization is complete, and thus the temperature dependence of the resistances directly reflects the temperature dependence of the majority carrier mobility.

Fig. 5.25 shows the measured substrate resistivity, the collector sheet resistance, the intrinsic base sheet resistance, the buried collector sheet resistance, and the silicided extrinsic base sheet resistance, from 30 to 300 K. A logarithmic scale is used for both resistance and temperature to facilitate examination of the validity of the current resistance scaling model $R = R_{T0}(T/T_0)^{AR}$. A straight line or linear relation of $\ln R$-$\ln T$ would indicate good applicability of the conventional model. Observe that such a linear relation is seen only at higher temperatures.

For the lightly-doped substrate and collector, $\ln R$ - $\ln T$ is linear above 100 K. For the intrinsic base, however, $\ln R$-$\ln T$ is much more complicated and it is only possible to identify a linear relationship over a smaller temperature range. This more complex temperature dependence, we believe, is due to the higher doping level, which is close to Mott-transition (the transition occurs at $\approx 3 \times 10^{18}\ cm^{-3}$ for boron in silicon). For the heavily-doped buried collector and silicided extrinsic base, $\ln R$ - $\ln T$ is linear above 150 K and becomes "flattened" below 100 K. The deviation of $\ln R$-$\ln T$ from linearity has two possible explanations: 1) the mobility variation with temperature can no longer be described using a single power relation, which is not surprising given the wide temperature range involved; and 2) the carrier concentration varies with temperature via incomplete ionization. For doping below and close to the Mott-transition, both variations are important, and hence we need to estimate their individual contributions to facilitate accurate modeling. For doping well above the Mott-transition, the resistance temperature dependence is determined directly by the mobility temperature dependence due to its complete ionization at all temperatures.

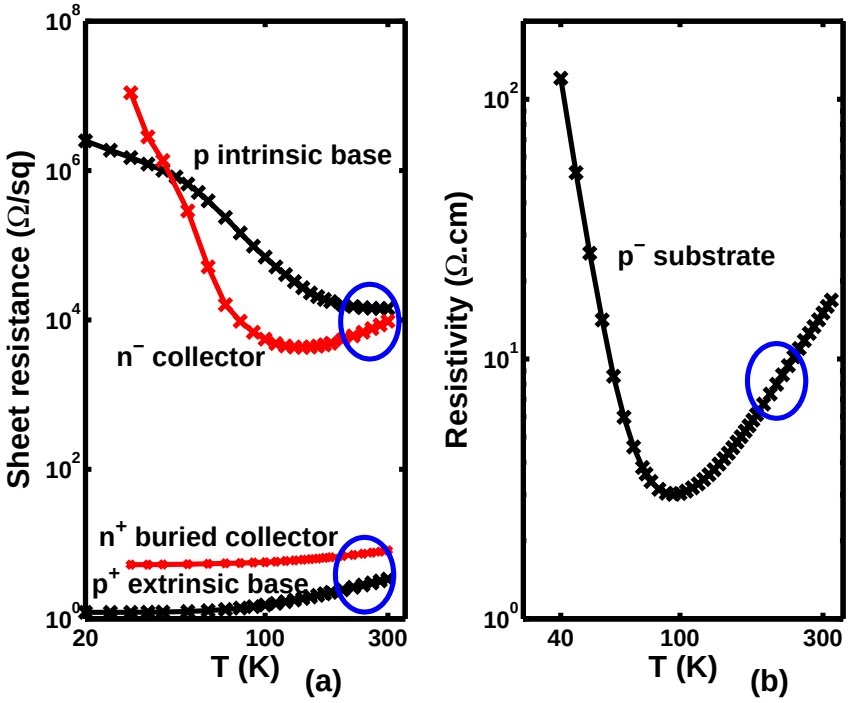

Figure 5.25: (a)Measured sheet resistance for collector, intrinsic base, silicided extrinsic base and buried layer from 30-300 K. (b) Measured substrate resistivity from 30-300 K.

To estimate the temperature dependence of the ionization rate $IR(T)$ for doping below and close to the Mott-transition, we need to obtain the temperature dependence of mobility. Here, we calculate mobility using PHUMOB, since it is widely used in device simulators. PHUMOB includes lattice scattering, impurity scattering, and carrier-carrier scattering, as well as their temperature dependences. We implemented this model in a Matlab program, and verified our implementation using Sentaurus Device [54]. Complete ionization is assumed in mobility calculation using PHUMOB.

Formally, *IR* is written as:

$$IR = \frac{N_{dop}^{-}}{N_{dop}}, \tag{5.72}$$

where N_{dop} is the active doping concentration. Using $N_{dop}^{-} = N_{dop} \times IR$ and $R = \left(q\mu N_{dop}^{-} W\right)^{-1}$, where R represents sheet resistance, we obtain:

$$\frac{R(T)}{R(T_0)} = \frac{\mu(T_0)}{\mu(T)} \frac{IR(T_0)}{IR(T)}. \tag{5.73}$$

The same relationship holds for resistivity. $\frac{IR(T)}{IR(T_0)}$ can thus be calculated from measured $\frac{R(T)}{R(T_0)}$ as:

$$\frac{IR(T)}{IR(T_0)} = \frac{\mu(T_0)}{\mu(T)} / \frac{R(T)}{R(T_0)}, \tag{5.74}$$

We will discuss the measured $\frac{R(T)}{R(T_0)}$ and calculated $\frac{\mu(T_0)}{\mu(T)}$ for doping below, close to and well above the Mott-transition in Section IV, V and VI, respectively. For doping well above the Mott transition, $IR = 1$. The comparison of measured $\frac{R(T)}{R(T_0)}$ with calculated $\frac{\mu(T_0)}{\mu(T)}$ should give us information on the accuracy of PHUMOB. For doping below and close to Mott-transition, *IR* varies so much with temperature that inaccuracy of PHUMOB should not be an issue for the purpose of estimating and modeling $IR(T)$.

PHUMOB, however, is too complicated for practical (efficient) compact modeling. So we will also examine the single power law mobility approximation, and show that it is useful for doping levels well below the Mott-transition. This results in a $IR(T)$ that can be successfully modeled using a classic incomplete ionization model. For doping close to Mott-transition, a new incomplete ionization model is developed based on the Altermatt incomplete ionization model. For doping well above Mott-transition, we will present two approaches, one using mobility modeling and complete ionization, and the other using single power law mobility approximation, but with an artificial incomplete ionization.

Doping below Mott-transition

Doping concentrations in the substrate and the collector are below the Mott-transition [33]. Here we discuss the substrate resistivity. Fig. 5.26(a) shows measured $\frac{R(T)}{R(T_0)}$ and $\frac{\mu(T_0)}{\mu(T)}$ calculated using PHUMOB and a single power law mobility model, for the substrate, over the range of 40-320 K. The parameters *AR* for a single power law model were determined from the slope of μ-T from 100 K to 300 K using PHUMOB. Above 100 K, the calculated $\frac{\mu(T_0)}{\mu(T)}$ using these two mobility models both are very close to measured $\frac{R(T)}{R(T_0)}$ data. This indicates that the impurities in the substrate are completely ionized above 100 K and PHUMOB can be simplified to a single power law.

Fig. 5.26(b) shows $\frac{IR(T)}{IR(T_0)}$ calculated using (5.74). $\frac{IR(T)}{IR(T_0)}$ begins to decrease from unity below 100 K. Although a single power law mobility approximation leads to lower *IR* than that of PHUMOB, the shape of *IR*-*T* is similar to that obtained from PHUMOB. Therefore, we opted to use a single power law mobility approximation in this case. A consequence is that the temperature dependence of the mobility is partially attributed to incomplete ionization below 100 K. This is acceptable for compact modeling, however, as long as $IR(T)$ can still be successfully modeled, which is the case here, as shown below.

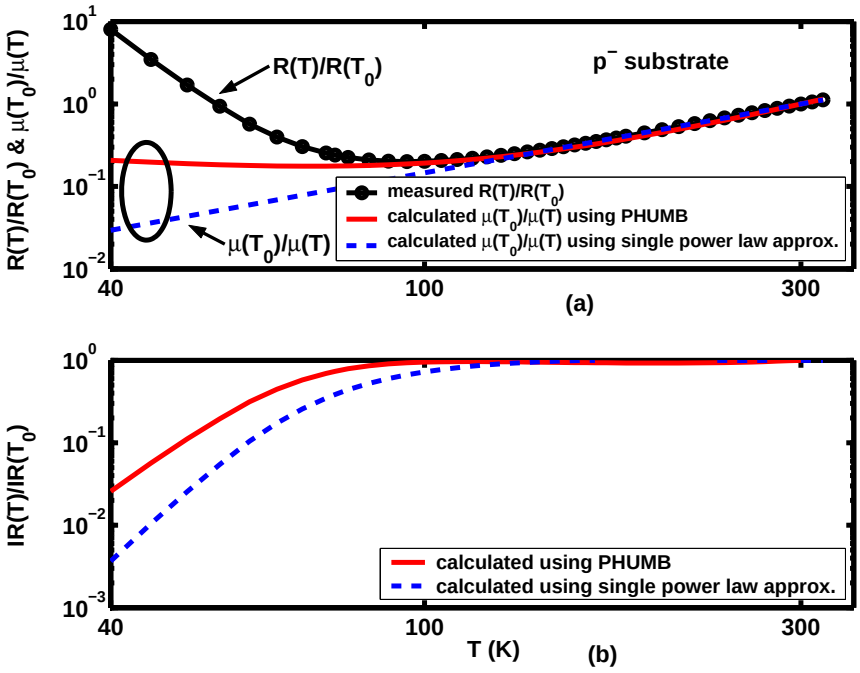

Figure 5.26: (a) Measured $\frac{R(T)}{R(T_0)}$, calculated $\frac{\mu(T_0)}{\mu(T)}$ using PHUMOB and single power law approximation, for the substrate, from 40-320 K. (b) Calculated $\frac{IR(T)}{IR(T_0)}$ using PHUMOB and a single power law approximation, for substrate, from 40-320 K.

Using $\mu = \mu_{T0}(T/T_0)^{-AR}$, $R(T)$, the resistance at temperature T can be related to that at T_0, $R(T_0)$, by:

$$R(T) = R_{T0}\left(\frac{T}{T_0}\right)^{AR}\frac{IR(T_0)}{IR(T)}, \tag{5.75}$$

(5.75) involves the calculation of IR at both T and T_0. This can be avoided by defining a fictitious nominal temperature, complete ionization resistance $R_{CI,T0}$:

$$R_{CI,T0} = R_{T0} \times IR(T0). \tag{5.76}$$

Note that $R_{CI,T0}$ is not the measured resistance at T_0, which always includes the impact of incomplete ionization. (5.75) can be rewritten as:

$$R(T) = R_{CI,T0} \left(\frac{T}{T0} \right)^{AR} \frac{1}{IR(T)}. \tag{5.77}$$

Numerous theories of how impurity concentration and temperature affect ionization rate have been developed in the past several decades [25] [26] [27] [28] [29] [30] [31] [32]. Here we will examine the popular model of using doping dependent activation energy [28][30][31][32][74] in the classic ionization model [25]. An explicit expression of this classic model IR can be found in [25]. We briefly review its derivation below, since it subsequently used in the work to derive IR for the most recent Altemmatt's incomplete ionization model [26][27], which will then be applied to the intrinsic base resistance. We will use a p-type dopant for the derivation, but all results can obviously be applied to n-type dopants as well.

The classic model assumes a Fermi-Dirac-like impurity distribution function. That is, the probability of finding an electron at an acceptor impurity energy E_A is given by [25]:

$$f(E_A) = \frac{1}{1 + g_A \exp \frac{(E_A - E_F)}{kT}}, \tag{5.78}$$

where $E_A = E_{dop} + E_V$, E_V is the valence band edge energy, E_{dop} is the impurity activation energy, E_F is the Fermi level and kT is the thermal energy, and g_A is degeneracy factor ($g_A = 4$ for boron).

N^-_{dop} is then given by:

$$N^-_{dop} = N_{dop} \times f(E_A) = \frac{N_{dop}}{1 + g_A \exp \frac{(E_A - E_F)}{kT}}, \tag{5.79}$$

Substituting $E_A = E_{dop} + E_V$ into (5.79) leads to

$$N_{dop}^{-} = \frac{N_{dop}}{1 + g_A \exp\left(\frac{E_{dop}}{kT}\right) \exp\left(\frac{E_V - E_F}{kT}\right)}. \tag{5.80}$$

The E_F-E_V term can be related to p and hence N_{dop}^{-} because:

$$p = N_V \exp\left(\frac{E_V - E_F}{kT}\right), \tag{5.81}$$

where N_V is the valence band effective density-of-states (DOS); $N_V = 3.14 \times 10^{19} \times \left(\frac{T}{300}\right)^{1.5} \mathrm{cm}^{-3}$ [75] is used here. Using $\exp\left(\frac{E_V - E_F}{kT}\right) = \frac{p}{N_V}$, $N_{dop}^{-} = N_{dop} \times IR$ and $p = N_{dop}^{-}$, one obtains a quadratic equation of IR from (5.80),

$$\begin{aligned} G^{-1} IR^2(T) + IR(T) - 1 = 0, \\ G = g_A^{-1} \frac{N_V}{N_{dop}} \exp\left(-\frac{E_{dop}}{kT}\right). \end{aligned} \tag{5.82}$$

Then $IR(T)$ is solved as[25]:

$$IR(T) = \frac{-G + \sqrt{G^2 + 4G}}{2}. \tag{5.83}$$

(5.83), together with (5.77), are implemented in Agilent ICCAP [62] to fit measured resistance vs. temperature data. Four model parameters are involved: the impurity activation energy E_{dop}, the impurity concentration N_{dop}, the fictitious nominal temperature complete ionization resistance $R_{CI,T0}$, and the mobility temperature coefficient AR. E_{dop}, $R_{CI,T0}$ and AR are dependent on doping level N_{dop}, dopant species and device geometry, and thus vary from technology to technology. Given process and layout information, their values can also be estimated from PHUMOB mobility model and Altermatt incomplete ionization model. As shown in Fig. 5.27, using this approach we obtain good modeling accuracy for the collector sheet resistance and the substrate resistivity, from 30-300 K. This, however, does not work for the other resistances as expected.

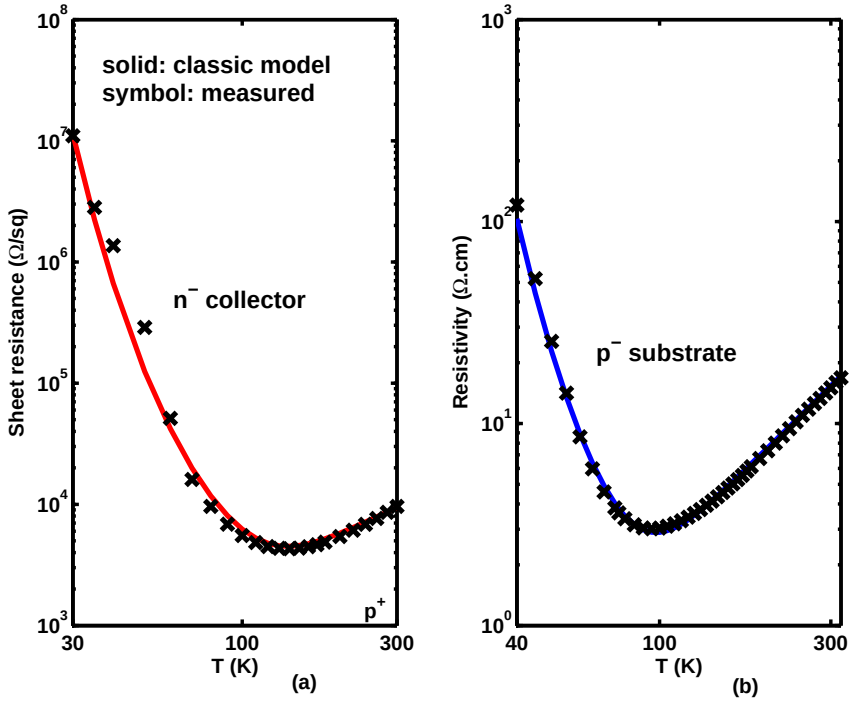

Figure 5.27: (a) Collector sheet resistance modeling using the classic model and doping dependent activation energy from 30-300 K. (b) Substrate resistivity modeling using the classic model and doping dependent activation energy from 40-320 K.

Doping close to Mott-transition

Fig. 5.28(a) shows the measured $\frac{R(T)}{R(T_0)}$ and $\frac{\mu(T_0)}{\mu(T)}$ calculated using PHUMOB and a single power law mobility model for the intrinsic base, whose peak doping is close to the Mott-transition. The parameter *AR* for the single power law model is determined from the average slope of μ-T from 30-300 K using PHUMOB. These two mobility models give almost the same $\frac{\mu(T_0)}{\mu(T)}$. This means that PHUMOB can indeed be simplified as single power law, and the $\frac{IR(T)}{IR(T_0)}$ obtained should be accurate. Due to incomplete ionization, the resulting $\frac{\mu(T_0)}{\mu(T)}$ for both models are much smaller than measured $\frac{R(T)}{R(T_0)}$ below 250 K, as shown by the $\frac{IR(T)}{IR(T_0)}$ curves in Fig. 5.28(b). The decrease of $\frac{IR(T)}{IR(T_0)}$ from unity starts at 250 K, much higher than the 100 K in the substrate case, because the doping is close to the Mott-transition.

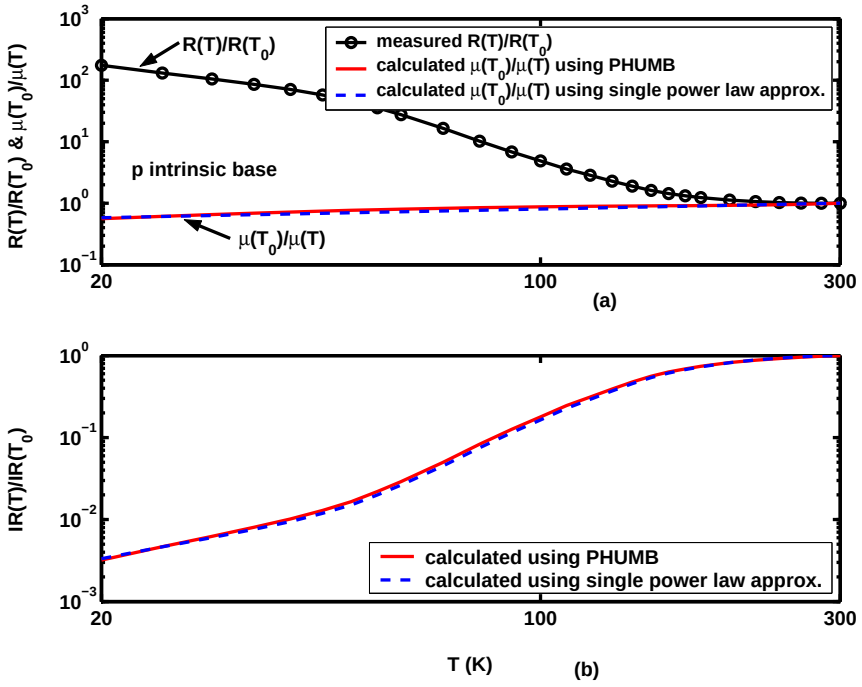

Figure 5.28: (a) Measured $\frac{R(T)}{R(T_0)}$, calculated $\frac{\mu(T_0)}{\mu(T)}$ using PHUMOB and a single power law approximation for intrinsic base, from 20-300 K. (b) Calculated $\frac{IR(T)}{IR(T_0)}$ using PHUMOB and a single power law approximation for the intrinsic base, from 20-300 K.

The classic incomplete ionization model is applied first to fit the $IR(T)$ obtained. However, it overestimates resistance below 100 K. The more recent Altermatt incomplete ionization model

[26][27] was then applied. However, it underestimates resistance at lower temperatures, particularly below 50 K. A new incomplete ionization model is therefore proposed by introducing temperature dependence into the bound state fraction factor in the Altermatt model. This new model enables modeling of the intrinsic base sheet resistance from 30-300 K. Fig. 5.29 shows the intrinsic base sheet resistance modeling results using the classic, the Altermatt, and the newly derived model, from 30-300 K. Fig. 5.30 plots the IR and $1/IR$ using the classic, the Altermatt, and the new ionization models.

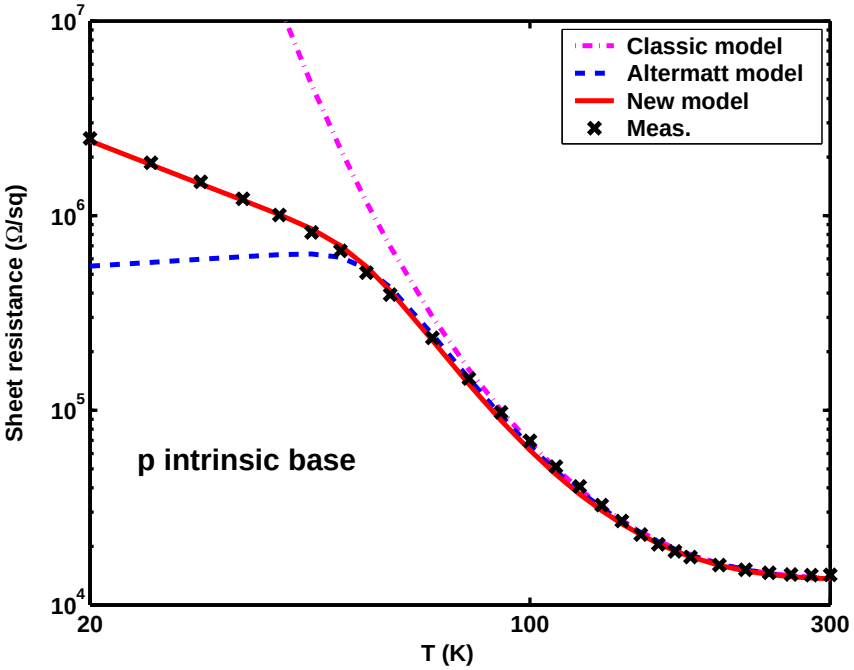

Figure 5.29: Intrinsic base sheet resistance modeling using the classic, the Altermatt, and the new model, from 30-300 K.

The overestimation of resistance by the classic model is caused by underestimation of the ionization rate. From (5.82), G reduces towards "0" when temperature decreases. Hence, from (5.83), IR decreases exponentially towards "0" and thus leads to an infinitely large resistance at low temperatures, as can be seen from the dot-dash line in Fig. 5.30. However, the measured resistance increase does not suffer from carrier freezeout as much as one would have naively expected from

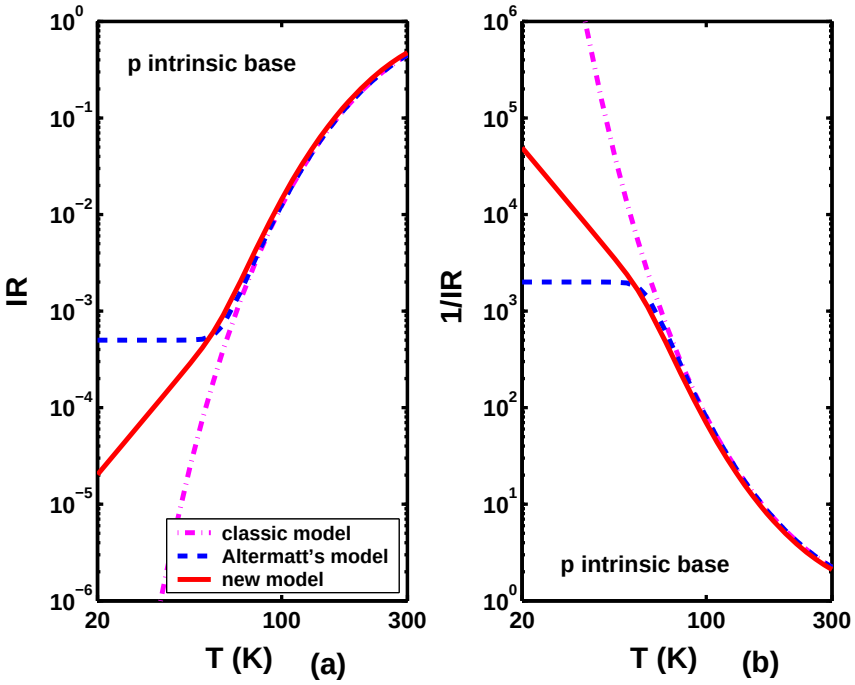

Figure 5.30: (a) Calculated *IR* for intrinsic base using the classical, the Altermatt, and the new model, from 30-300 K. (b) Calculated $1/IR$ for intrinsic base using the classic, the Altermatt, and the new model, from 30-300 K.

the classic ionization model, even if the activation energy is artificially made to decrease with increasing doping.

Altermatt incomplete ionization model In the recent Altermatt model [26][27], at high impurity concentration, some of the impurity states are no longer localized, and become free states. These impurity states are always completely ionized, independent of temperature and Fermi level position. Both the activation energy and the fraction of bound impurity states are functions of the doping concentration. Detailed physics considerations underlying this model can be found in [26] and [27]. We will describe here the essence of the model and then derive an explicit expression of *IR* for this model, since the original model was developed for numerical simulations and not compact modeling.

Again, consider p-type dopants with a concentration of N_{dop}. Denoting the fraction of bound impurity states as b, we have $(1-b)N_{dop}$ free impurity states that are always completely ionized. Out of the bN_{dop} bound states, $bN_{dop} \times f(E_A)$ are ionized. The total ionized concentration N_{dop}^{-} is given by:

$$N_{dop}^{-} = (1-b)N_{dop} + bN_{dop} \times f(E_A), \tag{5.84}$$

where the $(1-b)N_{dop}$ term represents the free states' contribution and the $bN_{dop} \times f(E_A)$ term represents the bound states' contribution. The ionization rate *IR* becomes:

$$IR(T) = (1-b) + bf(E_A). \tag{5.85}$$

Substituting (5.78) into (5.85) leads to:

$$IR(T) = (1-b) + \frac{b}{1 + g_A \exp\frac{E_{dop}}{kT} \exp\frac{(E_V - E_F)}{kT}}. \tag{5.86}$$

We then eliminate E_F-E_V using (5.81) to obtain $IR(T)$:

$$IR(T) = (1-b) + \frac{b}{1+G^{-1}IR(T)}, \tag{5.87}$$

(5.87) can be rewritten as a quadratic equation:

$$G^{-1}IR^2(T) + \left[1-(1-b)G^{-1}\right]IR(T) - 1 = 0. \tag{5.88}$$

An explicit solution of $IR(T)$ is thus obtained:

$$IR(T) = \frac{-G+(1-b)+\sqrt{[G-(1-b)]^2+4G}}{2}. \tag{5.89}$$

Besides E_{dop}, N_{dop}, R_{T0} and AR, an additional model parameter "b" is used. When b reaches its upper limit of "1", (5.89) reduces to the classical model. We apply (5.89) and (5.77) in IC-CAP to fit the intrinsic base sheet resistance vs. temperature data. During the fitting, we only adjusted the "b" value and kept E_{dop}, N_{dop}, $R_{CI,T0}$ and AR the same between the classic and Altermatt models. The results are shown in Fig. 5.29.

The intrinsic base resistance is underestimated below 50 K using the Altermatt model. This is expected, as $IR(T)$ has a minimum of $(1-b)$ within the model (e.g., (5.85) and (5.86)). When G decreases towards "0" with cooling, IR becomes "$1-b$". In Fig. 5.30, the Altermatt model gives us a larger ionization rate at low temperatures. Below 50 K, the ionization rate is fixed at $1-b = 0.05\%$, which is why the intrinsic base resistance is underestimated below 50 K. We note that in [26] and [27], "b" is temperature independent from 300 K to 30 K. Such a temperature independence of "b" inevitably leads to overestimation of the IR value at low temperatures.

New incomplete ionization model When the temperature is sufficiently low, ionization rate IR decreases exponentially towards "0" in the classic model and becomes "$1-b$" in the Altermatt model. To fit the measured intrinsic base sheet resistance below 50 K, we need to produce a $IR(T)$

that is in between the classic model and the Altermatt model, where the experimental value of $IR(T)$ lies. Such $IR(T)$ can only be obtained when "b" increases towards unity with cooling below certain threshold temperature. These results strongly suggest that "b" becomes temperature dependent at lower temperatures and further investigation into its physical interpretation is needed. For compact modeling, we propose the following empirical expression:

$$b = 1 - \frac{\beta}{1 + \left(\frac{T}{T0}\right)^{\alpha}}. \tag{5.90}$$

Two model parameters, β and α, are used. As shown by the solid line in Fig. 5.29, this new model enables accurate intrinsic base sheet resistance vs. temperature modeling from 30-300 K. If β is set to "0", "b" reduces to "1", and this new model reduces to the classic model. The same model equation can therefore be used for doping below or close to the Mott-transition.

For n-type dopants, the derivation is similar with obvious changes. The *IR* equation is given by:

$$\begin{aligned} IR(T) &= \frac{-G + (1-b) + \sqrt{[G-(1-b)]^2 + 4G}}{2}, \\ G &= g_D^{-1} \frac{N_C}{N_{dop}} \exp\left(-\frac{E_{dop}}{kT}\right), \end{aligned} \tag{5.91}$$

where $N_C = 2.8 \times 10^{19} \times \left(\frac{T}{300}\right)^{1.5} \mathrm{cm}^{-3}$ [75] is the effective density-of-states in the conduction band, and $g_D = 2$ for both arsenic and phosphorus.

Heavy doping above Mott-transition

For the heavily-doped buried collector, doping levels are well above Mott transition. Impurities are thus always completely ionized, even at cryogenic temperatures. Device simulation using the Altermatt model [26][27] through the physical model interface (PMI) in Sentaurus Device [54] indeed gives us ionization rate that is very close to unity from 300 K to 30 K. Therefore the temperature dependence of the mobility directly determines the temperature dependence of resistance. The same modeling methodology will be applied to the p^+ silicided extrinsic base

although it is not doping related. Here we use the buried collector for illustration. Fig. 5.31 shows the measured $\frac{R(T)}{R(T_0)}$, calculated $\frac{\mu(T_0)}{\mu(T)}$ using PHUMOB and a single power law mobility model for buried collector from 30-300 K. The parameter *AR* for the single power law model is determined from the slope of μ-T above 150 K using PHUMOB.

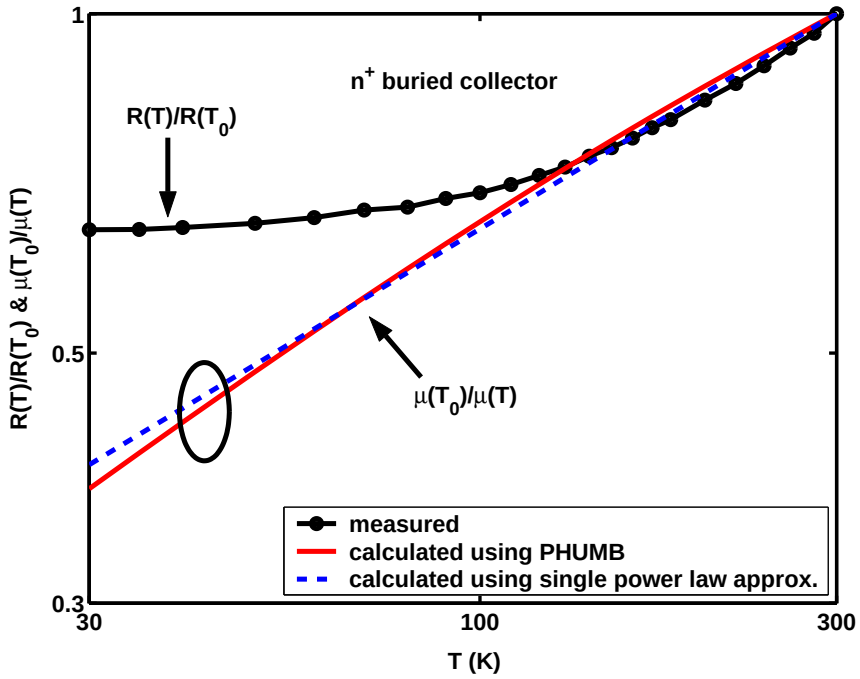

Figure 5.31: Measured $\frac{R(T)}{R(T_0)}$ and calculated $\frac{\mu(T_0)}{\mu(T)}$ using PHUMOB and a single power law approximation for the buried collector, from 30-300 K.

Over the whole temperature range, the PHUMOB gives a mobility temperature dependence that can be well-approximated with a single power law relation. However, a large difference is observed between calculated $\frac{\mu(T_0)}{\mu(T)}$ and measured $\frac{R(T)}{R(T_0)}$ below 150 K. This indicates that even the complicated PHUMOB model is not sufficiently accurate at low temperatures for the heavily doped buried collector. From Fig. 5.31, the $\ln(\frac{R(T)}{R(T_0)})$ - $\ln T$ is linear above 150 K and then becomes "flattened" with further cooling. For compact modeling, we have two options. The first option is to directly model the mobility temperature dependence. The second option is to continue to use the single power law mobility model, but model the deviation from the true mobility as a variation of *IR* with temperature. Both approaches work well, as we discuss below.

Dual power law mobility approximation with $IR = 1$ As $IR(T) = 1$, $\frac{R(T)}{R(T_0)}$ is essentially $\frac{\mu(T_0)}{\mu(T)}$. An inspection of the measured $\frac{R(T)}{R(T_0)}$ vs. temperature shows that we can combine two power law mobility temperature dependencies using Mathiessen's rule to produce the desired $\frac{R(T)}{R(T_0)}$. Such a dual power law mobility model can be written as:

$$\begin{aligned} &\frac{1}{\mu} = \frac{1}{\mu_1} + \frac{1}{\mu_2}, \\ &\mu_1 = \gamma_1 T^{\alpha}, \mu_2 = \gamma_2 T^{\beta}, \end{aligned} \tag{5.92}$$

where μ_1 and μ_2 represent two scattering mechanisms, γ_1 and γ_2 are two model parameters, and α and β are their temperature coefficients. By defining $\gamma = \frac{\gamma_2}{\gamma_1}$, $R(T)$ can be related to μ by:

$$R(T) = R_{T0} \frac{\frac{1}{\gamma_1 T^{\alpha}} + \frac{1}{\gamma_2 T^{\beta}}}{\frac{1}{\gamma_1 T_0^{\alpha}} + \frac{1}{\gamma_2 T_0^{\beta}}} = R_{T0} \frac{\gamma \frac{1}{T^{\alpha}} + \frac{1}{T^{\beta}}}{\gamma \frac{1}{T_0^{\alpha}} + \frac{1}{T_0^{\beta}}}, \tag{5.93}$$

(5.93) is implemented using IC-CAP to fit measured sheet resistance vs. temperature data. Here, γ, α, β and R_{T0} are used as model parameters. The modeling results are accurate from 30-300 K, as shown by solid lines in Fig. 5.32.

Empirical approach Instead of modeling the true mobility variation with a physical $IR = 1$, we can also continue to use the single power law mobility approximation (for numerical efficiency), and model the deviation from true mobility as a variation of *IR*. We implemented this approach using both the classic incomplete ionization model and the Altermatt model for the buried collector and the extrinsic base. We find that the Altermatt model works, whereas the classic model does not. As shown in Fig. 5.32, where the dotted lines are completely overlaid by solid lines, this approach enables accurate resistance vs. temperature modeling from 30-300 K. As we discussed in Section III, this approach is empirical, and gives us *IR* smaller than unity because part of the temperature dependence of mobility has been modeled by carrier freezeout. This approach, though empirical,

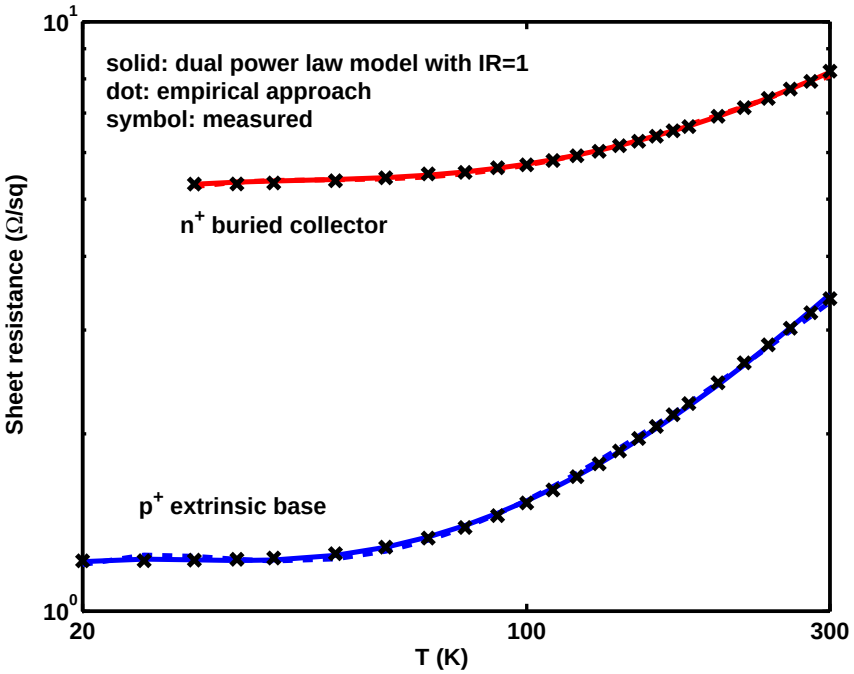

Figure 5.32: Silicided extrinsic base and buried collector sheet resistance modeling using dual power law approximation with $IR = 1$ and empirical approach, from 30-300 K.

does have the advantage of allowing the use of the same model equation for all resistances, which can be attractive for compact modeling efficiency.

5.11.4 Thermal resistance

Fig. 5.33 shows measured and modeled R_{TH}-T_{amb} on a log-log scale. Current R_{TH} T-scaling equation can only model the linear portion, so a 3rd order polynomial is used. The increase of R_{TH} with cooling below 150 K is consistent with thermal resistivity T-dependence reported in [76].

$$R_{th,Tamb} = aT^3 + bT^2 + cT + R_{th,nom}$$

5.11.5 Hot carrier current I_{HC} and epilayer space charge resistance SCR_{CV}

Hot-carrier current I_{HC} and epilayer space charge resistance SCR_{CV} strongly affect f_T roll-off. $I_{HC} \propto v_{sat}$, and $SCR_{CV} \propto 1/I_{HC}$. Both I_{HC} and SCR_{CV} are regarded as T-independent in MEXTRAM.

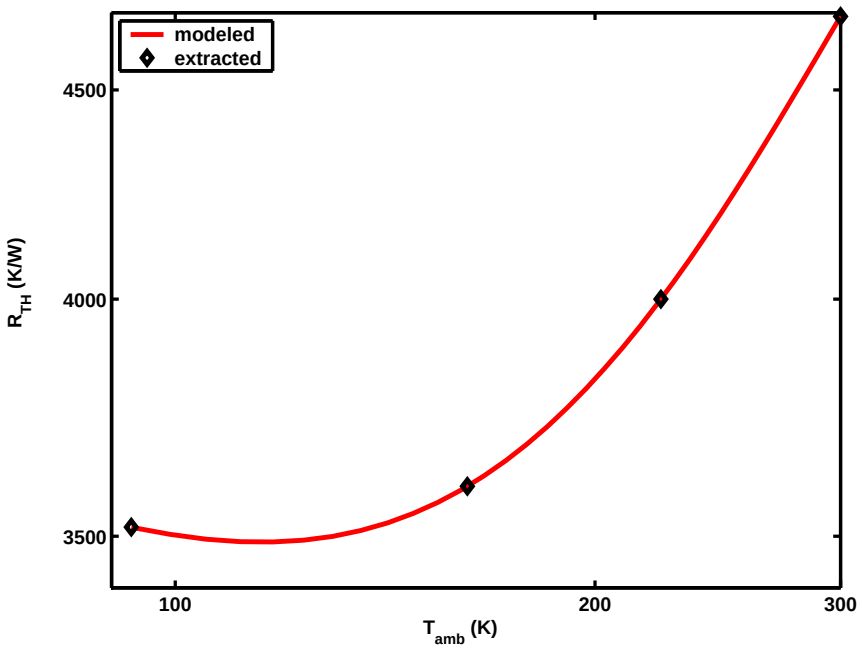

Figure 5.33: Extracted and modeled $\ln R_{TH}$-$\ln T_{amb}$.

Here we find it necessary to include T-dependence of v_{sat} into I_{HC} and SCR_{CV} as follows:

$$I_{HC}(T) = I_{HC,nom} t_N{}^{-\lambda_1(T-T_{nom})-\lambda_2},$$
$$SCR_{CV}(T) = SCR_{CV,nom} t_N{}^{\lambda_1(T-T_{nom})+\lambda_2}, \tag{5.94}$$

where $I_{HC,nom}$ and $SCR_{CV,nom}$ are nominal temperature values, and λ_1 and λ_2 are fitting parameters.

5.12 Summary

In our previous work [1], we pointed out ideality factor is necessary to accurately model the slope of *I-V* characteristics over wide temperature range. A new temperature scaling model of saturation current including the impact of ideality factor was developed. Also, in our previous work [2], a physics based trap-assisted tunneling current equation is presented to model the base current at low bias over wide temperature range.

In this chapter, new temperature scaling models for series resistance, thermal resistance R_{TH}, epilayer current parameter I_{HC} and SCR_{CV} are presented. Particularly, temperature characteristics of mobility and ionization rate, which are the two main factors affecting the temperature dependence of various device resistances, are investigated. The classic ionization model, together with a single power law mobility model, enables resistance vs. temperature modeling of the substrate and the collector region, where doping levels are below Mott-transition. Based on the Altermatt ionization model, a new incomplete ionization model that accounts for the temperature dependence of the bound state fraction factor is developed. This new model enables accurate temperature dependent modeling of the intrinsic base sheet resistance, which has a doping level close to the Mott-transition. For the buried collector and the silicided extrinsic base, where doping levels are well above the Mott-transition, two approaches are proposed and both give good results. The first approach uses a dual power law mobility model and complete ionization. The second approach uses the Altermatt incomplete ionization model and a single power law mobility approximation. The second approach allows one to use a single model equation for compact modeling of all resistances in SiGe HBTs.

Chapter 6

Parameter Extraction and Compact Modeling Results

A reliable, robust and unambiguous parameter extraction method is very important. The use of a very accurate compact model with poorly extracted parameters will produce bad prediction of device and circuit performance. The electrical parameter extraction includes low-current parameters extraction and high-current parameters extraction. Low-current parameters extraction is straightforward. However, high-current parameters extraction is much more difficult because in that regime many physics effects play a role. Table. 6.1 is the typical grouping of parameters extraction at reference temperature in Mextram [4]. In Mextram, most of the parameters can be extracted directly from measured data, including depletion capacitance C-V, dc Gummel plots, dc output characteristics, dc Early voltage measurement, and ac S-parameter measurement. Some special measurements are taken to extract terminal resistance, such as R_E-flyback and R_{Cc}-active methods.

There are different methods to extract temperature parameters. One method is to optimize the temperature parameters of all data over temperatures. The disadvantage of this method is that we do not extract the individual parameters at each parameter. If there are unexpected differences between the model simulation and hardware data, it is difficult to know whether it is the weakness of the electrical model or temperature scaling model. The second method is to extract the electrical parameters at all temperatures isothermally. The main advantage is that one can check the correctness of existing temperature scaling equations by comparing extracted and simulated electrical parameters [4].

Table 6.1: A typical grouping of parameters used in the extraction procedure in Mextram [4].

Base-emitter depletion capacitance	C_{jE}, p_E, (V_{d_E})
Base-collector depletion capacitance	C_{jC}, p_C, X_p
Collector-substrate depletion capacitance	C_{jS}, p_S, (V_{d_S})
Forward-Early	W_{avl}, V_{avl}
Reverse-Early	V_{er}
Forward-Early	V_{ef}
Forward-Gummel	I_s
Forward-Gummel	β_f, I_{Bf}, m_{Lf}
R_E-flyback	R_E
R_{Cc}-active	R_{Cc}
Reverse-Gummel	I_{Ss}, (I_{ks})
Reverse-Gummel	β_{ri}, I_{Br}, V_{Lr}
Output-characteristic	R_{th}, I_k
Forward-Gummel	R_{Cv}, (V_{d_C})
Cut-off frequency	SCR_{Cv}, I_{hc}, τ_E, τ_{epi}, (τ_B, α_{X_i})
Reverse-Gummel	X_{ext}

6.1 Parameter extraction methodology in this work

A wide temperature range (43-393 K) is covered in this work, hence isothermal parameter extraction is mainly used to verify the validity of existing temperature models. For example, as we discussed in chapter 5, Mextram's temperature models of saturation current and ideality factor no longer work below 110 K. In this work, complete DC and AC measurements are made at 393, 300, 223, 162, and 93 K Additional Gummel measurements are made at more temperatures to allow sufficient modeling of temperature dependence.

Self-heating has a large impact at high current parameters because of the strong temperature dependence of currents, making it difficult to accurately determine isothermal values of high injection parameters, especially at low temperatures. A 80 K junction temperature rise is much more significant for an ambient temperature of 43 K than for 300 K. To minimize the impact of the correlation between self-heating and high current parameters, in our work, we present following parameter extraction methodology, as shown in Fig. 6.1.

• Firstly, low injection parameters (saturation current I_S and ideality factor N_F, junction capacitance parameters, early voltage, avalanche parameters) are extracted isothermally and temperature mapped.

• Then parasitic resistances are extracted isothermally and temperature mapped;

• Then thermal resistances R_{TH} are extracted isothermally and temperature mapped;

• Then, high current parameters are extracted isothermally and temperature mapped, with the implementation of temperature mapped low injection parameters, parasitic resistances and R_{TH}. During this step, self-heating is turned on.

• Finally, once the electrical parameters are extracted and all the temperature scaling equations are updated, temperature parameters will be fine-tuned again within the whole temperature range, with self-heating turned on. Usually, several iterations between the last two steps are necessary.

In chapter 5, we present new temperature scaling models for saturation current, ideality factor, base tunneling current, series resistance, thermal resistance, hot carrier current and epilayer space charge resistance. In this chapter, we have not developed corresponding isothermal parameter

extraction functions based on our new temperature scaling models. Saturation current, ideality factor and base tunneling current parameters are extracted from the intercept and slope of *I-V* through customized transforms coded in Matlab. Junction capacitance parameters are extracted by using Mextram default functions `MXT_cbe` and `MXT_cbc`. Forward and reverse voltages are extracted by using Mextram default functions `MXT_VEF` and `MXT_VER`. Parasitic resistance and thermal resistance are extracted through customized transforms coded in Matlab. High current parameters are extracted through Verilog-A simulator together with global optimizer.

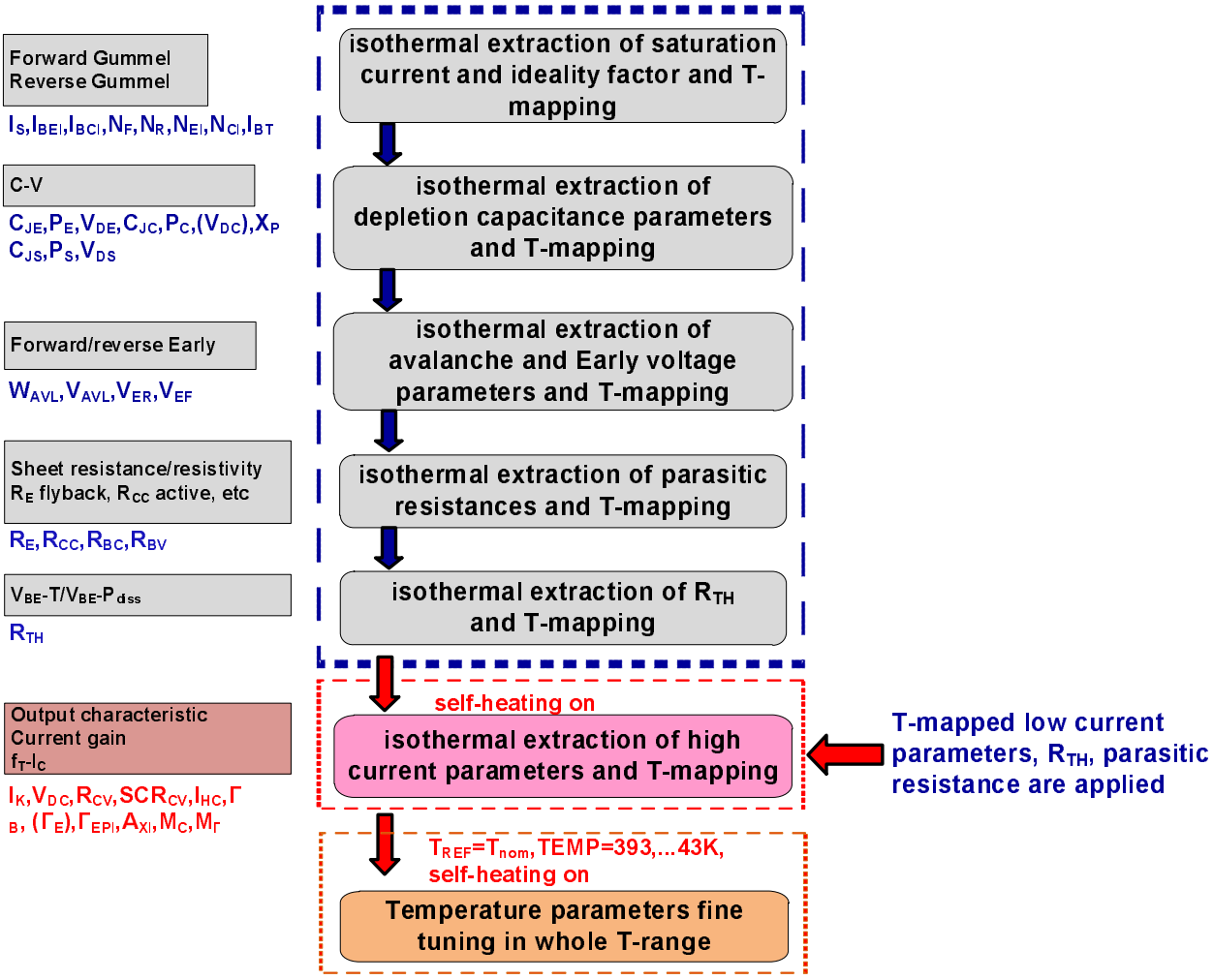

Figure 6.1: Proposed parameter extraction methodology in this work.

6.2 Saturation current and ideality factor

Let us take the collector current I_C-V_{BE} for example. The I_S and N_F are extracted from low bias region where the Early effects are negligible. Hence we can extract the saturation current I_S and ideality factor N_F from the linear region of semi-log I-V curve where the collector current I_C can be approximated as:

$$I_C \approx I_S(T)[\exp(\frac{V_{BE}}{N_F(T)V_T}) - 1] \tag{6.1}$$

I_S can be extracted from the interception of current at zero voltage, and N_F can be extracted from the slope of this linear region. Fig. 6.2 show the extraction range of I_S and N_F from I_C-V_{BE}.

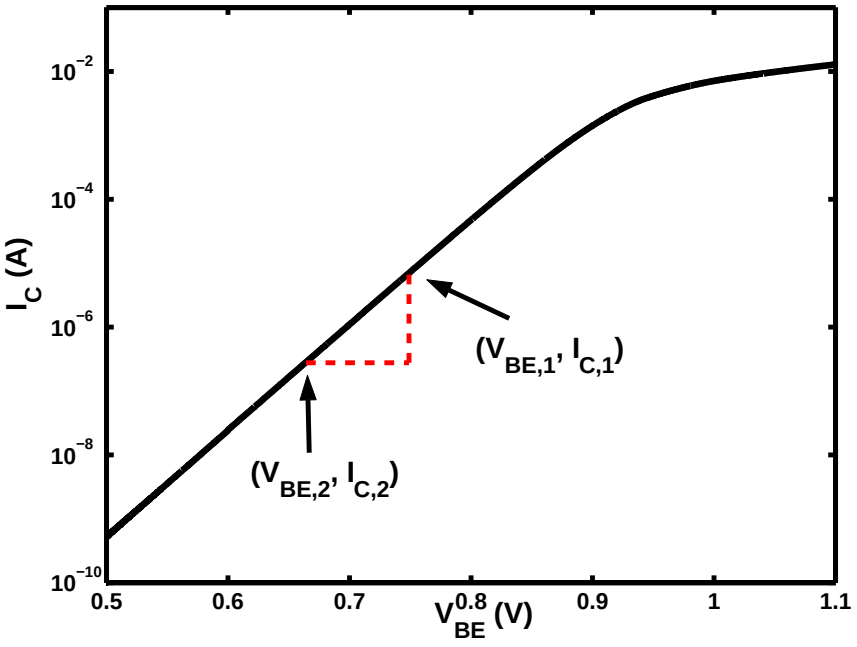

Figure 6.2: I_S and N_F extraction from the intercept and slope of I_C-V_{BE}.

6.3 Base tunneling current

At low temperatures, due to the large TAT current ($I_{S,TAT}e^{V_{BE}/V_{TUN}}$) and the sharp slope of base diffusion current ($I_{S,BE}e^{V_{BE}/V_{Diff}}$), it is difficult to directly identify such extreme V_{BE} ranges where either TAT or diffusion current overwhelmingly dominates. In [2], an iterative procedure is presented to separate the TAT current from the "ideal" base current. We achieve the fitting using the iterative procedure below:

(1) Select an ideal high V_{BE} region, perform linear fitting, determine $I_{S,BE}$ and V_{Diff} initial values.

(2) Subtract $I_{S,BE}e^{V_{BE}/V_{Diff}}$ from total I_B, fit the resulting current in a relatively lower V_{BE} region to determine $I_{S,TAT}$ and V_{TUN}.

(3) Subtract $I_{S,TAT}e^{V_{BE}/V_{TUN}}$ from total I_B. Perform linear fitting and update $I_{S,BE}$ and V_{Diff}.

(5) Repeat the Step 2, 3 and 4 until the difference of slope extracted by two successive times are smaller than a set limit.

Fig. 6.3.(a) shows the difference between linear fittings of base current with and without iteration at 43 K. Without iteration means that main current is directly fitted only by Step 1 from the "ideal" base region without excluding the TAT current. It shows that with iteration the summation of two linear fitting can better cover the measurement. Thus, the TAT current is recognized as the total base current subtracting the "ideal" I_B after iterated fitting. Fig. 6.3.(b) shows good overall fitting results of I_B-V_{BE} including TAT.

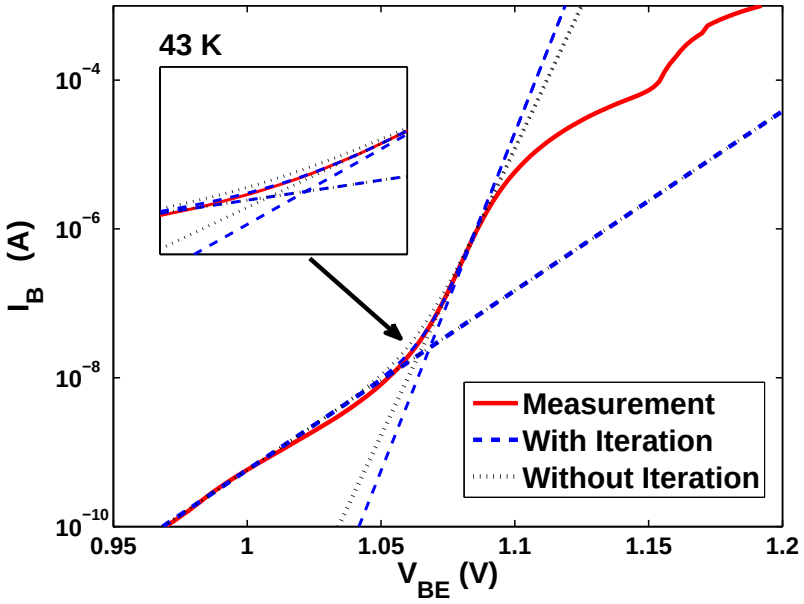

(a)

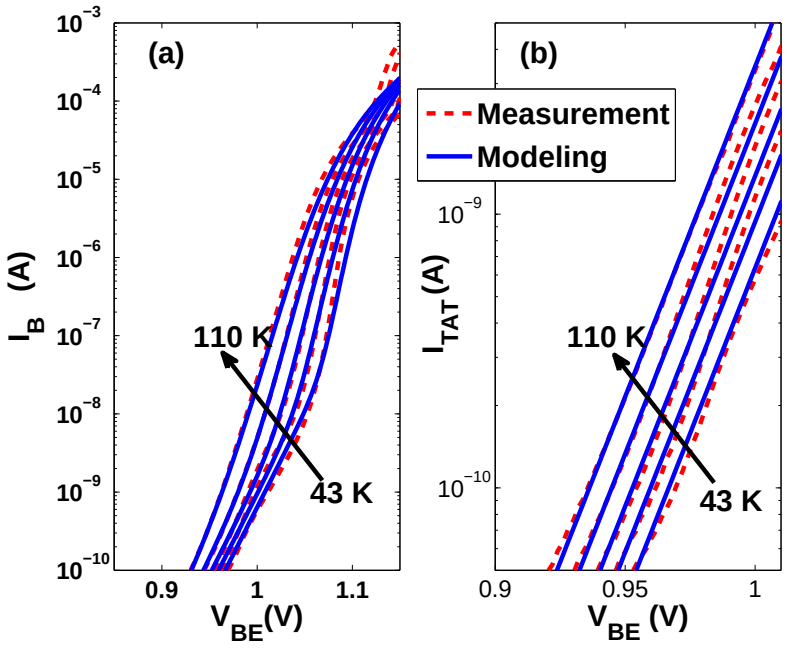

(b)

Figure 6.3: (a) Comparison of the direct linear fitting of I_B and fitting with iteration at 43 K. (b) I_B-V_{BE} modeling results including TAT [2].

6.4 Depletion capacitance

C-V data are obtained from performing S-parameter measurements on transistors biased in the "cold" operation (low current). Measurement is made from 100 MHz to 1 GHz with a lower frequency VNA for C-V purpose, so that the parasitic resistances have negligible effect. R_{SUB} and C_{SUB} are extracted from substrate Y-parameters Y_{22}+Y_{12} [77].

Base-emitter depletion capacitance

The measured base-emitter capacitance C_{BE} consists of a depletion capacitance, an overlap capacitance and a diffusion capacitance. The depletion capacitance and overlap capacitance dominate so long as V_{BE} is not so high.

The base-emitter capacitance can be written as [4]:

$$C_{BE} = \frac{s_E C_{jE}}{(1 - V_{jE}/V_{dE})^{p_E}} + \frac{(1 - s_E) C_{jE}}{(1 - V_{FE}/V_{dE})^{p_E}} + C_{BEO}. \tag{6.2}$$

This describes a transition from a normal depletion capacitance (if $s_E = 1$) to a constant capacitance ($s_E = 0$). The formula of V_{jE} and V_{FE} have been given in (5.11). In practical parameter extraction, the constant capacitance does not appear as it usually occurs at higher bias, where the diffusion capacitance dominates. C_{BEO} represents any overlay (peripheral) capacitance between base and emitter. Actually, the sum of C_{jE} and C_{BEO} give the overall zero bias capacitance and cannot be separated clearly.

The zero-bias C_{jE}, grading coefficient p_E and built-in potential V_{dE} can be extracted directly by applying (6.2) in IC-CAP [62] to fit measured C_{BE}-V_{BE} isothermally. Fig. 6.4 shows the extracted C_{BE}-V_{BE} from $\Im(1/(Y_{11}+Y_{12}))$ from 393 K to 93 K. Theoretically, the depletion capacitance will generally decrease with cooling due to the increase in junction built-in voltage. Additionally, our TCAD simulated C_{BE}-V_{BE} decreases with cooling monotonically whatever the carrier freezeout is taken into account or not. Also, the temperature dependence of base-emitter depletion capacitance C_{BE} is weaker than base-collector depletion capacitance C_{BC} due to higher doping in base than that

of collector. However, the C_{BE}-V_{BE} extracted from measurement do not give monotonic trend with temperatures, as shown in Fig. 6.4. Hence in our work, we model a weak temperature dependent C_{BE} by fitting the C_{BE}-T averagely.

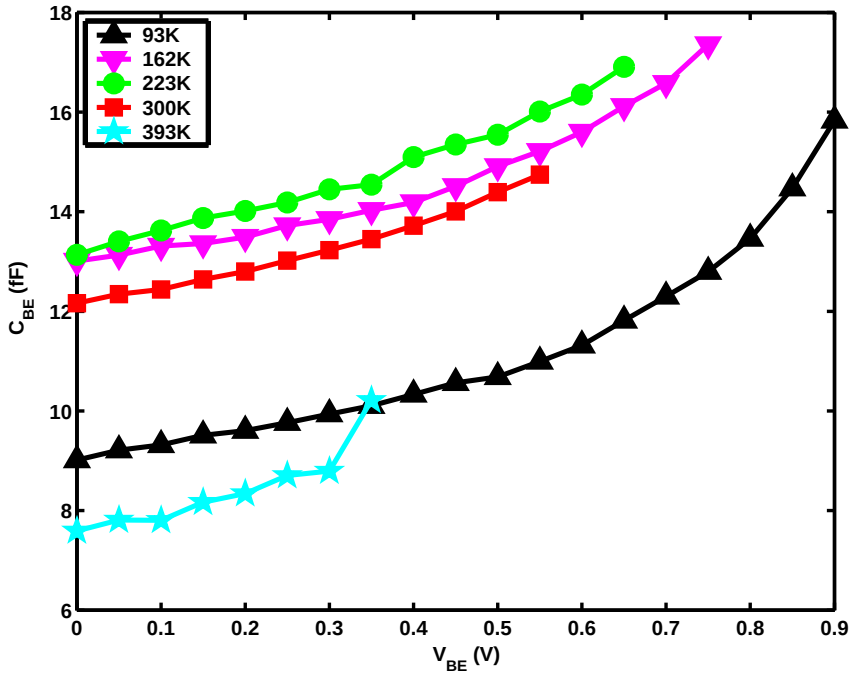

Figure 6.4: Extracted C_{BE}-V_{BE} from 93-300 K.

Base-collector depletion capacitance

The extraction of the base-collector depletion capacitance C_{BC} is similar to that of base-emitter capacitance. Parameter X_p is introduced to describe the finite thickness of collector epilayer. The base-collector depletion capacitance can be written as:

$$C_{BC} = \frac{s_C(1-X_p)C_{jC}}{(1-V_{jC}/V_{dC})^{p_C}} + \frac{(1-s_C)(1-X_p)C_{jC}}{(1-V_{FC}/V_{dC})^{p_C}} + X_p C_{jC} + C_{BCO}, \tag{6.3}$$

where $X_p C_{jC}$ models constant part when the base-collector depletion region reaches the collector buried layer.

Fig. 6.5 shows the extracted C_{BC}-V_{BC} from $\Im(-Y_{12})$ from 393 K to 93 K. The zero-bias C_{jC}, grading coefficient p_C and X_p can be extracted directly by applying (6.3) in IC-CAP [62] to fit measured C_{BC}-V_{BC} isothermally. Help parameter V_{dC} will be re-extracted with other high current parameter later, because it has strong impact on the current gain roll-off, cut-off frequency roll-off and output characteristics quasi-saturation region.

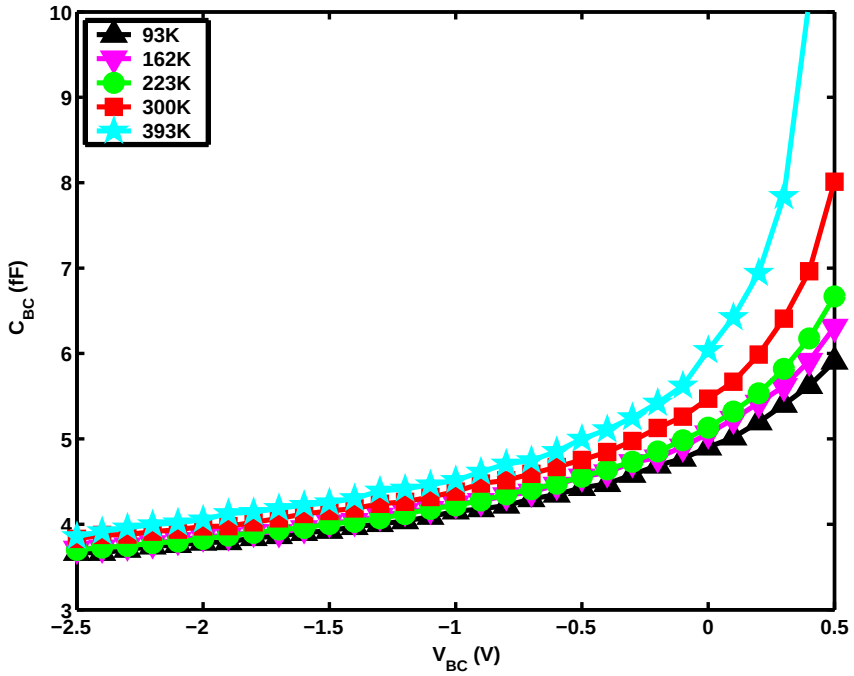

Figure 6.5: Extracted C_{BC}-V_{BC} from 93-300 K.

Collector-substrate depletion capacitance

To better model the device characteristics in high frequency range, we include a pair of substrate capacitance C_{SUB} and substrate resistance R_{SUB} in parallel with collector-substrate depletion capacitance C_{CS}, consisting substrate network, as shown in Fig. 5.2. The C_{CS}, C_{SUB} and R_{SUB} are extracted by fitting the real part and imaginary part of Z_{sub} ($Z_{sub} = (Y_{22} + Y_{12})^{-1}$) at different V_{CS}, as shown in Fig. 6.6 and Fig. 6.7. The extracted C_{SUB} is constant across temperatures. The extracted temperature dependence of R_{SUB} agrees with what we obtain from measured substrate resistivity, as shown in Fig. 6.7.(b).

The collector-substrate depletion capacitance can be written as:

$$C_{SC} = \frac{s_S C_{jS}}{(1 - V_{jS}/V_{dS})^{p_S}} + \frac{(1 - s_S) C_{jS}}{(1 - V_{FS}/V_{dS})^{p_S}}. \tag{6.4}$$

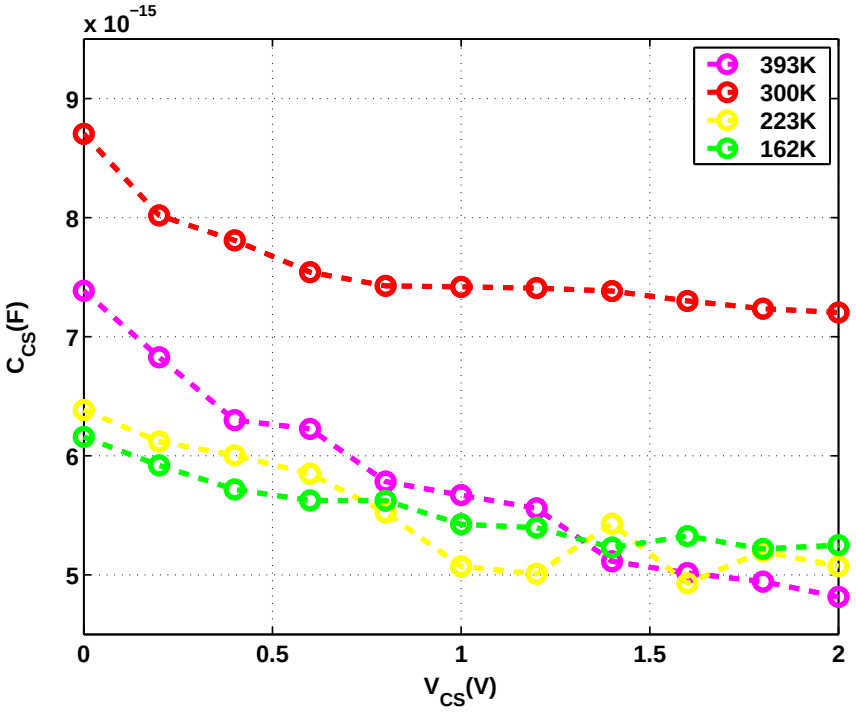

Figure 6.6: Extracted C_{CS}-V_{CS} from 162-393 K.

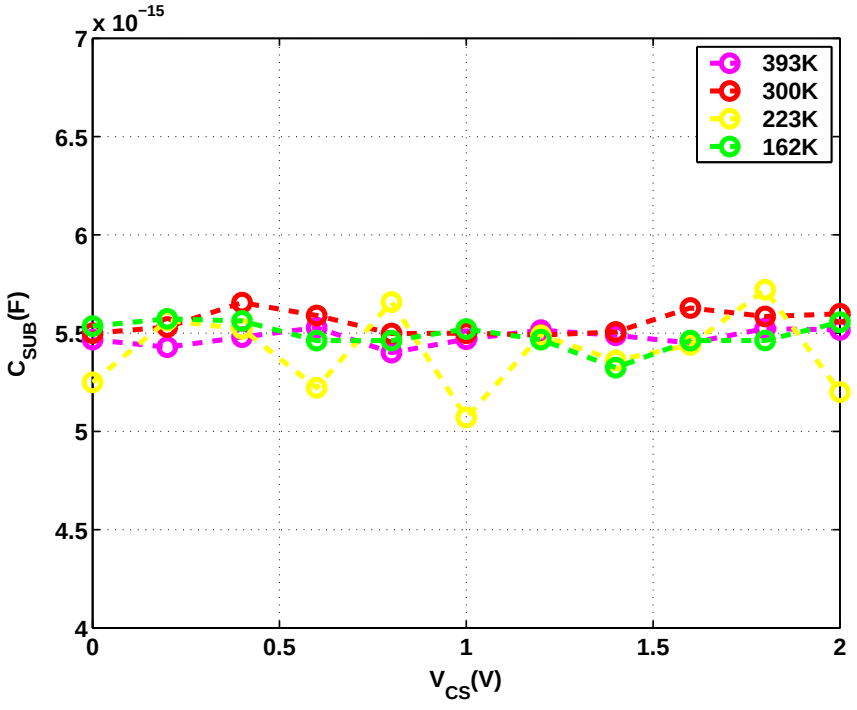

(a)

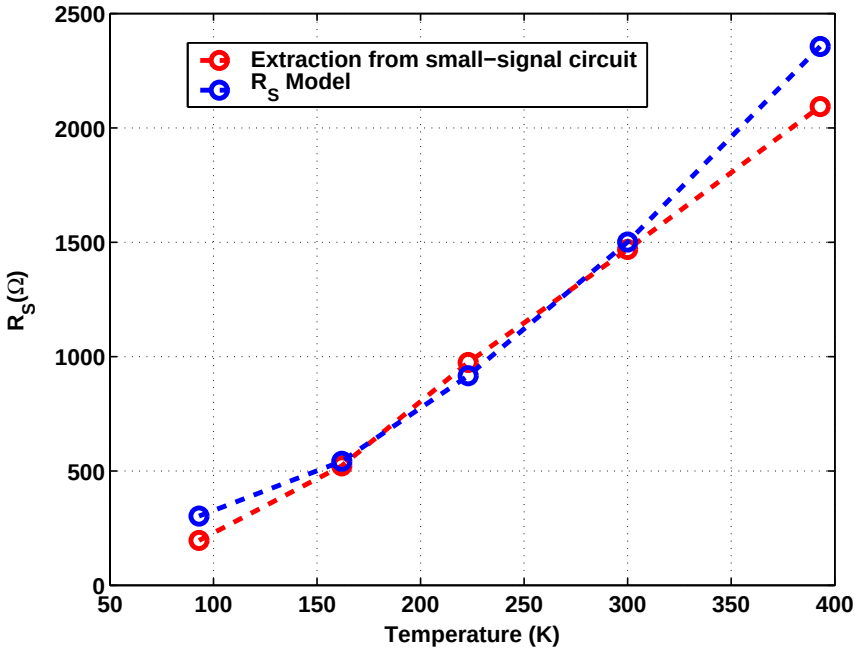

(b)

Figure 6.7: (a) Extracted C_{SUB}-V_{CS} from 162-393 K; (b) Extracted and modeled R_{SUB}-T.

6.5 Avalanche and Early voltage

Avalanche

Effective width of the epilayer for avalanche current W_{AVL} and voltage describing the curvature of the avalanche current V_{AVL} are extracted from the avalanche current I_{avl} and multiplication factor $M-1$ in the Forward-Early measurement. The avalanche current I_{avl} is the difference between the base current at $V_{CB}=0$ and at higher V_{CB}.

$$I_{avl} = I_{B0} - I_B, \tag{6.5}$$

where I_{B0} is a help parameter. I_{avl} can be expressed by [3]:

$$\begin{aligned} E_M &= \frac{V_{dc}+v_{CB}+2V_{avl}}{W_{avl}}\sqrt{\frac{V_{dc}+v_{CB}}{V_{dc}+v_{CB}+V_{avl}}}, \lambda_D = \frac{W_{avl}^2}{2V_{avl}}E_M, \\ G_{EM} &= \frac{A_n}{B_n}E_M\lambda_D\left\{\exp\left[-\frac{B_n}{E_M}\right] - \exp\left[-\frac{B_n}{E_M}\left(1+\frac{W_{avl}}{\lambda_D}\right)\right]\right\}, \\ I_{avl} &= I_C G_{EM}, \end{aligned} \tag{6.6}$$

where E_M is the maximum electric field in the depletion region, λ_D is the extrapolated depletion thickness where the electric field is zero, G_M is the generation coefficient. A_n and B_n are material constants, which are avalanche coefficient and critical electric field respectively.

Therefore:

$$M-1 = \frac{I_{AVE}}{I_C - I_{AVE}} = \frac{G_{EM}}{1-G_{EM}}. \tag{6.7}$$

Fig. 6.8 shows the extracted and modeled M-1-V_{CB} from 93-393 K. Forced-I_E measurement technique at a low current ($I_E = 12.5\mu A$) is used here to avid self-heating effect. In chapter 3, the current dependence of avalanche multiplication factor M-1 is investigated. Such current dependence of M-1 leads to a much higher breakdown voltage at high collector current. However, this current dependence of M-1 has not been modeled in compact modeling.

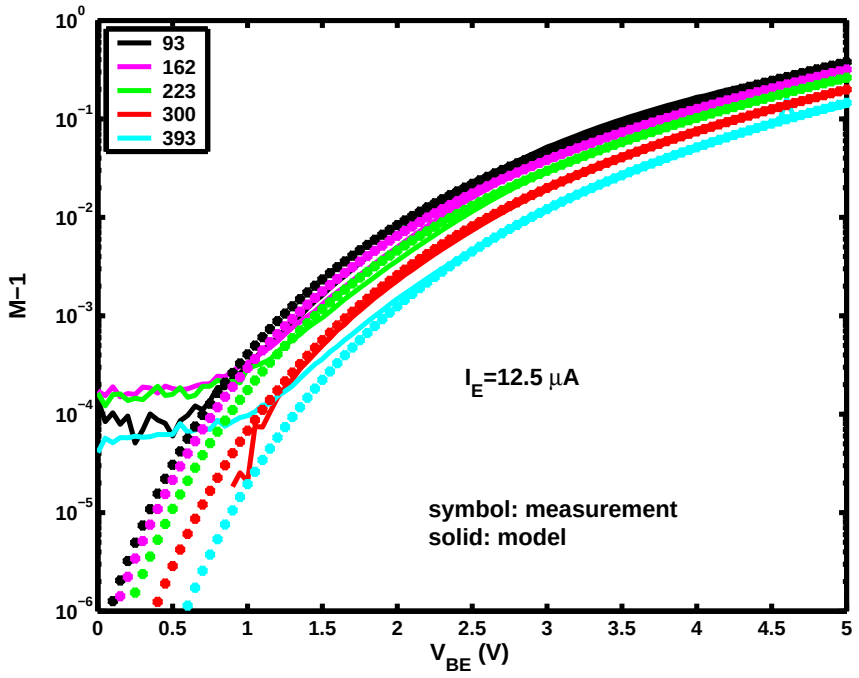

Figure 6.8: Extracted and modeled M-1-V_{CB} from 93-393 K.

Early voltage

The extraction of forward Early voltage V_{EF} and reverse Early voltage V_{ER} depend on the bandgap difference in base $\Delta E_g = E_g(0) - E_g(W_B)$. V_{EF} and V_{ER} have a value that corresponds to a pure Si transistor with the same doping as that of the SiGe transistor.

In this work, ΔE_g is estimated directly by using process knowledge and is fixed as a constant value over temperatures. And the effective Early voltage:

$$V_{Forw\_Early,eff} = I_C(\frac{\partial I_C}{\partial V_{CB}})^{-1} = V_{EF}\frac{e^{\Delta E_g/kT}-1}{\Delta E_g/kT},$$
$$V_{Rev\_Early,eff} = I_E(\frac{\partial I_E}{\partial V_{EB}})^{-1} = V_{ER}\frac{1-e^{-\Delta E_g/kT}}{\Delta E_g/kT}. \quad (6.8)$$

V_{EF} and V_{ER} are extracted isothermally from I_C-V_{CB} and I_E-V_{EB} respectively.

6.6 Emitter resistance

R_E flyback method

One of the simplest way to extract the emitter resistance is from the Giacoletto method [78]. The collector current is kept zero and the V_{BE} is increased . The collector-emitter saturation voltage can be estimated as $V_{CES} \approx I_E R_E$. Then the emitter resistance can be obtained by taking the derivative of V_{CES} with regard to I_E:

$$R_E = \frac{\partial V_{CES}}{\partial I_E}. \tag{6.9}$$

Fig. 6.9-Fig. 6.10 illustrate the measured V_{CES} and the derivation of the measured V_{CES} with regard to the I_E in the R_E flyback measurement. Physically, the series emitter resistance of the heavily doped emitter region is expected to be current independent. However, the derivation of measured V_{CES} with regard to the I_E decreases as function of I_E. If it has reached a plateau, the value there will be the R_E. If the plateau is not reached one will over-estimate the R_E.

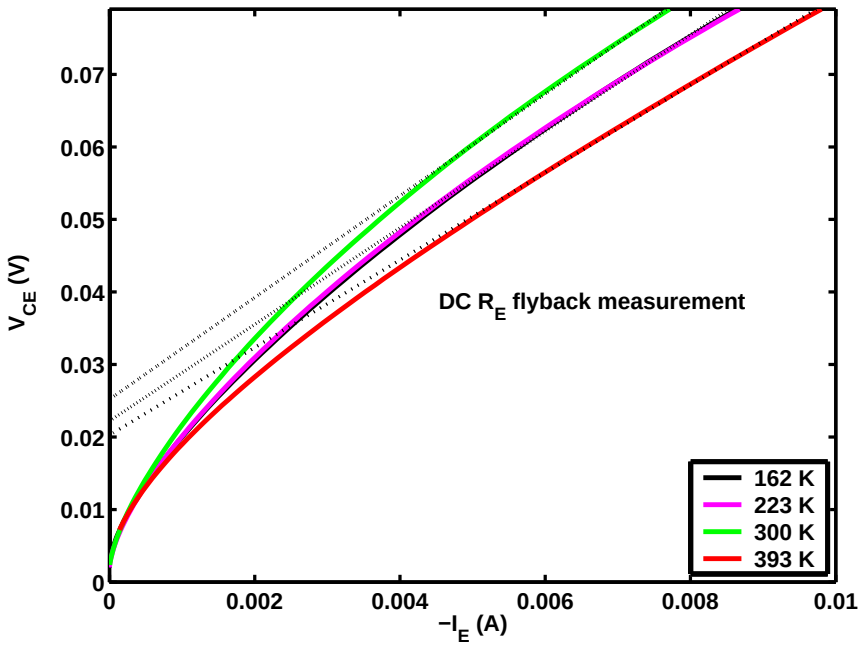

Figure 6.9: The measured V_{CES} versus -I_E in the R_E flyback measurement for the R_E extraction.

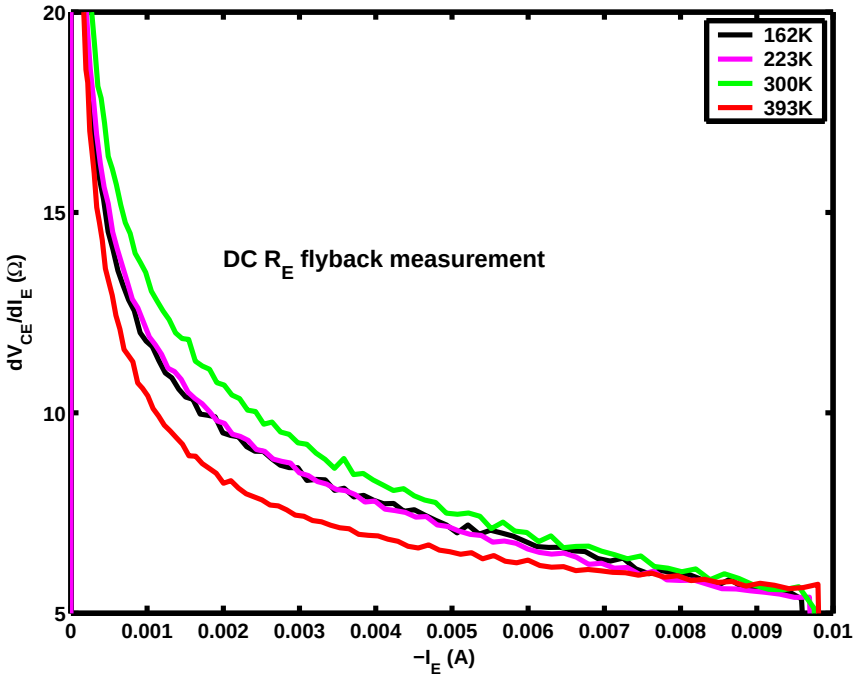

Figure 6.10: Derivation of the measured V_{CES} w.r.t the I_E in the R_E flyback measurement for the R_E extraction.

Extracted from Z_{12}

In our work, the *ac* S-parameter measurement is also taken to extract R_E for comparison. In the high frequency range, the real part of Z_{12} is the sum of dynamic input resistance r_e of the emitter base junction and emitter resistance R_E.

$$\Re(Z_{12}) = r_e + R_E. \tag{6.10}$$

The dynamic input resistance is defined by:

$$r_e = \frac{\partial V_{BE}}{\partial I_E} \approx \frac{\partial V_{BE}}{\partial I_C} = \frac{1}{I_S e^{\frac{V_{BE}}{N_F V_T}} \frac{1}{N_F V_T}} \approx \frac{N_F V_T}{I_E}, \tag{6.11}$$

Hence,

$$\Re(Z_{12}) = \frac{N_F V_T}{I_E} + R_E,$$

. (6.12)

R_E can be extracted by extrapolating $\Re(Z_{12})$ versus $\frac{1}{I_E}$ from the intercept.

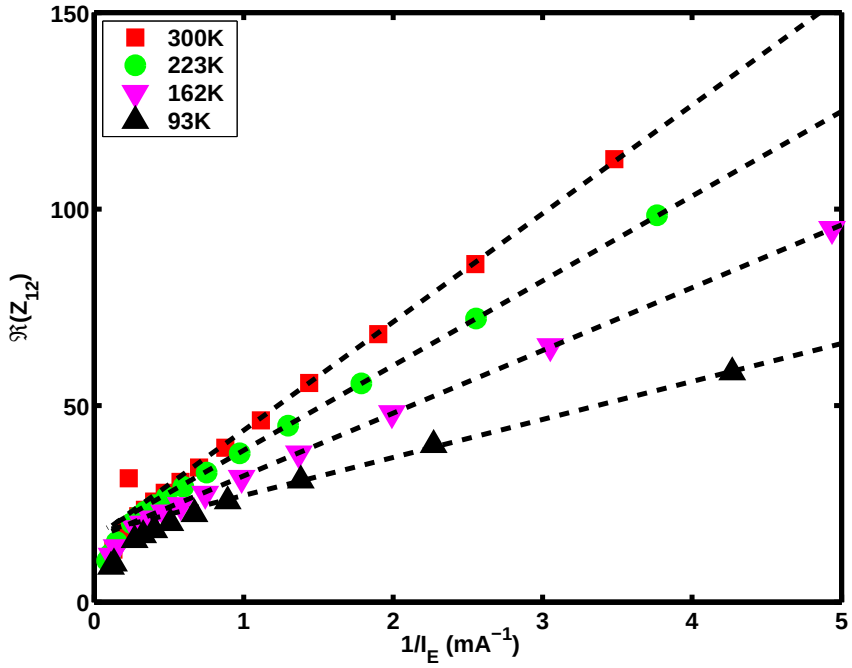

Figure 6.11: $\Re(Z_{12})$ versus $\frac{1}{I_E}$ from 93-300 K.

6.7 Base resistance

dc method

The deviation between ideal and measured base current I_B at high current levels is due to voltage drops ΔV_{BE} across base resistance R_B and emitter resistance R_E [79].

$$\Delta V_{BE} = V_{BE} - V_{B_2E_1} = R_E \times I_E + R_B(I_B) \times I_B,$$
$$= R_E \times I_E + (R_{B_C} + R_{BV}(I_B)) \times I_B. \tag{6.13}$$
$$\tag{6.14}$$

Once emitter resistance R_E is determined, the total base resistance $R_{B_C} + R_{BV}(I_B)$ as function of current can be extracted from Gummel curves.

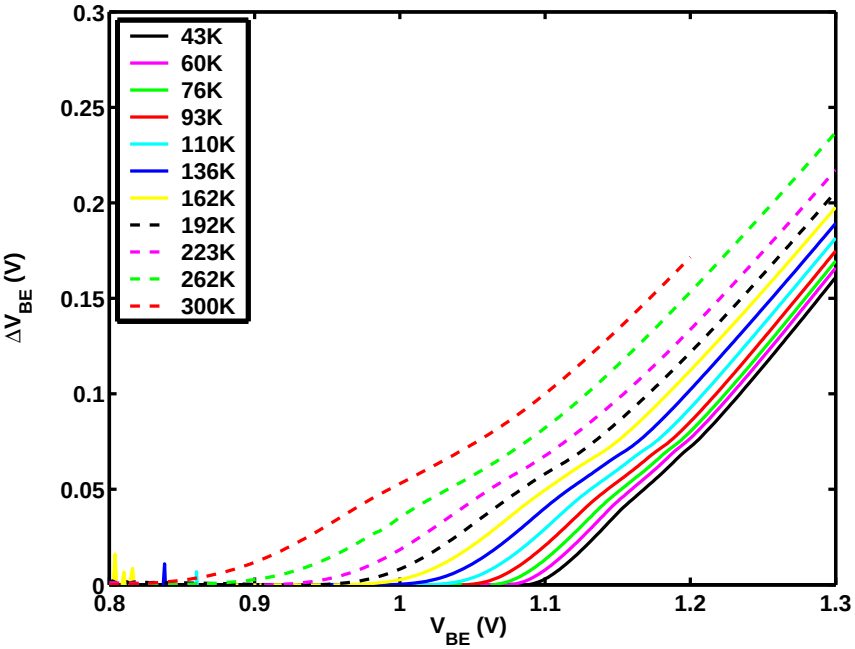

Figure 6.12: ΔV_{BE}-V_{BE} from 43-300 K.

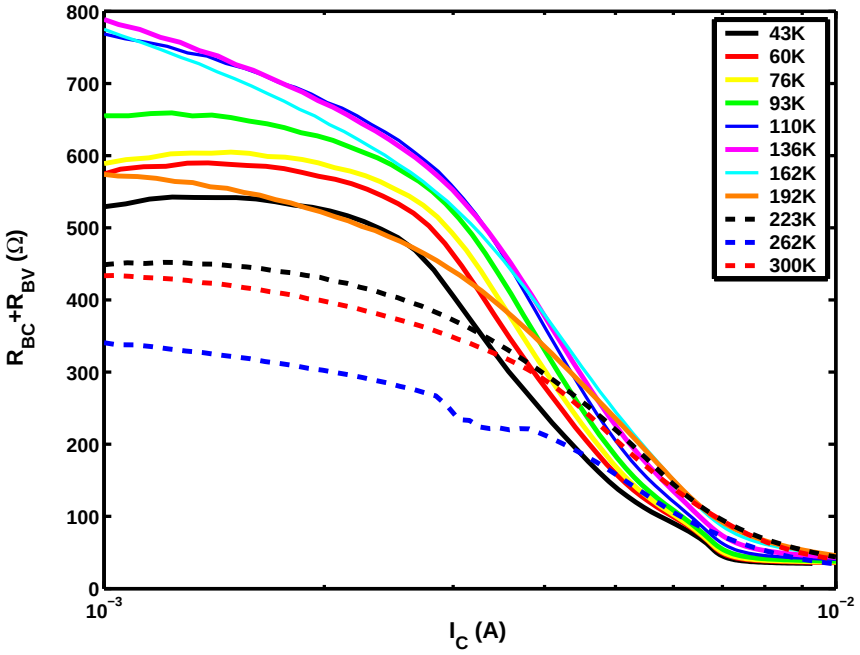

Figure 6.13: Extracted $(R_{BC}+R_{BV})$-I_C from 43-300 K.

ac method

Two *ac* methods are applied here to extract base resistances by using s-parameter data.

At very high frequency, $1/\Re(Y_{11})$-ω^{-2} curves can be fitted by a straight line with an intercept of $r_e + r_b$ [80], where r_e and r_b are *ac* emitter and *ac* base resistances respectively.

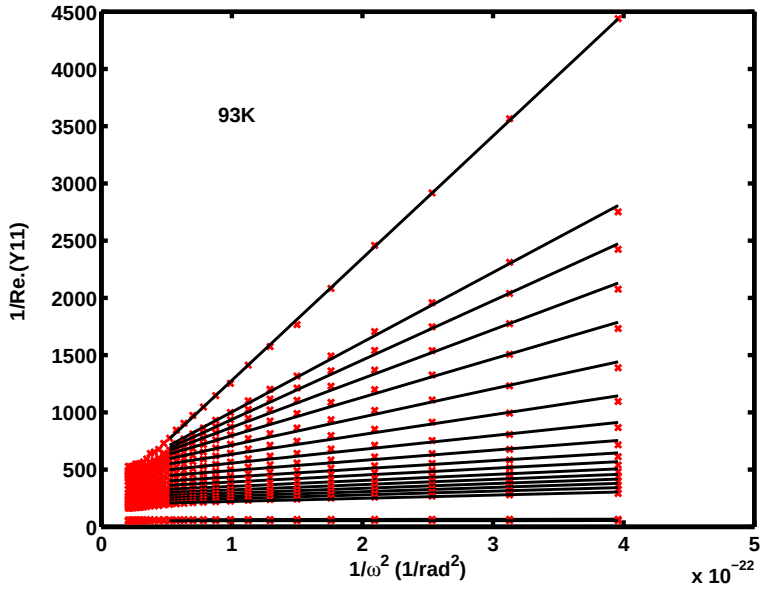

Figure 6.14: Extraction of $r_e + r_b$ at 93 K by fitting the high-frequency portion of $1/\Re(Y_{11})$-ω^{-2}.

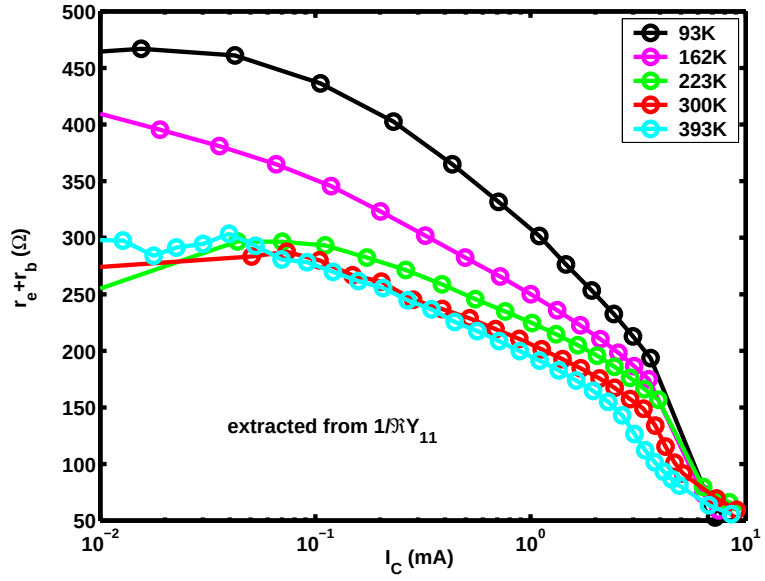

Figure 6.15: Extracted $r_e + r_b$-I_C from 43-393 K by fitting the high-frequency portion of $1/\Re(Y_{11})$-ω^{-2}.

Another popular technique to extract small signal base resistance r_b is to use the input impedance with a shorted output, which by definition is equal to h_{11}.

$$\begin{aligned} h_{11} &= r_e + \frac{1}{\frac{1}{r_b} + j\omega C_{bv}} + \frac{1}{g_{be} + j\omega C_{\pi}}, \\ &= \left(r_e + r_b + \frac{g_{be}}{g_{be}^2 + \omega^2 C_{\pi}^2} \right) - j\omega \left(\frac{C_{\pi}}{g_{be}^2 + \omega^2 C_{\pi}^2} \right), C_{\pi} = C_{be} + C_{bc}. \end{aligned} \tag{6.15}$$

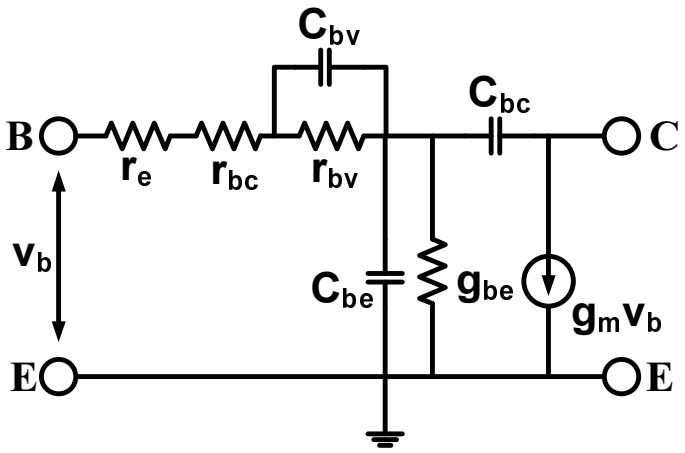

Figure 6.16: Equivalent circuit used in extraction of r_b using circuit impedance method.

The $(\Re(h_{11}), \Im(h_{11}))$ ordered pairs at different frequencies form a semicircle on the complex impedance plane. The $(\Re(h_{11}), \Im(h_{11}))$ impedance point moves clockwise with increasing frequency. the center of this circle is $x_0 = r_b + r_e + \frac{1}{2g_{be}}$, the radius is $r = \frac{1}{2g_{be}}$. This circle is shown as the dotted circle in Fig. 6.17.

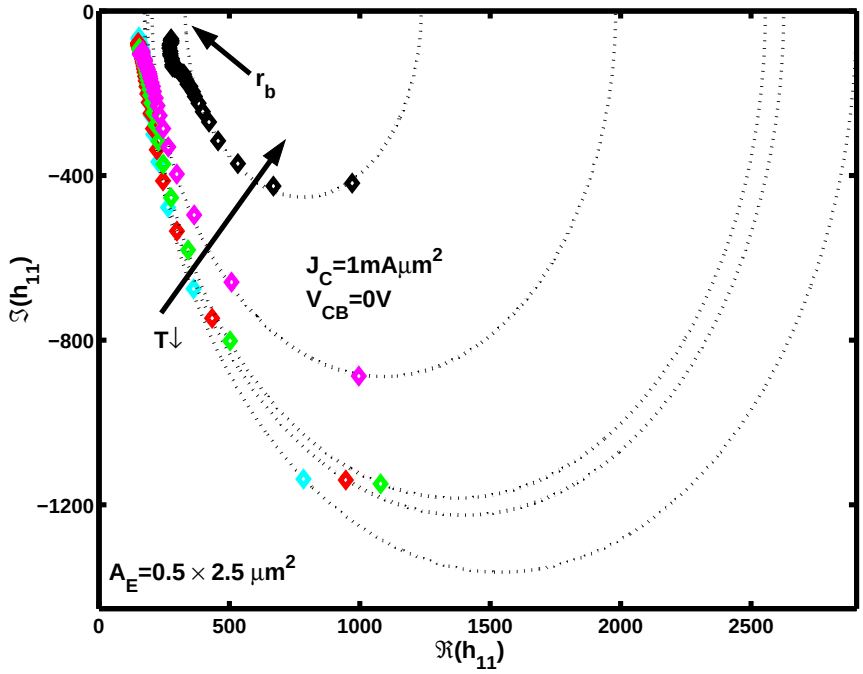

Figure 6.17: Extracted of r_b using the circle impedance method from 300-93 K, $J_C = 1mA/\mu m^2$.

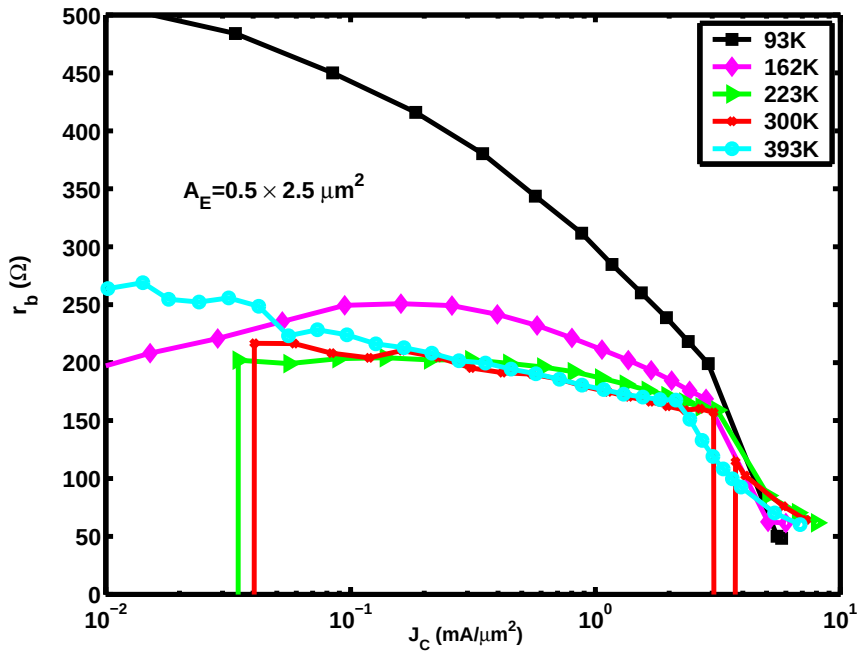

Figure 6.18: Extracted r_b-J_C using half-circle method from 300-93 K.

6.8 Collector resistance

Similarly to R_E-flyback measurement, if the emitter and collector are interchanged to operate in a common-collector configuration with zero emitter current, the extrinsic collector resistance R_{Cc} can be obtained by taking the derivative of V_{CES} with regard to I_C:

$$R_{Cc} = \frac{\partial V_{CES}}{\partial I_C}. \tag{6.16}$$

Fig. 6.19 illustrates the derivation of the measured V_{CES} with regard to the I_C in the R_C flyback measurement. The increasing of R_C with increasing I_C at 93 K and 43 K may due to self-heating effect. Therefore, the accuracy of the extracted R_C at low temperature are in doubt.

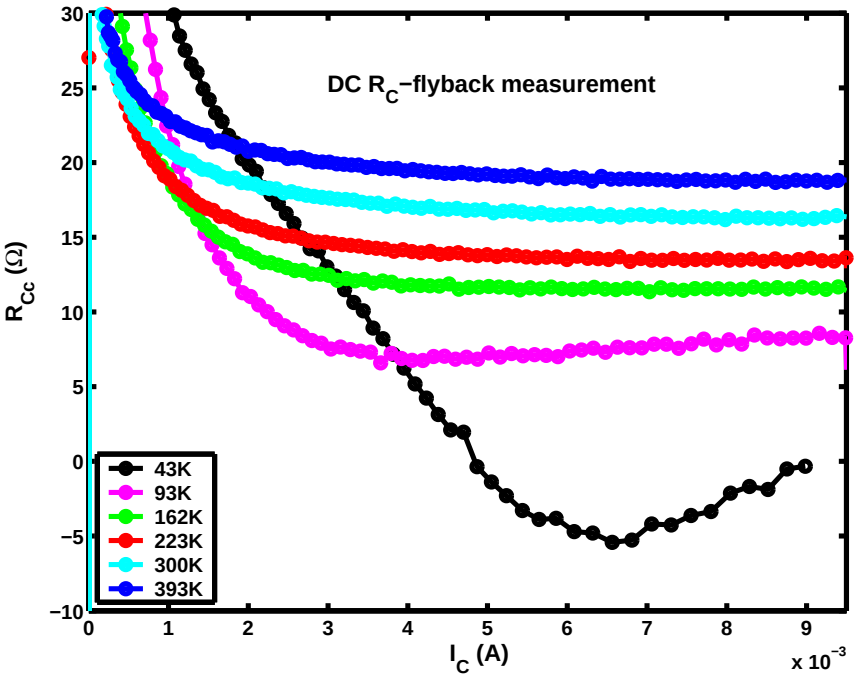

Figure 6.19: Derivation of the measured V_{CES} w.r.t the I_C in the R_C flyback measurement for the R_C extraction.

6.9 Thermal resistance

Accurate information of device junction temperature is of importance in predicting the device performance. For Mextram's default extraction method, R_{TH} is extracted from V_{BE}-V_{CE} relation of output characteristics. However, in this way, R_{TH}'s extraction relies on the accuracy of base resistance and emitter resistance, which are also challenges at low temperatures.

Thermal resistance can be extracted from the relation between the power dissipation P_{diss} and the junction temperature T_{junc}, for which a temperature-sensitive electrical parameter (TSEP) is utilized in order to link the two parameters experimentally [81]. Here, base-emitter voltage V_{BE} is used as TSEP. The first step is biasing device with fixed emitter current I_E and collector-base voltage $V_{CB} = 0$ V, and then V_{BE} is measured for different substrate temperatures T_S swept around a center temperature (300 K, 223 K, 162 K and 93 K) with 10 K temperature step. Secondly, the device is biased with the same I_E with fixed substrate temperatures T_S (300 K, 223 K, 162 K and 93 K) and V_{BE} is measured for different power dissipation ($P_{diss} = I_C V_{CE} + I_B V_{VBE}$) with sweeping V_{CB}. The relation between T_S and P_{diss} can be extracted by eliminating V_{BE} from these two measurements. In our measurement, emitter current I_E is chose near peak f_T to represents the actual power range in practical operation of device. More details about this measurement setup can be found in [81].

Fig. 6.20 shows the junction temperature as a function of dissipated power over ambient temperature 93-300 K. The thermal resistance R_{TH} can be extracted by $T_{junc} = T_{amb} + R_{TH} P_{diss}$.

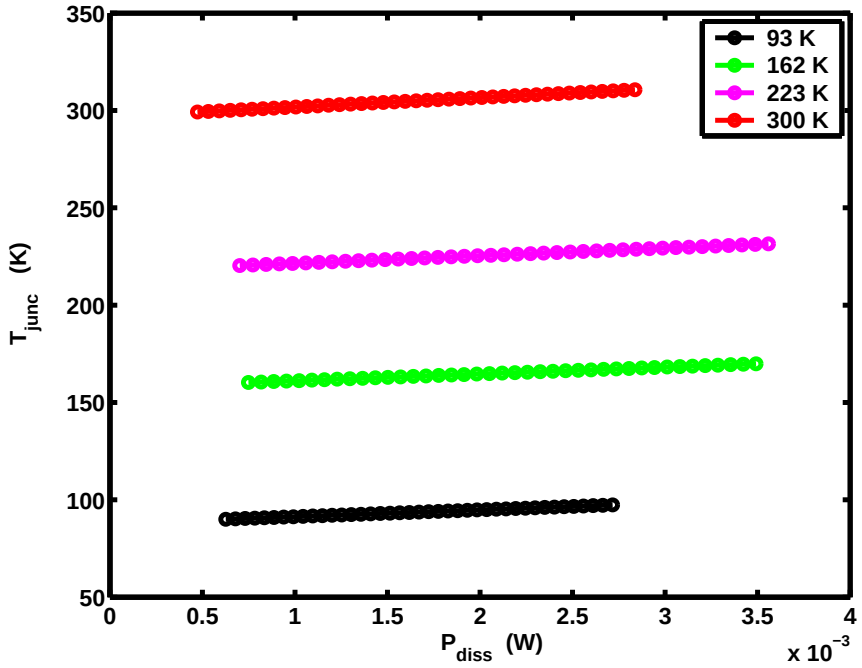

Figure 6.20: Measured junction temperature versus power dissipation over 93-300 K. The I_E is fixed near peak f_T

6.10 High current parameters

The initial values of high current parameters can be estimated from process information and layout geometries [4]. However, due to strong correlation between each other, the extraction of the high-current parameters is not as straightforward as that of the low current parameters. In Fig. 6.21-Fig. 6.25, we simulate the influences of I_K, R_{CV}, V_{DC}, I_{HC} and SCR_{CV} on output characteristic, f_T and current gain, respectively. In each simulation, we change only one high current parameter and fix others. Ambient temperature is 300 K and V_{CB}=0 V for current gain and f_T simulations. It can be seen that I_K affects both the output characteristic at high V_{CB}, f_T roll off and current gain roll off. The quasi-saturation parameters R_{CV}, V_{DC}, I_{HC} and SCR_{CV} affect output characteristic at low V_{CB}, f_T roll off and current gain roll off.

Basically, during parameter extraction, I_K can be extracted from forward-Gummel measurement (current gain measurement) or can be extracted from output characteristic at high V_{CE} alternatively, where quasi-saturation is of minor importance. R_{CV} and V_{DC} are strongly correlated. They can be extracted from current gain roll off region. The base transit time τ_b and emitter transit time τ_e can be extracted near peak f_T, as shown in Fig. 6.26.(a). In modern SiGe HBT technology, base transit time τ_b is dominant over emitter transit time τ_e in determining f_T because τ_e is reciprocally proportional to the *ac* current gain. This is particularly true at decreased temperatures since the current gain of SiGe HBT is enhanced with cooling. In this work, we fix emitter transit time τ_e=0 and hence it is far easier to tune τ_b only to fit peak f_T. Epilayer parameter τ_{epi} can be extracted from f_T roll off, as shown in Fig. 6.26.(b).

Several iterations between these high current parameters are inevitable. For example, knee current I_K needs to be repeated after R_{CV} and V_{DC} extraction because the collector current I_C has been changed.

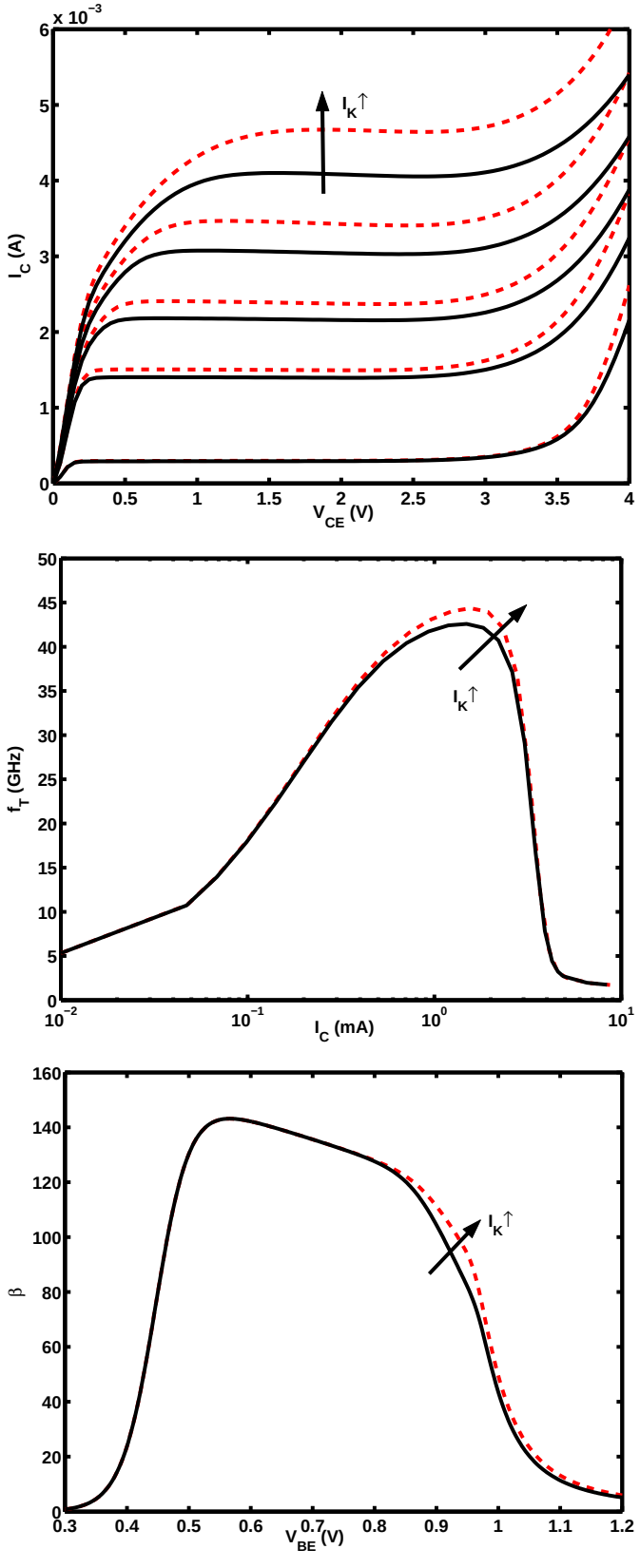

Figure 6.21: Impact of parameter I_K on: (a) Force-I_B output characteristics; (b) f_T-I_C; (c) β-V_{BE}.

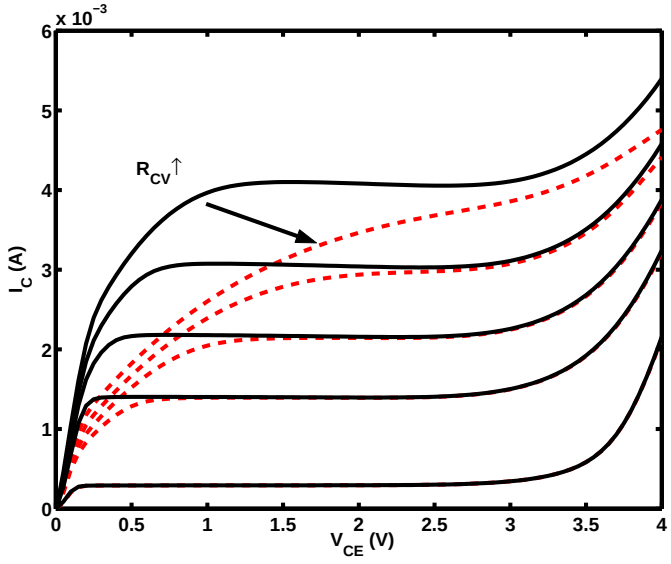

(a)

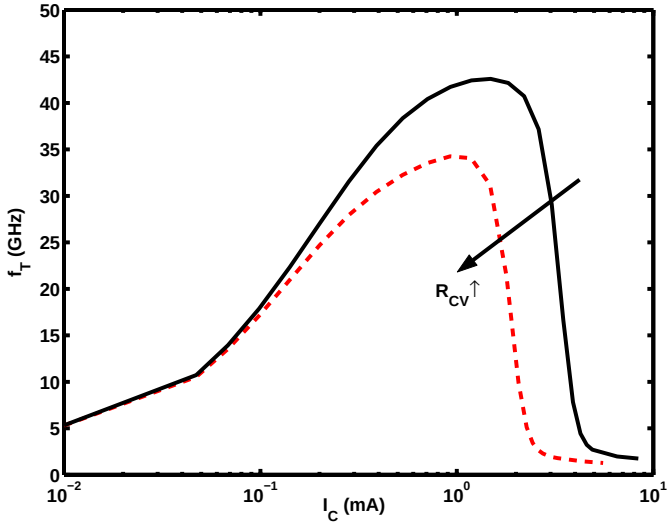

(b)

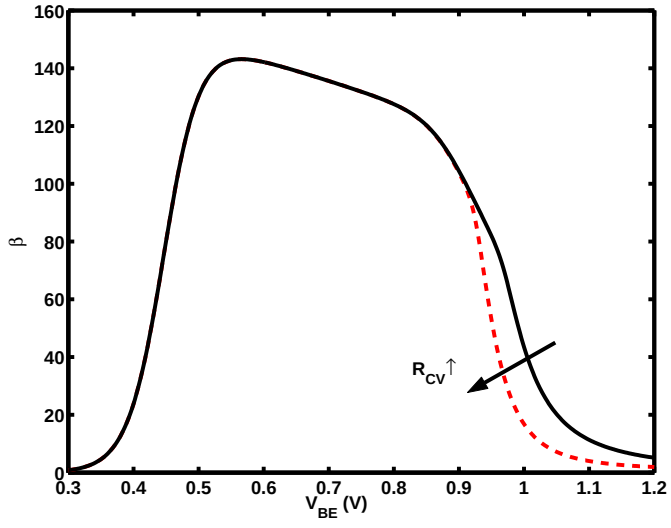

(c)

Figure 6.22: Impact of parameter R_{CV} on: (a) Force-I_B output characteristics; (b) f_T-I_C; (c) β-V_{BE}.

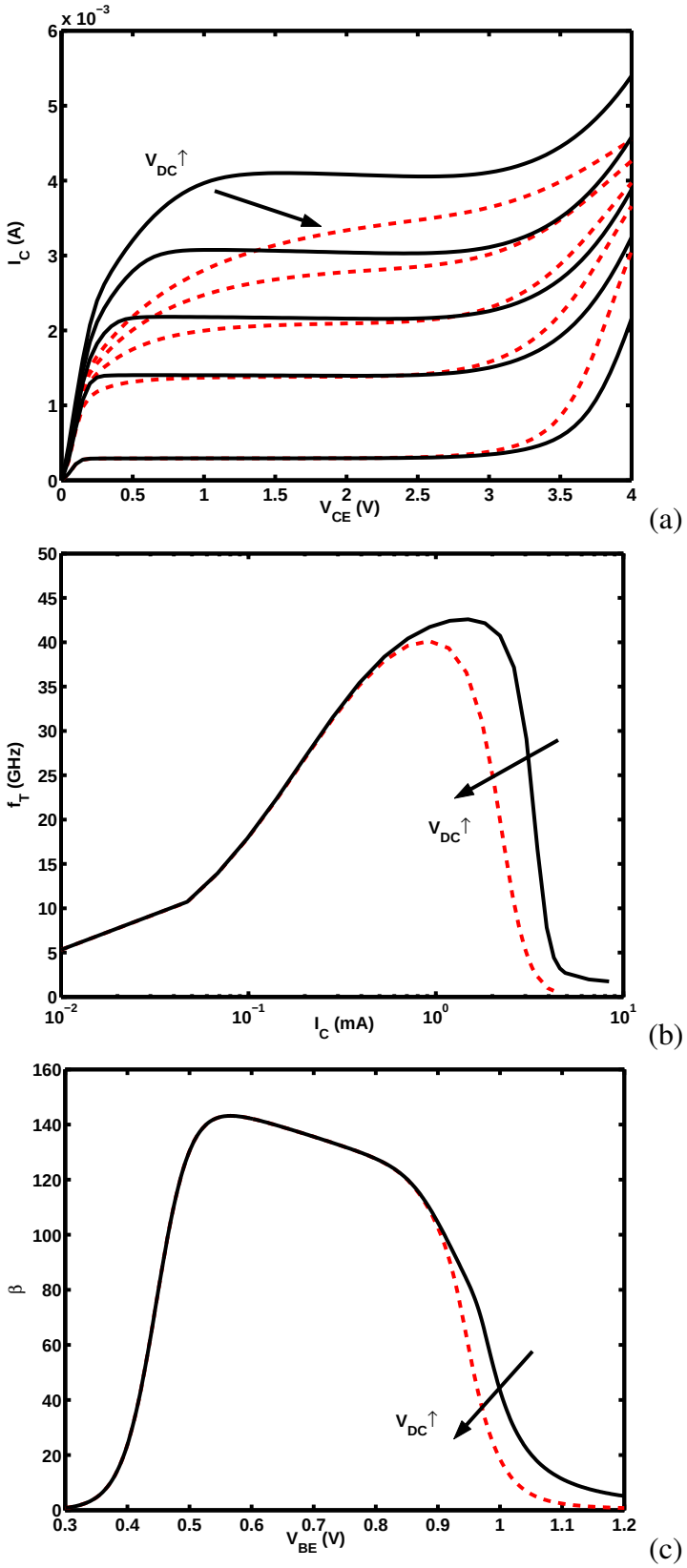

Figure 6.23: Impact of parameter V_{DC} on: (a) Force-I_B output characteristics; (b) f_T-I_C; (c) β-V_{BE}.

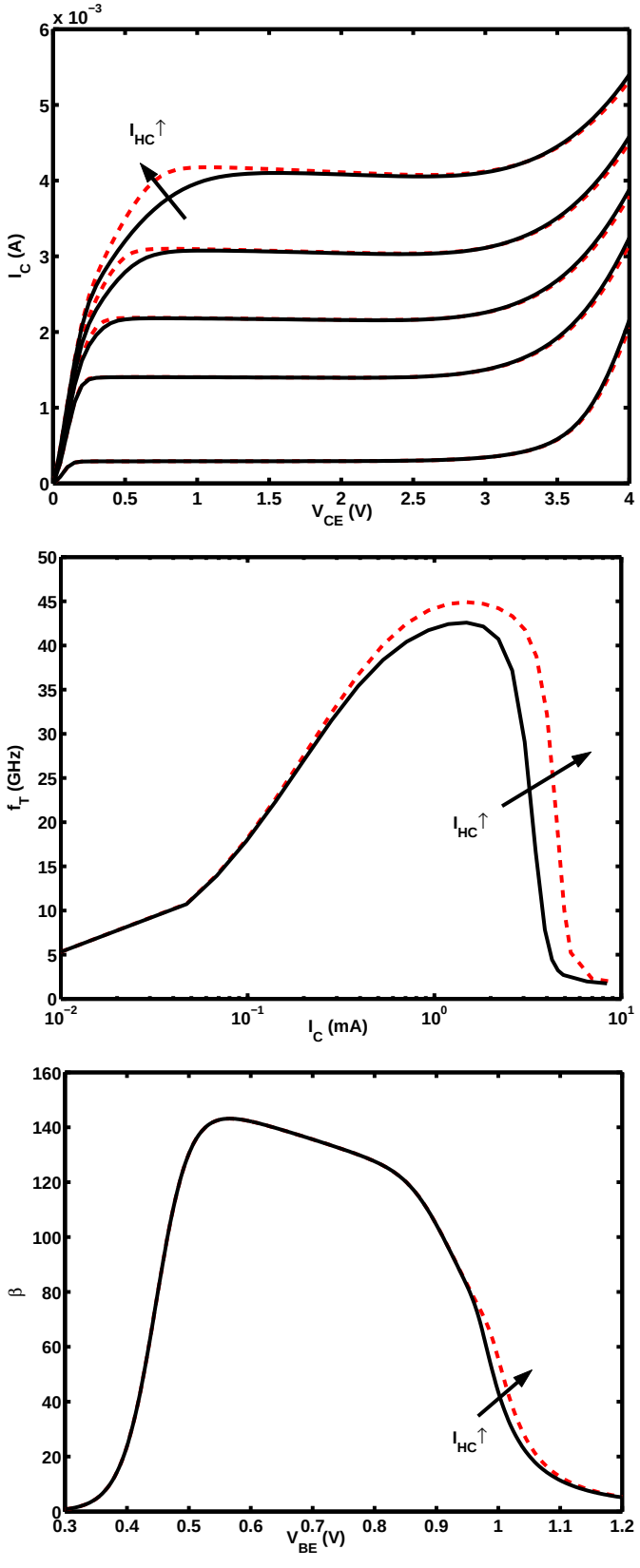

Figure 6.24: Impact of parameter I_{HC} on: (a) Force-I_B output characteristics; (b) f_T-I_C; (c) β-V_{BE}.

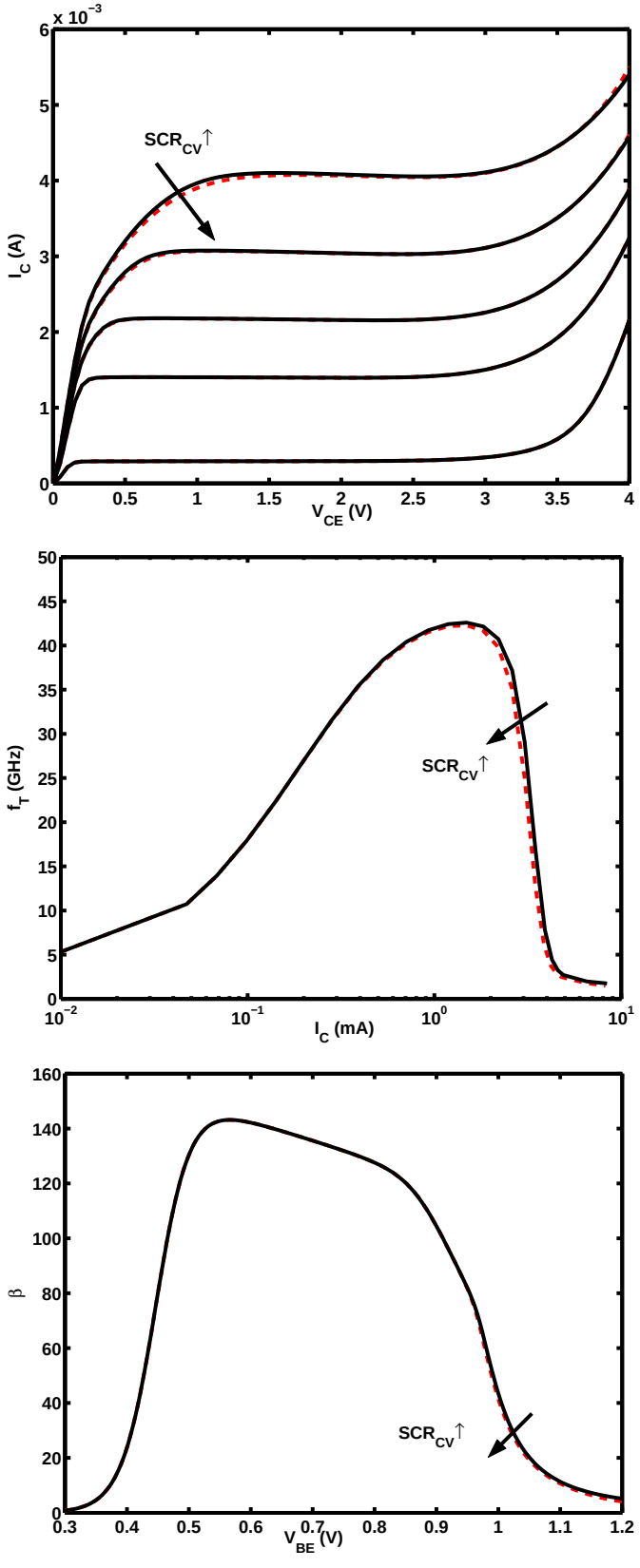

Figure 6.25: Impact of parameter SCR_{CV} on: (a) Force-I_B output characteristics; (b) f_T-I_C; (c) β-V_{BE}.

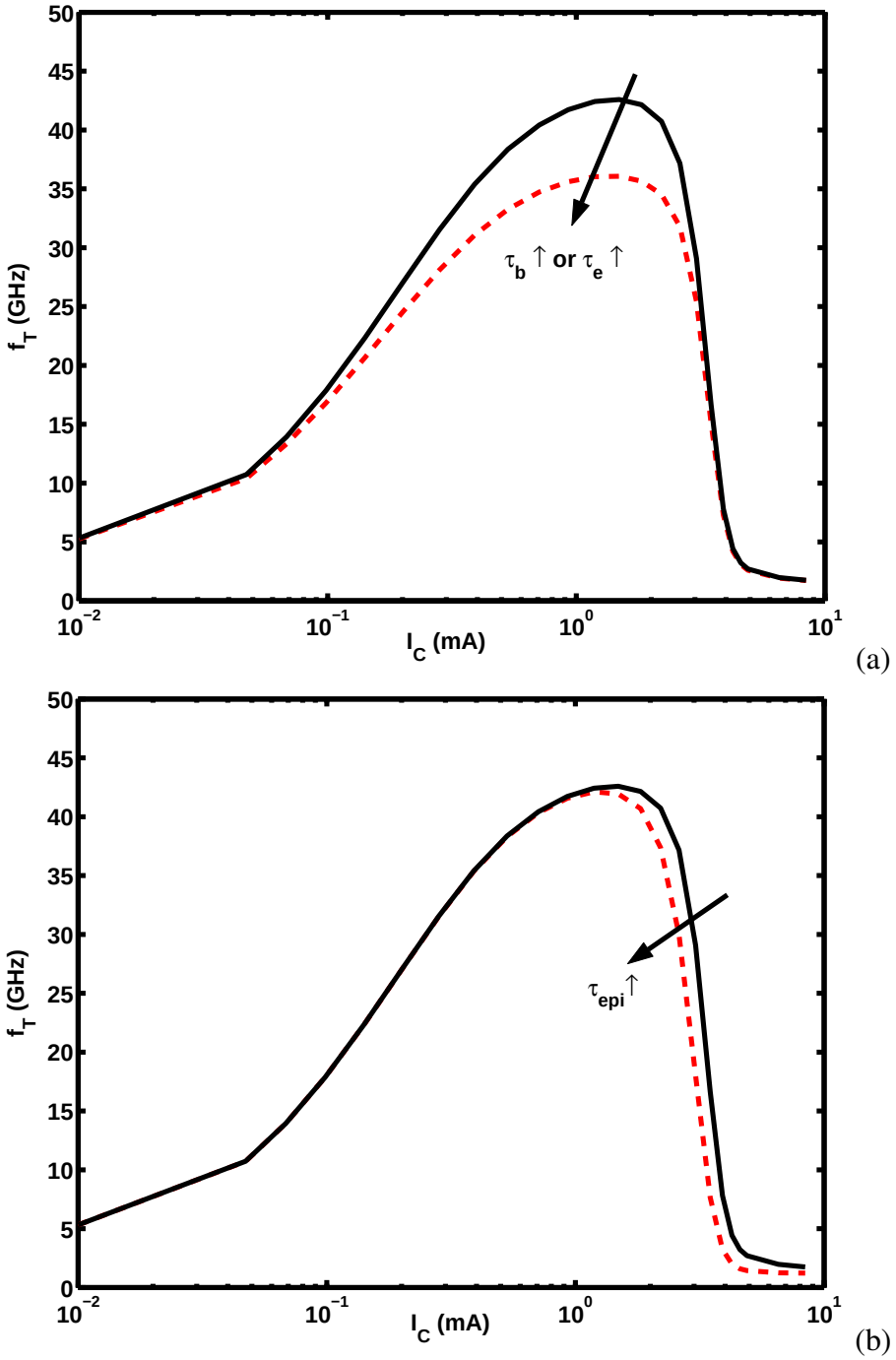

Figure 6.26: (a) Impact of parameter τ_b and τ_e on f_T-I_C; (b) Impact of parameter τ_{epi} on f_T-I_C.

6.11 Temperature parameter extraction

The initial parameters can be obtained by using the parameter extraction methods discussed in previous sections.

Fig. 6.27 shows the extracted and modeled I_S and N_F of collector current as functions of temperature. Fig. 6.28 shows the extracted and modeled I_{BEI} and N_{EI} of "ideal" forward base current I_B-V_{BE} as functions of temperature. Fig. 6.29 is the extracted zero bias C_{jE}-T from Fig. 6.4. The measurement data of base-emitter depletion capacitance C_{BE} are not very reasonable and a weak temperature-dependent fitted line is used in our modeling. Fig. 6.30 is the extracted zero bias C_{jC}-T from Fig. 6.5. Fig. 6.31 is the extracted forward and reverse Early voltages.

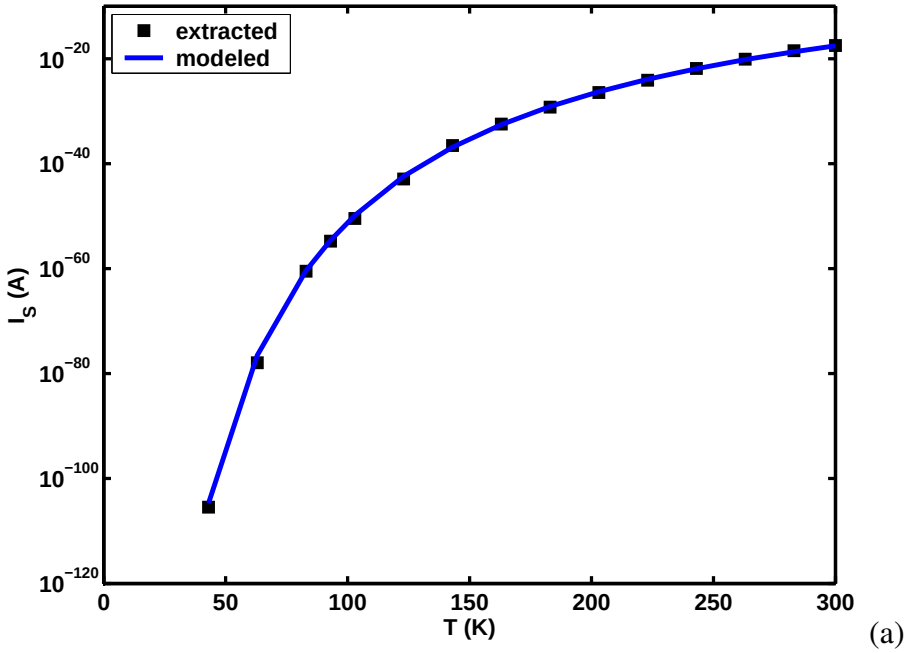

(a)

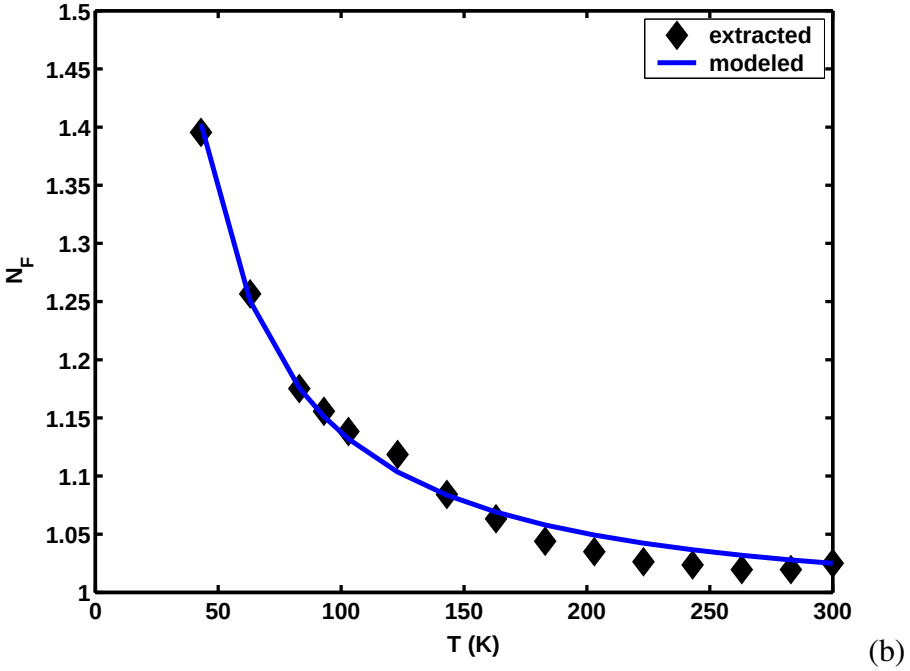

(b)

Figure 6.27: (a) Extracted and modeled I_S for collector current as a function of temperature; (b) Extracted and modeled N_F for collector current as a function of temperature.

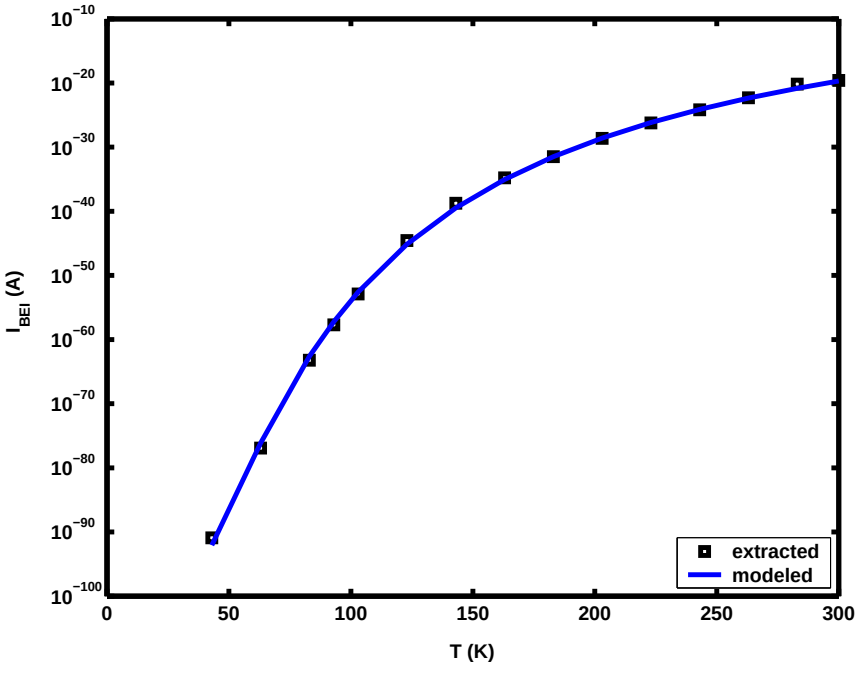

(a)

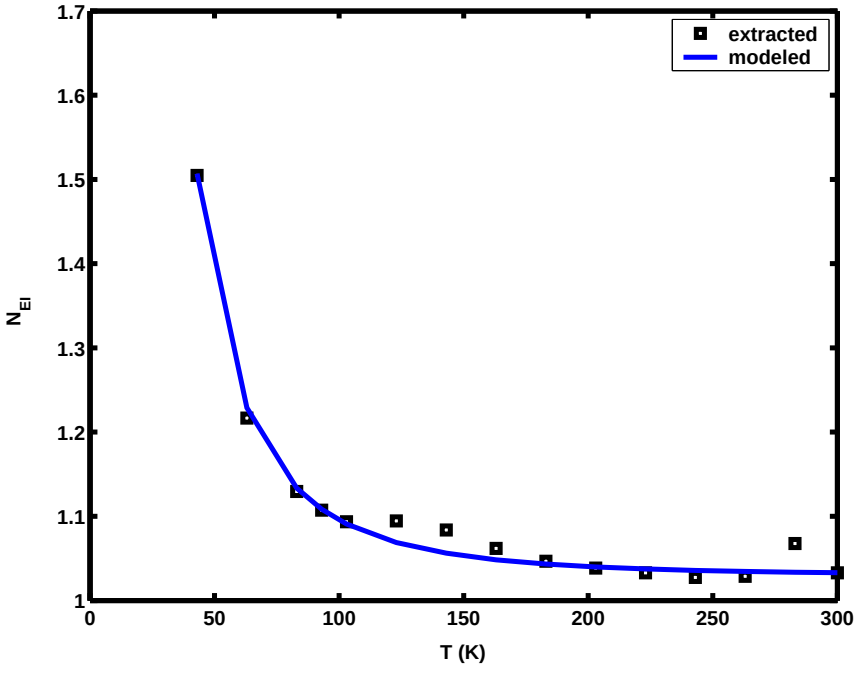

(b)

Figure 6.28: (a) Extracted and modeled I_{BEI} for base current as a function of temperature; (b) Extracted and modeled N_{EI} for base current as a function of temperature.

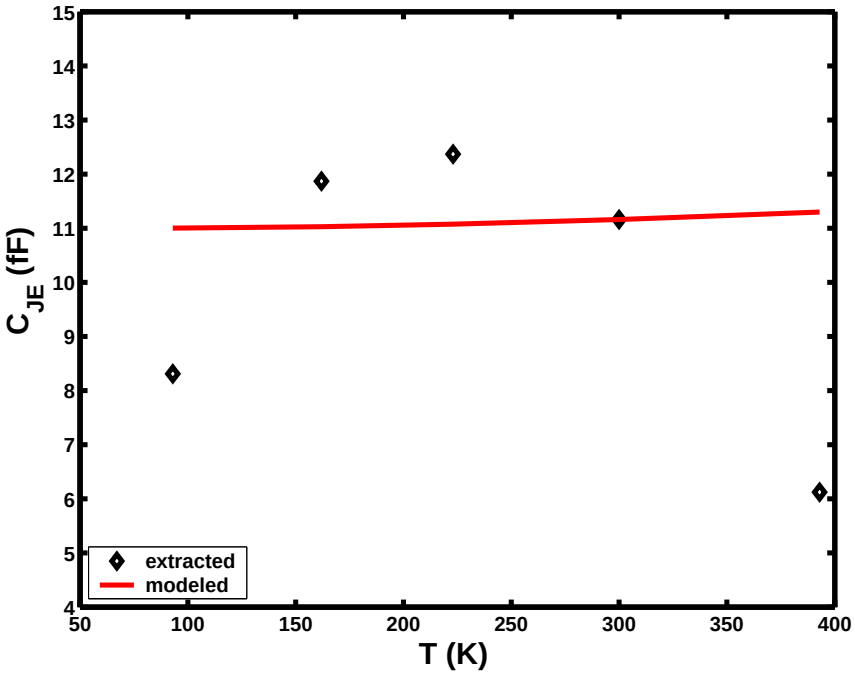

Figure 6.29: Extracted and modeled C_{JE}-T.

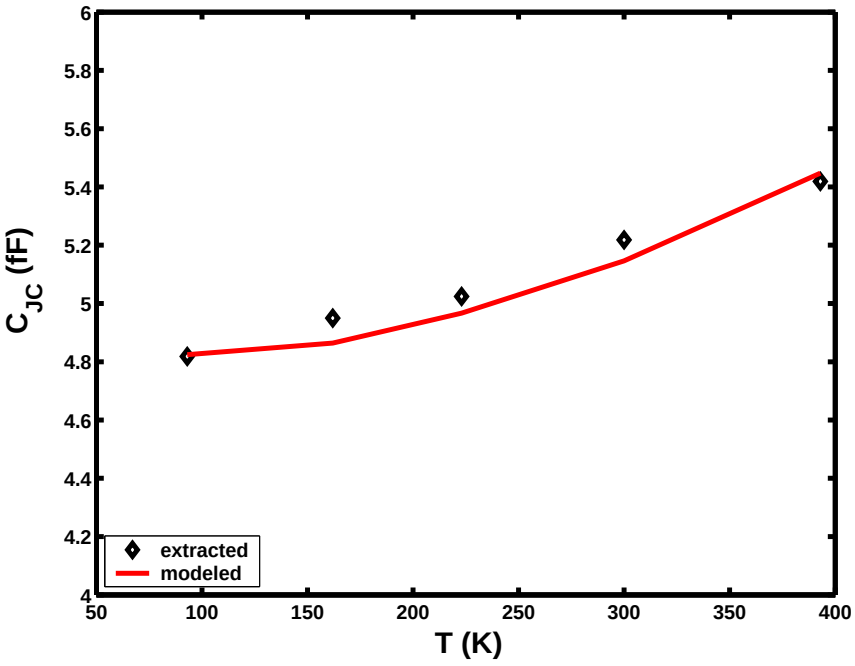

Figure 6.30: Extracted and modeled C_{JC}-T.

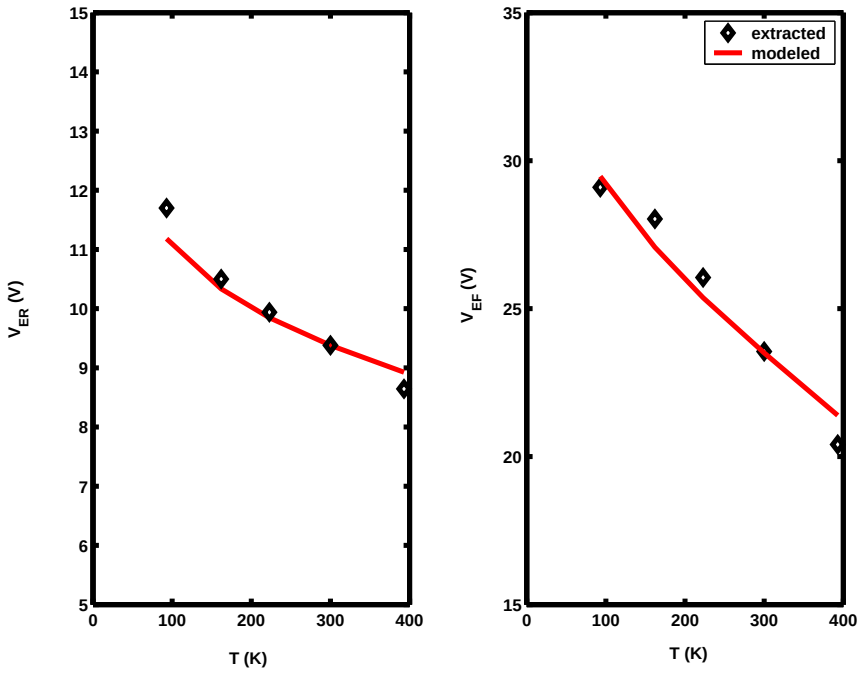

Figure 6.31: Extracted and modeled Early voltage V_{ER} and V_{EF} from 93-393 K.

Although the initial values of parasitic resistances can be obtained from specific *dc* and *ac* measurements we discussed, due to their coupling with high current parameters near and above peak f_T, in order to achieve good fitting of frequency dependence, the parasitic resistances need to be tuned in the last step together with high current parameters, as shown in Fig. 6.1.

Fig. 6.32 and Fig. 6.33 are the measured and modeled frequency dependence of Y_{11} and Y_{21} at 300K. Four bias conditions are chosen near peak f_T. Here, by changing the R_{BC} by 25%, the difference of simulated Y_{11} and Y_{21} can be found at high frequencies. Similar comparison of changing R_{BV} and R_E by 25% can be found in Fig. 6.34-Fig. 6.37.

Fig. 6.38-Fig. 6.41 are the extracted parasitic resistances as function of temperature.

Fig. 6.42 shows measured and modeled thermal resistance R_{TH} versus ambient temperature T_{amb} on a log-log scale. Current R_{TH} T-scaling equation can only model the linear portion, so a 3rd order polynomial is used.

Fig. 6.43-Fig. 6.48 show the extracted high current parameters, I_K, R_{CV}, V_{DC}, I_{HC}, τ_B and τ_{epi}.

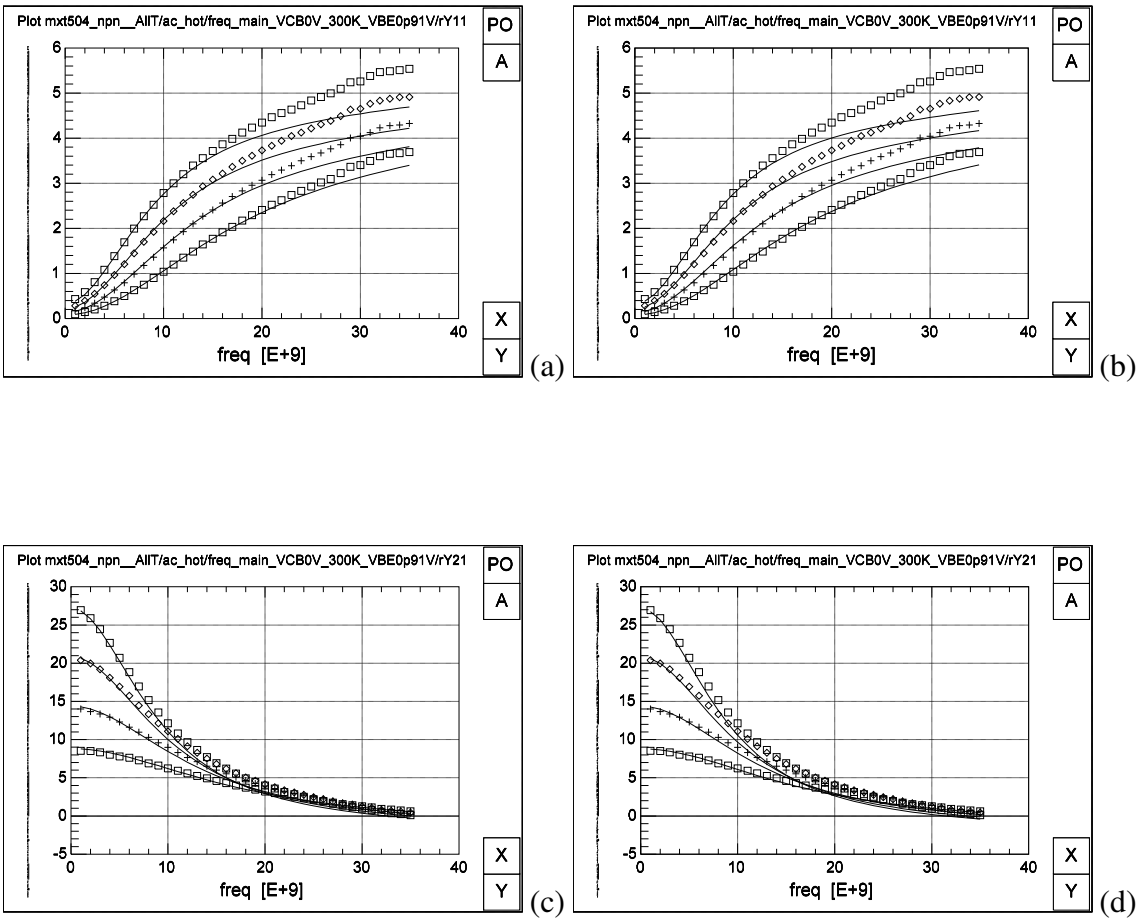

Figure 6.32: Measured (symbols) and modeled (lines) frequency dependence of real part y-parameters at 300K. Four bias conditions are chosen near peak f_T: (a) real part Y_{11}, R_{BC}=28 Ω; (b) real part Y_{11}, R_{BC}=34 Ω; (c) real part Y_{21}, R_{BC}=28 Ω; (d) real part Y_{21}, R_{BC}=34 Ω.

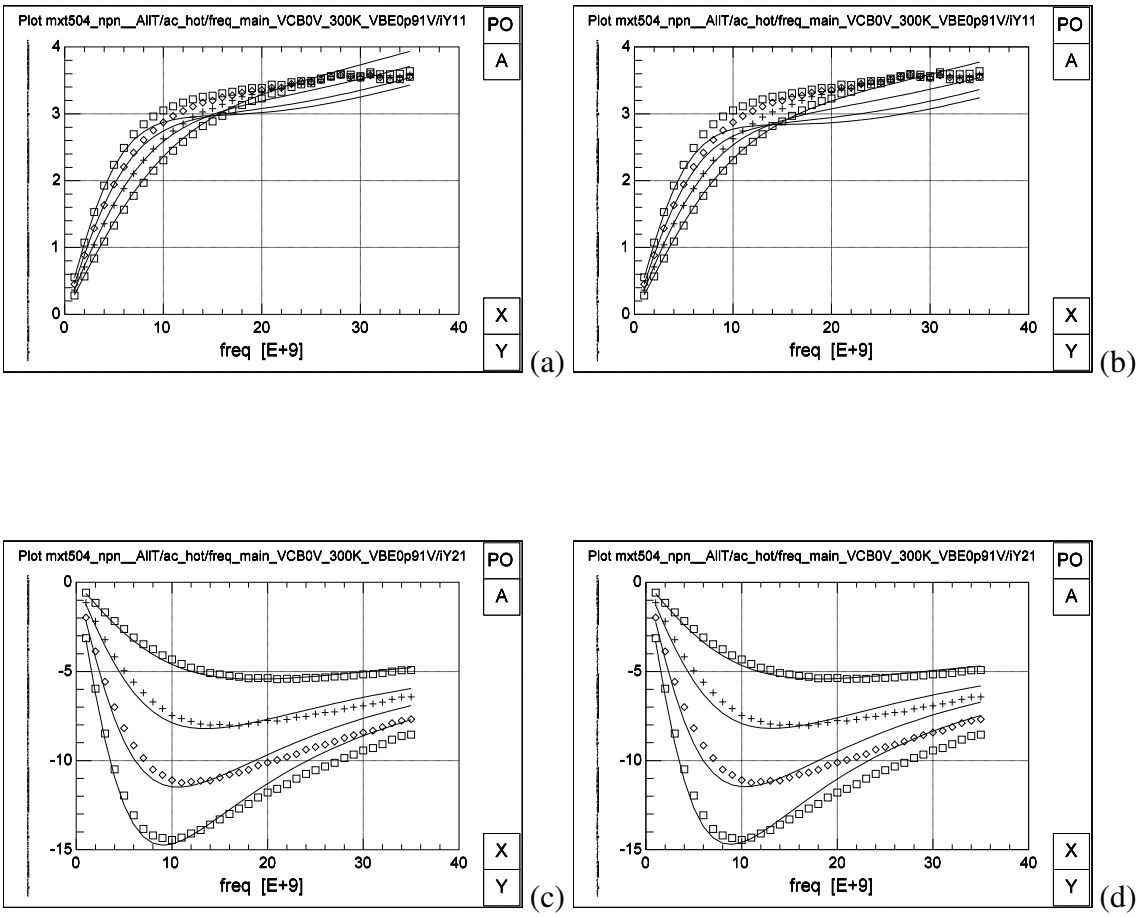

Figure 6.33: Measured (symbols) and modeled (lines) frequency dependence of imaginary part y-parameters at 300K. Four bias conditions are chosen near peak f_T: (a) imaginary part Y_{11}, R_{BC}=28 Ω; (b) imaginary part Y_{11}, R_{BC}=34 Ω; (c) imaginary part Y_{21}, R_{BC}=28 Ω; (d) imaginary part Y_{21}, R_{BC}=34 Ω.

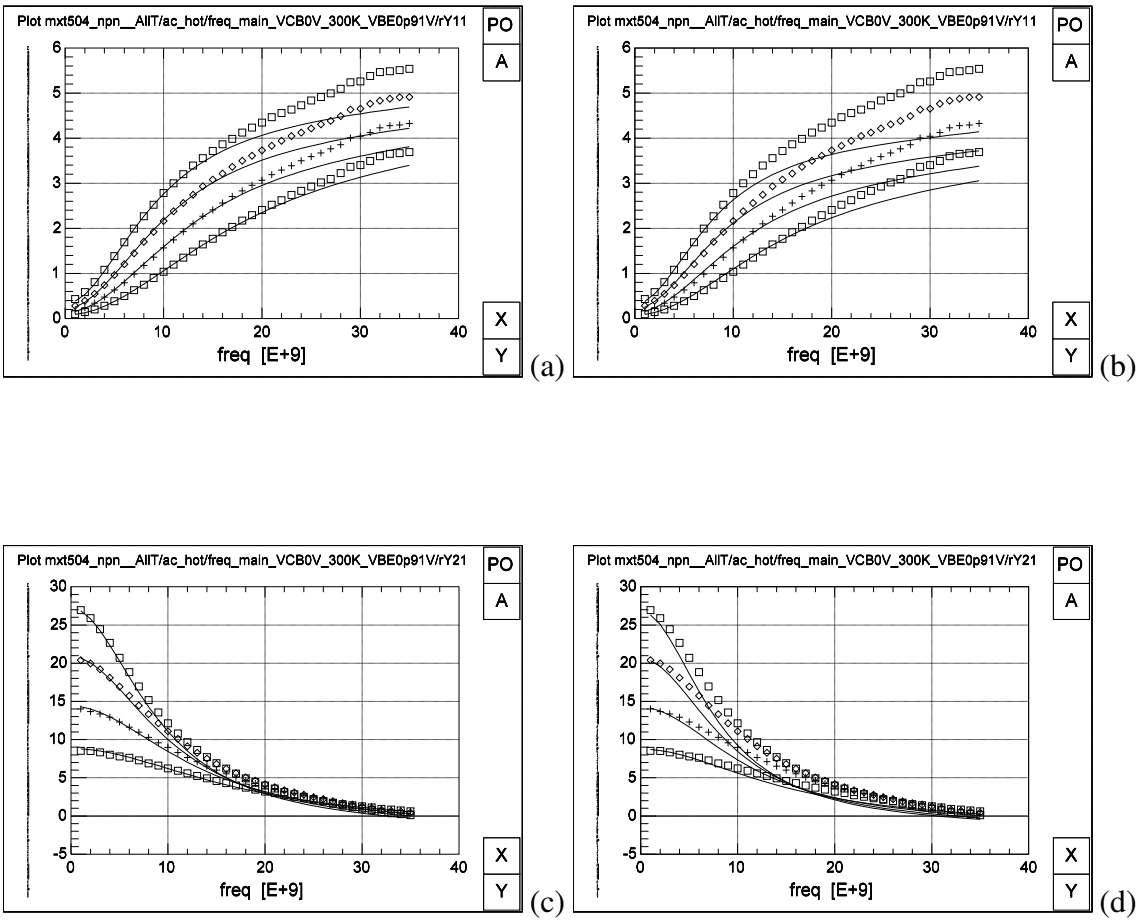

Figure 6.34: Measured (symbols) and modeled (lines) frequency dependence of real part y-parameters at 300K. Four bias conditions are chosen near peak f_T: (a) real part Y_{11}, R_{BV}=288 Ω; (b) real part Y_{11}, R_{BV}=348 Ω; (c) real part Y_{21}, R_{BV}=288 Ω; (d) real part Y_{21}, R_{BV}=348 Ω.

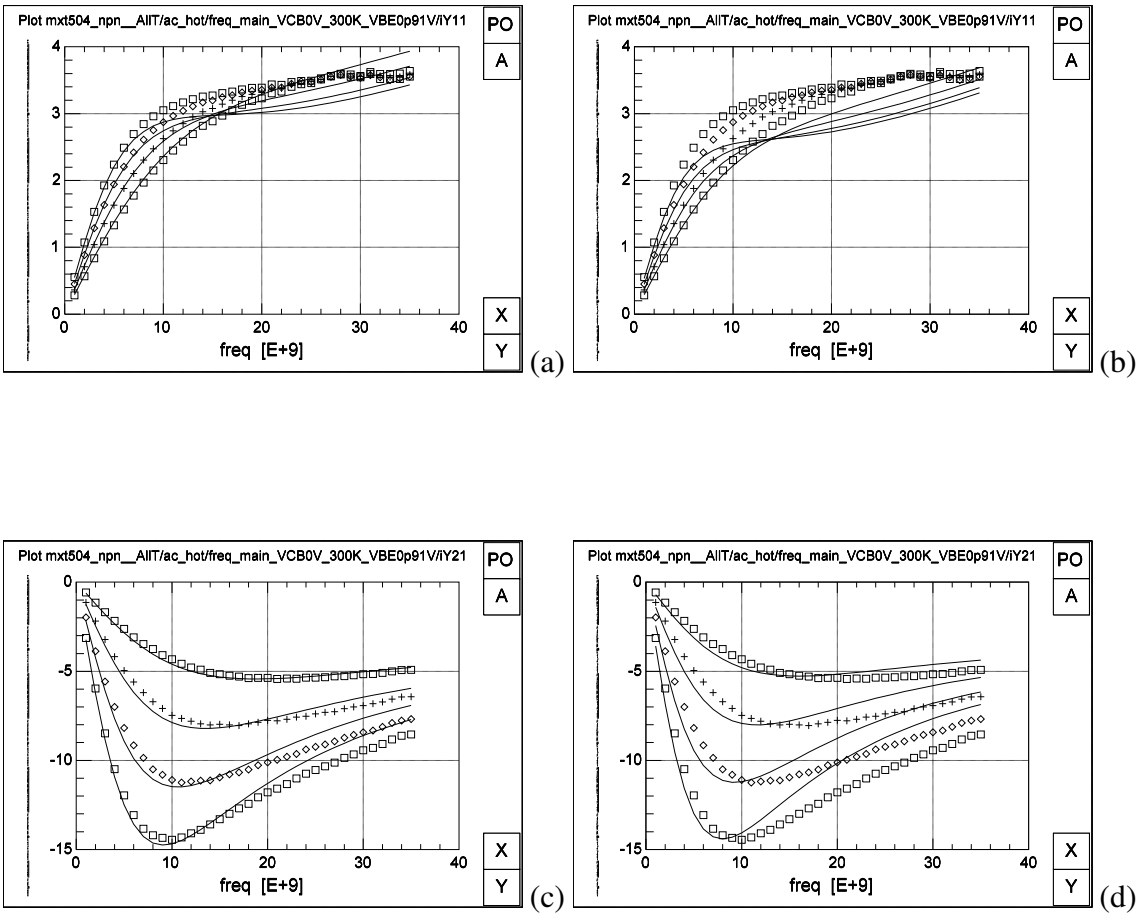

Figure 6.35: Measured (symbols) and modeled (lines) frequency dependence of imaginary part y-parameters at 300. Four bias conditions are chosen near peak f_TK: (a) imaginary part Y_{11}, R_{BV}=288 Ω; (b) imaginary part Y_{11}, R_{BV}=348 Ω; (c) imaginary part Y_{21}, R_{BV}=288 Ω; (d) imaginary part Y_{21}, R_{BV}=348 Ω.

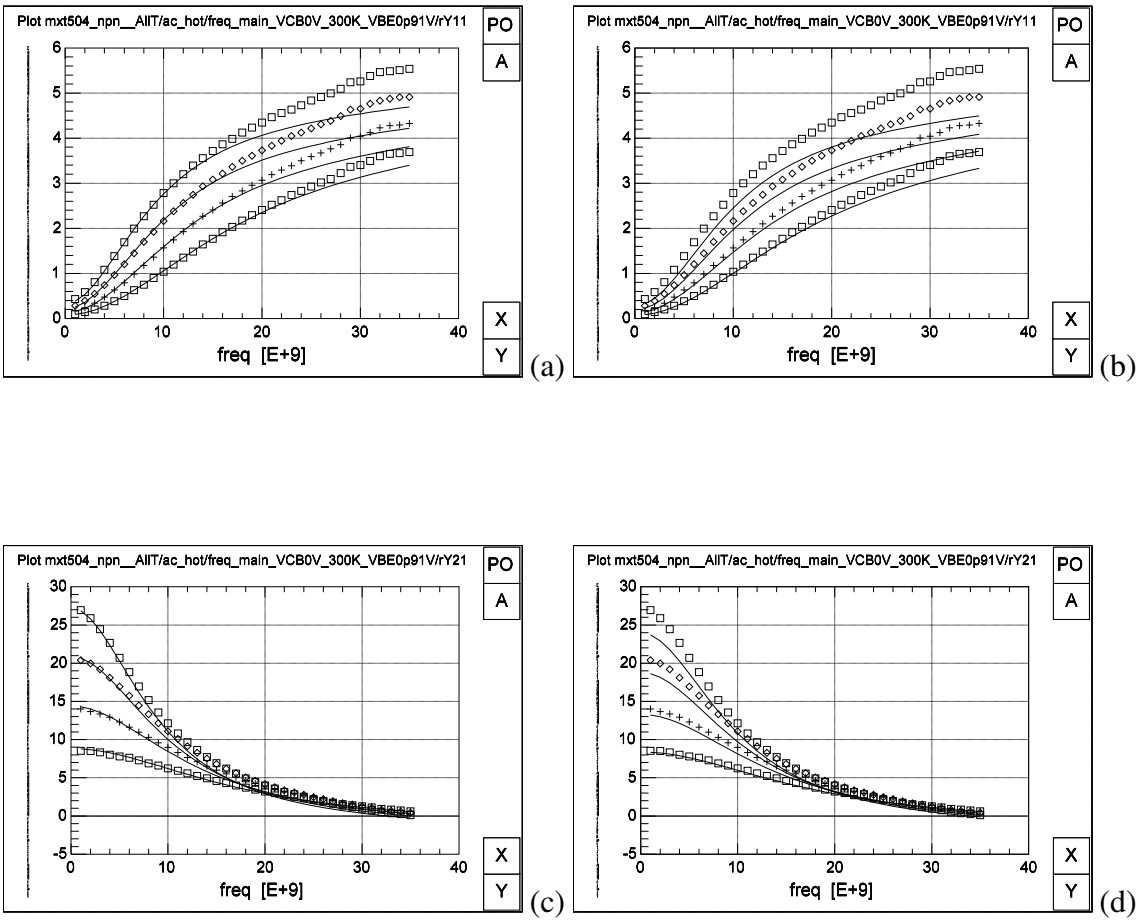

Figure 6.36: Measured (symbols) and modeled (lines) frequency dependence of real part y-parameters at 300K. Four bias conditions are chosen near peak f_T: (a) real part Y_{11}, R_E=12 Ω; (b) real part Y_{11}, R_E=15 Ω; (c) real part Y_{21}, R_E=12 Ω; (d) real part Y_{21}, R_E=15 Ω.

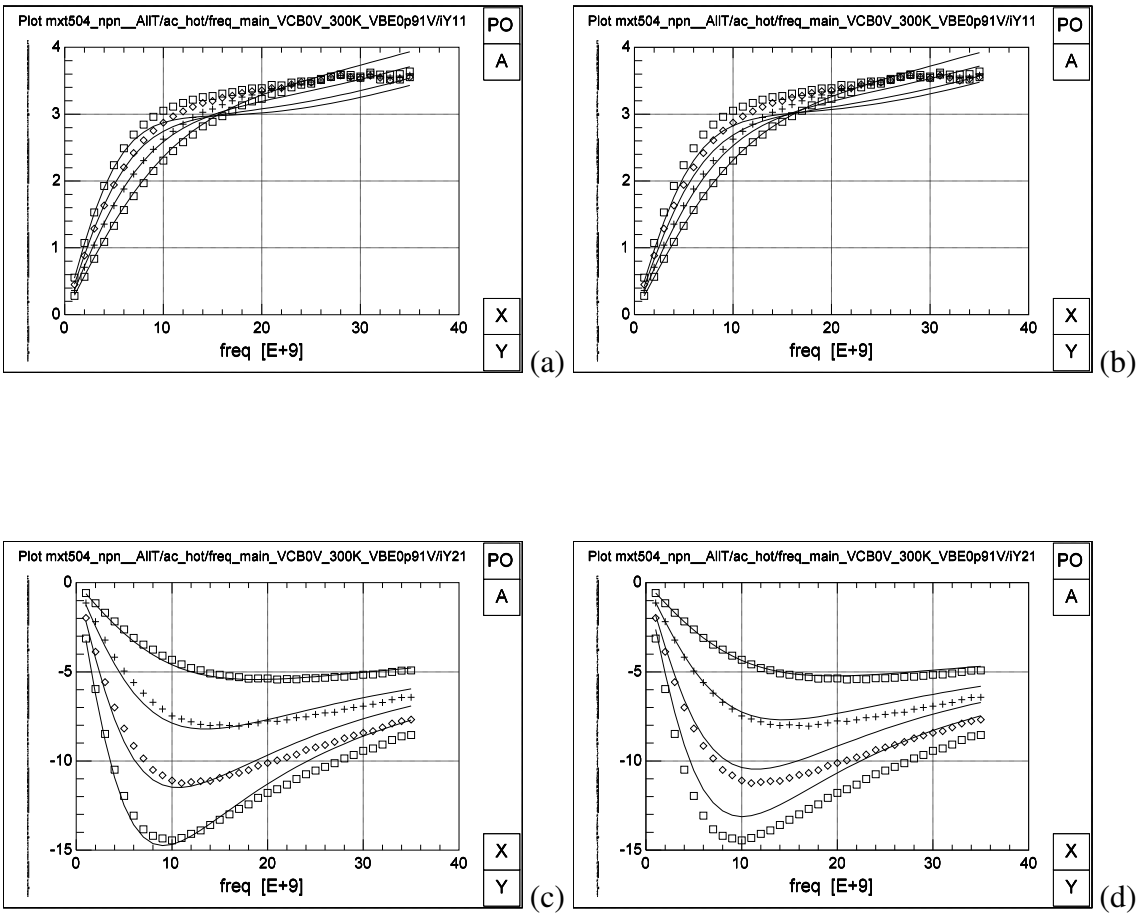

Figure 6.37: Measured (symbols) and modeled (lines) frequency dependence of imaginary part y-parameters at 300K. Four bias conditions are chosen near peak f_T: (a) imaginary part Y_{11}, R_E=12 Ω; (b) imaginary part Y_{11}, R_E=15 Ω; (c) imaginary part Y_{21}, R_E=12 Ω; (d) imaginary part Y_{21}, R_E=15 Ω.

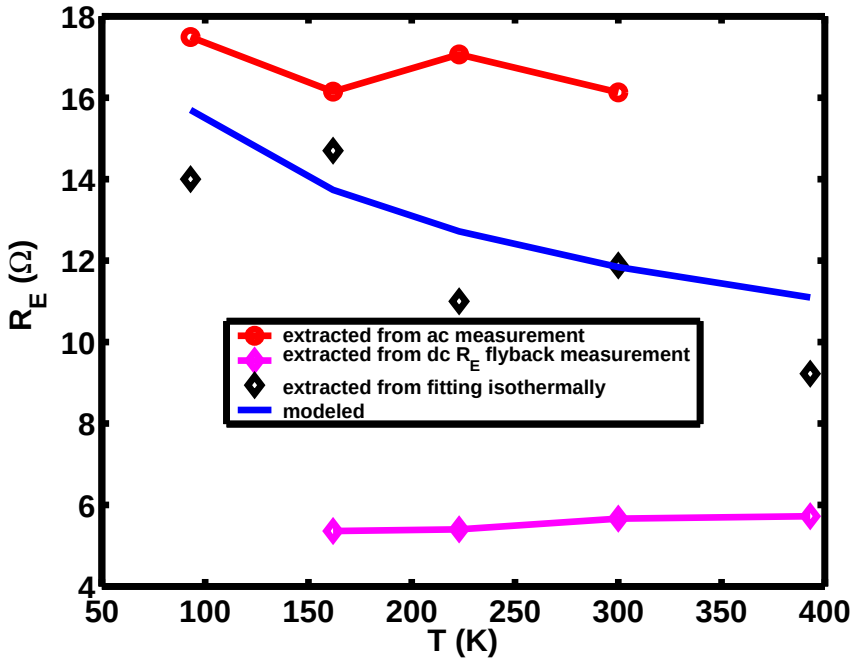

Figure 6.38: Extracted and modeled R_E-T.

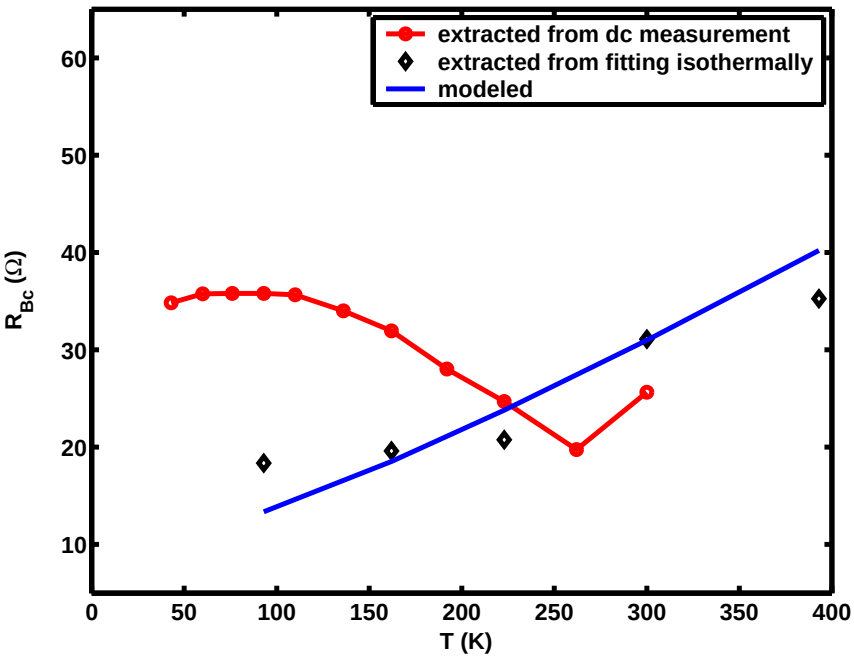

Figure 6.39: Extracted and modeled R_{Bc}-T.

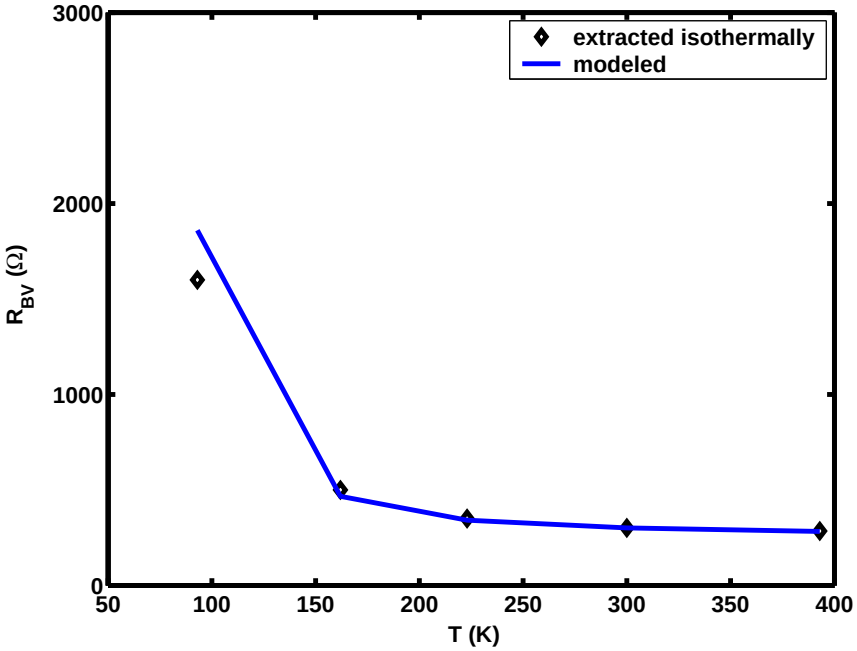

Figure 6.40: Extracted and modeled R_{BV} from 93-300 K.

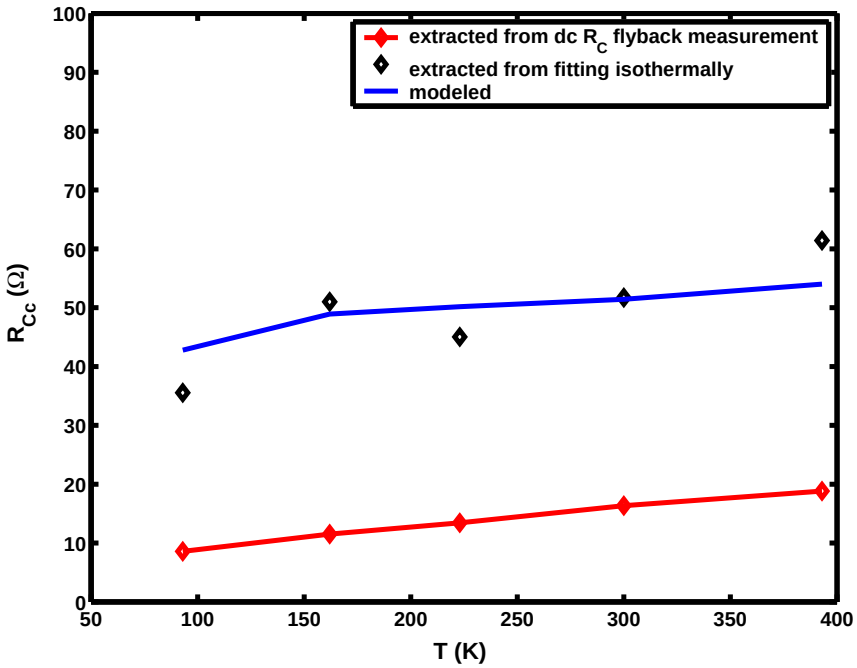

Figure 6.41: Extracted and modeled R_{Cc}-T.

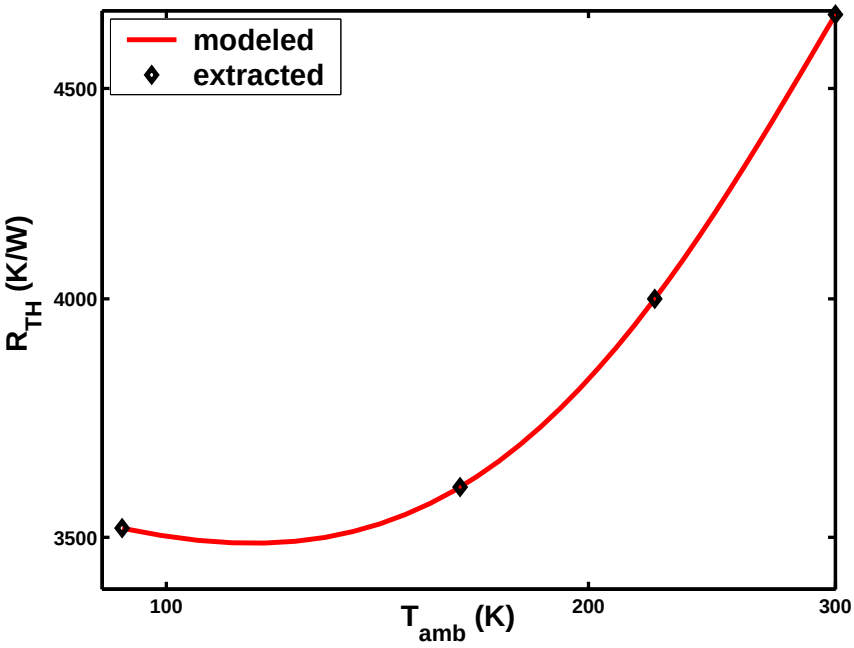

Figure 6.42: Extracted and modeled thermal resistance R_{TH} from 93-300 K.

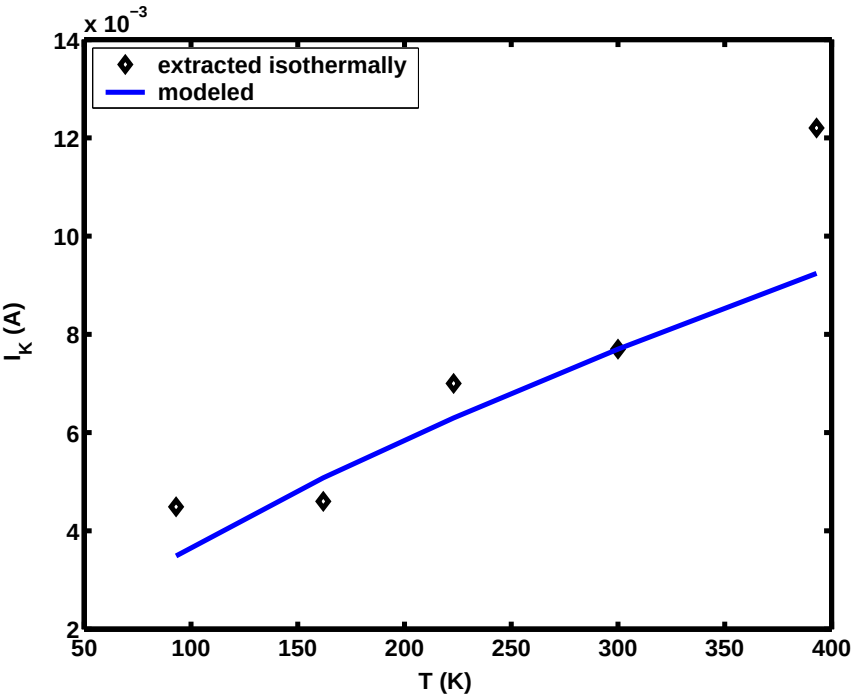

Figure 6.43: Extracted and modeled I_K from 93-300 K.

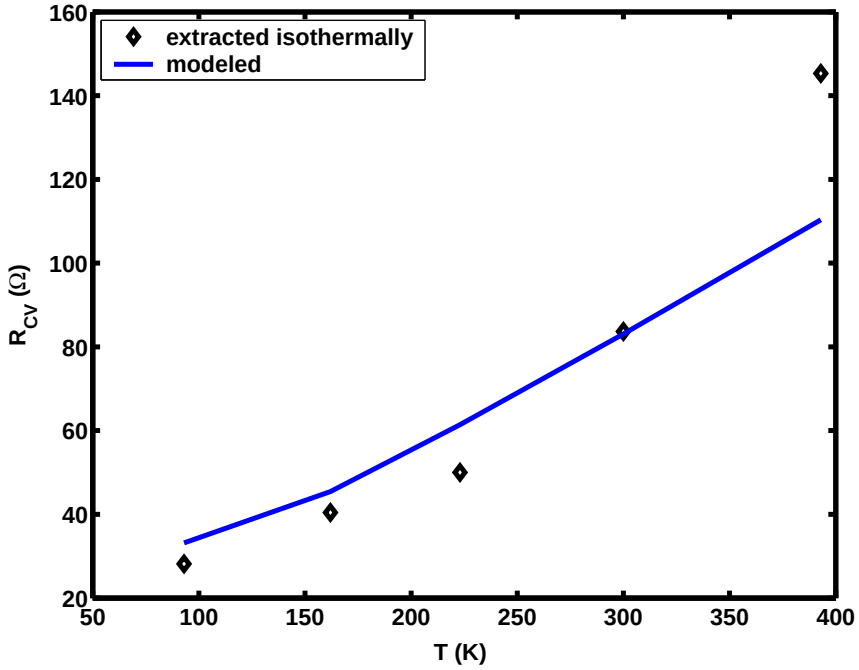

Figure 6.44: Extracted and modeled R_{CV} from 93-300 K.

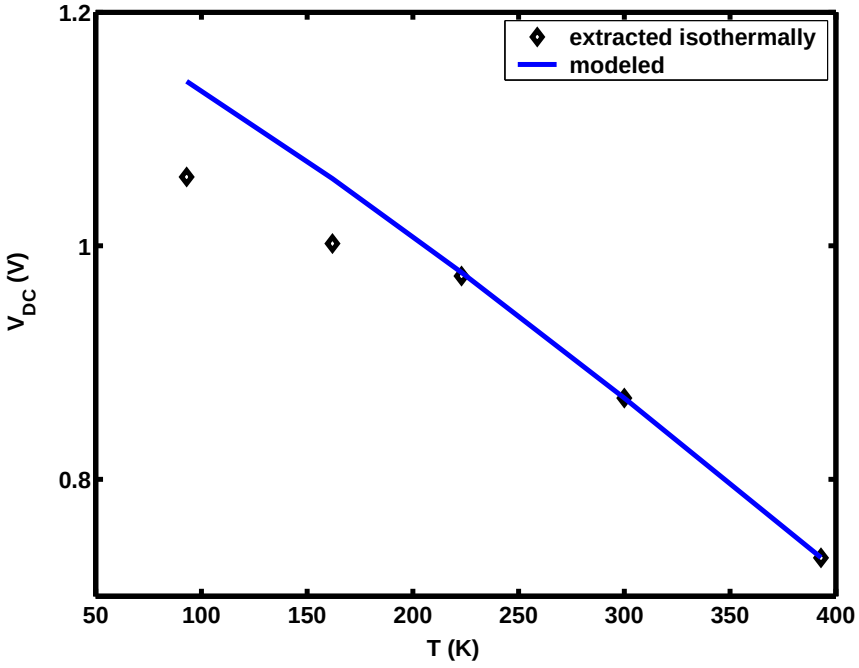

Figure 6.45: Extracted and modeled V_{DC} from 93-300 K.

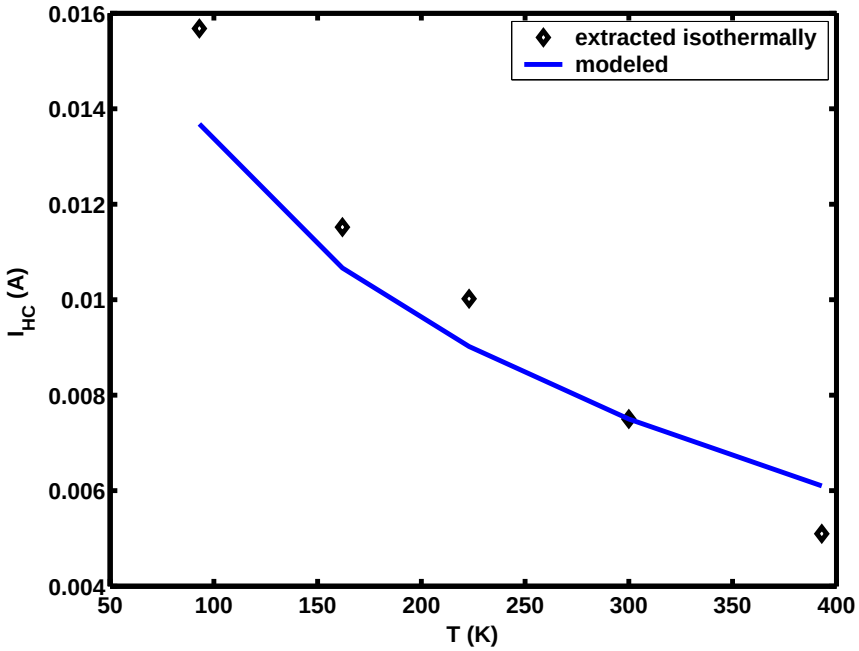

Figure 6.46: Extracted and modeled I_{HC} from 93-300 K.

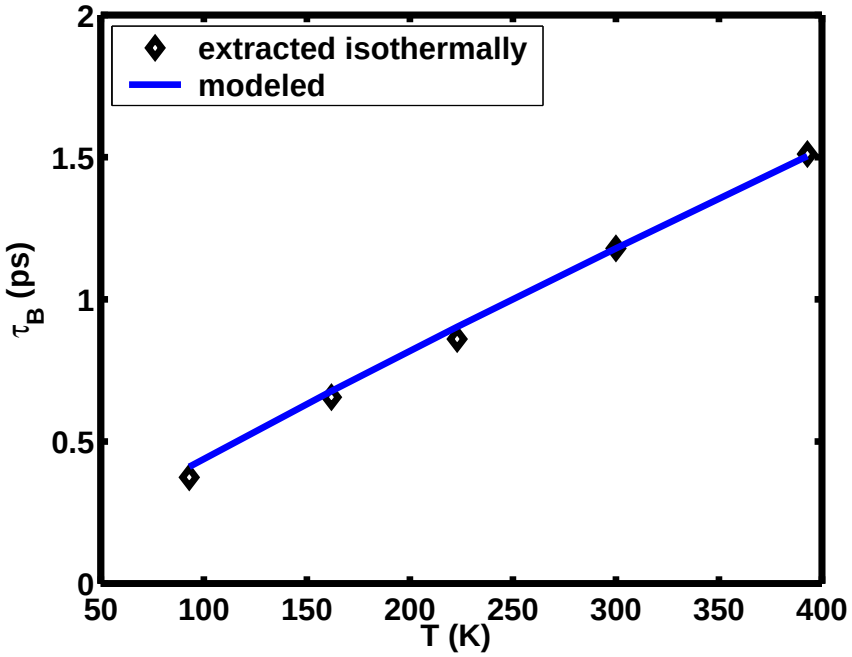

Figure 6.47: Extracted and modeled τ_B from 93-300 K.

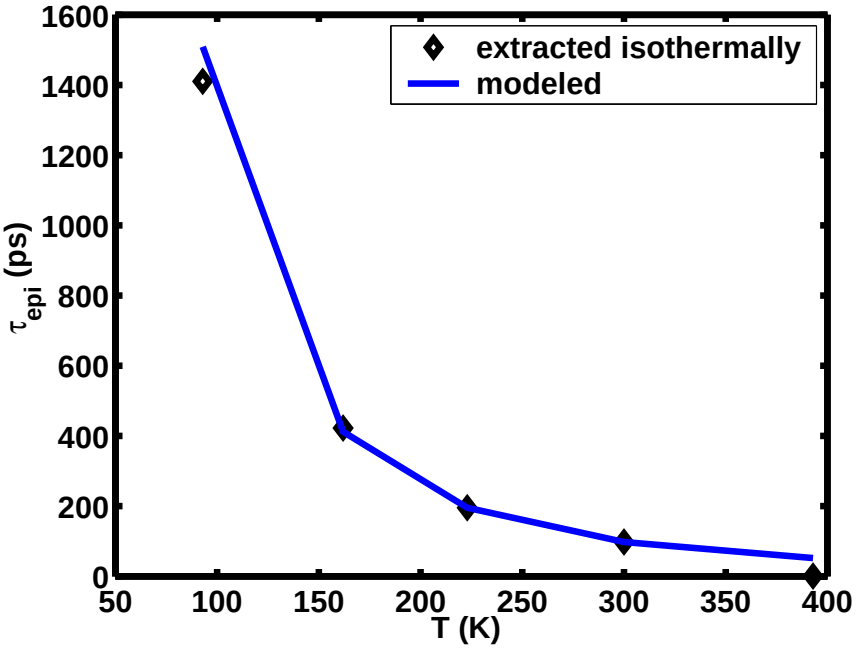

Figure 6.48: Extracted and modeled τ_{epi} from 93-300 K.

6.12 SiGe HBT compact modeling results

Fig. 6.49 (a)-(d) show the I_C-V_{BE} and I_B-V_{BE} modeling results from 43-393 K. For both I_C and I_B, the new saturation current and ideality factor scaling equations are essential for the good fitting in the medium current range, particularly below 100 K. Trap-assisted tunneling current is well modeled, as can be seen from Fig. 6.49 (d).

Fig. 6.50.(a) and Fig. 6.50.(b) show the measured and modeled I_C-V_{CE} and V_{BE}-V_{CE} for forced low I_B bias over 93-393 K respectively. Fig. 6.51.(a) and Fig. 6.51.(b) show the measured and modeled I_C-V_{CE} and V_{BE}-V_{CE} for forced high I_B bias over 93-393 K respectively.

Fig. 6.52 shows f_T-I_C from 93-393 K at $V_{CB} = 0, 1, 2V$. Fig. 6.53 shows the measured and modeled H_{21}-J_C and MUG-J_C at 5GHz from 93-393 K. Fig. 6.54 shows measured and modeled Y-parameters at 1,2,3 and 5 GHz for 162 K.

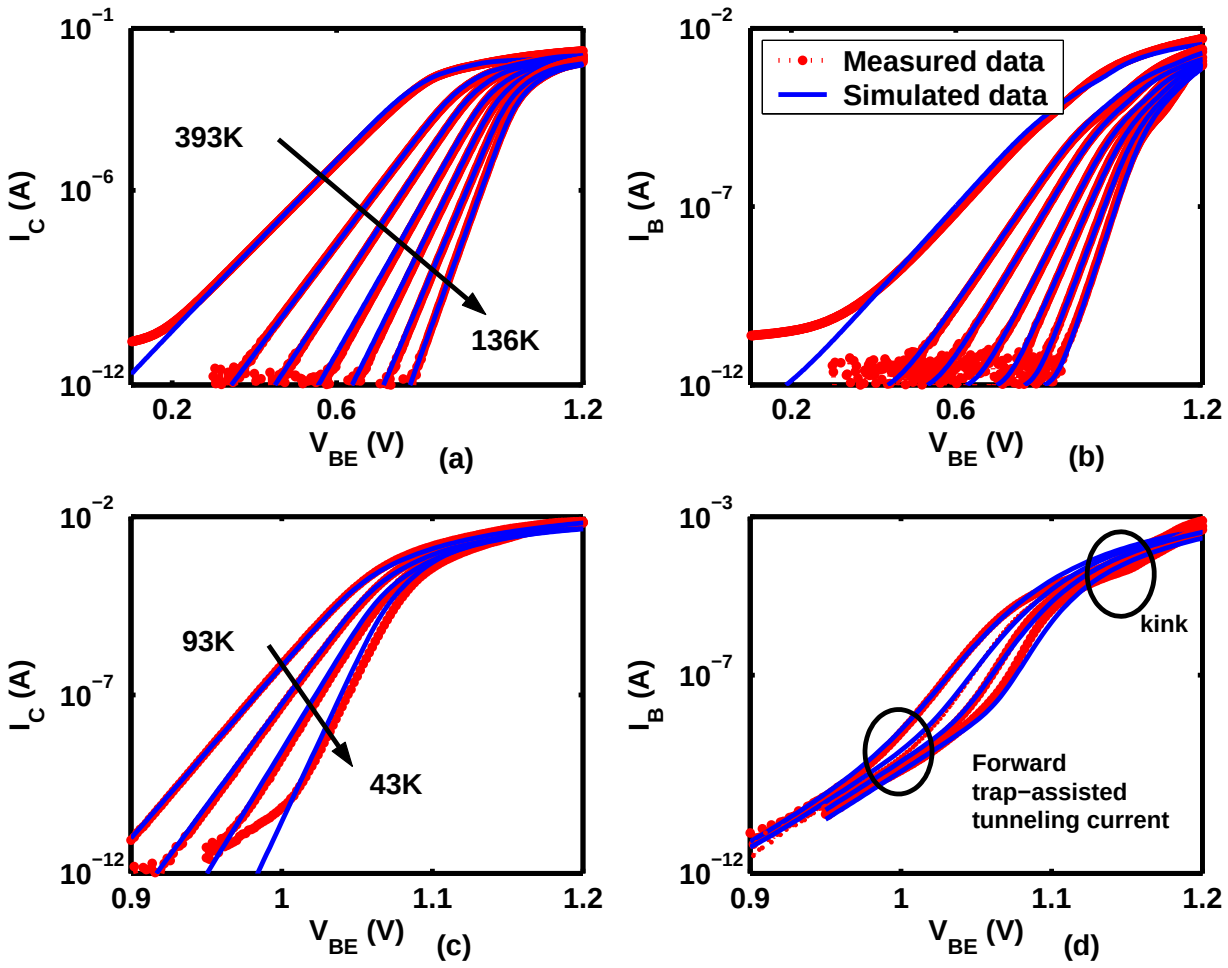

Figure 6.49: (a)Measured and modeled I_C-V_{BE} from 136-393 K. (b)Measured and modeled I_B-V_{BE} from 136-393 K. (c)Measured and modeled I_C-V_{BE} from 93-43 K. (d)Measured and modeled I_B-V_{BE} from 93-43 K.

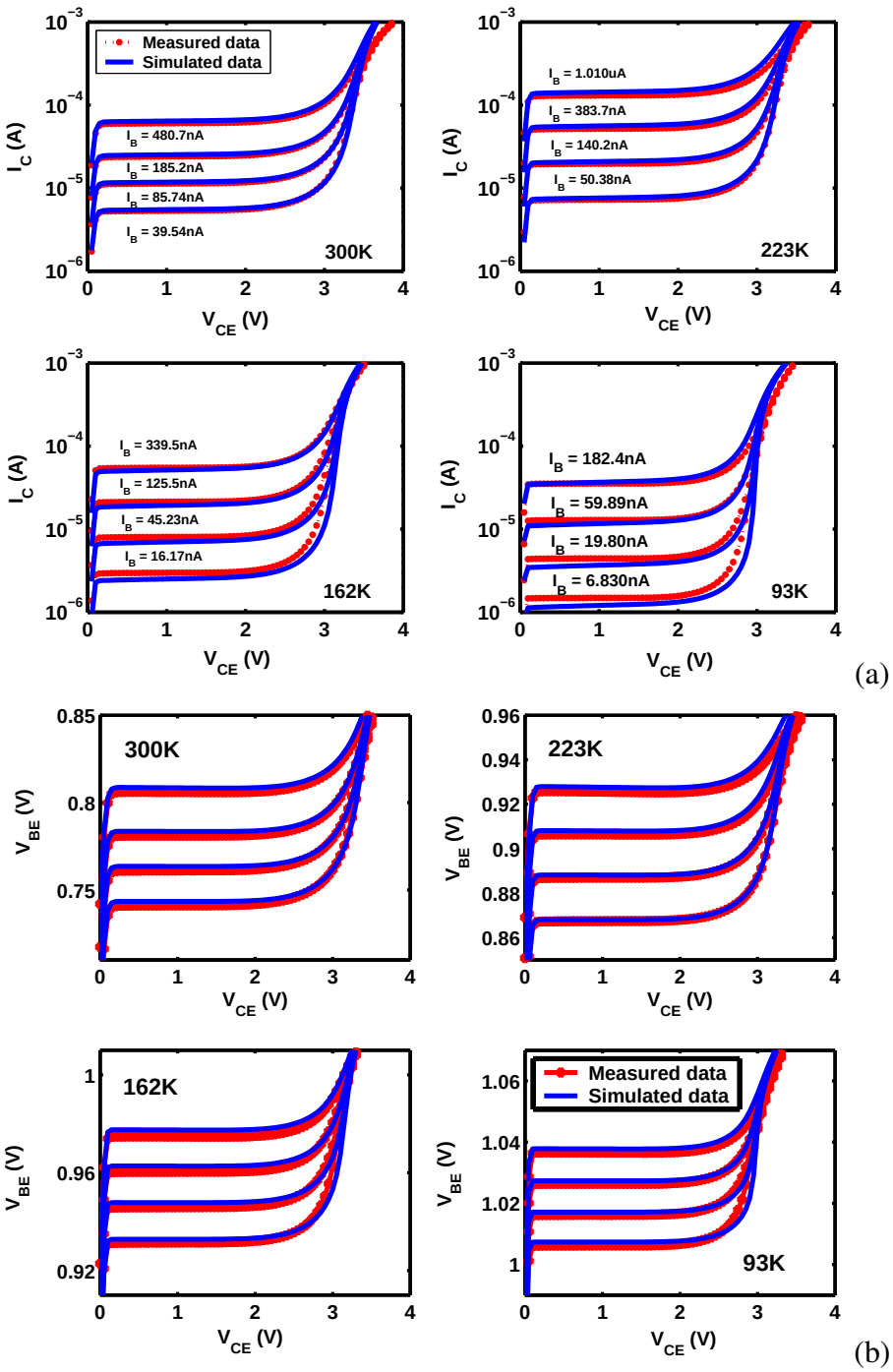

Figure 6.50: Measured and modeled forced-I_B output characteristics at low I_B. (a) I_C-V_{CE}; (b) V_{BE}-V_{CE}.

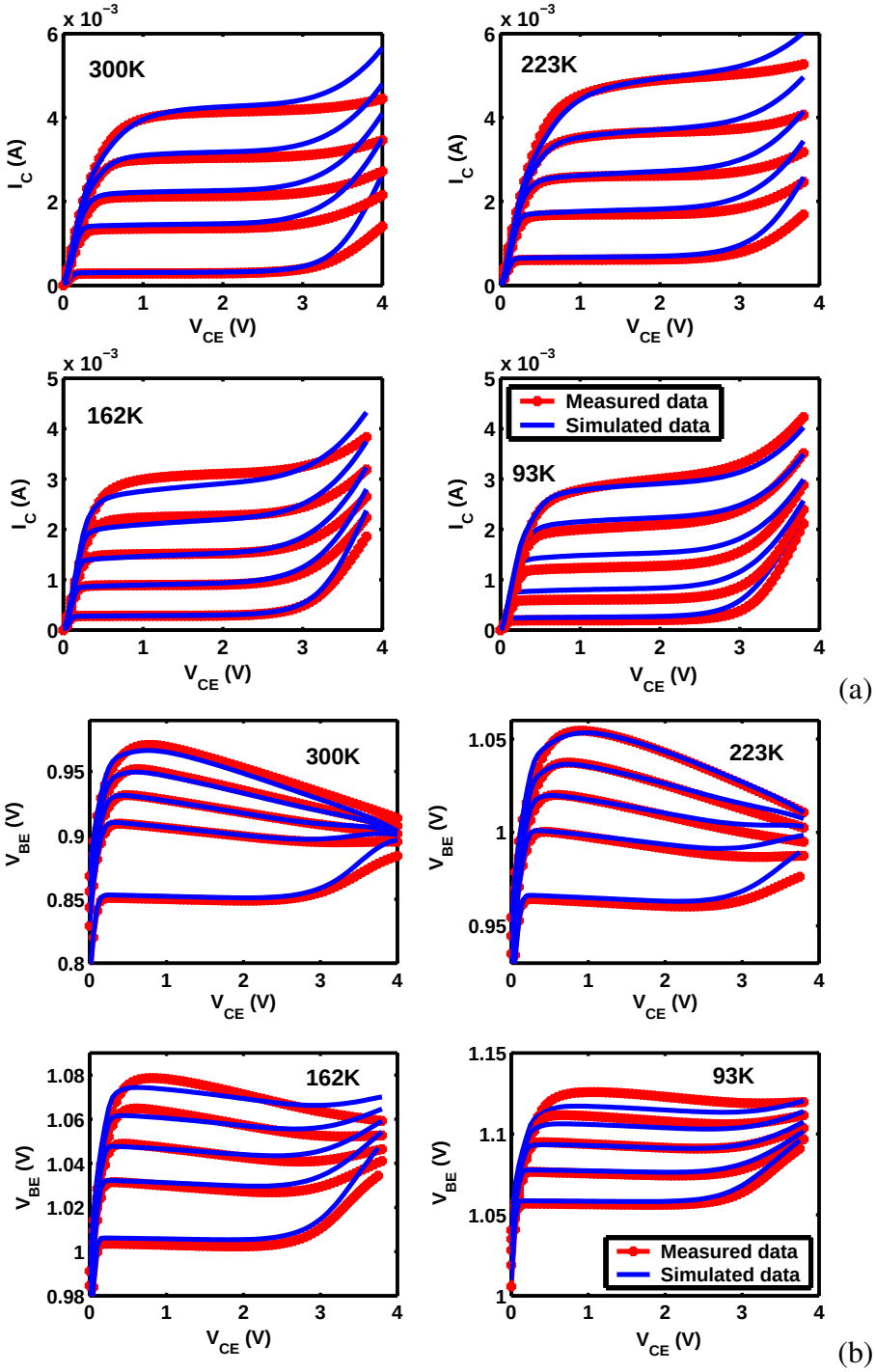

Figure 6.51: Measured and modeled forced-I_B output characteristics at high I_B. (a) I_C-V_{CE}; (b) V_{BE}-V_{CE}.

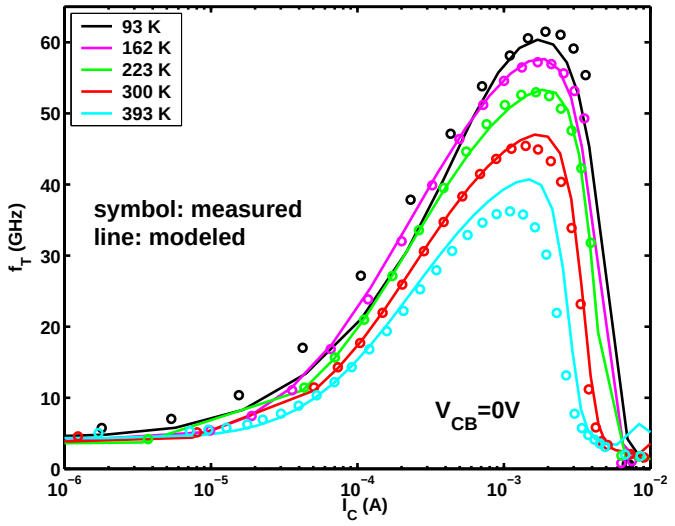

(a)

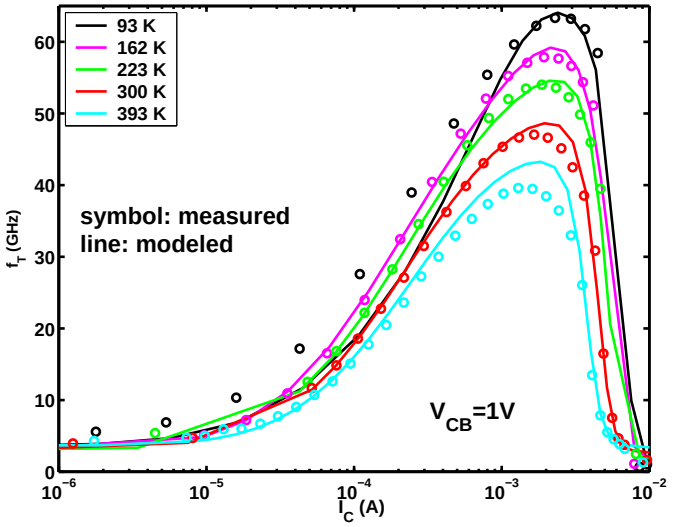

(b)

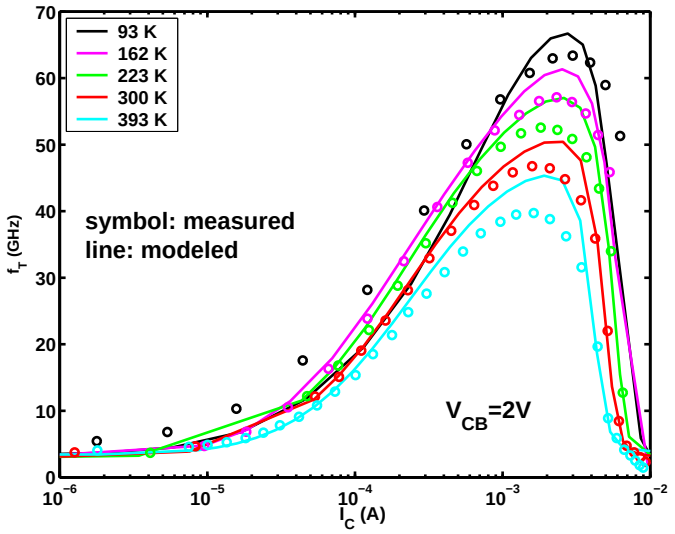

(c)

Figure 6.52: Measured (symbol line) and modeled (solid line) f_T-I_C from 93-393 K. (a) $V_{CB} = 0V$. (b) $V_{CB} = 1V$. (c) $V_{CB} = 2V$.

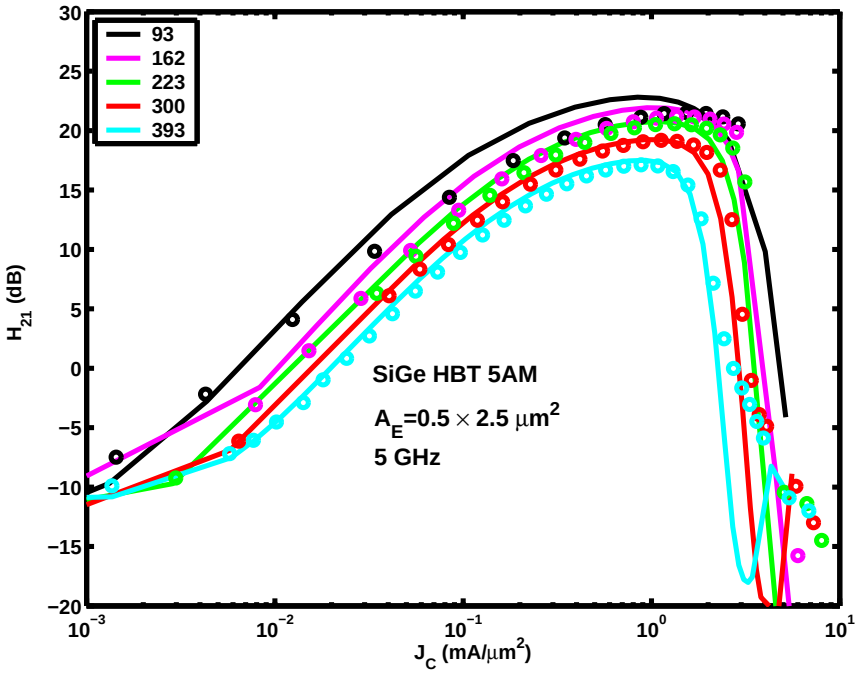

(a)

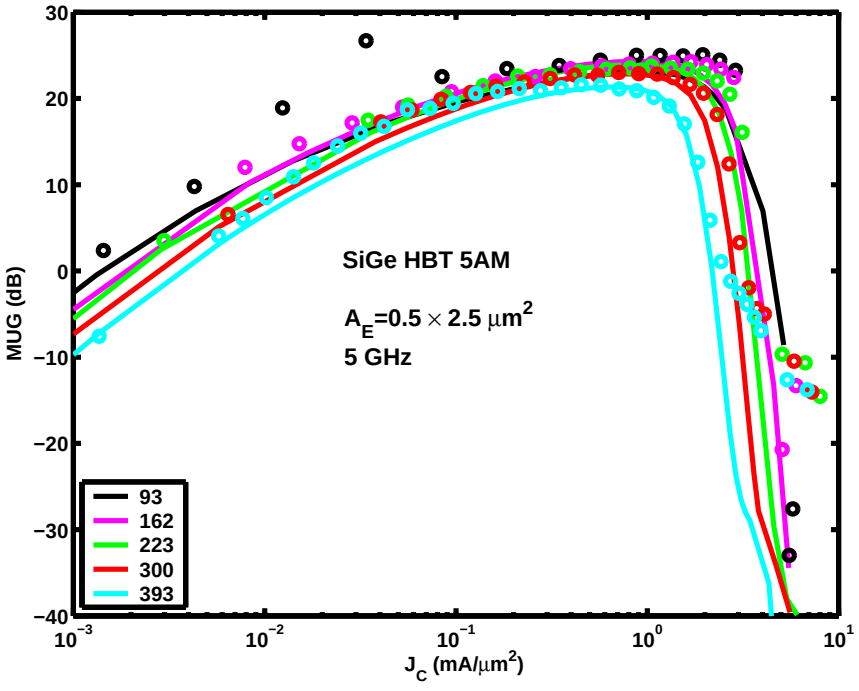

(b)

Figure 6.53: (a) Measured (symbols) and modeled (curves) H_{21}-J_C at 5 GHz from 93-393 K. (b) Measured (symbols) and modeled (curves) MUG-J_C at 5 GHz from 93-393 K.

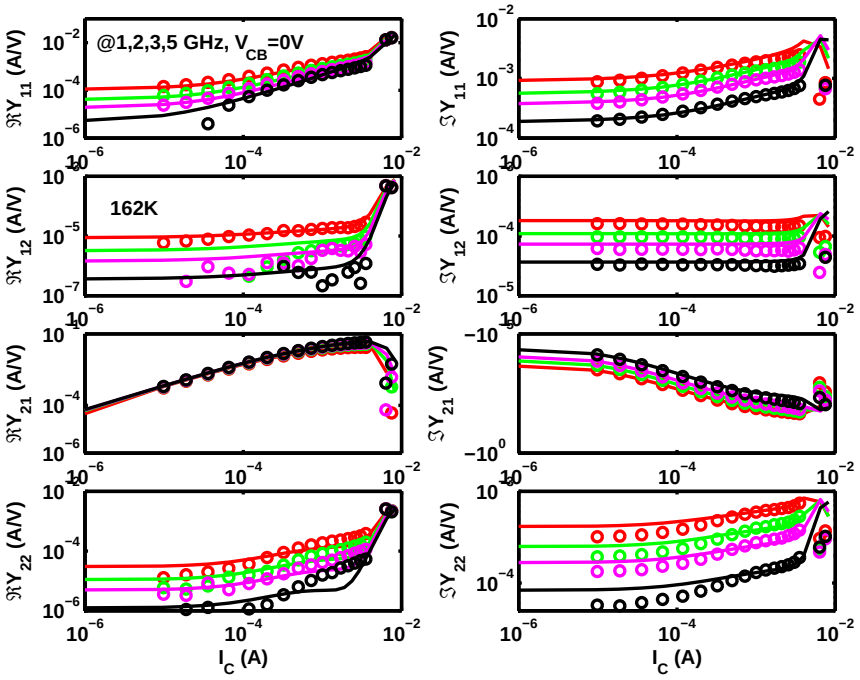

Figure 6.54: Measured (symbols) and modeled (curves) Y-parameters at 1,2,3 and 5 GHz for 162 K, $V_{CB} = 0V$.

6.13 Summary

In this chapter, a wide temperature range parameter extraction strategy is presented.

• Firstly, low injection parameters (saturation current I_S and ideality factor N_F, junction capacitance parameters, early voltage, avalanche parameters) are extracted isothermally and temperature mapped.

• Then parasitic resistances are extracted isothermally and temperature mapped;

• Then thermal resistances R_{TH} are extracted isothermally and temperature mapped;

• Then, high current parameters are extracted isothermally and temperature mapped, with the implementation of temperature mapped low injection parameters, parasitic resistances and R_{TH}. During this step, self-heating is turned on.

• Finally, once the electrical parameters are extracted and all the temperature scaling equations are updated, temperature parameters will be fine-tuned again within the whole temperature range, with self-heating turned on. Usually, several iterations between the last two steps are necessary.

With the extracted model parameters, we obtain reasonably accurate fitting of the *dc* characteristics from 393 to 43 K for a first-generation SiGe HBT. Good *ac* fitting from 393 to 93 K have been achieved.

Chapter 7

Band Gap Reference Circuit Modeling Application

7.1 Introduction

Precision bandgap references (BGRs) are extensively used in a wide variety of circuits required for such missions, and have been demonstrated to work well at cryogenic temperatures [82] [83]. To further optimize BGR performance at cryogenic temperatures, it is necessary to understand and model the non-idealities found in existing designs, which we address in this work for the first time.

Typical BGR design assumes an ideal temperature dependence of the I_C-V_{BE} characteristics predicted from Shockley's transistor theory, with various degrees of assumptions on the temperature dependence of the bandgap. At cryogenic temperatures, however, the slope of measured I_C-V_{BE} significantly deviates from ideal $1/V_T$ [84] [1]. As we discussed previously, a temperature dependent non-ideality factor $N_F(T)$ is necessary to describe the slope of I_C-V_{BE}. The measured intercept of I_C-V_{BE}, known as the saturation current I_S, also shows a temperature dependence drastically different from traditional theory below 200 K [84] [1]. It is therefore logical to examine how these device-level deviations from traditional theories affect BGR output at cryogenic temperatures. In addition, a key question centers of whether we can successfully model BGR performance over extremely-wide temperature ranges using the transistor $I_C - V_{BE}$ model of [1]. The first-order BGR design from [82] is used here, which was fabricated using a first-generation SiGe BiCMOS technology with 50 GHz cut-off frequency at room temperature.

7.2 Technical approach and results

Fig.7.1 shows the schematic of the BGR analyzed [82]. M_4-M_7 and Q_1-Q_2, along with resistor R_1, generate the PTAT bias current I_{PTAT}, which is set by ΔV_{BE}. Q_1 and Q_3 consists of four parallel

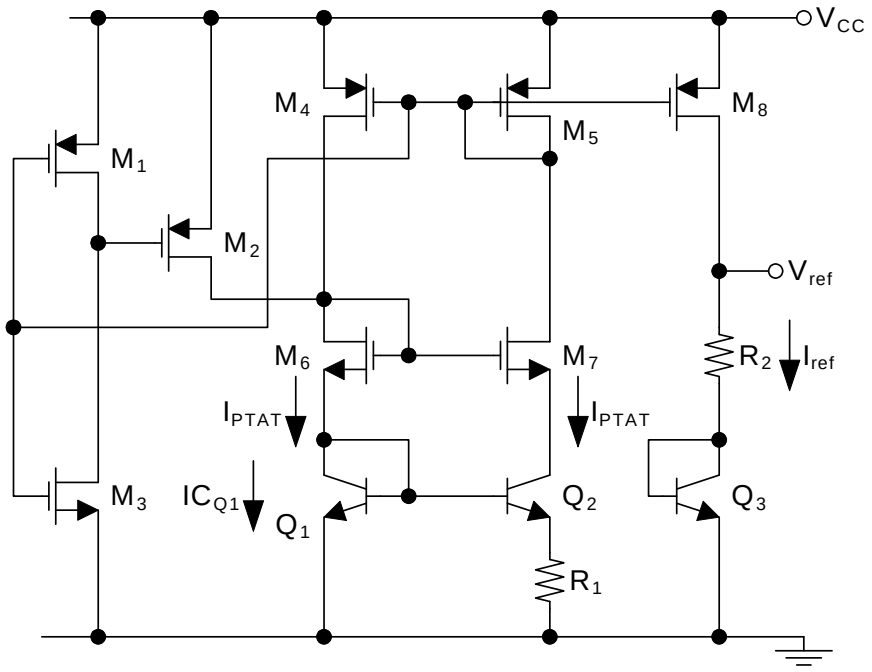

Figure 7.1: Schematic of a first-order SiGe bandgap reference [2].

copies of $0.5\times2.5\ \mu m^2$ SiGe HBTs. The emitter area of Q_2 is eight times of that of Q_1 and Q_3. V_{BE} of Q_3 is controlled by I_{PTAT}, and increases with cooling. V_{ref} is the sum of V_{BE} of Q_3 and the voltage across R_2, PTAT voltage proportional to ΔV_{BE} through $I_{ref}(T)$.

7.2.1 Slope of I_C-V_{BE} and impact on $\Delta V_{BE}(T)$ and $I_{ref}(T)$

The "PTAT" $\Delta V_{BE}(T)$ is generated from the V_{BE} difference of Q_1 and Q_2, two transistors operating at different current densities. Shockley theory predicts a $I_C - V_{BE}$ slope of $1/V_T$, and a ΔV_{BE} of $V_T \ln\left(\frac{A_{Q_2}}{A_{Q_1}}\right)$, which is $V_T \ln(8)$. However, the measured ΔV_{BE} of the BGR clearly deviates from $V_T \ln(8)$ below 200 K, which is shown in Fig. 7.2(a). This deviation from strict PTAT behavior originates from deviation of $I_C - V_{BE}$ slope from $1/V_T$, and can be modeled using a non-ideality factor $N_F(T)$ [1]. $\Delta V_{BE}(T)$ is then given by:

$$\Delta V_{BE}(T) = N_F(T) V_T \ln(8). \tag{7.1}$$

$N_F(T)$ can be modeled using [1]:

$$N_F(T) = N_{F,nom}\left(1 - \frac{T - T_{nom}}{T_{nom}}\left(A_{NF}\frac{T_{nom}}{T}\right)^{X_{NF}}\right), \tag{7.2}$$

where T_{nom} is nominal temperature, $N_{F,nom}$ is non-ideality factor at nominal temperature, which is close to unity, and A_{NF} and X_{NF} are technology dependent fitting parameters. Using (7.2), $N_F(T)$ and consequently $\Delta V_{BE}(T)$ can be well-modeled, as shown in Fig. 7.2(b).

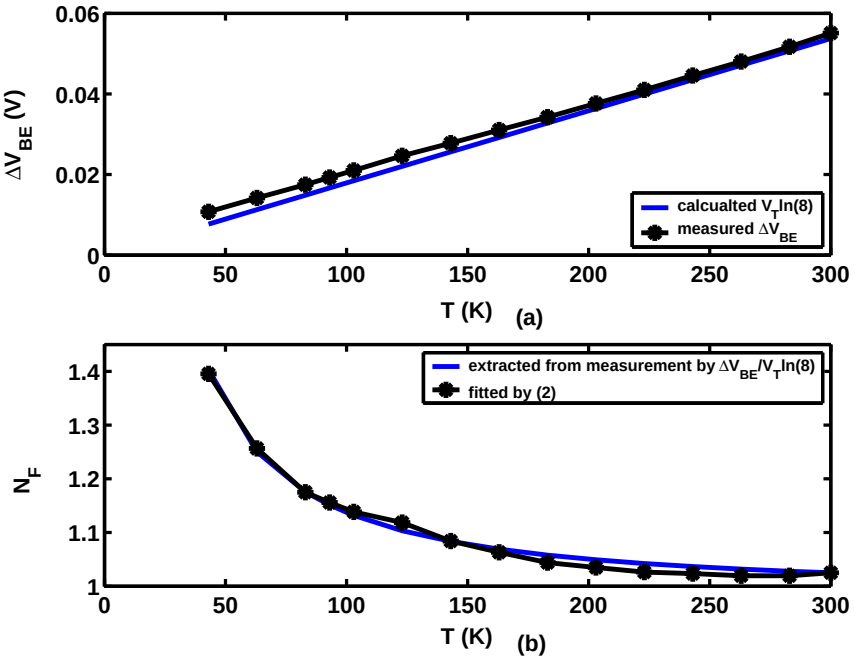

Figure 7.2: (a) Measured ΔV_{BE}-T and calculated $V_T \ln(8)$-T from 43 to 300 K. (b) N_F-T from 43-300 K.

Transistors M_4-M_5 and M_6-M_7 are identically-sized pairs. I_{PTAT} is then amplified through transistor M_8, with an amplification factor $k = (W/L)_{M_8} / (W/L)_{M_5}$.

$$I_{ref}(T) = kI_{PTAT}(T) = k\frac{N_F(T)V_T \ln(8)}{R_1}. \tag{7.3}$$

Table 7.1: Models examined in this work.

Name	Model 1	Model 2	Model 3
$N_F(T)$	1.025	(7.2)	(7.2)
$I_S(T)$	(5.67)	(5.67)	(5.69)

We mention in passing that the "PTAT" designation is no longer strictly accurate below 200 K because $N_F(T) > 1$. The slope of I_C-V_{BE}, or $1/N_F(T)V_T$, directly affects the BGR's $\Delta V_{BE}(T)$ and hence $I_{ref}(T)$, which then determines V_{BE} of Q_3, as detailed below.

7.2.2 $I_S(T)$ and impact on $V_{BE}(T)$

V_{BE} of Q_3, $V_{BE,3}$ is given by:

$$V_{BE,3} = N_F(T)V_T \ln \frac{I_{ref}(T)}{I_{S,3}(T)} = N_F(T)V_T \ln \frac{k\frac{\Delta V_{BE}(T)}{R_1}}{I_{S,3}(T)}, \tag{7.4}$$

where $I_{S,3}$ is the I_S of Q_3.

We have seen that the slope of $I_C - V_{BE}$ affects $V_{BE,3}$ through the $N_F(T)V_T$ term. The intercept of I_C-V_{BE}, $I_S(T)$, further affects $V_{BE,3}$ through the $I_{S,3}(T)$ term in (7.4).

We now examine the impact of $I_S(T)$ on $V_{BE,3}$. To examine the roles of the $I_C - V_{BE}$ slope and intercept, that is, $N_F(T)$ and $I_S(T)$, we chose 3 model combinations, as shown in Table 1. Model 1 produces the classic slope and intercept models, both of which are "wrong" at lower temperatures. Model 2 produces the correct slope but the "wrong" intercept. Model 3 produces the correct slope and the correct intercept of I_C-V_{BE}.

Fig. 7.3 shows I_C-V_{BE} for a $0.5\times2.5\ \mu m^2$ SiGe HBT at 300 K and 43 K. The symbols represent the $(V_{BE,3}, I_{ref}/4)$ pair using (7.3) and (7.4). The factor of "4" represents the multiplicity number of Q_3. At 300 K, the nominal temperature, all of the three models have the same I_{ref} value, and give the same $V_{BE,3}$, because they all have the same N_F and I_S at 300 K, as expected.

At 43 K, with $N_F(T)$, the slope of $I_C - V_{BE}$ is correctly modeled by both model 2 and model 3. Model 2 and 3 thus have the same and correct I_{ref}. However, for model 2, I_S is underestimated by traditional theory, leading to a much higher $V_{BE,3}$ than model 3.

For model 1, the situation is more complex. The slope of $I_C - V_{BE}$ is overestimated as N_F is fixed at its 300 K value. The intercept of $I_C - V_{BE}$ (I_S) is underestimated. The final $I_C - V_{BE}$ from a model that gives a wrong slope and a wrong intercept, however, is surprisingly not too far off from measured data in the current range of interest for producing $V_{BE,3}$. As a result, the $V_{BE,3}$ from model 1, the traditional model, is much closer to model 3 than model 2, which actually has the correct slope.

The above process can be repeated for all temperatures to yield $V_{BE,3}$-T, which is shown in Fig. 7.4. This is completely equivalent to a calculation using (7.4), but the graphical illustration yields a much better intuitive understanding of the model differences. Model 3 successfully reproduces the measured $V_{BE,3}$-T characteristics. The $V_{BE,3}$-T prediction from traditional theory, model 1, is not terribly inaccurate, because of the cancellation between underestimated intercept, $I_S(T)$, and the overestimated slope, $1/N_F(T)V_T$. This cancellation is circuit design dependent, however, and is to a large extent a coincidence for the BGR design analyzed.

7.2.3 $V_{ref}(T)$

The BGR output V_{ref} is given by:

$$V_{ref}(T) = V_{BE,3}(T) + I_{ref}(T)R_2 = V_{BE,3}(T) + K\Delta V_{BE}(T), \tag{7.5}$$

where $K = kR_2/R_1$. The temperature dependence of K can be negligibly small by choosing high precision, low temperature coefficient resistors and careful layout design to minimize resistor mismatch. The resistor used in the BGR exhibits a temperature coefficient of 17.8 ppm/°C over the temperature range of 43-300 K. In practice, K is often chosen to make the positive temperature

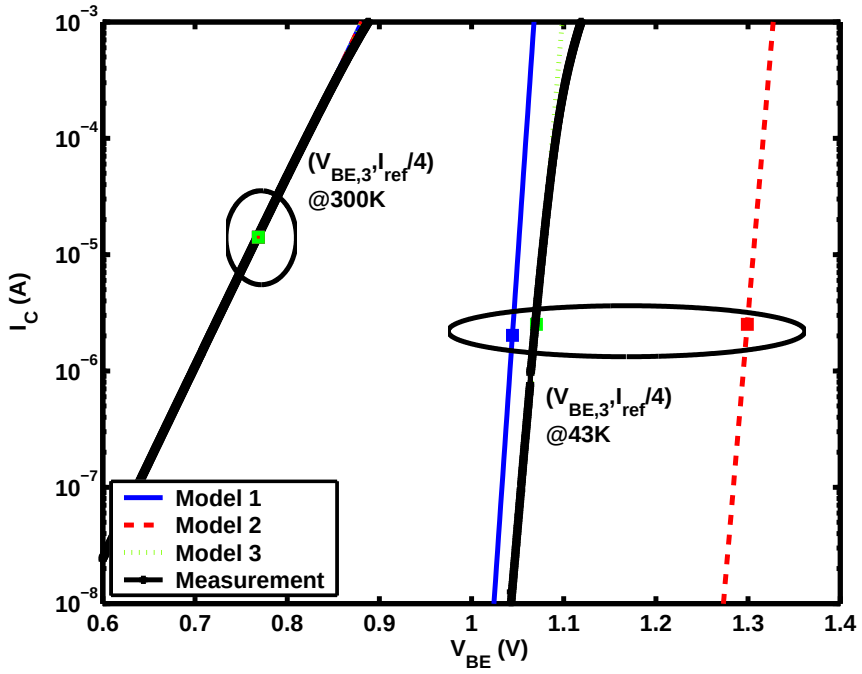

Figure 7.3: Measured and modeled I_C-V_{BE} for single 0.5×2.5 μm^2 SiGe HBT at 43 K and 300 K.

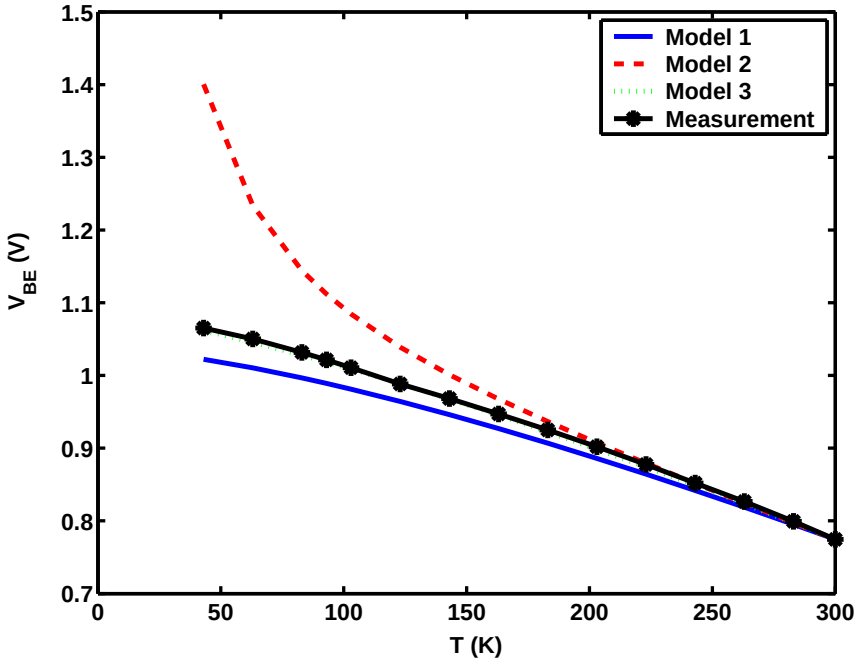

Figure 7.4: Measured and modeled V_{BE} from 43-300 K.

coefficient of $\Delta V_{BE}(T)$ cancel the negative temperature coefficient of $V_{BE}(T)$, to produce a zero temperature coefficient $V_{ref}(T)$ at a nominal temperature, usually 300 K [71] [85].

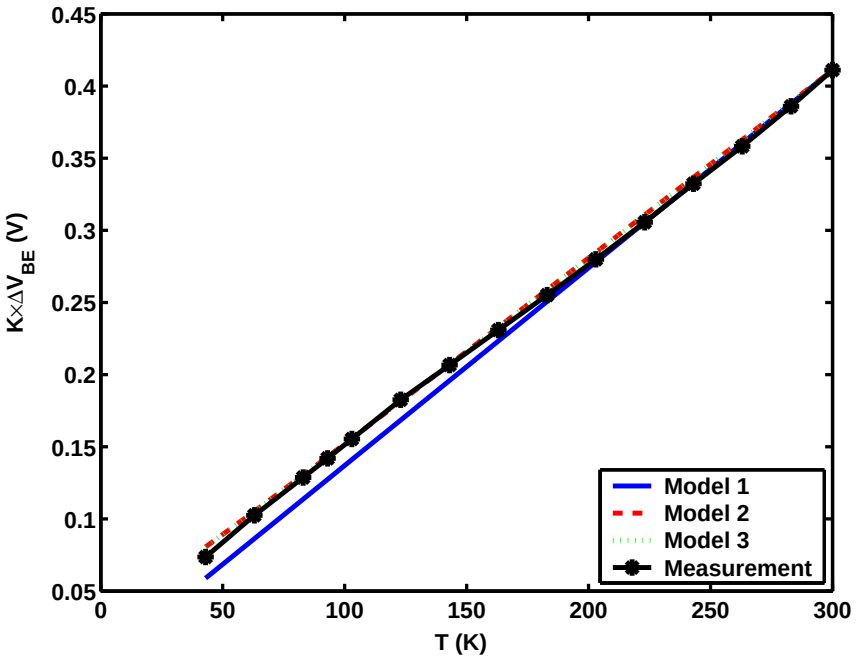

Figure 7.5: Measured and modeled $K \times \Delta V_{BE}$ from 43-300 K.

Fig. 7.5 shows the measured and modeled $K \times \Delta V_{BE}$ versus temperature. Due to the use of a constant N_F, model 1 deviates from measurements below 200 K. Model 2 and 3 accurately capture $K \times \Delta V_{BE}$.

The sum of $V_{BE,3}(T)$ and $K \times \Delta V_{BE}(T)$ gives V_{ref}, which is shown in Fig. 7.6. Additional calculation shows that the $V_{BE,3}(T)$ difference between the models dominates over the $K \times \Delta V_{BE}$ differences. Model 2 has the largest $V_{BE,3}$ and hence V_{ref} deviation from measurement. Traditional theory, model 1, is not terrible in predicting V_{ref}, because of coincidental cancellation between underestimated intercept, $I_S(T)$, and overestimated slope, $1/N_F(T)V_T$.

On the other hand, we observe that the overall V_{ref} variation with temperature for model 3 is less than that for model 1. The difference is that model 3 accounts for the deviations of both the slope and intercept of $I_C - V_{BE}$ from traditional Shockley transistor theory, model 1. This suggests that such deviations actually help make the BGR output vary less with temperature than traditional theories

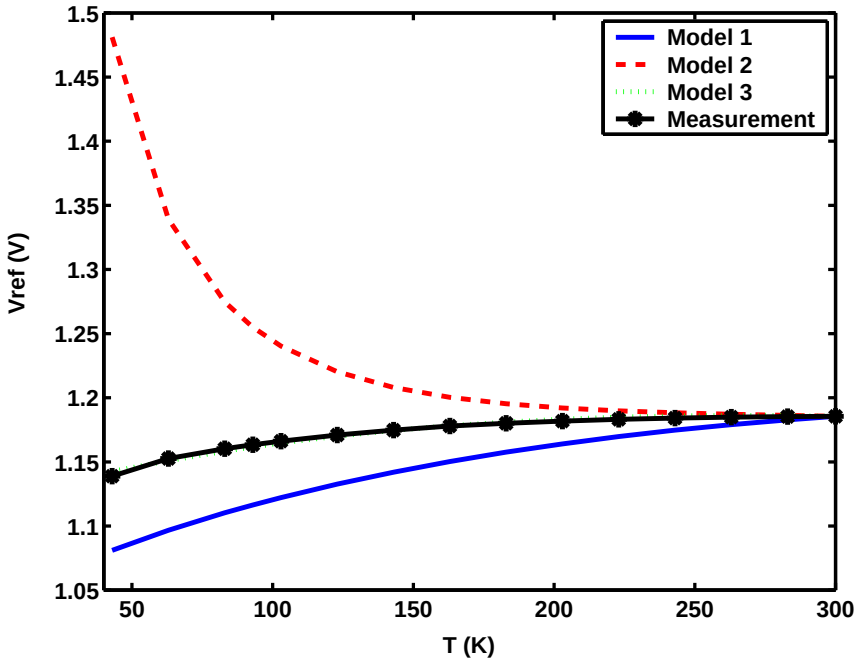

Figure 7.6: Measured and modeled V_{ref} from 43-300 K.

would predict, and explains why BGRs experimentally perform much better than predictions using traditional BGR design equations at lower temperatures.

7.3 Summary

In this chapter, we examine the impact of the non-ideal temperature dependence of I_C-V_{BE} in SiGe HBTs across temperature on the output of a first-order SiGe bandgap reference. These non-idealities are shown to actually help make the BGR output voltage vary less at cryogenic temperatures than traditional Shockley theory would predict. For the particular BGR design examined, the overall $V_{ref}(T)$ prediction from Shockley theory is not too bad, because of the cancellation between underestimated intercept and overestimated slope. Successful cryogenic temperature modeling of both ΔV_{BE} and V_{BE} components of the BGR output is demonstrated for the first time. The modeling method presented provides basis for further optimization of SiGe BGRs operating across extremely wide temperature ranges, and down to deep cryogenic temperatures, where existing design equations fail.

Chapter 8

Conclusions

In this dissertation, physics and compact Modeling of SiGe HBT for wide temperature range operation were investigated.

Chapter 1 gave an introduction of the motivation. SiGe HBT technologies are being increasingly deployed in "extreme environments", including operation to very low temperature (e.g., to 77 K or even 4.2 K). Thorough understanding of SiGe HBT physic at cryogenic temperature is very necessary. Meanwhile, to enable circuit design, robust and accurate compact models that can work over a wide temperature range are truly important to be developed. The SiGe HBT investigated and measured in this work is a first-generation, 0.5 μm SiGe HBT with f_T/f_{max} of 50 GHz/65 GHz and BV_{CEO}/BV_{CBO} of 3.3 V/10.5 V at 300 K, with base doping below but close to the Mott-transition (about $3 \times 10^{18}\ cm^{-3}$ for boron in silicon).

Chapter 2 analyzed several import physics, including bandgap energy E_g, electron and holes density of states N_C/N_V, intrinsic carrier concentration n_i, bandgap narrowing BGN, carrier mobility μ, carrier saturation velocity v_{sat} and carrier freezeout effect. Following, the dc and ac performance of SiGe HBT were discussed. During the analysis, not only the influence of temperature, but also the impact of germanium was illustrated with details. The bandgap engineering generally produces positive influence on the low temperature operations of bipolar transistors, including higher current gain β, larger Early voltage V_A, lower base transit time τ_B and hence higher cut-off frequency f_T.

Chapter 3 extended the substrate current based avalanche multiplication technique down to 43 K. This measurement technique gave the current dependence of avalanche multiplication factor M-1 at low temperatures. However conventional techniques fail because of self-heating at high current densities. Lower M-1 was observed at higher current densities where cut-off frequency is high (of interest to practical circuits). In chapter 4, the forced-I_E pinch-in maximum output voltage limit

in SiGe HBTs operating at cryogenic temperatures was investigated. A decrease of the voltage limit was observed with cooling. We attributed it to the increase of intrinsic base resistance due to freezeout as well as increase of avalanche multiplication factor M-1. A practically high I_E was shown to alleviate the decrease of V_{CB}^* with cooling, primarily due to the decrease of M-1 with increasing emitter current I_E. The fact that the maximum operation voltage range does not degrade as much with cooling at such high current density is certainly good news for circuit applications.

In chapter 5, wide temperature range compact models of SiGe HBTs were presented based on Mextram and some new temperature scaling models were presented. In particular, the temperature characteristics of mobility and ionization rate were investigated. The classic ionization model, together with a single power law mobility model, enables resistance vs. temperature modeling of the substrate and the collector region, where doping levels are below Mott-transition. Based on the Altermatt ionization model, a new incomplete ionization model that accounts for the temperature dependence of the bound state fraction factor was developed. This new model enables accurate temperature dependent modeling of the intrinsic base sheet resistance, which has a doping level close to the Mott-transition. For the buried collector and the silicided extrinsic base, where doping levels are well above the Mott-transition, two approaches were proposed and both give good results. In chapter 6, a new parameter extraction strategy was implemented. Isothermal electrical parameters extraction and temperature parameters extraction were illustrated in detail. With the extracted model parameters, reasonably accurate fitting of the *dc* characteristics from 393 to 43 K, and good *ac* fitting from 393 to 93 K have been achieved.

Typical BGR design assumes an ideal temperature dependence of the I_C-V_{BE} characteristics predicted from Shockley's transistor theory, with various degrees of assumptions on the temperature dependence of the bandgap. At cryogenic temperatures, however, the slope of measured I_C-V_{BE} significantly deviates from ideal $1/V_T$. A temperature dependent non-ideality factor $N_F(T)$ is necessary to describe the slope of I_C-V_{BE}. The measured intercept of I_C-V_{BE}, known as the saturation current I_S, also shows a temperature dependence drastically different from traditional theory below 200 K. Chapter 7 examined the impact of the non-ideal temperature dependence of I_C-V_{BE} in SiGe

HBTs on the output of a BGR. These non-idealities were shown to actually help make the BGR output voltage vary less at cryogenic temperatures than traditional Shockley theory would predict. Successful cryogenic temperature modeling of both ΔV_{BE} and V_{BE} components of the BGR output was demonstrated for the first time.

Bibliography

[1] Z. Xu, X. Wei, G. Niu, L. Luo, D. Thomas, and J. D. Cressler, "Modeling of temperature dependent I_C-V_{BE} characteristics of SiGe HBTs from 43-400k," in *Dig. of IEEE BCTM*, pp. 81–84, oct 2008.

[2] Z. Xu, G. Niu, L. Luo, and J. D. Cressler, "A physics-based trap-assisted tunneling current model for cryogenic temperature compact modeling of SiGe HBTs," in *ECS Trans.*, vol. 33, pp. 301–310, 2010.

[3] J. C. J. Paasschens, W. J. Kloosterman, and R. v. d. Toorn, *Model derivation of Mextram 504: the physics behind the model*. Nat Lab Unclassified Report, NL-UR 2002/806, Koninklijke Philips Electronics, Oct 2004.

[4] J. C. J. Paasschens, W. J. Kloosterman, and R. J. Havens, *Parameter extraction for the bipolar transistor model Mextram*. Nat Lab Unclassified Report, NL-UR 2001/801, Koninklijke Philips Electronics, May 2001.

[5] J. D. Cressler, "On the potential of SiGe HBTs for extreme environment electronics," in *Proceedings of the IEEE*, vol. 93, pp. 1559–1582, Sep 2005.

[6] Z. Xu, G. Niu, L. Luo, J. D. Cressler, M. L. Alles, R. Reed, H. A. Mantooth, J. Holmes, and P. W. Marshall, "Charge collection and SEU in SiGe HBT current mode logic operating at cryogenic temperatures," *IEEE Transactions on Nuclear Science*, vol. 57, pp. 3206–3211, December 2010.

[7] J. D. Cressler and G. F. Niu, *Silicon-Germanium Heterojunction Junction Bipolar Transistors*. Artech House, 2003.

[8] H. K. Gummel and H. C. Poon, "An integral charge control model of bipolar transistors," *The Bell System Technique Journal*, pp. 827–852, May 1970.

[9] C. C. McAndrew, J. A. Seitchik, D. F. Bowers, M. Dunn, M. Foisy, I. Getreu, M. McSwain, S. Moinian, J. Parker, D. J. Roulston, M. Schroter, P. van Wijnen, and L. F. Wagner, "VBIC95, the vertical bipolar inter-company model," *IEEE Journal of Solid-State Circuits*, vol. 31, no. 10, pp. 1476–1483, 1996.

[10] A. Koldehoff, M. Schroter, and H. M. Rein, "A compact bipolar transistor model for very-high-frequency applications with special regard to narrow emitter stripes and high current densities," *Solid-State Electronics*, vol. 36, pp. 1035–1048, July 1993.

[11] H. C. Graaff and W. J. Kloosterman, "New formulation of the current and charge relations in bipolar transistor modeling for CACD purposes," *IEEE Transactions on Electron Devices*, vol. 32, pp. 2415–2419, 1985.

[12] I. E. Getreu, *Modeling the Bipolar Transistor*. Amsterdam: Elsevier, 1978.

[13] H. C. de Graaff and F. M. Klaassen, *Compact Transistor Modeling for Circuit Design*. Vienna, Austria: Springer-Verlag, 1990.

[14] G. Kull, L. Nagel, S.-W. Lee, P. Lloyd, E. Prendergast, and H. Dirks, "A unified circuit model for bipolar transistors including quasi-saturation effects," *IEEE Transactions on Electron Devices*, vol. 32, pp. 1103–1113, Jun 1985.

[15] J. Pan, G. Niu, J. Tang, Y. Shi, A. J. Joseph, and D. L. Harame, "Substrate current based avalanche multiplication measurement in 120 GHz SiGe HBTs," *IEEE Electron Devices Letters*, vol. 24, pp. 736–738, December 2003.

[16] L. Luo, G. Niu, D. Thomas, J. Yuan, and J. D. Cressler, "Forced-I_E pinch-in maximum output voltage limit in SiGe HBTs operating at cryogenic temperatures," in *Dig. of IEEE BCTM*, pp. 41–44, oct 2008.

[17] L. Luo, G. Niu, K. A. Moen, and J. D. Cressler, "Compact modeling of the temperature dependence of parasitic resistances in SiGe HBTs down to 30 K," *IEEE Transactions on Electron Devices*, vol. 56, pp. 2169–2177, Oct 2009.

[18] L. Luo, G. Niu, L. Najafizadeh, and J. D. Cressler, "Impact of the non-ideal temperature dependence of I_C-V_{BE} on ultra-wide temperature range SiGe HBT bandgap reference circuits," in *Dig. of IEEE BCTM*, pp. 220–223, Oct 2010.

[19] W. Bludau, A.Onton, and W.Heinke, "Temperature dependence of the band gap in silicon," *Journal of Applied Physics*, vol. 45, no. 4, pp. 1846–1848, 1974.

[20] G. MacFarlane, J. P. McLean, J. E. Quarrington, and V. Roberts, "Fine structure in the absorption-edge spectrum of Si," *Physical Review B*, vol. 111, pp. 1245–1254, May 1958.

[21] T. Fromherz and G. Bauer, *Properties of strained and relaxed Silicon Germanium*. INSPEC, London, 1995.

[22] Z. Matutinovic-Krstelj, V. Venkataraman, E. J. Prinz, J. C. Sturm, and C. W. Magee, "Base resistance and effective bandgap reduction in npn Si/Si1-xGex/Si HBT's with heavy base doping," *IEEE Transactions on Electron Devices*, vol. 43, pp. 457–466, March 1996.

[23] R. People, "Indirect band gap of coherently strained ge_xsi_{1-x} bulk alloys on ãŁˆ001ãŁ‰ silicon substra," *Physical Review B*, vol. 32, pp. 1405–1408, July 1985.

[24] J. W. Slotboom and H. C. D. Graaff, "Measurements of bandgap narrowing in *si* bipolar transistors," *Solid-State Electronics*, vol. 19, pp. 857–862, 1976.

[25] J. Lindmayer and C. Y. Wrigley, *Fundamentals of Semiconductor Devices*. Van Nostrand Reinhold Company, 1965.

[26] P. P. Altermatt, A. Schenk, and G. Heiser, "A simulation model for the density of states and for incomplete ionization in crystalline silicon. I. establishing the model in Si:P," *Journal of Applied Physics*, vol. 100, pp. 113715–1137157, 2006.

[27] P. P. Altermatt, A. Schenk, B. Schmithen, and G. Heiser, "A simulation model for the density of states and for incomplete ionization in crystalline silicon. II. investigation of Si:As and Si:B and usage in device simulation," *Journal of Applied Physics*, vol. 100, pp. 113714–11371410, 2006.

[28] G. L. Pearson and J. Bardeen, "Electrical properties of pure silicon and silicon alloys containing boron and phosphorus," *Physical Review*, vol. 75, pp. 865–883, Mar 1949.

[29] F. J. Morin and J. P. Maita, "Electrical properties of silicon containing arsenic and boron," *Physical Review*, vol. 96, pp. 28–35, Oct 1954.

[30] T. F. Lee and T. C. McGill, "Variation of impurity-to-band activation energies with impurity density," *Journal of Applied Physics*, vol. 46, pp. 373–380, Jan 1975.

[31] G. D. Mahan, "Energy gap in si and ge: Impurity dependence," *Journal of Applied Physics*, vol. 51, pp. 2634–2646, May 1980.

[32] S. R. Dhariwal, V. N. Ojha, and G. P. Srivastava, "On the shifting and broadening of impurity bands and their contribution to the effective electrical bandgap narrowing in moderately doped semiconductors," *IEEE Transactions on Electron Devices*, vol. 32, pp. 44–48, Jan 1985.

[33] N. F. Mott, "Metal-insulator transition," *Reviews of Modern Physics*, vol. 40, pp. 677–683, Oct 1968.

[34] D. B. M. Klaassen, "A unified mobility model for device simulation-i. model equations and concentration dependence," *Solid-State Electronics*, vol. 35, no. 7, pp. 953–959, 1992.

[35] D. B. M. Klaassen, "A unified mobility model for device simulation-ii. temperature dependence of carrier mobility and lifetime," *Solid-State Electronics*, vol. 35, no. 7, pp. 961–967, 1992.

[36] F. J. Morin and J. P. Maita, "Electrical properties of Silicon containing arsenic and boron," *Physical Review*, vol. 96, pp. 28–35, October 1954.

[37] G. W. Ludwig and R. L. Watters, "Drift and conductivity mobility in Silicon," *Physical Review*, vol. 101, pp. 1699–1701, March 1956.

[38] A. B. Sproul, M. A. Green, and A. W. Stephens, "Accurate determination of minority carrier- and lattice scattering-mobility in silicon from photoconductance decay," *Journal of Applied Physics*, vol. 72, pp. 4161–4171, November 1992.

[39] M. V. Fischetti and S. Laux, "Band structure, deformation potentials, and carrier mobility in strained Si, Ge and SiGe alloys," *Journal of Applied Physics*, vol. 80, no. 4, pp. 2234–2252, 1996.

[40] G. Hock and E. K. et al., "High hole mobility in $Si_{0.17}Ge_{0.83}$ channel metal-oxide-semiconductor field-effect transistors grown by plasma-enhanced chemical vapor deposition," *Applied Physical Letters*, vol. 76, pp. 3920–3922, June 2000.

[41] T. Krishnamohan, *Physics and Technology of High Mobility, Strained Germanium Channel, Heterostructure MOSFETs*. PhD Dissertation, Stanford University, 2006.

[42] L. E. Kay and T. W. Tang, "Monte Carlo calculation of strained and unstrained electron mobilities in $Si_{1-x}Ge_x$ using an improved ionized impurity model," *Journal of Applied Physics*, vol. 70, pp. 1483–1488, August 1991.

[43] F. M. B. et al., "Low- and high-field electron-transport parameters for unstrained and strained $Si_{1-x}Ge_x$," *IEEE Electron Device Letters*, vol. 18, pp. 264–266, June 1997.

[44] J.-S. Rieh, P. K. Bhattacharya, and E. T. Croke, "Temperature dependent minority electron mobilities in strained $Si_{1-x}Ge_x$ ($0.2 \geq x \leq 0.4$) layers," *IEEE Transactions on Electron Devices*, vol. 47, pp. 883–890, April 2000.

[45] R. Quay, C. Moglestue, V. Palankovski, and S. Selberherr, "A temperature dependent model for the saturation velocity in semiconductor materials," *Materials Science in Semiconductor Processing*, vol. 3, pp. 149–155, March 2000.

[46] V. Palankovski and R. Quay, *Analysis and simulation of heterostructure devices*. Springer-Verlag Wien NewYork, 2004.

[47] H. Kroemer, "Tow integral relations pertaining to electron transport through a bipolar transistor with a nonuniform energy gap in the base region," *Solid-State Electronics*, vol. 28, pp. 1101–1103, 1985.

[48] J. M. Early, "Effects of space-charge layer widening in junction transistors," in *Proceedings of Institute of Radio Engineers*, vol. 40, pp. 1401–1406, November 1952.

[49] A. J. Joseph, J. D. Cressler, and D. M. Richey, "optimization of early voltage for cooled SiGe HBT precision current sources," *Journal De PhysiqueQ IV*, vol. 6, pp. 125–129, 1996.

[50] M. Rickelt, H. M. Rein, and E. Rose, "Influence of impact-ionization-induced instabilities on the maximum usable output voltage of Si-bipolar transistors," *IEEE Transactions on Electron Devices*, vol. 48, pp. 774–783, Apr 2001.

[51] G. Niu, J. D. Cressler, S. Zhang, U. Gogineni, and D. C. Ahlgren, "Measurement of collector-base junction avalanche multiplication effects in advanced UHV/CVD SiGe HBT's," *IEEE Transactions on Electron Devices*, vol. 46, pp. 1007–1015, May 1999.

[52] H. M. R. M. Rickelt and E. Rose, "Low-temperature avalanche multiplication in the collector-base junction of advanced n-p-n transistors," *IEEE Transactions on Electron Devices*, vol. 37, pp. 762–767, Mar 1990.

[53] J. H. Klootwijk, J. W. Slotboom, M. S. Peter, V. Zieren, and D. B. de Mooy, "Photo carrier generation in bipolar transistors," *IEEE Transactions on Electron Devices*, vol. 49, pp. 1628–1631, September 2002.

[54] S. Device, "2-d device simulator, version 10.0, synopsys," *Synopsys*, 2006.

[55] J. Yuan, J. D. Cressler, Y. Cui, G. Niu, S. Finn, and A. Joseph, "On the profile design of *sige hbts* for *rf* lunar applications down to 43 *k*," in *Dig. of IEEE BCTM*, pp. 25–28, oct 2008.

[56] J. J. Ebers and J. L. Moll, "Large-signal behavior of junction transistor," in *Proceedings of Institute of Radio Engineers*, vol. 42, pp. 1761–1772, December 1954.

[57] H. Stubing and H. M. Rein, "A compact physical large-signal model for high-speed bipolar transistors at high current densities-part i: One-dimensional model," *IEEE Transactions on Electron Devices*, vol. 34, pp. 1741–1751, August 1987.

[58] H. Stubing and H. M. Rein, "A compact physical lar e-signal model for high-speed bipolar transistors at high current densities-part ii: Two-dimensional model and experimental results," *IEEE Transactions on Electron Devices*, vol. 34, pp. 1752–1761, August 1987.

[59] W. J. Kloosterman, *Comparison of Mextram and the Vbic95 bipolar transistor model*. Nat Lab Unclassified Report, NL-UR 034/96, Philips Electronics, 1996.

[60] J. D. Cressler, ed., *Silicon Heterostructure Handbook: Materials, Fabrication, Devices, Circuits, and Applications of SiGe and Si Strained-Layer Epitaxy*. CRC press, 2006.

[61] S. Salmon, J. D. Cressler, R. C. Jaeger, and D. L. Harame, "The influence of Ge grading on the bias and temperature characteristics of SiGe HBTs for precision analog circuits," *IEEE Transactions on Electron Devices*, vol. 47, pp. 292–298, Feb 2000.

[62] *Agilent 85190A IC-CAP 2006 user's guide*. Agilent Technologies, 2006.

[63] J. A. D. Alamo and R. M. Swanson, "Forward-bias tunneling: a limitation to bipolar device scalings," *IEEE Electron Devices Letters*, vol. 7, pp. 629–631, Nov 1986.

[64] S. M. Sze, *Physics of semiconductor devices*. Wiley, New York, 1981.

[65] R. S. Muller and T. I. Kamins, *Device electronics for integrated circuits*. Wiley, New York, 1986.

[66] J. Paasschens, W. Kloosterman, and R. Havens, "Modelling two SiGe HBT specific features for circuit simulation," in *Dig. of IEEE BCTM*, pp. 38–41, oct 2001.

[67] R. L. Pritchard, "Two-dimensional current flow in junction transistors at high frequencies," *Proceedings of Institute of Radio Engineers*, vol. 46, pp. 1152–1160, June 1958.

[68] H. N. Ghosh, "A distributed model of the junction transistor and its application in the prediction of the emitter-base diode characteristic, base impedance, and pulse response of the device," *IEEE Transactions on Electron Devices*, vol. 12, pp. 513–531, oct 1965.

[69] M. P. J. G. Versleijen, "Distributed high frequency effects in bipolar transistors," in *Proceedings of Bipolar Circuits and Technology Meeting*, pp. 85–88, Sep 1991.

[70] C. Kittel and H. Kroemer, *Thermal Physics*. Freeman & Co., 1980.

[71] Y. P. Tsividis, "Accurate analysis of temperature effects in I_C-V_{BE} characteristics with application to bandgap reference sources," *IEEE Journal of Solid-State Circuits*, vol. 15, pp. 1076–1084, Dec 1980.

[72] C. D. Thurmond, "The standard thermodynamic functions for the formation of electrons and holes in Ge, Si, GaAs, and GaP," *Journal of Electrochemical Society*, vol. 122, no. 8, pp. 1133–1141, 1975.

[73] G. Niu, S. Zhang, J. D. Cressler, A. J. Joseph, J. S. Fairbanks, L. E. Larson, C. S. Webster, W. E. Ansley, and D. L. Harame, "Noise modeling and SiGe profile design tradeoffs and RF applications," *IEEE Transactions on Electron Devices*, vol. 47, pp. 2037–2044, Nov 2000.

[74] M. R. Shaheed and C. M. Maziar, "A physically based model for carrier freeze-out in *si*- and *sige*- base bipolar transistors suitable for implementation in device simulators," in *Dig. of IEEE BCTM*, pp. 191–194, 1994.

[75] M. A. Green, "Intrinsic concentration, effective densities of states, and effective mass in silicon," *Journal of Applied Physics*, vol. 67, pp. 2944–2954, Mar 1990.

[76] C. J. Glassbrenner and G. A. Slack, "Thermal conductivity of silicon and germanium from 3 K to the melting point," *Physical Review*, vol. 134, pp. 1058–1069, May 1964.

[77] Z. Xu, G. Niu, L. Luo, P. S. Chakraborty, P. Cheng, D. Thomas, and J. D. Cressler, "Cryogenic RF small-signal modeling and parameter extraction of SiGe HBTs," in *Digest. of IEEE Topical Meeting on Silicon Monolithic Integrated Circuits in RF Systems*, pp. 1–4, 2009.

[78] L. J. Giacoletto, "Measurement of emitter and collector series resistances," *IEEE Transactions on Electron Devices*, vol. 19, pp. 692–693, May 1972.

[79] T. Ning and D. Tang, "Method for determining the emitter and base series resistances of bipolar transistors," *IEEE Transactions on Electron Devices*, vol. 31, pp. 409–412, April 1984.

[80] W. Z. Cai and S. Shastri, "Extraction of base and emitter series resistances from the net transadmittance parameter," *IEEE Transactions on Electron Devices*, vol. 52, pp. 622–626, April 2005.

[81] J. S. Rieh, D. Greenberg, B. Jagannathan, G. Freeman, and S. Subbanna, "Measurement and modeling of thermal resistance of high speed SiGe heterojunction bipolar transistors," *Digest. of IEEE Topical Meeting on Silicon Monolithic Integrated Circuits in RF Systems*, pp. 110–113, Sep 2001.

[82] L. Najafizadeh, A. K. Sutton, R. M. Diestelhorst, M. Bellini, B. Jun, J. D. Cressler, P. W. Marshall, and C. J. Marshall, "A comparison of the effects of X-Ray and proton irradiation on the performance of SiGe precision voltage references," *IEEE Transactions on Nuclear Science*, vol. 54, pp. 2238–2244, Dec 2007.

[83] L. Najafizadeh, J. S. Adams, S. D. Phillips, K. A. Moen, J. D. Cressler, T. R. Stevenson, and R. M. Meloy, "Sub-1-K operation of SiGe transistors and circuits," *IEEE Electron Device Letters*, vol. 30, pp. 508–510, May 2009.

[84] Z. Feng, G. Niu, C. Zhu, L. Najafizadeh, and J. D. Cressler, "Temperature scalable modeling of SiGe HBT DC current down to 43 K," in *ECS Trans.*, vol. 3, pp. 927–936, 2006.

[85] P. R. Gray and R. G. Meyer, eds., *Analysis and Design of Analog Integrated Circuits*. New York: Wiley, 2001.

Appendices

Appendix A

Appendix A Full List of Temperature Scaling Equations

The actual device temperature is expressed as:

$$T = TEMP + DTA + 273.15 + V_{dT}, \tag{A.1}$$

where $TEMP$ is the ambient temperature in degree centigrade, DTA specifies a constant temperature shift to ambient temperature. V_{dT} is the increase in temperature ΔT due to self-heating. The difference in thermal voltage is given by:

$$\frac{1}{V_{\Delta T}} = \frac{1}{V_T} - \frac{1}{V_{T_{nom}}} = \frac{q}{k}\left(\frac{1}{T} - \frac{1}{T_{nom}}\right).$$
$$t_N = \frac{T}{T_{nom}} \tag{A.2}$$

A.1 Compact model parameter list

Table A.1: Compact model parameters overview.

#	*Symbol*	*Name*	*Description*
1	LEVEL	LEVEL	Model Level
2	EXMOD	EXMOD	Flag for extended modeling of the external regions
3	EXPHI	EXPHI	Flag for extended modeling of distributed HF effects in transients
4	EXAVL	EXAVL	Flag for extended modeling of avalanche current
5	MULT	MULT	Number of parallel transistors modeled together
6	T_{REF}	TREF	Reference temperature
7	Δ_{TA}	DTA	Difference between the local and global ambient temperatures
8	I_S	IS	Collector-emitter saturation current at T_{nom}
9	${}^{*}X_{TI}$	XTI	Temperature coefficient of I_S
10	${}^{*}E_{a,nom}$	Ea_nom	Temperature coefficient of I_S
11	I_{BEI}	IBEI	Forward base saturation current at T_{nom}
12	${}^{*}X_{TE}$	XTE	Temperature coefficient of I_{BEI}
13	${}^{*}E_{a,BEI,nom}$	EaBEI_nom	Temperature coefficient of I_{BEI}
14	I_{BCI}	IBCI	Reverse Base saturation current at T_{nom}
15	${}^{*}X_{TC}$	XTC	Temperature coefficient of I_{BCI}
16	${}^{*}E_{a,BCI,nom}$	EaBCI_nom	Temperature coefficient of I_{BCI}
17	N_F	NF	Forward collector-emitter current ideality factor at T_{nom}
18	${}^{*}X_{NF}$	XNF	Temperature coefficient of the N_F
19	${}^{*}A_{NF}$	ANF	Temperature coefficient of the N_F
20	N_R	NR	Reverse collector-emitter current ideality factor at T_{nom}
21	${}^{*}X_{NR}$	XNR	Temperature coefficient of the N_R
22	${}^{*}A_{NR}$	ANR	Temperature coefficient of the N_R
23	N_{EI}	NEI	Forward base current ideality factor at T_{nom}
24	${}^{*}X_{NE}$	XNE	Temperature coefficient of the N_{EI}
25	${}^{*}A_{NE}$	ANE	Temperature coefficient of the N_{EI}
26	N_{CI}	NCI	Reverse base current ideality factor T_{nom}
27	${}^{*}X_{NC}$	XNC	Temperature coefficient of the N_{CI}
28	${}^{*}A_{NC}$	ANC	Temperature coefficient of the N_{CI}
29	I_{BT}	IBT	Base tunneling current at T_{nom}
30	${}^{*}K_{TN}$	KTN	Temperature coefficient of I_{BT}
31	${}^{*}V_{TUN}$	VTUN	Temperature coefficient of base tunneling current

#	*Symbol*	*Name*	*Description*
32	${}^{*}N_{dop,RE}$	*Ndop_RE*	Temperature coefficient of the R_E
33	${}^{*}E_{dop,RE}$	*Edop_RE*	Temperature coefficient of the R_E
34	${}^{*}\alpha_{RE}$	*alpha_RE*	Temperature coefficient of the R_E
35	${}^{*}\beta_{RE}$	*beta_RE*	Temperature coefficient of the R_E
36	${}^{*}A_{RE}$	A_RE	Temperature coefficient of the R_E
37	${}^{*}R_{E}$	R_E	Emitter resistance at T_{nom}
38	${}^{*}N_{dop,RBC}$	*Ndop_RBC*	Temperature coefficient of the R_{BC}
39	${}^{*}E_{dop,RBC}$	*Edop_RBC*	Temperature coefficient of the R_{BC}
40	${}^{*}\alpha_{RBC}$	*alpha_RBC*	Temperature coefficient of the R_{BC}
41	${}^{*}\beta_{RBC}$	*beta_RBC*	Temperature coefficient of the R_{BC}
42	${}^{*}A_{RBC}$	A_RBC	Temperature coefficient of the R_{BC}
43	${}^{*}R_{BC}$	R_BC	Constant part of the base resistance at T_{nom}
44	${}^{*}N_{dop,RBV}$	*Ndop_RBV*	Temperature coefficient of the R_{BV}
45	${}^{*}E_{dop,RBV}$	*Edop_RBV*	Temperature coefficient of the R_{BV}
46	${}^{*}\alpha_{RBV}$	*alpha_RBV*	Temperature coefficient of the R_{BV}
47	${}^{*}\beta_{RBV}$	*beta_RBV*	Temperature coefficient of the R_{BV}
48	${}^{*}A_{RBV}$	A_RBV	Temperature coefficient of the R_{BV}
49	${}^{*}R_{BV}$	R_BV	Variable part of the base resistance at zero-bias and at T_{nom}
50	${}^{*}N_{dop,RCV}$	*Ndop_RCV*	Temperature coefficient of the R_{CV}
51	${}^{*}E_{dop,RCV}$	*Edop_RCV*	Temperature coefficient of the R_{CV}
52	${}^{*}\alpha_{RCV}$	*alpha_RCV*	Temperature coefficient of the R_{CV}
53	${}^{*}\beta_{RCV}$	*beta_RCV*	Temperature coefficient of the R_{CV}
54	${}^{*}A_{RCV}$	*A_RCV*	Temperature coefficient of the R_{CV}
55	${}^{*}R_{CV}$	R_CV	Resistance of the un-modulated epilayer at T_{nom}
56	${}^{*}N_{dop,RCC}$	*Ndop_RCC*	Temperature coefficient of the R_{CC}
57	${}^{*}E_{dop,RCC}$	*Edop_RCC*	Temperature coefficient of the R_{CC}
58	${}^{*}\alpha_{RCC}$	*alpha_RCC*	Temperature coefficient of the R_{CC}
59	${}^{*}\beta_{RCC}$	*beta_RCC*	Temperature coefficient of the R_{CC}
60	${}^{*}A_{RCC}$	A_RCC	Temperature coefficient of the R_{CC}
61	${}^{*}R_{CC}$	R_CC	Constant part of the collector resistance at T_{nom}
62	${}^{*}N_{dop,RSUB}$	*Ndop_RSUB*	Temperature coefficient of the R_{SUB}
63	${}^{*}E_{dop,RSUB}$	*Edop_RSUB*	Temperature coefficient of the R_{SUB}
64	${}^{*}\alpha_{RSUB}$	*alpha_RSUB*	Temperature coefficient of the R_{SUB}
65	${}^{*}\beta_{RSUB}$	*beta_RSUB*	Temperature coefficient of the R_{SUB}
66	${}^{*}A_{RSUB}$	*A_RSUB*	Temperature coefficient of the R_{SUB}
67	${}^{*}R_{SUB}$	*R_SUB*	Substrate resistance at T_{nom}

#	*Symbol*	*Name*	*Description*
68	C_{JE}	CJE	Zero-bias emitter-base depletion capacitance
69	V_{DE}	VDE	Emitter-base diffusion voltage
70	P_E	PE	Emitter-base grading coefficient
71	C_{BEO}	CBEO	Emitter-base overlap capacitance
72	XC_{j_E}	XCJE	Sidewall fraction of the emitter-base depletion capacitance
73	${}^*V_{GB}$	VGB	Band-gap voltage of the base
74	C_{JC}	CJC	Zero-bias collector-base depletion capacitance
75	V_{DC}	VDC	Collector-base diffusion voltage
76	P_C	PC	Collector-base grading coefficient
77	X_P	XP	Constant part of C_{j_c}
78	M_C	MC	Coefficient for current modulation of CB depletion capacitance
79	C_{BCO}	CBCO	Collector-base overlap capacitance
80	XC_{jC}	XCJC	Fraction of CB depletion capacitance under the emitter
81	${}^*V_{GC}$	VGC	Band-gap voltage of the collector
82	C_{JS}	CJS	Zero-bias collector-substrate depletion capacitance
83	V_{DS}	VDS	collector-substrate diffusion voltage
84	P_S	PS	collector-substrate grading coefficient
85	${}^*V_{GS}$	VGS	band-gap voltage of the substrate
86	C_{CS}	CCS	Substrate capacitance
87	C_{DT}	CDT	Substrate distributive capacitance
88	M_τ	MTAU	Non-ideality factor of the emitter stored charge
89	τ_E	TAUE	Minimum transit time of stored emitter charge
90	τ_B	TAUB	Transit time of stored base charge
91	τ_{epi}	TEPI	Transit time of stored epilayer charge
92	τ_R	TAUR	Transit time of reverse extrinsic stored base charge
93	${}^*A_{\tau_E}$	AB_TAUE	Temperature coefficient of the resistivity of the τ_E
94	${}^*dV_{g\tau_E}$	DVGTE	Band-gap voltage difference of emitter stored charge
95	${}^*A_{\tau_B}$	ATAUB	Temperature coefficient of the resistivity of the τ_B
96	${}^*A_{\tau_{EPI}}$	$AEPI\_TEPI$	Temperature coefficient of the resistivity of the τ_{epi}
97	I_{HC}	IHC	Critical current for velocity saturation in the epilayer
98	SCR_{CV}	SCRCV	Space charge resistance of the epilayer
99	${}^*A_{IHC}$	AIHC	Temperature coefficient of I_{HC}
100	${}^*B_{IHC}$	BIHC	Temperature coefficient of I_{HC}
101	V_{AVL}	VAVL	Voltage determining curvature of avalanche current
102	W_{AVL}	WAVL	Epilayer thickness used in weak-avalanche model
103	S_{FH}	SFH	Current spreading factor of avalanche model when EXAVL=1
104	A_{XI}	AXI	Smoothness parameter for the onset of quasi-saturation

#	*Symbol*	*Name*	*Description*
105	${}^{*}A_S$	AS	Temperature coefficient of the I_{S_S} and I_{K_S}
106	I_{SS}	ISS	Base-substrate saturation current
107	I_{KS}	IKS	Base-substrate high injection knee current
108	I_K	IK	Forward collector-emitter high injection knee current
109	${}^{*}AB_{I_K}$	*ABIK*	Temperature coefficient of I_K
110	I_{KR}	IKR	Reverse collector-emitter high injection knee current
111	${}^{*}A_{IKR}$	AIKR	Temperature coefficient of I_{KR}
112	${}^{*}X_{IKR}$	XIKR	Temperature coefficient of I_{KR}
113	I_{KEX}	IKEX	Collector-emitter high injection knee current for Iex
114	${}^{*}A_{IKEX}$	AIKEX	Temperature coefficient of I_{KEX}
115	${}^{*}X_{IKEX}$	XIKEX	Temperature coefficient of I_{KEX}
116	V_{ER}	VER	Reverse Early voltage
117	V_{EF}	VEF	Forward Early voltage
118	ΔE_g	DEG	Bandgap difference over the base
119	X_{REC}	XREC	Pre-factor of the recombination part of I_{b_1}
120	${}^{*}A_{QBO,VER}$	*AQBO_VER*	Temperature coefficient of the V_{ER}
121	${}^{*}A_{QBO,VEF}$	*AQBO_VEF*	Temperature coefficient of the V_{EF}
122	${}^{*}A_{QBO,DEG}$	*AQBO_DEG*	Temperature coefficient of the ΔE_g
123	I_{BF}	IBF	Saturation current of the non-ideal forward base current
124	M_{LF}	MLF	Non-ideality factor of the non-ideal forward base current
125	*VGJ	VGJ	Band-gap voltage recombination emitter-base junction
126	I_{BR}	IBR	Saturation current of the non-ideal reverse base current
127	V_{LR}	VLR	Cross-over voltage of the non-ideal reverse base current
128	XI_{B_1}	XIBI	Part of ideal base current that belongs to the sidewall
129	X_{EXT}	XEXT	Part of currents and charges that belong to extrinsic region

#	*Symbol*	*Name*	*Description*
130	A_F	AF	Exponent of the Flicker-noise
131	K_F	KF	Flicker-noise coefficient of the ideal base current
132	K_{FN}	KFN	Flicker-noise coefficient of the non-ideal base current
133	K_{AVL}	KAVL	Switch for white noise contribution due to avalanche
134	R_{TH}	RTH	Thermal resistance
135	C_{TH}	CTH	Thermal capacitance
136	A_{TH}	ATH	Temperature coefficient of the thermal resistance
137	${}^{*}C_{1,R_{TH}}$	*C1_RTH*	Temperature coefficient of R_{TH}
138	${}^{*}C_{2,R_{TH}}$	*C2_RTH*	Temperature coefficient of R_{TH}
139	${}^{*}C_{3,R_{TH}}$	*C3_RTH*	Temperature coefficient of R_{TH}

A.2 Saturation current and ideality factor

Ideality factor and saturation current of forward I_C-V_{BE}

$$N_F(T) = N_F \left[1 - \frac{T - T_{nom}}{T_{nom}} \left(A_{NF} \frac{T_{nom}}{T} \right)^{X_{NF}} \right], \tag{A.3}$$

where nominal temperature ideality factor N_F and temperature coefficient A_{NF}, X_{NF} are model fitting parameters.

$$\begin{aligned} E_{a,t} &= E_{a,nom} - \frac{\alpha\beta {T_{nom}}^2}{(T_{nom}+\beta)^2} + \frac{\alpha\beta T T_{nom}}{(T+\beta)(T_{nom}+\beta)}, \\ I_S(T) &= I_{S,nom} \left(\frac{T}{T_{nom}} \right)^{\frac{X_{IS}}{N_F(T)}} \exp\left(\frac{-E_{a,t}\left(1 - \frac{T}{T_{nom}}\right)}{N_F(T) V_T} \right), \end{aligned} \tag{A.4}$$

where $E_{a,nom}$ is the extrapolated 0 K E_g at nominal temperature and $I_{S,nom}$ is I_S at nominal temperature. X_{IS} includes the temperature coefficient of mobility and density of states, α=4.45 $\times 10^{-4}$ V/K, β=686 K. $E_{a,nom}$, $I_{S,nom}$, and X_{IS} are model fitting parameters.

#	*Parameter*	*Unit*	*Values*
1	N_F	-	1.004
2	A_{NF}	-	0.006115
3	X_{NF}	-	0.944
4	$E_{a,nom}$	eV	1.089
5	$I_{S,nom}$	A	2.723E-18
6	X_{IS}	-	4.195

Ideality factor and saturation current of reverse I_E-V_{BC}

$$N_R(T) = N_R \left[1 - \frac{T - T_{nom}}{T_{nom}} \left(A_{NR} \frac{T_{nom}}{T} \right)^{X_{NR}} \right], \tag{A.5}$$

where nominal temperature ideality factor N_R and temperature coefficient A_{NR}, X_{NR} are model fitting parameters.

$$\begin{aligned} E_{a,t} &= E_{a,nom} - \frac{\alpha\beta {T_{nom}}^2}{(T_{nom}+\beta)^2} + \frac{\alpha\beta T T_{nom}}{(T+\beta)(T_{nom}+\beta)}, \\ I_{SR}(T) &= I_{S,nom} \left(\frac{T}{T_{nom}} \right)^{\frac{X_{IS}}{N_R(T)}} \exp\left(\frac{-E_{a,t}\left(1 - \frac{T}{T_{nom}}\right)}{N_R(T) V_T} \right), \end{aligned} \tag{A.6}$$

#	*Parameter*	*Unit*	*Values*
1	N_R	-	1
2	A_{NR}	-	0.08383
3	X_{NR}	-	2

Ideality factor and saturation current of forward I_B-V_{BE}

$$N_{EI}(T) = N_{EI} \left[1 - \frac{T - T_{nom}}{T_{nom}} \left(A_{NE} \frac{T_{nom}}{T} \right)^{X_{NE}} \right], \tag{A.7}$$

where nominal temperature ideality factor N_{EI} and temperature coefficient A_{NE}, X_{NE} are model fitting parameters.

$$E_{a,BEI,t} = E_{a,BEI,nom} - \frac{\alpha\beta {T_{nom}}^2}{(T_{nom}+\beta)^2} + \frac{\alpha\beta T T_{nom}}{(T+\beta)(T_{nom}+\beta)},$$
$$I_{BEI}(T) = I_{BEI,nom}\left(\frac{T}{T_{nom}}\right)^{\frac{X_{IBEI}}{N_{EI}(T)}} \exp\left(\frac{-E_{a,BEI,t}\left(1-\frac{T}{T_{nom}}\right)}{N_{EI}(T)V_T}\right), \tag{A.8}$$

where $I_{BEI,nom}$, X_{IBEI} and $E_{a,BEI,nom}$ are model fitting parameters.

#	*Parameter*	*Unit*	*Values*
1	N_{EI}	-	1.02
2	A_{NE}	-	0.09063
3	X_{NE}	-	2.986
4	$E_{a,BEI,nom}$	eV	1.091
5	$I_{BEI,nom}$	A	2.498E-20
6	X_{IBEI}	-	5.323

Ideality factor and saturation current of reverse I_B-V_{BC}

$$N_{CI}(T) = N_{CI}\left[1 - \frac{T-T_{nom}}{T_{nom}}\left(A_{NC}\frac{T_{nom}}{T}\right)^{X_{NC}}\right], \tag{A.9}$$

where nominal temperature ideality factor N_{CI} and temperature coefficient A_{NC}, X_{NC} are model fitting parameters.

$$E_{a,BCI,t} = E_{a,BCI,nom} - \frac{\alpha\beta {T_{nom}}^2}{(T_{nom}+\beta)^2} + \frac{\alpha\beta T T_{nom}}{(T+\beta)(T_{nom}+\beta)},$$
$$I_{BCI}(T) = I_{BCI,nom}\left(\frac{T}{T_{nom}}\right)^{\frac{X_{IBCI}}{N_{CI}(T)}} \exp\left(\frac{-E_{a,BCI,t}\left(1-\frac{T}{T_{nom}}\right)}{N_{CI}(T)V_T}\right), \tag{A.10}$$

where $I_{BCI,nom}$, X_{IBCI} and $E_{a,BCI,nom}$ are model fitting parameters.

#	*Parameter*	*Unit*	*Values*
1	N_{CI}	-	0.9997
2	A_{NC}	-	0.1194
3	X_{NC}	-	2.798
4	$E_{a,BCI,nom}$	eV	0.9948
5	$I_{BCI,nom}$	A	1.343E-19
6	X_{IBCI}	-	8.38

A.3 Base tunneling current

$$I_{B,tun} = I_{BT}(T)\exp\left(\frac{V_{B_2E_1}}{V_{TUN}}\right)$$

$$I_{BT}(T) = I_{BT}\sqrt{t_N}\exp\left(K_{TN}\left(E_{g,TN} - E_{g,T}\right)\right)$$

I_{BT} is the nominal temperature saturation current and V_{TUN} represents the temperature independent slope of $I_{B,tun}$-V_{BE}. V_{TUN}, I_{BT}, K_{TN} are three model parameters specific to TAT. $E_{g,TN}$ and $E_{g,T}$ are the band gap at T_{nom} and T.

#	*Parameter*	*Unit*	*Values*
1	V_{TUN}	V	0.018
2	I_{BT}	A	60.85E-31
3	K_{TN}	-	192.11
4	$E_{g,TN}$	eV	1.02451923

A.4 Non-ideal base current

$$I_{BF}(T) = I_{BF}t_N^{(6-2M_{LF})}\exp\left[\frac{-V_{GJ}}{M_{LF}V_{\Delta T}}\right],$$
$$I_{BR}(T) = I_{BR}t_N^2\exp\left[\frac{-V_{GC}}{2V_{\Delta T}}\right]. \tag{A.11}$$

#	*Parameter*	*Unit*	*Values*
1	I_{BF}	A	1.002E-16
2	V_{GJ}	V	1.18
3	M_{LF}	-	2.2
4	I_{BR}	A	4.441E-31
5	V_{GC}	V	1.222

A.5 Early voltage

We introduce individual temperature parameter $A_{QB0,V_{EF}}$, $A_{QB0,V_{ER}}$ and $A_{QB0,\Delta E_g}$ for V_{EF}, V_{ER} and ΔE_g respectively.

$$\begin{aligned} V_{EF}(T) &= V_{EF} t_N^{A_{QB0,V_{EF}}} \left[(1 - X_P) \left(\frac{V_{dC}}{V_{dCT}} \right)^{PC} + X_P \right]^{-1}, \\ V_{ER}(T) &= V_{ER} t_N^{A_{QB0,V_{ER}}} \left(\frac{V_{dE}}{V_{dET}} \right)^{-p_E}, \\ \Delta E_g(T) &= \Delta E_g t_N^{A_{QB0,\Delta E_g}}. \end{aligned} \tag{A.12}$$

#	*Parameter*	*Unit*	*Values*
1	V_{EF}	V	23.55
2	$A_{QBO,VEF}$	-	-0.138
3	V_{ER}	V	9.379
4	$A_{QBO,VER}$	-	-0.138
5	$A_{QB0,\Delta E_g}$	-	0

A.6 *pn* junction diffusion voltage

Base-emitter junction diffusion voltage V_{dE}

$$V_{dE,T} = -3V_T \ln t_N + t_N V_{dE} + (1 - t_N) V_{GB}, \tag{A.13}$$

where V_{dE} is the nominal temperature base-emitter junction diffusion voltage, V_{GB} is the bandgap voltage of the base. V_{dE} and V_{GB} are model fitting parameters.

#	*Parameter*	*Unit*	*Values*
1	V_{dE}	V	1.028
2	V_{GB}	V	1.07

Base-collector junction diffusion voltage V_{dC}

$$V_{dC,T} = -3V_T \ln t_N + t_N V_{dC} + (1 - t_N) V_{GC}, \tag{A.14}$$

where V_{dC} is the nominal temperature base-collector junction diffusion voltage, V_{GC} is the bandgap voltage of the collector. V_{dC} and V_{GC} are model fitting parameters.

#	*Parameter*	*Unit*	*Values*
1	V_{dC}	V	0.8697
2	V_{GC}	V	1.222

Collector-substrate junction diffusion voltage V_{dS}

$$V_{dS,T} = -3V_T \ln t_N + t_N V_{dS} + (1 - t_N) V_{GS}, \tag{A.15}$$

where V_{dS} is the nominal temperature collector-substrate junction diffusion voltage, V_{GS} is the bandgap voltage of the substrate. V_{dS} and V_{GS} are model fitting parameters.

#	*Parameter*	*Unit*	*Values*
1	V_{dS}	V	1.102
2	V_{GS}	V	1.102

A.7 Depletion capacitance

$$
\begin{aligned}
C_{jE,T} &= C_{jE}\left(\frac{V_{dE}}{V_{dET}}\right)^{PE}, \\
C_{jC,T} &= C_{jC}\left[(1-X_P)\left(\frac{V_{dC}}{V_{dCT}}\right)^{PC}+X_P\right]^{-1}, X_{P,T} = X_P\frac{C_{JC}}{C_{JCT}}, \\
C_{jST} &= C_{jS}\left(\frac{V_{dS}}{V_{dST}}\right)^{PS},
\end{aligned}
\tag{A.16}
$$

#	*Parameter*	*Unit*	*Values*
1	C_{jE}	fF	12.42
2	PE		0.2562
3	C_{jC}	fF	5.897
4	PC		0.6789
5	X_P		0.515
6	C_{jS}	fF	8.8
7	PS		0.160

A.8 Parasitic resistances

$$
\begin{aligned}
N_C &= 2.8\times10^{19}\times\left(\frac{T}{300}\right)^{1.5}, \\
N_V &= 3.14\times10^{19}\times\left(\frac{T}{300}\right)^{1.5}.
\end{aligned}
\tag{A.17}
$$

Emitter resistance R_E

$$
\begin{aligned}
G &= g_D^{-1}\frac{N_C}{N_{dop,RE}}\exp\left(-\frac{E_{dop,RE}}{kT}\right), g_D = 2, \\
b &= 1-\frac{\beta_{RE}}{1+\left(\frac{T}{T0}\right)^{\alpha_{RE}}},, \\
IR(T) &= \frac{-G+(1-b)+\sqrt{[G-(1-b)]^2+4G}}{2}, \\
R_E(T) &= R_E\left(\frac{T}{T_{nom}}\right)^{A_{RE}}\frac{1}{IR(T)},
\end{aligned}
\tag{A.18}
$$

where the impurity concentration $N_{dop,RE}$, the impurity activation energy $E_{dop,RE}$, the fraction of bound impurity states coefficients β_{RE} and α_{RE}, the fictitious nominal temperature complete ionization resistance R_E and the mobility temperature coefficient A_{RE} are model fitting parameters.

#	*Parameter*	*Unit*	*Values*
1	$N_{dop,RE}$	cm^{-3}	4.177E18
2	$E_{dop,RE}$	mV	5.366
3	α_{RE}	-	-0.4506
4	β_{RE}	-	1
5	A_{RE}	-	-0.2409
6	R_E	Ω	11.84

Constant part of the base resistance R_{BC}

$$
\begin{aligned}
G &= g_A^{-1}\frac{N_V}{N_{dop,RBC}}\exp\left(-\frac{E_{dop,RBC}}{kT}\right), g_A = 4,\\
b &= 1-\frac{\beta_{RBC}}{1+\left(\frac{T}{T0}\right)^{\alpha_{RBC}}},,\\
IR(T) &= \frac{-G+(1-b)+\sqrt{[G-(1-b)]^2+4G}}{2},\\
R_{BC}(T) &= R_{BC}\left(\frac{T}{T_{nom}}\right)^{A_{RBC}}\frac{1}{IR(T)},
\end{aligned}
\tag{A.19}
$$

where the impurity concentration $N_{dop,RBC}$, the impurity activation energy $E_{dop,RBC}$, the fraction of bound impurity states coefficients β_{RBC} and α_{RBC}, the fictitious nominal temperature complete ionization resistance R_{BC} and the mobility temperature coefficient A_{RBC} are model fitting parameters.

#	*Parameter*	*Unit*	*Values*
1	$N_{dop,RBC}$	cm^{-3}	1.564E18
2	$E_{dop,RBC}$	mV	6.641
3	α_{RBC}	-	-0.7477
4	β_{RBC}	-	0.9897
5	A_{RBC}	-	1.108
6	R_{BC}	Ω	28.02

Constant part of the collector resistance R_{CC}

$$
\begin{aligned}
G &= g_D^{-1} \frac{N_C}{N_{dop,RCC}} \exp\left(-\frac{E_{dop,RCC}}{kT}\right), g_D = 2, \\
b &= 1 - \frac{\beta_{RCC}}{1 + \left(\frac{T}{T0}\right)^{\alpha_{RCC}}}, , \\
IR(T) &= \frac{-G + (1-b) + \sqrt{[G-(1-b)]^2 + 4G}}{2}, \\
R_{CC}(T) &= R_{CC} \left(\frac{T}{T_{nom}}\right)^{A_{RCC}} \frac{1}{IR(T)},
\end{aligned}
\tag{A.20}
$$

where the impurity concentration $N_{dop,RCC}$, the impurity activation energy $E_{dop,RCC}$, the fraction of bound impurity states coefficients β_{RCC} and α_{RCC}, the fictitious nominal temperature complete ionization resistance R_{CC} and the mobility temperature coefficient A_{RCC} are model fitting parameters.

#	*Parameter*	*Unit*	*Values*
1	$N_{dop,RCC}$	cm^{-3}	7.438E18
2	$E_{dop,RCC}$	mV	41.54
3	α_{RCC}	-	-0.4506
4	β_{RCC}	-	1
5	A_{RCC}	-	0.6656
6	R_{CC}	Ω	34.89

Resistance of the un-modulated epilayer R_{CV}

$$
\begin{aligned}
G &= g_D^{-1}\frac{N_C}{N_{dop,RCV}}\exp\left(-\frac{E_{dop,RCV}}{kT}\right), g_D = 2,\\
b &= 1-\frac{\beta_{RCV}}{1+\left(\frac{T}{T0}\right)^{\alpha_{RCV}}},,\\
IR(T) &= \frac{-G+(1-b)+\sqrt{[G-(1-b)]^2+4G}}{2},\\
R_{CV}(T) &= R_{CV}\left(\frac{T}{T_{nom}}\right)^{A_{RCV}}\frac{1}{IR(T)},
\end{aligned}
\tag{A.21}
$$

where the impurity concentration $N_{dop,RCV}$, the impurity activation energy $E_{dop,RCV}$, the fraction of bound impurity states coefficients β_{RCV} and α_{RCV}, the fictitious nominal temperature complete ionization resistance R_{CV} and the mobility temperature coefficient A_{RCV} are model fitting parameters.

#	*Parameter*	*Unit*	*Values*
1	$N_{dop,RCV}$	cm^{-3}	8.118E16
2	$E_{dop,RCV}$	mV	22.83
3	α_{RCV}	-	-4.142
4	β_{RCV}	-	1
5	A_{RCV}	-	-1.34
6	R_{CV}	Ω	82.5

Variable part of the base resistance at zero-bias R_{BV}

$$
\begin{aligned}
G &= g_A^{-1}\frac{N_V}{N_{dop,RBV}}\exp\left(-\frac{E_{dop,RBV}}{kT}\right), g_A = 4,\\
b &= 1-\frac{\beta_{RBV}}{1+\left(\frac{T}{T0}\right)^{\alpha_{RBV}}},,\\
IR(T) &= \frac{-G+(1-b)+\sqrt{[G-(1-b)]^2+4G}}{2},\\
R_{BV}(T) &= R_{BV}\left(\frac{T}{T_{nom}}\right)^{A_{RBV}}\frac{1}{IR(T)},
\end{aligned}
\tag{A.22}
$$

where the impurity concentration $N_{dop,RBV}$, the impurity activation energy $E_{dop,RBV}$, the fraction of bound impurity states coefficients β_{RBV} and α_{RBV}, the fictitious nominal temperature complete ionization resistance R_{BV} and the mobility temperature coefficient A_{RBV} are model fitting parameters.

#	*Parameter*	*Unit*	*Values*
1	$N_{dop,RBV}$	cm^{-3}	5.314E16
2	$E_{dop,RBV}$	mV	54.05
3	α_{RBV}	-	-1.36
4	β_{RBV}	-	0.2958
5	A_{RBV}	-	-0.1434
6	R_{BV}	Ω	288.6

Substrate resistance R_{SUB}

$$
\begin{aligned}
G &= g_A^{-1} \frac{N_V}{N_{dop,RSUB}} \exp\left(-\frac{E_{dop,RSUB}}{kT}\right), g_A = 4, \\
b &= 1 - \frac{\beta_{RSUB}}{1 + \left(\frac{T}{T0}\right)^{\alpha_{RSUB}}}, , \\
IR(T) &= \frac{-G + (1-b) + \sqrt{[G-(1-b)]^2 + 4G}}{2}, \\
R_{SUB}(T) &= R_{SUB} \left(\frac{T}{T_{nom}}\right)^{A_{RSUB}} \frac{1}{IR(T)},
\end{aligned} \tag{A.23}
$$

where the impurity concentration $N_{dop,RSUB}$, the impurity activation energy $E_{dop,RSUB}$, the fraction of bound impurity states coefficients β_{RSUB} and α_{RSUB}, the fictitious nominal temperature complete ionization resistance R_{SUB} and the mobility temperature coefficient A_{RSUB} are model fitting parameters.

#	*Parameter*	*Unit*	*Values*
1	$N_{dop,RSUB}$	cm^{-3}	5.011E14
2	$E_{dop,RSUB}$	mV	59.4
3	α_{RSUB}	-	-4.309
4	β_{RSUB}	-	0
5	A_{RSUB}	-	1.676
6	R_{SUB}	Ω	1500

A.9 I_{HC} and SCR_{CV}

$$
\begin{aligned}
I_{HC,T} &= I_{HC} t_N{}^{-A_{IHC}(T-T_{nom})-B_{IHC}}, \\
SCR_{CV,T} &= SCR_{CV} t_N{}^{A_{IHC}(T-T_{nom})+B_{IHC}},
\end{aligned} \tag{A.24}
$$

#	*Parameter*	*Unit*	*Values*
1	A_{IHC}	-	0.0008409
2	B_{IHC}	-	0.6874

A.10 Knee current

We introduce individual temperature parameters for I_K, I_{KR} and I_{KEX}.

$$
\begin{aligned}
I_K(T) &= I_K t_N^{1-AB_{IK}}, \\
I_{KR}(T) &= I_{KR} t_N^{A_{IKR}} \exp\left(\frac{-X_{IKR}(1-t_N)}{V_T}\right), \\
I_{KEX}(T) &= I_{KEX} t_N^{A_{IKEX}} \exp\left(\frac{-X_{IKEX}(1-t_N)}{V_T}\right),
\end{aligned}
\tag{A.25}
$$

#	*Parameter*	*Unit*	*Values*
1	I_K	A	0.0077
2	AB_{IK}	-	0.3254
3	I_{KR}	A	0.015
4	A_{IKR}	-	0.02
5	X_{IKR}	-	0.09
6	I_{KEX}	A	0.01058
7	A_{IKEX}	-	0.07
8	X_{IKEX}	-	0.005

A.11 Transit times

We introduce individual temperature parameter A_{τ_E}, A_{τ_B} and $A_{\tau_{epi}}$ for τ_E, τ_B and τ_{epi} respectively.

$$\begin{aligned}
\tau_E(T) &= \tau_E t_N^{(A_{\tau_E}-2)} \exp(-\frac{dV_{g\tau_E}}{V_{\Delta T}}),\\
\tau_B(T) &= \tau_B t_N^{(A_{\tau_B}-1)},\\
\tau_{epi}(T) &= \tau_{epi} t_N^{(A_{\tau_{epi}}-1)},\\
\tau_R(T) &= \tau_R \frac{\tau_B(T)+\tau_{epi}(T)}{\tau_B+\tau_{epi}}.
\end{aligned} \tag{A.26}$$

#	*Parameter*	*Unit*	*Values*
1	τ_E	s	0
2	A_{τ_E}	-	1
3	$dV_{g\tau_E}$	-	0.1099
4	τ_B	s	1.179E-12
5	A_{τ_B}	-	1.9
6	τ_{epi}	s	9.74E-11
7	$A_{\tau_{epi}}$	-	-1.34
8	τ_R	-	1.3E-9

A.12 Thermal resistance

$$R_{TH,T_{amb}} = C_{1,R_{TH}} {T_{amb}}^3 + C_{2,R_{TH}} {T_{amb}}^2 + C_{3,R_{TH}} T_{amb} + R_{TH}. \tag{A.27}$$

#	*Parameter*	*Unit*	*Values*
1	R_{TH}	°C/W	4235
2	$C_{1,R_{TH}}$	-	-0.0001154
3	$C_{2,R_{TH}}$	-	0.09645
4	$C_{3,R_{TH}}$	s	-17.64

A.13 Substrate Currents

$$I_{SS}(T) = I_{SS} t_N^{(4-A_S)} \exp(-\frac{V_{GS}}{V_{\Delta T}}),$$
$$I_{KS}(T) = I_{KS} t_N^{(1-A_S)} (\frac{IS(T)}{I_S})(\frac{I_{SS}}{I_{SS}(T)}). \quad \text{(A.28)}$$

#	*Parameter*	*Unit*	*Values*
1	I_{SS}	A	3.661E-21
2	I_{KS}	A	0.5
3	A_S	-	0.5